UNIVERSITY OF BIRMINGHAM

Formation, flow and dynamic stability of foams generated from viscous shear-thinning fluids

By

Saifullah Jabarkhyl

A thesis submitted to

The University of Birmingham

For the degree of

DOCTOR OF PHILOSPHY

School of Chemical Engineering

College of Engineering and Physical Sciences

University of Birmingham

April 2020

Abstract

Foams are complex, multi-component, structures that are present in a wide range of industrial applications such as foods, pharmaceuticals, mineral transport, oil and gas. Specifically, in the food industry, foaming is ubiquitous since many foamed products, for example ice cream, whipped cream and chocolate mousse contain air in the form of microscopic bubbles. These bubbles reduce the number of calories, impart better texture and improve organoleptic properties. Therefore, a foaming operation which can achieve a good degree of control of the air volume fraction and bubble size distribution is of paramount importance. In this research study, an advanced, non-invasive, X-ray micro-Computed Tomography technique is adopted to probe the three-dimensional microstructure of a range of wet foams generated from viscous pseudoplastic fluids using a pilot-scale continuous rotor-stator device. For the first time ever, an extensive study is conducted to elucidate the combined influence of processing parameters (rotor speed and gas-liquid volumetric flowrate (G/L) ratio) and liquid properties (surfactant content and xanthan gum concentration) on foam formation from shear-thinning fluids using a multi-stage rotor-stator unit. Rotor speed, residence time and G/L ratio were the dominant factors responsible for achieving fine-textured and highly statically stable foams. In addition, operating at $N > 2000$ rpm is undesirable both in terms of energy efficiency and product microstructure. The dynamic foam stability is investigated by passing wet foams through narrow orifice constrictions. It is established that the microstructure of wet foams is preserved when allowed to flow through a narrow orifice constriction provided there is a minimal pressure drop (< 5000 Pa). For foam flows with a high pressure drop (> 36000 Pa), however, a combination of foam expansion and bubble coalescence is responsible for the loss of air volume and bubble coalescence. Furthermore, by increasing the rotor speed (i.e. energy input), surfactant

concentration and continuous phase apparent viscosity, the rate of bubble coalescence can be significantly reduced. The effects of rotor speed, however, became only significant at a rotor speed of N = 2000 rpm. Such a wet foam, with a more uniform bubble size distribution, was able to pass through a narrow orifice constriction with a relatively less bubble coalescence. An extensive study of steady shear and dynamic oscillatory rheometry of wet foams generated from viscous shear-thinning fluids is also conducted as part of this research. At air volume fractions of $\phi < \approx 0.60$, the bubble size distribution had a negligible effect on the steady shear flow curves and viscoelastic properties of the foam. However, at air volume fractions of $\phi \approx > 0.60$, the apparent viscosity and storage moduli increase significantly as bubble size becomes smaller and more uniform with increasing rotor speed. Moreover, a novel simultaneous in-situ foam microstructure visualisation and rheometry are conducted to explicate the flow complexities that can arise when such structured fluids are imposed to higher shear rates. Simultaneous in-situ visualisation of the foams under shear confirmed the absence of bubble breakage and, for the first time, unravelled the existence of inward radial shear-induced migration of liquid, which is responsible for the time-dependence of the foams.

Dedication

This thesis is dedicated to the family of Shair's Mohammed Jabarkhyl. I am grateful to Allah and my beloved parents, siblings & my wife for their continued support throughout this research study which seems to be unending journey.

"Be kind, for whenever kindness becomes part of something, it beautifies it. Whenever it is taken from something, it leaves it tarnished ...." (sayings of beloved Prophet Mohammed p.b.u.h).

Acknowledgements

First and foremost, I would like to sincerely thank my academic supervisor, Prof. Mostafa Barigou, for his continuous encouragement, support, and his contribution to this research study. Without his encouragement, I would not have completed this study. Secondly, I would like to thank my industrial supervisors from Unilever, Dr. Shiping Zhu and his colleagues: Dr. Pip Rayment; Dr. Damiano Rosetti; Dr. David Lloyd; and Dr. Bill Frith for their support and industrial steer to this study. My sincere thanks also go to Prof. Farid Benyahia; Lynn Draper; and her colleagues, especially Christine Dickinson. I would also like to thank our Mechanical Engineering workshop legends especially Bob for his endless support. Finally, I would like to thank my office colleagues including Mustapha, Naser Khan, Gianluca, Samir, George, Sidra, Adam, Sulaiman, Abdul, Syeda, Abdullah, Mandar, Ahmed, …. for their company and good times.

Table of Content

List of Figures

List of Tables

Chapter 1: Introduction and Background

1.1 Introduction

A foam is a complex multiphase dispersion consisting of gas bubbles immersed in a continuous liquid, semi-liquid, or a solid phase. The foam unique mechanical properties give rise to numerous applications in the fields of food engineering, construction, mineral transport, firefighting, oil, and gas industries. Specifically, in the food industry, aerated products such as chocolate mousse, ice cream, and whipped cream are ubiquitous and are very popular amongst consumers. Inclusion of micro-bubbles inside these aerated products imparts a unique and luxurious taste (Campbell and Mougeot, 1999). In addition, it leads to a significant reduction in the number of calories, enhances the texture, mechanical and organoleptic properties. The air volume fraction (ϕ) and the bubble size distribution (BSD) are the two main components that contribute to the internal microstructure and hence, a good degree control of the air volume fraction and BSD is desirable for several industries.

In most industrial applications, stable and fine-textured foams are of utmost importance. Generally speaking, most aqueous foams are statically stable for a few hours to several days, but some foams have shown extraordinary static stability including many months (Cox,Aldred and Russell, 2009, Green *et al.*, 2013). This, however, requires a surfactant with excellent stabilisation properties. Specifically, during mechanical foaming using a continuous rotor-stator device, a surfactant possessing excellent stabilisation properties and fast adsorption kinetics is desirable due to the very short residence time that can exist within these devices (Müller-

Fischer,Suppiger and Windhab, 2007b). One such emulsifier which has shown this potential is a commercially available non-ionic emulsifier - polyglycerol ester of fatty acids (PGE 55) (Duerr-Auster *et al.*, 2007, Duerr-Auster,Gunde and Windhab, 2008). Currently, there are very few papers dedicated to foam formation and stabilisation using non-Newtonian fluids and commercially available non-ionic food-grade surfactants (Müller-Fischer and Windhab, 2005, Kroezen,Groot Wassink and Bertlein, 1988a, Kroezen and Wassink, 1987, Müller-Fischer,Suppiger and Windhab, 2007b). Most studies, however, utilised Newtonian fluids with high-molecular weight protein as a foam stabiliser (Mary *et al.*, 2013, Seguineau De Preval *et al.*, 2014b). Without a doubt, these studies are useful to enhance the fundamental knowledge of aqueous foam formation and stabilisation. In most cases, however, it does not mimic the actual formulation, especially, such as those utilised in the food processing industry. Therefore, a detailed study on foam formation and stabilisation using complex, viscous, non-Newtonian fluids at a pilot-scale continuous rotor-stator device is of a huge demand. Consequently, one of the objectives of this thesis were to fill this gap in the open literature.

A good degree control of the air volume fraction and BSD requires tools and techniques which can accurately predict these properties. Generally speaking, to determine the Sauter mean bubble diameter (D_{32}), with much less emphasise placed on reporting a representative BSD, most studies reported so far have used intrusive two-dimensional techniques such as light microscopy. Depending on the nature of the foams, such techniques are prone to several errors which when combined can significantly under or over-predict the true average mean bubble diameter and BSD (Gaillard *et al.*, 2017). For these reasons, it is necessary to adopt a measurement technique which can eliminate all or at least some of these errors and hence give a much better representation of the actual three-dimensional microstructure. One such

technique, which has attracted a much-needed attention, is X-ray micro-Computed Tomography (X-ray micro-CT). So far, very few studies have probed the 3-D microstructure of wet foams using X-ray micro-CT. To fill this gap, in this thesis, a non-invasive 3D X-ray micro-CT is employed to visualise the internal microstructure of a range of wet foams generated using a multistage rotor-stator device.

By nature, foams are complex thermodynamically and kinetically unstable fluids and the understanding of its behaviour becomes even more challenging when it starts to flow. Knowledge pertaining to foam flow behaviour is essential since in most industrial applications foams are allowed to flow through narrow complex geometries with unintended and undesirable consequences. Therefore, empirical studies pertaining to probing such flow behaviour is of a huge interest especially for food processing industry, i.e. Unilever. In the design of a food foam flow system, it is therefore important to consider the possible effects on the end-of-pipe structure and, hence, quality attributes of the foam. These effects may have serious practical implications and must be carefully considered as preservation of product microstructure and quality is important. To date, there are very limited studies that investigated this dynamic flow behaviour especially through narrow complex geometries with a rapid pressure drop (Calvert, 1988, Calvert, 1990, Deshpande and Barigou, 2000, Deshpande and Barigou, 2001a, Deshpande and Barigou, 2001b).

Bulk foams are opaque and therefore obtaining detailed microstructural information at the bubble scale to formalise into models to capture the 3D physical phenomena is hard and currently unattainable. To overcome this situation, most experimental studies have resorted to confining foams between two glass plates forming a 2D bubble monolayer, which renders the

structure transparent (see for example Badve and Barigou, 2020). Such 2D idealised systems are useful for obtaining detailed morphological transformation but do not necessarily represent actual industrial processes (Badve and Barigou, 2020). Currently, there is a total lack of empirical studies that investigated industrially relevant flows with complex non-Newtonian properties. Mathematical modelling is seriously lagging behind experimental work and cannot currently cope with the complexities of foam flows. Experimental studies of this kind are, however, essential to inform the modelling of these complex systems and help advance the field.

Another aspect of the foam behaviour which, however, is extensively investigated but equally important is foam rheometry. The well-controlled nature of such experiments has successfully identified the main factors responsible for the foam flow behaviour with most studies concluding foams to be shear-thinning fluids sometimes with a yield stress. The underlying assumption, however, in several of these studies is that little to negligible perturbation occurs to the complex microstructure during flow. As noted previously, foams are complex fluids with an unpredictable nature when they start to flow. Several complexities can arise including the commonly stated wall-slip and shear-banding (Lexis and Willenbacher, 2014). It is therefore of a paramount importance to conduct such flow experiments while simultaneously probing its microstructure. Proposing and implementing such a technique is of a considerable importance for examining the flow behaviour of several complex fluids including foams, emulsions and particle suspensions. Furthermore, there are scarce empirical studies that examined the foam rheology at the point of a packing transition region corresponding to an air volume fraction range of ~ 0.74 – 0.78.

In summary, this thesis aims to study the formation, flow and dynamic stability of wet foams generated from shear-thinning model fluids using a continuous multi-stage rotor-stator device. Highly statically stable foams are generated by varying the processing conditions (rotor speed, G/L ratio, residence time) and liquid properties (surfactant content and hydrocolloid content). The flow and dynamic stability are investigated by using a new simultaneous visualisation and rheometry set-up and narrow orifice plates as a flow constriction.

1.2 Business case

Unilever PLC, one of the leading consumer conglomerates, is the collaborator of this project. Currently, Unilever PLC has worked on and developed several patented technologies to stabilise air bubbles in ice cream formulations which contains among other ingredients dairy proteins and fats. These formulations can be either aerated in a batch mode (for instance using kitchen type Hobart mixer) or in a continuous mode using high-shear rotor-stator devices. In addition, Unilever has developed model fluids that have rheological properties equivalent to ice cream consisting of sugars, thickeners and an emulsifier. Once aerated, the bubbles are stable within few days to weeks against disproportionation at static conditions. This is mainly due to the continuous phase possessing a yield stress or high zero-shear viscosity which prevents the process of bubble creaming. However, it is known that during processing, the presence of flow constrictions such as a bend and filling nozzle can bring about drastic changes to the characteristics of aerated products, i.e. bubble coarsening and loss of bubble volume which is undesirable. Therefore, the aim of this thesis is to understand the formation, flow and dynamic stability of foams generated from shear-thinning model fluids using a multistage continuous rotor stator device. By doing so, a processing window will be established which will enable

Unilever PLC to manufacture and process aerated products with a minimal compromise to its product quality.

1.3 Objectives

- To compare and contrast suitable foam imaging techniques for 2D and 3D microstructure characterisation of a wide range of wet foams (Chapter 3).

- To investigate and optimise a range of processing parameters and fluid composition for the generation of stable wet foams from shear-thinning fluids using a multistage rotor-stator device (Chapter 4).

- To examine the quasi – and dynamic stability of a range of wet foams by passing it through a narrow orifice flow constriction [$0.133 \geq d_0/D \leq 0.06$ & $37 \geq Re \leq 300$] with and without significant pressure drop (Chapter 5).

- To elucidate the complex flow phenomena by performing a detailed in-situ foam visualisation and rheometry (steady & oscillatory) studies using a novel experimental set-up (Chapter 6).

1.4 Thesis outline

An introduction, a business case, aims and objectives of this thesis are presented in **Chapter 1**. **Chapter 2** provides a general background encompassing fundamental knowledge of foam formation, structure, flow and dynamic stability. Recent advances in foam rheology and studies pertaining to foam flow through flow constrictions will also be highlighted. **Chapter 3** will compare two foam imaging techniques namely 2D light microscopy and 3D X-ray micro-Computed Tomography (X-ray micro-CT) techniques. In **Chapter 4** a detailed study is conducted on foam generation using a multistage rotor-stator device. A combined effects of processing parameters (rotor speed, residence time and gas-liquid volumetric flowrate (G/L) ratio) and liquid formulation (surfactant and thickener concentration) on air volume fraction and bubble size distribution is exemplified. Currently, there are very few studies dedicated to the foam flow and dynamic stability. In this thesis, a detailed study of foam flow through narrow orifice constriction is discussed in **Chapter 5**. **Chapter 6** will provide a detailed study on foam rheology (steady shear and oscillatory rheometry) and in-situ foam visualisation using a new experimental set-up. An overall summary of thesis along with potential future work is provided in **Chapter 7**.

1.5 Publications, conferences and awards

The results and discussion presented within this thesis are published as follows:

Jabarkhyl, S., Zhu, S., Rayment, P., Lloyd, D.M., Rossetti, D., Barigou, M., (2019). Foams generated from viscous non-Newtonian shear-thinning liquids in a continuous multi rotor-stator device. Innovative Food Science and Emerging Technologies, Vol. 59.

Jabarkhyl, S., Barigou, M., Badve, M., Zhu, S., (2020). Rheological properties of wet foams generated from viscous pseudoplastic fluids. Innovative Food Science and Emerging Technologies, Vol. 64.

Jabarkhyl, S., Barigou, M, Zhu, S., (Accepted in Journal of Food Engineering). Dynamic interactions of foamed viscous shear-thinning fluids with an orifice flow constriction.

The results and discussion presented within this thesis were presented in the followings:

Poster presentations:

Jabarkhyl, S., Zhu, S., Barigou, M., (2018), Effects of liquid properties and processing conditions of a pilot-scale continuous rotor-stator device on foam generation. ChemEngDay-2018, Leeds, UK.

Oral Presentations:

Jabarkhyl, S., Zhu, S., Barigou, M., (2018), Rheology and dynamic stability of foams generated from viscous non-Newtonian liquids in a continuous rotor-stator device. 16th Conference of the International Association of Colloid and Interface Scientists, 21st – 25th May 2018, Rotterdam, the Netherlands.

Jabarkhyl, S., Zhu, S., Rayment, P., Barigou, M., (2018), Rheological and flow properties of foams generated from viscous shear-thinning liquids using a continuous rotor-stator device. EUFoam, 10th – 12th July 2018, Liege, Belgium.

Jabarkhyl, S., Zhu, S., Rayment, P., Lloyd, D.M., Rossetti, D., Barigou, M., (2019), Rheology and microstructure of foams generated from viscous shear-thinning liquids using a continuous rotor-stator device. The 8th International Symposium on Food Rheology and Structure – ISFRS 17th – 20th June 2019, Zurich Switzerland.

Awards:

BP best poster award at ChemEngDay – 2018 Leeds, UK.

Chapter 2: General Background

Summary

The sole purpose of the following chapter is to give an overall introduction to foam properties as well as mechanisms of foam formation, stabilisation, flow and dynamic stability. First, a general definition of a foam is given along with description of a foam microstructure and the three main foam destabilisation mechanisms namely gravity drainage, coalescence and disproportionation. Subsequently, a summary about interfacial tension and the different types of surfactants available to stabilise an air-water interface will be provided. Subsequently, foam formation using mechanical methods will be outlined. Specifically, foaming using a continuous rotor-stator device will be discussed and the mechanism of air incorporation will be highlighted. Towards the end, literature pertaining to foam flow and dynamic stability will also be deliberated and relevant open literature highlighted. In addition, fundamental problems pertaining to foam formation, flow and dynamic stability will also be highlighted accordingly.

2.1 Foam definition and properties

A foam is a complex dispersion consisting of gas bubbles (dispersed phase, commonly in the size range of 0.1 – 3.0 mm) embedded in a continuous liquid, semi-liquid or a solid phase. The volume fraction of the dispersed phase can range from 0.05 to 0.99 giving rise to a variety of foams of different microstructures and mechanical properties (Walstra, 1989). Generally, foams are broadly classified into two distinct geometrical bubble structures: (i) 'wet foams' which have spherical cells with a thick lamella and a low gas volume fraction (Fig. 2.1a); (ii) 'dry foams' which have polyhedral cells with a thin lamella and a high gas volume fraction as shown in Fig. 2.1b. Depending on the gas volume fraction and bubble size distribution (BSD), however, a packing transition region is reached when the gas volume fraction reaches approximately 0.64 for a monodispersed foam and or 0.74 – 0.78 for a foam of a polydisperse nature (Lexis & Willenbacher, 2014; Sjoblom, 2001).

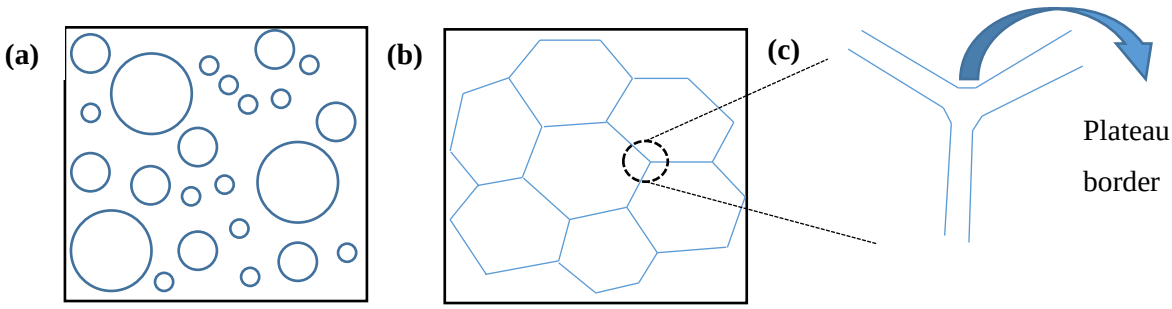

Fig. 2.1: Schematic showing (a) wet foam with spherical bubbles; (b) dry foam with polyhedral bubbles; and (c) Three film meeting forming a Plateau border.

Foams are ubiquitous and are often encountered in our daily lives. As noted previously, it has found applications in a wide range of industries such as food processing, cosmetics, firefighting, oil and gas, construction, mineral transport, etc. Specifically, in the food industry, foams are either incorporated into a product as a unit operation or found as finished ready-to-eat products. In all the aforementioned applications, the air volume fraction and BSD plays a pivotal role in

terms of functionality, stability and rheological properties (Du *et al.*, 2001). In the food industry, for example, the inclusion of air bubbles in products such as ice cream, champagne, bread, whipped cream, beer, etc. increases the product perception and quality attributes. A product with a fine and uniform BSD is desirable for good shelf life, whereas, a product with a wide BSD is an advantageous when a specific mouthfeel response is required (Cullen, 2009).

For effective foam application, however, a good degree of control of air volume fraction and BSD is essential. Therefore, to study the BSD, many experimental techniques have been developed and proposed. These include conductivity probe, the optical fibre-based method, advanced image analysis technique, light transmission, freezing and visualising cross-sections, X-ray micro-Computed Tomography (X-ray micro-CT), ultrasonic reflectance spectroscopy, confocal scanning laser microscopy (CLSM) and digital photography methods with and without a microscope as summarised in Table 2.1 (Kulmyrzaev,Cancelliere and McClements, 2000, Lim and Barigou, 2004, Jang *et al.*, 2005, Cullen, 2009, Stevenson, 2012) . Each of these methods have their own advantages and drawbacks. For example, experimental techniques involving probe sensors are often intrusive and require the systems to be very dilute (Cullen, 2009). Similarly, light microscopy, which is commonly used, is usually intrusive as it often requires sampling the foam and sometimes diluting the sample especially when the bubble size is small, and the bubble density is high. Other techniques suffer from similar limitations which involve significant tampering with the foam samples. In contrast, X-ray micro-CT is a non-invasive and no prior sample preparation is required (Lim and Barigou, 2004, Barigou and Douaire, 2013). In addition, it provides a detailed 3D internal microstructure of foams.

Table 2.1: Bubble size techniques for different food systems adapted from (Sahu and Niranjan, 2009).

Material	Technique	Bubble size (μm)	Reference
Bread dough	Freezing of sample and slicing	20 – 50	(Primo-Martín *et al.*, 2005)
Whipped cream	Photography and image analysis	10 – 40	(Jakubczyk and Niranjan, 2006b)
Model cake batter	Photography and Image analysis	20 – 50	(Massey and Niranjan, 2001)
Macro-aerated chocolate	X-ray tomography (X-ray micro-CT)	600 – 1400	(Haedelt *et al.*, 2005)
Milk foam	CLSM	60 – 100	(Silva *et al.*, 2008)
Beer	Optical probe	20 – 120	(Bisperink,Ronteltap and Prins, 1992)
Whey protein solution	Ultrasonic reflectance spectroscopy	10 – 160	(Kulmyrzaev,Bryant and McClements, 2000)
Ice cream	Confocal scanning laser microscopy	50 – 150	(Bisperink,Ronteltap and Prins, 1992)

2.2 Foam destabilisation mechanisms

Analogous to all colloidal dispersions, foams are also complex multiphase system with a huge interfacial area and hence free interfacial energy. To minimise this interfacial energy, given enough time, a foam will eventually disintegrate into its individual phases. The three main foam destabilisation processes are: (i) gravity driven drainage; (ii) bubble coalescence; and (iii) disproportionation (also known as Ostwald ripening). In the sections to follow, each of these destabilisation processes is described individually, however, in a 3D foam it is interconnected and hence occurs simultaneously. For example, foam coarsening (aka disproportionation) leads to larger bubble with a larger film which in turn influences gravity driven drainage (Ellis and Lazidis, 2018).

2.2.1 Gravity driven drainage

The liquid content of foams drains continuously, due to the action of gravity, through channels known as Plateau borders (PB) interconnected at the nodes until an equilibrium state is reached. However, some liquid remains due to the action of capillary forces. The process of liquid drainage is therefore a complex physicochemical hydrodynamic process. Once the process of drainage is complete, the structure of foams becomes more fragile and thinner which can lead to its eventual collapse. The rate of foam drainage is therefore a good indicator for the prediction of its stability, i.e. a foam possessing a faster drainage is expected to indicate that it is less stable and vice versa (Park and Hermanowicz, 2014).

Foams can collapse if the liquid is completely drained and when the thickness of the lamellae reaches a critical thickness of 50-100 Å (Wang,Nguyen and Farrokhpay, 2016). The opposing force to liquid drainage and hence film thinning is provided by the Gibbs-Marangoni effect (Pugh, 2016). The time variation of surface tension is known as the Marangoni effect. Whereas, on the other hand, the change in surface tension due to variation in concentration of the surface-active agent is known as the Gibbs effect (Pugh, 2016). In essence, Gibbs-Marangoni effect are two separate mechanisms (film elasticity theories) that are superimposed and can occur simultaneously. The Gibbs-Marangoni mechanism commences once a surfactant concentration difference is set-up, i.e. during film stretching/thinning. Due to the local concentration difference, the region of lower surfactant concentration (thinner spot) automatically draws liquid towards it to minimise the difference. As a result, the film thinning is not just prevented, but also replenished. These opposing and restoring forces are referred to as Gibbs-Marangoni effect (Wang,Nguyen and Farrokhpay, 2016, Pugh, 2016a). Fig. 2.2 is a schematic depicting the mechanism of Gibbs-Marangoni effect.

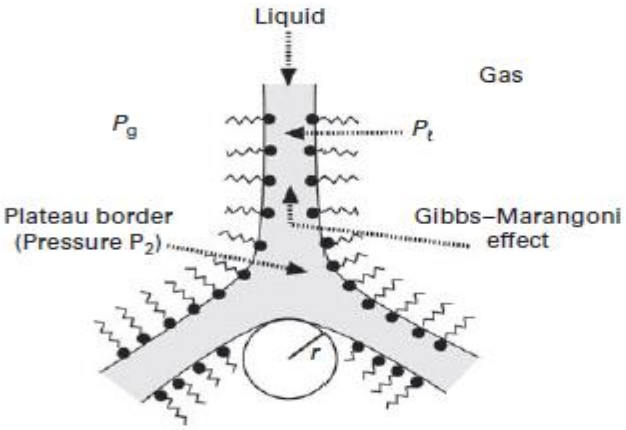

Fig. 2.2: A schematic showing the drainage of liquid between foam air cells (Pugh, 2016)

The rate of liquid drainage from the film lamella is given by:

$$V = 2h^3(\Delta P)/3\mu R^2 \qquad \text{(Eq. 2.1)}$$

Where: h is lamella film thickness, μ is dynamic viscosity, R is the radius of the bubble, and ΔP is the pressure difference between the capillary hydrostatic pressure (P_C) and the disjoining pressure (π_d) between the interfaces of the lamella film (Damodaran, 2005, Karakashev and Grozdanova, 2012).

As mentioned above, the stability of foams is ultimately dependent on the lifetime of the thin film (lamellae) that surrounds the bubbles and this stability can be represented by a quantity known as disjoining pressure, P_d (Aronson *et al.*, 1994, Lech *et al.*, 2015). The disjoining pressure is simply defined as "the net force per unit area normal to the two flat parallel surfaces". It is due to the combinations of three forces that act simultaneously and consist of: (1) electrostatic repulsion among charged species on the bubble surface; (2) steric/hydration due to interaction among the tightly packed adsorbed species on bubble surface; and (3) van

der Waals attraction forces due to dipole-dipole interaction among the adsorbed species (Khristov,Exerowa and Minkov, 2002, Krustev and Müller, 1999).

The variation of disjoining pressure (P_d) with film thickness (h) is known as disjoining pressure isotherm. Depending on h, two distinct regions can be identified which corresponds to the Common Black Film (CBF) and a second thermodynamically unstable region, Newton Black Film (NBF). The CBF region occurs when the electrostatic repulsive forces dominate over van der Waals attractive forces as shown in Fig. 2.3. In this region, the film thickness is in the range of 10-100 nm. Whereas, in the NBF region the steric/hydration forces initiate a very steep repulsive branch, which corresponds to film thickness of less than 10 nm (Fauser,von Klitzing and Campbell, 2015). A mechanical equilibrium condition is approached when the disjoining pressure (P_d) is equal to the pressure difference in the film as shown in Eq. 2.2 and 2.3.

$$P_d\,(h) = P_N - P_B \qquad \text{(Eq. 2.2)}$$

$$P_d(h) = P_d(h)_{electrostatic} + P_d(h)_{vdW} + P_d(h)_{steric} + P_d(h)_{hydration} \qquad \text{(Eq. 2.3)}$$

Where: P_N is the pressure normal to the plane-parallel film surface and P_B is the intrinsic pressure in the initial bulk phase volume (Fauser,von Klitzing and Campbell, 2015, Khristov,Exerowa and Minkov, 2002, Karakashev and Grozdanova, 2012).

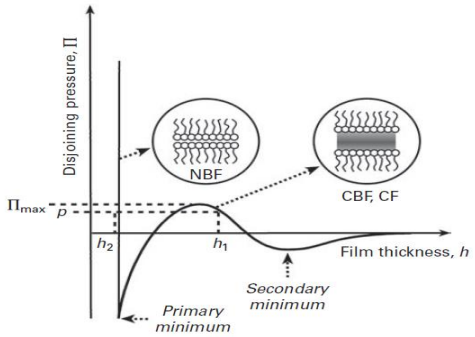

Fig. 2.3: An idealised disjoining pressure isotherm for an anionic surfactant (Pugh, 2016)

Depending on the type of surfactant used for foam stabilisation, there are a number of variables that can have an influence on the value of disjoining pressure and hence the stability of the film surrounding the bubbles. This includes surfactant type, surfactant concentration, electrolyte concentration, pH, temperature, surfactant chain length, head group polymerisation, short-range interaction, stereochemistry and chain branching (Wang,Nguyen and Farrokhpay, 2016). To determine the effects of these variables on the stability of the thin film as well as the stability of the bulk foam, numerous approaches have been considered by a number of authors involving the measurement of these properties (Chen *et al.*, 2017, Lech *et al.*, 2015, Nguyen,Yusa and Phan, 2016, IJMER,Reza and Ariffin, 2014, Kostoglou,Georgiou and Karapantsios, 2011, Karakashev and Grozdanova, 2012).

2.2.2 Bubble coalescence

As mentioned above, the process of coalescence occurs when the interfacial film (lamella) separating two neighbouring bubbles ruptures as a result of gravity driven drainage. The combination of kinetic and gravitational forces acting on the bubbles leads to the formation of a single larger bubble (Eisner *et al.*, 2007). As shown in Fig. 2.4 the bubbles appear spherical due to the large distance '*h*' between the bubbles and if this distance decreases to an extent

where the bubbles can contact each other, the combination of intermolecular and hydrodynamic forces can lead to the process of merging known as coalescence (Ivanov,Danov and Kralchevsky, 1999).

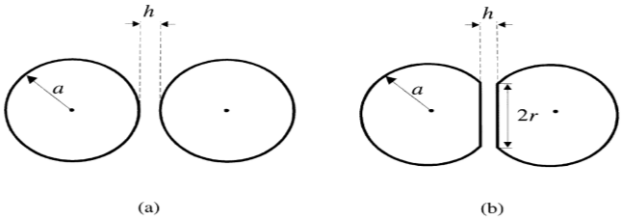

Fig. 2.4: Schematic showing how the approaching of two film bubbles leads to bubble coalescence (Ivanoy et al., 1998).

To summarise, the rate of bubble coalescence is influenced by: (1) the stability of the thin film; (2) any physical process where the probability of bubble collision increases; and (3) by the combined intermolecular forces including attractive and repulsive. The combined influence can be essentially grouped into a single Weber number definition such as:

$$Weber\ number = \frac{Combined\ external\ stresses}{Laplace\ pressure} \qquad \text{(Eq. 2.4)}$$

The combined external stresses include hydrodynamical, colloidal and mechanical forces. Whereas the Laplace pressure is dependent on the surface tension and the bubble radius (as defined in Eq. 2.8). In pure water, Duineveld (1995) combined the bubble coalescence rate between two bubbles into the following equation:

$$We\ (2) = \frac{\rho V^2}{2\sigma}\left(\frac{1}{r_{b1}} + \frac{1}{r_{b2}}\right) \qquad \text{(Eq. 2.5)}$$

where the 2 in bracket refers to the fact that two bubbles are in contact, ρ is the bulk density, V is the velocity of the thinning of the foam film, σ is the surface tension. In the presence of a surfactant, Nguyen (2003) modified the above equation and derived the below:

$$We\ (2) = \frac{16\rho r_{b1} r_{b2}}{\sigma(r_{b1} + r_{b2})}\left(\frac{dR_f}{dt}\right) \qquad \text{(Eq. 2.6)}$$

where R_f is the film radius (Karakashev and Grozdanova, 2012, Nguyen, 2003). It is therefore apparent that the rate of bubble coalescence is ultimately dependent on the rate of film thinning. In summary, any parameter/process that can improve the stability of the thin film essentially leads to improved resistant of foam to bubble coalescence.

2.2.3 Bubble disproportionation (aka coarsening)

Aqueous foams are also prone to a destabilisation process known as disproportionation (commonly known as Ostwald ripening in emulsions) and it is usually the most important destabilisation mechanism in foams (Walstra, 1989). Disproportionation occurs whenever two bubbles of different sizes (one smaller relative to the other) are present in foams and because of the capillary pressure variation inside the bubbles, the larger bubble will grow in size at the expense of the smaller bubble (Walstra, 1989, Dutta *et al.*, 2004, Eisner *et al.*, 2007). As captured by the famous Young-Laplace equation, for any curved air-water interface (i.e. bubble/droplet), there will always be a pressure gradient set-up as a result of surface tension, which can be predicted by:

$$\Delta P = \gamma\,(\frac{1}{R_1} + \frac{1}{R_2}) \qquad \text{(Eq. 2.7)}$$

where γ is the surface tension and R_1 and R_2 are the principle radii of the curvature. For a spherical bubble, however, $R_1 = R_2 = R$, and therefore (Eq.2.7)) simplifies to:

$$\Delta P = \frac{2\gamma}{R} \qquad \text{(Eq. 2.8)}$$

According to (Eq. 2.8), the pressure difference between the continuous medium and a bubble with a smaller radius will be much greater than a bubble with a larger radius. As a result, two bubbles of different radii in the vicinity of each other will result in the transfer of gas from the smaller to the larger bubble leading to the mechanism of disproportionation. An estimate of the characteristic coarsening time (t_{coars}) can be predicted by:

$$t_{coars} = \frac{R^2}{D_{eff} f(\theta) h} \qquad \text{(Eq. 2.9)}$$

where R is the average radius of bubble, h is the film thickness, D_{eff} is an effective diffusion coefficient and $f(\theta)$ is the total area of the bubble covered by film (Rio *et al.*, 2013).

The rate of foam coarsening is strongly dependent on the solubility of the dispersed phase (i.e. air) in the continuous phase (i.e. water). Therefore, coarsening is expected to be much slower for the least soluble gas, i.e. for a similar BSD, the rate of coarsening will be much slower for bubbles containing nitrogen gas in comparison to bubbles containing carbon dioxide (Ellis and Lazidis, 2018). Apart from varying the diffusion of gas based on solubility, the rate of foam coarsening is also influenced by the interfacial characteristics of the surfactant (more details to be provided on the section to follow) and hence on the dispersed phase (i.e. bubble). By increasing the interfacial elasticity, the rate of coarsening can be significantly reduced (Ellis and Lazidis, 2018). As will be outlined later, one such food-grade surfactant which has shown

an incredible interfacial elasticity and hence resistant to foam coarsening is polyglycerol ester of fatty acids, PGE 55 (Duerr-Auster *et al.*, 2007). Furthermore, it can be reduced by decreasing the surface tension.

Specifically, in foams, all destabilisation mechanisms can take place simultaneously and at any rate depending on the air volume fraction, BSD, physicochemical properties of the liquid (such as viscosity, interfacial properties and density) and environmental conditions such as temperature and pressure. For example, in wet foams, gravity drainage is often the predominant mechanism. On the other hand, coarsening (disproportionation) and coalescence is often prevalent in dry foams - due to the thinner films separating the neighbouring bubbles – and polydisperse BSD allowing faster diffusion due to larger difference in Laplace pressure.

Currently, there are very few empirical studies that investigated the combined effects of gravity drainage and coarsening especially for bubbly liquids and wet foams generated from non-Newtonian media. For example, Daugelaite (2011) and Daugelaite *et al.,* (2016) studied the coarsening and gravity drainage of egg-white sucrose foams using a 2D optical imaging microscopy and a modified resistivity technique of Barigou, Deshpande and Wiggers (2001). Air volume fractions in the range of 0.60 – 0.81 were investigated. Unlike surfactant foams, egg-white sucrose foams were found to be highly statically stable especially against gravity drainage. In addition, the bubble size evolution for foam generated at air volume fraction of 0.78 was satisfactorily fitted to a power law (R approx. equal to $t^{0.34}$). In contrast, foam generated at 0.65 did not follow the power law fit (R equal to $t^{1/3}$) and this was attributed to a significant contribution from gravity drainage (Daugelaite *et al.,* 2016, Daugelaite, 2011, Marigo,Deshpande and Wiggers, 2001).

Similarly, Durr-Auster (2008) investigated the gravity drainage of wet foams generated from polyglycerol ester of fatty acids (PGE 55) and sucrose with non-Newtonian shear-thinning characteristics. When stored under identical condition, foam generated from solution with a lower pH (equal to 3) was shown to be more stable against gravity drainage in comparison to a foam generated at a higher pH (equal to 9). The difference in static stability was attributed to the aggregation and network formation of vesicles inside the foam film and Plateau borders providing more resistance to the flow of liquid. In their study, coarsening was not considered (Durr-Auster, 2008).

Recently, Arjmandi-Tash *et al.* (2016) investigated the free drainage of wet foams generated from non-Newtonian polymeric solutions. A theoretical model combined with simulation was developed and compared to experimental data. The foam drainage was assumed to take place in the Plateau border with a Poiseuille-like flow having an immobile interface. In addition, the bubble size was assumed to be uniform with negligible foam coarsening. The experimental time evolution of foam height and liquid content were satisfactorily predicted by the derived model solved using finite element method especially for foams generated from the lower viscosity fluids. However, there was a significant deviation found for the higher viscosity fluids and the model failed to accurately predict the liquid drainage at short time scales. The discrepancy was attributed to the assumption of immobile interface of the Plateau border and Poiseuille-like flow (Arjmandi-Tash *et al.*, 2016). Clearly, liquid drainage for foams generated from non-Newtonian fluids is complex and there are several additional factors which can play a significant role. Therefore, experimental studies probing such behaviour is of a huge interest.

Moreover, recently, many studies have been conducted to probe the effects of addition of xanthan gum (XG) on static stability of foams. XG is an anionic polysaccharide widely employed in the food, personal care, oil recovery, agriculture and related sectors to impart non-Newtonian viscous properties to dispersions (Katzbauer, 1998). It is an anionic heter-polysaccride widely used in the food industry to impart stability to foams and emulsions. This particular food hydrocolloid has many useful properties such as high zero-shear viscosity and shear thinning properties at high shear rates (Xie and Hettiarachchy, 1998, Xu *et al.*, 2013, Zhong *et al.*, 2013, Laporte *et al.*, 2014, Laporte *et al.*, 2015, Laporte *et al.*, 2016).

2.3 Interfacial tension and surfactants

2.3.1 Interfacial tension

A pure liquid, such as water, has a high surface tension due to the lack of attraction forces experienced by the molecules at the air-water interface. Therefore, surface tension can be defined as the amount of work or energy necessary to generate an air-water interface. Also, it is frequently defined as the "contracting force per unit length around the perimeter of a liquid surface (m.N m^{-1})". To measure the interfacial tension, many experimental techniques exist such as Wilhelmy plate, pendant drop, Du Nouy ring, capillary rise, etc.

For determination of equilibrium interfacial tension, a Wilhelmy plate method is commonly used as shown in Fig. 2.5. In this method, a thin plate made of platinum or any other suitable material is slowly inserted into a known volume of solution. The force acting (F) on the plate is then recorded along with plate dimensions are then used to determine the interfacial tension, thus:

$$F = l_w \sigma \cos(\alpha) \qquad \text{(Eq. 2.10)}$$

where l_w is the length of the Wilhelmy plate (m), σ is the interfacial tension (mNm^{-1}) and α is the contact angle (degrees). Eq. 2.10 can be simplified when $\alpha \approx 0$ degrees to:

$$\sigma = \frac{F}{2l_w} \qquad \text{(Eq. 2.11)}$$

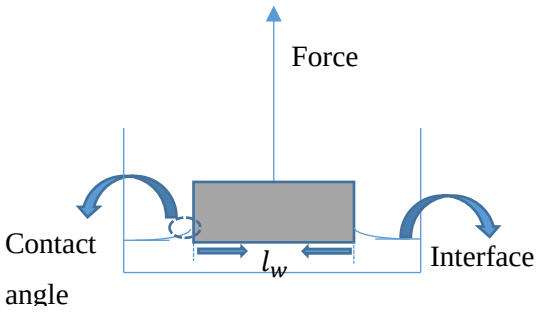

Fig. 2.5: Schematic of a Wilhelmy plate method.

In contrast, a pendant drop method (as depicted in Fig. 2.6) is widely employed to measure the equilibrium or dynamic interfacial tension. A bubble or a droplet of a known volume is formed at the end of a syringe needle tip and the spherical shape is fitted by the software to the Young-Laplace equation (Eq. 2.8).

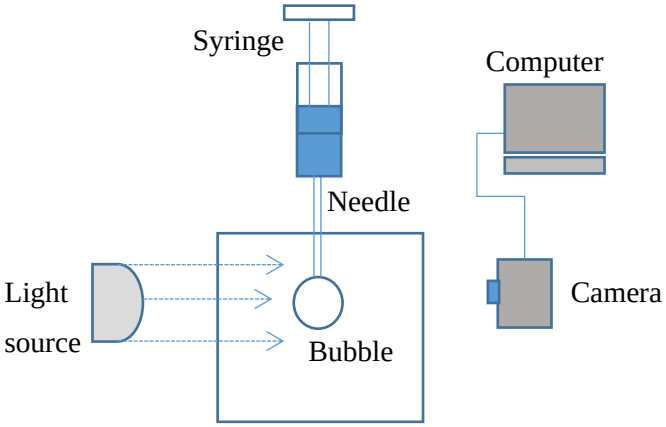

Fig. 2.6: Schematic of a pendant drop method.

2.3.2 Surfactants

Surfactants (also commonly known as emulsifiers in the food industry) are amphiphilic molecules with a hydrophobic tail - which has a high affinity for gas - and hydrophilic head - which has a high affinity for water. The dual characteristics of these molecules present a number of useful properties that are mainly linked to its adsorption behaviour at the interface and self-assembly in the solution (Eastoe and Tabor, 2014). Once in solution, the surfactant molecules are capable of diffusing to an air-water interface and hence reduces the interfacial tension. Due to the superior stabilisation properties of most surfactants, they are widely used in food, pharmaceutical, petroleum and related industries.

Presently, there are numerous different types of surface-active agents available and they can be grouped into three main classes: (i) low molecular weight (LMW) surfactants; (ii) polymeric surfactants; and (iii) surface-active particles. The LMW surfactants can be further categorised into four sub-groups, and their characterisation is based on the charge associated with their head group as follows:

- **Cationic** – consist of positively charged head group (surface-active portion),
- **Anionic** – consist of negatively charged head group,
- **Non-ionic –** neutrally charged head group,
- **Zwitterionic** (amphoteric) **–** the surface-active part consists of both negative and positive charges and it can vary with pH (Dickinson and McClements, 1995).

In addition, Griffin (1949) introduced and categorised surfactant molecules based on their hydrophile-lipophile balance (HLB). To determine the HLB number for a specific surfactant molecule, Eq. 2.12. can be used (Griffin, 1949). According to this equation, a surfactant with a high HLB number (10 – 18) is considered, mostly, a hydrophilic (have high affinity for water) whereas a surfactant with a low HLB number (7 – 9) is considered, mostly, a hydrophobic (have high affinity for air). The surface activity of the surfactant can be predicted by knowing its HLB value (Damodaran, 2005).

$$Ca = HLB = 7 + \sum(hydrophilic\ group\ numbers) - \sum(lipophilic\ group\ numbers) \quad \text{(Eq. 2.12)}$$

Surfactants can spontaneously adsorb at the air-water interface and form a single monolayer. The adsorption kinetics depends mainly on the molecular structure and this in turns depends on the properties of its head group - as outlined above. The surface tension of the interface decreases rapidly as the concentration of the surfactant increases, until a clear break is observed, as shown in Fig. 2.7. The discontinuity occurs once the concentration of the surfactant molecules reaches a critical value known as critical micelle concentration (cmc). Upon reaching this concentration, surfactant molecules spontaneously aggregate into clusters known as micelle (see Fig. 2.7). The self-aggregation (micelle) takes place because at concentration greater than cmc, it is more thermodynamically favourable for the surfactant molecules to cluster together than to contact the water molecules (Eastoe and Tabor, 2014). Normally, the micelle takes a spherical form, however, cylindrical and lamellar forms have also been observed at concentration much greater than cmc, as shown in Fig. 2.8 (McClements, 2004).

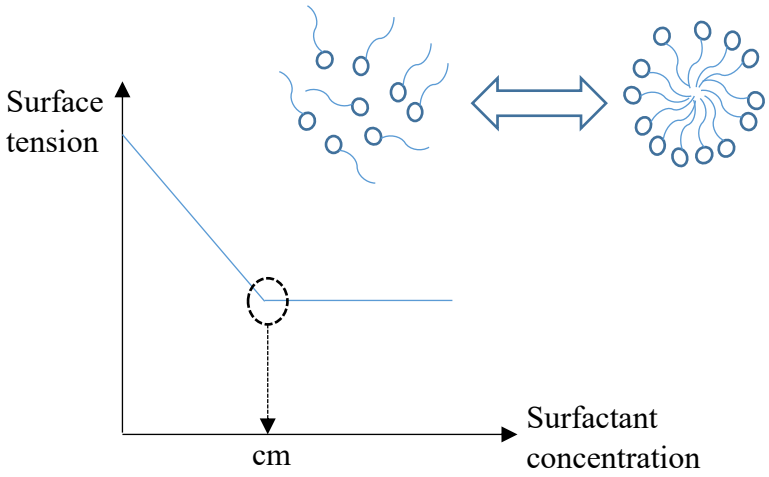

Fig. 2.7: Schematic showing cmc and micelle formation.

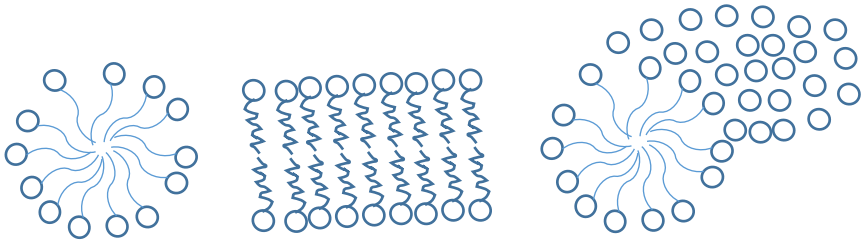

Fig. 2.8: Schematic of different types of micelle.

2.3.2.1 High molecular weight surfactants – proteins

Proteins have been widely exploited, especially in the food industry, to impart stability to food-based emulsions and foams including salad dressing, cream, mayonnaise and ice cream (Eisner *et al.*, 2007, Singh, 2011, Lazidis *et al.*, 2016, Ewert *et al.*, 2016, Chen *et al.*, 2017). Proteins consist of a sequence of amino acids, linked to each other by peptide bonds, to form their primary structure. The polypeptide chains fold in turn, resulting in atoms of backbone interaction, giving rise to their secondary structure. The interaction of various R-groups within the amino acids' chain length gives a protein molecule its overall three-dimensional structure known as its tertiary structure. Most proteins possess a tertiary structure; however, some

proteins consist of multiple polypeptide chains (subunits), which when combined can give rise to their quaternary structure (Kralova and Sjöblom, 2009).

In comparison to low molecular weight surfactants (as will be shown later), proteins are also amphiphilic macromolecules, which have a hydrophobic region (amino acid residues) and a hydrophilic region. However, they are considered the least effective at reducing the interfacial tension, mainly, due to their complex structural properties (Zoheidi *et al.*, 2016, Damodaran, 2005). In addition, proteins also tend to form strong and immobile interfacial networks (due to steric and electrostatic interaction), unlike surfactants that tend to form mobile interfacial structures (Ewert *et al.*, 2016, Maldonado-Valderrama and Langevin, 2008, Saint-Jalmes, 2006). Furthermore, the adsorption kinetics of protein onto the bubble interface is slow in comparison to smaller molecular weight surfactants such as Sodium Dodecyl Sulfate aka SDS as shown in Fig. 2.9 (Pugh, 2016).

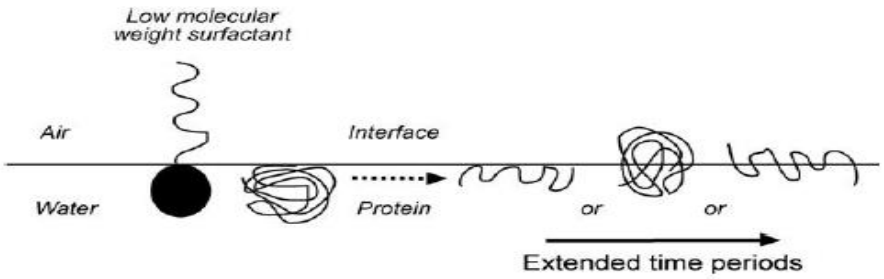

Fig. 2.9: Comparison of adsorption behaviour for low molecular weight surfactant and high molecular surfactant (i.e. protein, Fameau and Salonen 2014).

The stabilisation of foams by proteins is by a sequence of mechanisms, which occurs in order to reduce the interfacial tension of the air-water interface. This consists of: (i) adsorption; (iii) partial denaturation; and (iii) exposition of the hydrophobic entity of the protein macromolecules to the interface. Once at the interface, the protein macromolecules forms

aggregate and a quasi-two-dimensional network (Ewert *et al.*, 2016, Sagis *et al.*, 2001). The adsorption of protein at the air-water interface is mainly due to the hydrophobic nature of proteins (from amino acid residue), which is relatively shielded away from the aqueous phase by the hydrophilic region (Murray, 2007). The adsorption kinetics depends on a number of factors including protein structure, the net charge (pH), the exposed hydrophobicity, size and the presence of non-protein additives, i.e. sugars, polysaccharides, etc. (Fameau and Salonen, 2014). It is widely known that at a pH closer to the isoelectric point (PI), defined as the pH at which the charge on the protein macromolecule becomes neutral, the rate of diffusion and adsorption increases significantly. This is due to the low level of intra-molecular and electro-static interactions (Foegeding,Luck and Davis, 2006, Gharsallaoui *et al.*, 2009, Lexis and Willenbacher, 2014, Asghari *et al.*, 2016). The ubiquitous utilisation of proteins as foaming agents is simply due to their excellent surface-active properties including strong adsorption at the air-water interface. In addition, proteins also provides effective steric and electrostatic stabilisation properties and hence can impart great structural coherence to the film (Murray, 2007).

As will be outlined later, it is essential to consider both the foaming ability and foam stability when choosing a particular protein for the stabilisation of foams. Foaming ability refers to the capacity of the protein to rapidly adsorb and unfold at the air-water interface. It depends on a number of factors including their composition (e.g. protein content, the presence of salt, sugar, etc.) and their physical and structural characteristics (e.g. molecular size, exposed hydrophobicity, bulkiness, amphiphilic nature, etc.). Whereas, foam stability refers to the ability of a protein to form strong, cohesive and flexible films that can resist and therefore inhibit the process of coalescence. A protein possessing good foaming characteristics does not

necessarily mean that it will also have good stability, and vice versa (Ewert *et al.*, 2016, Asghari *et al.*, 2016). The most commonly used food-based proteins are egg white (EWP) and milk (β-Casein and whey protein) due to their excellent foaming ability and in the case of egg-white and whey protein, their stability (Sagis *et al.*, 2001, Asghari *et al.*, 2016, Zoheidi *et al.*, 2016, Chen *et al.*, 2017) Wilson, 1979. The excellent foaming ability of β-casein protein is mainly due to its hydrophobic nature, flexibility, and relatively small size. This allows the β-casein molecules to rapidly diffuse and hence reduce the interfacial tension of the air-water interface. The foaming ability of proteins can be enhanced by either increasing the flexibility or by exposing the hydrophobic residue by a heat-treatment.

Recently, the use of aggregated protein structures for the stabilisation of foams have attracted a much needed attention due to their desirable foaming properties (Lazidis *et al.*, 2016, Fameau and Salonen, 2014, Oboroceanu *et al.*, 2014). Proteins can be aggregated either by a heat or by a pressure treatment process. The final foaming property of the aggregate depends, mainly on the solution condition, the nature, structure and size of protein. Therefore, by controlling the medium conditions (such as pH, ionic force, heating temperature and protein concentration) aggregates of various sizes and shapes can be obtained (Nicolai and Durand, 2013). Upon heating, proteins undergo a structural change (denaturation) which results in unfolding and exposition of its hydrophobic entities (Raikos, 2010). In addition, it also has a number of disadvantages that must be taken into consideration such as the slow diffusion of the aggregated structures in comparison to the original protein.

In the last decade, hydrophobins, consisting of relatively small proteins with amino acid residues in the range of 65-100, are found to possess excellent stabilising characteristics (Hektor

and Scholtmeijer, 2005, Cox *et al.*, 2007, Cox and Hooley, 2009, Cox,Aldred and Russell, 2009, Linder, 2009, Tchuenbou-Magaia,Norton and Cox, 2009, Blijdenstein *et al.*, 2013, Magarkar *et al.*, 2014, Burke *et al.*, 2014, Dimitrova *et al.*, 2016, Dimitrova *et al.*, 2017, Schor *et al.*, 2016). Hydrophobins can be divided into two distinct classes: class I, which are the most surface-active, highly insoluble and undergo conformational changes once adsorbed onto the air-water interface and class II, which are more water soluble and forms an elastic monolayer once adsorbed onto the air-water interface. Similar to surfactants, hydrophobins are also amphiphilic, which have a hydrophobic region (high affinity for air/oil) and hydrophilic region (high affinity for water). In addition, once adsorbed onto the air-water interface, hydrophobins spontaneously self-assemble and imparts excellent surface elasticity that is often an order of magnitude higher than other surfactants (Magarkar *et al.*, 2014). According to Tchuenbou-Magaia, Norton and Cox, the high viscoelasticity imparted by the adsorption of hydrophobins onto the air-water interface provides excellent protection against disproportionation (Tchuenbou-Magaia,Norton and Cox, 2009).

2.3.2.2 Surface active particles

The foam stabilisation properties of solid particles have been known for a very long time and it was initially realised by Ramsden (1903) and then by Pickering (1907). Later, Hoffmann (1913) recognised and indicated that foams and froth can be stabilised by finely divided particles (Pugh, 2016). Since then, several studies have been published focusing mainly on finding particles that are effective at stabilising foam-based products (Horozov, 2008, Lam,Velikov and Velev, 2014, Fameau and Salonen, 2014, Du *et al.*, 2015, Zhang *et al.*, 2015, Kim *et al.*, 2016). In addition, in the past few years, much more attention has been paid to finding particles that

are of a biological origin and hence can be used for food and biomedical applications (Lam,Velikov and Velev, 2014).

The presence of solid particles in foams can either suppress foaming or it can drastically increase its stability (Fameau and Salonen, 2014). The actual behaviour and interaction of the particles with an air-water interface can be predicted from their nature such as the degree of hydrophobicity and hydrophilicity. This in turn influences the contact angle that the particle makes with the interface. According to Fameau and Salonen (2014), a hydrophobic particle will have a large contact angle ($\theta > 90°$) and it will be mainly immersed in the air phase, whereas, a hydrophilic particle will have a small contact angle ($\theta < 90°$) and it will be mostly immersed in the aqueous phase as shown in Fig. 2.10. A particle with an intermediate wettability will have a contact angle in the vicinity of 90° and it will sit squarely at the air-water interface (Fameau and Salonen, 2014, Horozov, 2008). It is well-known that particles possessing hydrophobicity are good antifoaming agents and are therefore widely utilised for such applications (Kruglyakov *et al.*, 2008, Krägel,Derkatch and Miller, 2008). In comparison, hydrophilic and particles with an intermediate wettability will often possess excellent foam stabilising properties (Fameau and Salonen, 2014). The mechanism and the extent of stabilisation depends on a number of factors and this includes their shape, size, concentration, surface charge, state of aggregation, surface area, density and the degree of hydrophilicity (Alargova *et al.*, 2004, Horozov, 2008).

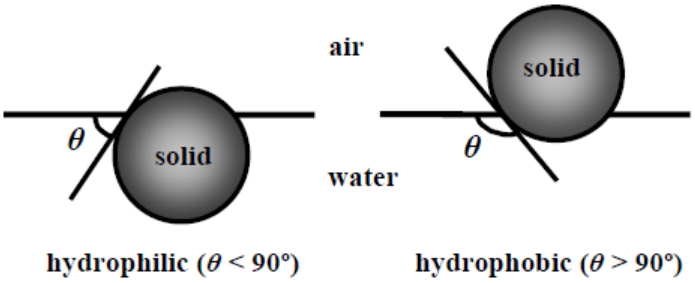

Fig. 2.10: Schematic showing the contact angle created by the solid particle with air-aqueous interface (Maestro *et al.*, 2014).

The particle size, roughness and energy of attachment dictates whether it will stabilise or destabilise a foam (Green *et al.*, 2013, Lam,Velikov and Velev, 2014, Maestro *et al.*, 2015). For example, according to Lam, Velikov and Velev (2014), a stable foam is achieved when the particle size is in the range of 10-30 µm and has a corresponding three-phase contact angle of 60° and 90° respectively.

Particles of a higher degree of hydrophobicity can be modified to improve their foam stabilising properties. An optimum particle hydrophobicity can be achieved by three main routes: (1) changing the pH or electrolyte concentration of the aqueous medium; (2) addition of multivalent ions by adjusting the surface charge density; and (3) by adding an appropriate surfactant molecules such as sodium dodecyl sulfate (SDS) or cationic hexadecyltrimethylammonium (CTAB) that can adsorb to the surface of colloidal particles and hence alter its surface properties (Dickinson, 2010).

In contrast to surfactant molecules, which can readily adsorb and desorb from the air-water interface, the adsorption of Pickering particles is irreversible. The irreversibility is attributed to the strong energy of attachment (Horozov, 2008, Stocco *et al.*, 2011, Lv *et al.*, 2015, Farhadi *et*

al., 2016, Binks, 2002). The energy required to remove a particle from a fluid-fluid interface can be estimated by:

$$E = \pi r^2 \gamma_{\alpha\beta}((1 \pm cos\theta)^2 \quad \text{(Eq. 2.13)}$$

Where: *E* represents the energy required to remove the particle from the interface, *r* is the radius of the particle (m), γ is the interfacial tension between the fluid-fluid (α and β) interface and θ is the wettability angle that the particle makes with the interface. The sign in the bracket should be taken negative when the particle is removed into an aqueous phase and positive when it is removed either to an oil or air phase (Binks, 2002).

2.3.2.3 Low molecular weight surfactants

The variety of LMW surfactants available for the food industry is limited due to the strict and stringent regulations of several countries. However, the most common ones are the anionic and non-ionic bipolar compounds consisting of a long-chain hydrophobic alkyl and a hydrophilic headgroup with or without a charge. The commonly used LMW surfactants include sucrose esters, mono-diglycerides, phospholipids, polysorbates (Tweens), monooleate (Span 80) etc. For a detailed review of these surfactants, the reader is advised to refer to a book published by (Kralova and Sjöblom, 2009).

Polyglycerol esters of fatty acids (PGE) is one type of LMW, non-ionic compound with excellent foam stabilisation properties. It consists of hydrophilic polyglycerol group and a hydrophobic fatty acid chains of octadecanoic and hexadecanoic acid (Duerr-Auster *et al.*, 2007, Duerr-Auster,Gunde and Windhab, 2008, Duerr-Auster *et al.*, 2009, Curschellas *et al.*,

2012a, Curschellas *et al.*, 2013, Curschellas *et al.*, 2013b, Gupta *et al.*, 2016). Once in aqueous solution, the phase behaviour of PGE 55 is critical to its stabilising properties.

In this thesis, a commercially available non-ionic surfactant, polyglycerol esters of fatty acids (PGE 55) was chosen to generate aerated products with a well-defined microstructure. In the literature, it is well-known that, after following a specific preparation protocol, PGE 55 possess excellent foam stabilising properties. This has been attributed to its complex mixture consisting of fatty acids esterified with glycerol back-bone of mostly hexadeconic (54%) and octadeconic (45%) acid. Once in aqueous solution and above its chain-melting temperature (Kraft temperature of 58 °C) the biphasic surfactant dispersion is transformed into a multi-lamellar liquid crystalline phase (MLV_{α}). After cooling back to below the chain melting temperature, this complex mixture is then transformed back into a multi-lamellar gel phase ($MLV_{\beta'}$) which is responsible for the interfacial properties. The phase diagram depicting this behaviour is shown in Fig. 2.11.

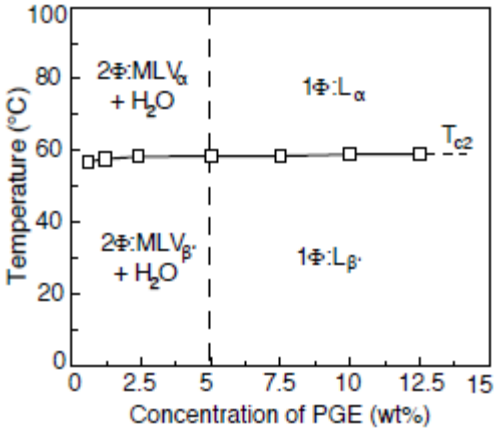

Fig. 2.11: Phase diagram of PGE 55 (Durr-Auster, 2008).

However, at ambient conditions, the absorption kinetics and hence the interfacial properties of the multi-lamellar vesicles in the gel phase has been found to be rather poor. Therefore, to

enhance the absorption kinetics and hence the foaming ability of this complex surfactant mixture, a number of studies have found that the absorption kinetics of these multi-lamellar vesicles is drastically improved if either the pH or the electrolyte content of the dispersion is altered. In its native pH, approx. 7 – 8, the multi-lamellar vesicles are very stable with a small fraction of the hydrophobic bilayer core being exposed to the air-water interface. However, decreasing the pH to a value of 2-3, the excess hydrogen ions were found to make these multi-lamellar vesicles unstable leading to a much faster absorption kinetics and hence a much better foaming ability (Duerr-Auster *et al*., 2008). For example, Duerr-Auster *et al*., (2008) showed that at a pH 3 a 1 wt% dispersion of PGE 55 - mechanically agitated using a food mixer for 100 s – generated a much greater volume of foam (3 L) in comparison to PGE 55 dispersion agitated at pH 9 (< 0.2 L). Similarly, the addition of electrolytes such as sodium chloride (NaCl) has been found to result in a faster absorption kinetics. This is believed to be due to the complexation of sodium ions with negatively charged free fatty acids impurities at a concentration of 1.4 wt% (Curschellas *et al*., 2013).

In addition, it is known that PGE dispersion having already experienced one heating-cooling cycle above the chain melting temperature (Kraft temperature, 58 °C) has better absorption kinetics at higher temperature, ≥ 40 °C (Durr-Auster, 2008). At this temperature, the mobility of the PGE 55 molecules (multi-lamellar vesicles of L_β) is significantly increased leading to a much faster absorption kinetics. This is of an advantage since a faster absorption kinetics means more surfactant is available at the air-water interface for effective foam stabilisation. This is the reason why the aeration efficiency increases when operating at a higher temperature. In addition, the poor absorption kinetics of PGE 55 at ambient conditions is due to the low critical aggregation concentration (cac) (Durr-Auster, 2008).

2.4 Foam generation

There are multitude of ways in which a foam can be generated in laboratory or manufactured at an industrial scale. These methods, however, can be simply grouped into two distinct categories namely physical and chemical foaming methods. Physical foaming methods can be further sub-divided into mechanical and phase transition. Mechanical methods include gas sparging, shaking, whipping, mechanical agitation, ultrasound, etc. (Pugh, 2016b).

2.4.1 Mechanical foaming

2.4.1.1 Batch methods

The simplest mechanical foam generation method is by shaking an aqueous mixture in the presence of a surface-active agent or by agitating the gas-liquid interface using a paddle stirrer. For example, in the kitchen, planetary mixers such as Hobart and Kenwood are commonly employed to aerate food recipes such as egg whites, ice cream, mousse, whipped cream, etc. (Fig. 2.12). These mixers are well-suited for foaming a viscous solution due to the vigorous mixing action generated by the whisks, which is not possible using alternative techniques such as gas sparging. In addition, these devices are also ideal for performing preliminary studies or model experiments prior to scale-up. However, the rate of air incorporation and the bubble size distribution are more difficult to control since foaming is often conducted under atmosphere conditions. During aeration, initially larger air bubbles are entrapped which are then broken down into smaller and smaller bubbles using a combination of disrupting stresses such as shear, inertial and normal forces (K. S. Chesterton *et al.*, 2011, Politova *et al.*, 2018). The rate of air incorporation is therefore a function of both liquid properties (viscosity, surface tension) and processing conditions (mixer speed, time). To obtain a higher air entrapment rate and a uniform

BSD, it is necessary to use sufficient surfactant with a good adsorption kinetics for the rapid stabilisation of newly generated air-water interface. However, after a prolong continuous shearing, the rate of bubble breakage may equal that of bubble coalescence and hence an equilibrium is established.

Fig. 2.12: Images of planetary mixers.

2.4.1.2 Continuous methods

At industrial scale, however, foams are generated using either a conventional dynamic or static mixers which include scrape surface heat exchanger (Mendez,Djelveh and Gros, 1993, Djelveh and Gros, 1995) SMX static mixer (Thakur *et al.*, 2003), continuous rotor-stator units (Hanselmann and Windhab, 1998, Balerin *et al.*, 2007, Mary *et al.*, 2013, Mezdour *et al.*, 2017) and mechanical agitated columns (Djelveh,Gros and Cornet, 1998, Thakur,Vial and Djelveh, 2003, Narchi,Vial and Djelveh, 2009).

In-line static, also known as motionless, mixers are relatively simple but effective mixing devices with no moving parts that can be readily incorporated into empty cylindrical pipes or other processing geometries. The principle of operation relies on pressure drop by splitting, rearranging, recombining and twisting the flow with the aim of achieving a homogenous

flowing field for effective heat and mass transfer. Due to its superior mixing performance, it has found applications in a wide range of industries including in food foaming and emulsification, pharmaceutical, blending of polymers, waste-water treatment, etc. In addition, in contrast to traditional mechanical driven agitators such as bubble column and stirred tank reactors, they are cheap, easily retrofitted to existing processes, requires a minimal space for instalment and has a plug-flow like residence time distribution with little back-mixing (Thakur *et al.*, 2003). Images of the in-line motionless mixer are shown in Fig. 2.13.

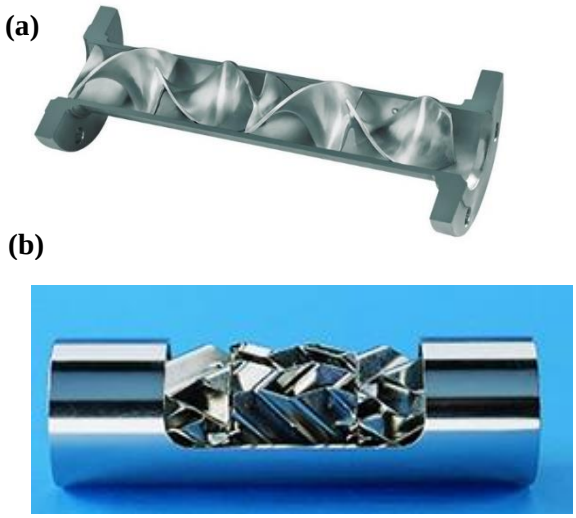

Fig. 2.13: Images of in-line static mixers: (a) Kenics; and (b) SMV.

Most food foams are manufactured using conventional dynamic mixers (Müller-Fischer,Suppiger and Windhab, 2007b). A dynamic mixer consists of a rotor-stator arrangement (see Fig. 2.14) with whipping blades, which with the aid of a controlled flow field, generated by the rotor, disperse the gaseous bubbles. Continuous rotor-stator mixers are frequently used for industrial applications especially in food processing industry. In these devices, both the rotor and the stator have several blades to which are attached a certain number of pins with a specific dimension. The rotor and its pins are attached and fixed to a shaft, which is rotated by an

electrical motor. Whereas the pins on the stator are welded directly onto the housing. A continuous flow of foam can be generated utilising this device and the flowrate controlled by adjusting the respective volumetric gas and liquid feeding rates. In these devices, the liquid to be foamed and the gas is simultaneously mixed before entering the mixing-head chamber, where it undergoes the process of foaming. The kinetic energy and flow forces (shear, inertia and elongation) generated by the rotation of the rotor in the whipping head ensures complete dispersion of the gas and the breakage of larger gas bubbles into smaller ones (Müller-Fischer,Suppiger and Windhab, 2007b, Seguineau De Preval *et al.*, 2014a).

Fig. 2.14: Images of continuous multi-stage rotor-stator.

There are very few papers dedicated to the generation of food-based foams using continuous rotor-stator devices and therefore the literature is still lacking in terms of food-based foams that possess complex rheological characteristics. From various studies carried out, it has been determined that the mechanical energy input is the most influential parameter and has a significant impact on the properties of the final foamed product. The mechanical energy input is in turn linked to the fluid viscosity, rotor speed and the residence time of the gas-aqueous mixture in the device (Müller-Fischer *et al*., 2007; Pugh, 2016). Currently, there exist a wide

variety of rotor-stator devices with varying geometry and sizes, i.e. gap size, number of blades, number of pins, etc. The fine-tuned dispersion of the gaseous phase and the small size of bubbles obtained by these devices are the main reasons why they are widely exploited for industrial applications (Pugh, 2016b). In addition, rotor-stator devices are also capable of producing consistent foam qualities with a range of foam production rates (Kroezen and Wassink, 1987).

In the rotor-stator device, the Power number (P_0, defined as the ratio of mechanical driving force to the inertial force) and Reynolds number (*Re*, defined as the ratio of inertial to viscous forces) are often used to characterise and describe the foaming process and flow conditions occurring in the whipping head (Müller-Fischer,Suppiger and Windhab, 2007b, Drenckhan and Saint-Jalmes, 2015). The relationship between the two is commonly known as the power characteristics ($P_0 = f(Re)$), thus:

$$P_0 = \frac{P}{\rho . n^3 . D^5} \qquad \text{(Eq. 2.14)}$$

$$Re = \frac{n . D^2 . \rho}{\mu} \qquad \text{(Eq. 2.15)}$$

where P is the net power, ρ is the dispersion density, n is the rotational speed, D is the rotor diameter and μ is the dispersion viscosity (Kroezen,Groot Wassink and Bertlein, 1988b, Müller-Fischer,Suppiger and Windhab, 2007b). According to Nagata (1975), in laminar flow regime, the Power number (P_0) is linearly dependent on the Reynolds number (*Re*):

$$P_0 = \frac{C_1}{Re} \qquad \text{(Eq. 2.16)}$$

where C_1 is the mixer specific constant (Nagata, 1975, Müller-Fischer,Suppiger and Windhab, 2007b). The values of C_1 is dependent on a number of parameters including the number of rotor-stator pairs, the number of pins per blade and the gap between rotor-stator device. Whereas, in the turbulent flow regime, the Power number (P_0) is independent of the Reynolds number (*Re*):

$$P_0 = constant = C_2 \quad \text{(Eq. 2.17)}$$

The values of C_2 is also dependent on the mixer geometry, i.e. the number of rotor-stator pairs, the facial area of a rotor unit and the number of pins per row.

Moreover, a transition regime exists between the laminar and turbulent flow regimes, which is difficult to quantify and describe. Correspondingly, the power dissipation rate in the laminar flow regime is proportional to the number of pins per blade, the number of rotor-stator pairs, the length and width of pins and the gap between the rotor and stator. Whereas, in the turbulent flow regime, the power dissipation rate is proportional to the number of rotor-stator units, facial area of a rotor pin and the number of pins per row (Müller-Fischer,Suppiger and Windhab, 2007b).

As stated previously, in all multiphase systems (such as emulsion and foams), the droplet or the bubble size distribution (DSD or BSD) plays a vital role in product quality attributes such as texture and shelf life. In addition, knowledge pertaining to BSD is crucial for effective and a well-controlled mass or heat transfer related processes. The Sauter mean diameter (D_{32}) combined with gas holdup is essential for interfacial area estimation. Generally, most mechanistic models proposed to predict the mean bubble or droplet size in mechanically

agitator columns are based on the Kolmogoroff's and Hinze's theory of turbulence (Hinze, 1955). The turbulence theory assumes a homogenous and isotropic flow field and it was originally developed for a dilute system. Even in cases, however, where this is not strictly true the Kolmogoroff's/Hinze's theory is usually assumed. For more concentrated dispersion, however, the effects of additional parameters (such as the disperse phase volume fraction, viscosity and density of continuous and dispersed phases) are taken into account.

A single bubble or a droplet exposed to stresses (shear, elongational or inertial) will breakup into smaller bubbles provided the magnitude and duration of the stresses applied is sufficient. Numerous empirical and theoretical studies have been reported on bubble/droplet breakup in simple laminar flow and these studies were instigated by the famous work of Taylor (1935). Taylor (1935) was the first to carry out a detailed and systematic study on emulsion droplets breakup in laminar flow. His famous work was summarised into two dimensionless numbers: capillary number (*Ca*), defined as the ratio of disruptive shear forces trying to deform the bubble to the restorative interfacial forces try to maintain the spherical shape; and viscosity ratio (λ) is the ratio of disperse phase to the continuous phase, thus:

$$Ca = \frac{\mu_0 r \dot{\gamma}}{\sigma} \qquad \text{(Eq. 2.18)}$$

$$\lambda = \frac{\mu_d}{\mu_0} \qquad \text{(Eq. 2.19)}$$

where r is the radius of the droplet, σ is the interfacial tension, $\dot{\gamma}$ is the imposed shear rate and μ_0 and μ_d are the viscosity of the continuous and dispersed phase respectively.

Later, many more empirical and theoretical studies were published proving and progressing the renowned work of Taylor (1935). Similarly, Grace (1982) showed that droplet breakup was more effective in elongational flow in contrast to simple shear and Fig. 2.15 is the famous Taylor-Grace plot (Grace†, 1982, Costeux *et al.*, 2011). To date, studies pertaining to droplet breakup in simple shear and in laminar flow field is well understood.

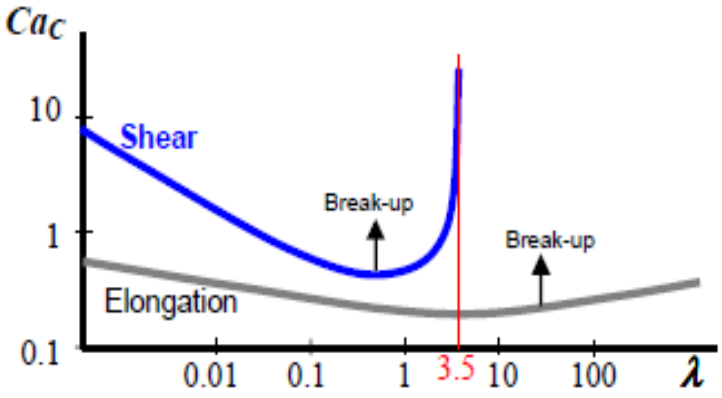

Fig. 2.15: Grace-Taylor plot showing the critical capillary number above which drop breakup occurs (Costeux *et al.*, 2011).

In contrast to bubble breakup in laminar flow field, bubble breakup in turbulent flow is much more complex and less well understood. The first studies pertaining to turbulent flow regime during emulsification was conducted by Kolmogorov (1949) and Hinze (1955). Fig. 2.16 shows the famous Kolmogorov's turbulent energy spectrum. As well captured by the energy spectrum, in turbulent flow regime, eddies of various length and energies exist from the scale of the impeller diameter to the smallest Kolmogrov's length scale. The energy is cascaded along these eddy scales until the kinetic energy is finally dissipated into heat.

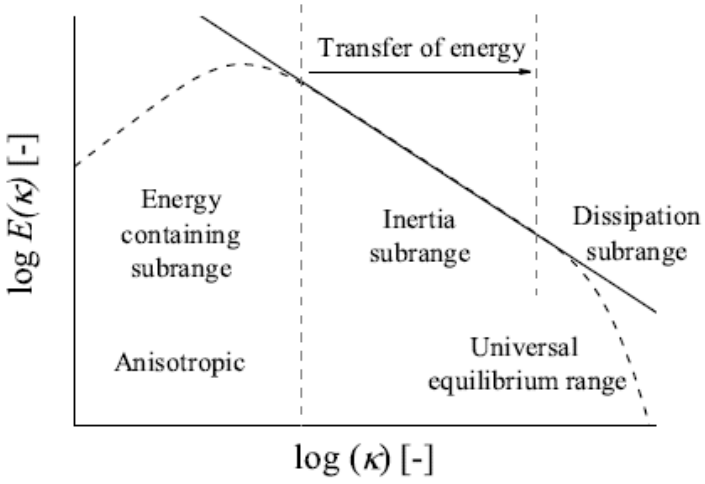

Fig. 2.16: Schematic of Kolmogorov's energy spectrum (Shalaby, 2007).

In addition, it is postulated and empirically proved that bubble/droplet breakup occurs in two distinct flow regimes namely 'turbulent inertial' and 'turbulent viscous' regime. In the former, the droplets diameter is assumed to be larger than the smallest eddies size (Kolmogorov length scale) in the continuous phase (Fig. 2.17a). Whereas in the latter, the droplet diameters are assumed to be smaller than the size of the smallest eddies in the continuous phase (Fig. 2.17b).

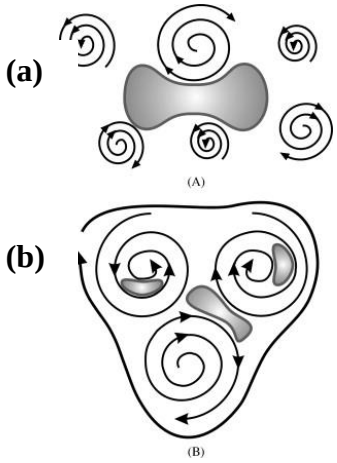

Fig. 2.17: Schematic showing bubble deformation in turbulent regime: (a) Turbulent inertial; and (b) Turbulent viscous (Vankova *et al.*, 2007).

The Weber number (*We*, representing the ratio of viscous forces acting to deform the bubble to its capillary pressure force acting to retain the spherical shape) is used to characterise the bubble size distribution in turbulent flow regime defined by:

$$We = \frac{\tau . d}{4\sigma} \qquad \text{(Eq. 2.20)}$$

where σ is the interfacial tension, τ is the shear stress and *d* is the bubble diameter. If the shear stress acting on the bubble reaches a critical limit, the bubble is broken down into two or more bubbles. To determine the maximum bubble diameter at a given shear conditions, thus, a critical Weber number (We_c) can be defined as:

$$We_{critical} = \frac{\tau . d_{max}}{4 . \sigma} \qquad \text{(Eq. 2.21)}$$

where d_{max} is the maximum bubble diameter. Eq. 2.18 above was initially derived by Hinze (1949) and then later empirically proved by several authors (Calabrese,Chang and Dang, 1986, Leng and Calabrese, 2004, Hall *et al.*, 2011). Till date, many mechanistic models exist to capture the bubble breakage and coalescence phenomena in turbulent flow regime. For more details on these models, one can refer to work reported by (Calabrese,Chang and Dang, 1986).

2.5 Foam flow and dynamic stability

In the past 40 odd years, studies pertaining to foam flow have been the subject of many authors. According to Herzhaft (1999), they can be generally divided into three main categories: (i) experimental studies involving conventional rheometers; (ii) measurements of rheology

involving conditions similar to the one encountered in underbalanced drilling operation; and (iii) theoretical studies using microscopic models to describe the rheological behaviour of foams (Herzhaft,Kakadjian and Moan, 2005). For excellent literature reviews on aqueous foam rheology studies, performed 30 odd years ago, one can refer to an article published by (Heller and Kuntamukkula, 1987).

Currently, there are numerous standard correlations available to capture and predict accurately the pressure drop of a conventional two-phase flow and this include a correlation derived by Lockhart-Martinelli (1949) which can predict up to an accuracy of 30%. Such a correlation (Kreith,Manglik and Bohn, 2012), however, when used to predict the pressure drop of a foam flow can give rise to erroneous results which can be fatal especially when used in design calculations (Calvert, 1990). Therefore, many authors have carried out experimental investigations with the aim of developing and proposing models that can accurately predict the pressure drop of a flowing foam.

Herzhaft *et al*. (2005) investigated the aqueous foam flow behaviour using a recirculating pipe rheometer and visualisation cell. With the aid of a visualisation cell, inserted into the flow loop, it was determined that a steady state was only reached after the foam was sheared for at least 20 minutes at a shearing rate of 120 s^{-1}. A continuous evolution of the aqueous foam was observed for a period of up to 20 minutes. Whilst, Briceno and Joseph (2003) investigated the flow characteristics and simultaneous visualisation of aqueous foams through a thin flow channel and a round pipe. For foam quality of less than 79%, they observed bubble size segregation, i.e. largest bubbles were found at the top and smaller ones at the bottom respectively (Briceño and Joseph, 2003).

Depending on the experimental conditions employed, foam flow can be characterised into distinct flow regimes. For example, with the aid of a digital photography, Deshpande and Barigou (2000) and Hoffer and Rubin (1969) identified three flow regimes consisting of plug flow, turbulent flow and bubble column with an increasing gas flow rates in a vertical pipe flow (Hoffer and Rubin, 1969). Whereas on the other hand, Briceno and Joseph (2003) observed seven distinct flow regimes for foams flowing in a horizontal pipe and a thin flow channel with various gas volume fractions. For a gas volume fraction less than 73%, two distinct fluid layers were observed, with largest bubbles at the top and smallest at the bottom of the conduit. Whilst, for gas volume fractions greater than 98%, the foam flowed as a series of slugs which was retarded by the wall friction (Briceño and Joseph, 2003). Recently, Bogdanovic, Gajbhiye and Kam (2009) developed a new concept of low- and high-quality flow regimes for foam flowing in horizontal pipes of varying lengths and diameters. They noted that foam consisting of low quality showed good stability and negligible pressure fluctuation in comparison to foam of high quality, which showed a large pressure fluctuation and unstable behaviour (Bogdanovic,Gajbhiye and Kam, 2009). Later, Gajbhiye and Kam (2012) carried out a similar investigation looking at the effects of pipe inclination angles on the resulting foam flow regimes (Gajbhiye and Kam, 2012). Their investigation also confirmed that the flow of a foam consisted of low- and high-quality regimes, as previously observed by Bogdanovic, Gajbhiye and Kam (2009).

For foam flow through processing equipment such as pipe fittings (e.g. valve, constriction, bend, 90° elbow, etc.) or when they exit from a pressurised system or from a product dispenser such as a nozzle can bring about drastic changes to the quality of the aerated products (Deshpande and Barigou, 2001a, Deshpande and Barigou, 2001, Heuer *et al.*, 2007, Haedelt *et al.*, 2005, Murray *et al.*, 2005, Söderberg,Dickinson and Murray, 2003, Murray *et al.*, 2006).

As foams are structured complex fluids and therefore any perturbation brought about, for example, by a sudden drop in pressure, shear or elongational forces can drastically change the morphology of the foam which is undesirable. In the case of a rapid pressure drop, occurring, as the foam exits from a filling chamber or a nozzle it can lead to the process of bubble coalescence (Murray *et al.*, 2006, Heuer *et al.*, 2007).

Calvert (1987; 1988) was the first to examine the effects of geometric constrictions (commercial diaphragm, global and ball valves) on firefighting foams. It was found that a flow constriction (global valve) with an intricate flow path (high shear rates) and a high residence time led to a complete loss of foam microstructure in contrast to a diaphragm or ball valve. Prior to experimental measurements, foam was generated using an opposed jet type device and passed through at three different liquid flow rates (7.9, 11.3 and 14.8 cm^3/s) through each valve, either at 25% or fully open. It was determined that, at the two high liquid flowrates, the global valve had much more effect on bubble size in comparison to both diaphragm and global valves respectively. This phenomenon was consistent and therefore in agreement with the wider observation in the firefighting industry, where it is a common knowledge that a global valve has the potential to completely suppress a foam whereas a gate valve, at the same pressure drop, will give a stable foam. In addition, it was concluded that the degradation of foam occurs, especially, in flows comprising of high shear rates and with long residence times (Calvert, 1988).

To further examine and to fill the gap in the open literature on flow of foams through geometrical constrictions such as pipe fittings (e.g. bend, expansion, constriction and elbow), Deshpande and Barigou (2001a and 2001b) performed several experimental investigations. This included sparging (either though a single orifice or two sintered glass discs) nitrogen gas

at various gas flowrates through an aqueous solution of sodium dodecyl benzene sulphonate (NaDBS) contained in a vertical column with constriction (90° elbow, 90° bend, expansion, contraction, orifice and perforated plates). By adopting a gamma-ray absorption technique to measure the local liquid holdup, it was found that the liquid holdup decreased significantly downstream of the fitting, especially, during contraction of the flow (Barigou,Deshpande and Wiggers, 2001, Deshpande and Barigou, 2001, Deshpande and Barigou, 2000).

In contrast, Murray *et al.* (2006) investigated the effects of rapid pressure change as a result of expansion on coalescence of protein-stabilised air bubbles using a previously in-house built apparatus (Söderberg,Dickinson and Murray, 2003). By changing the bulk protein concentration in the presence of food hydrocolloids (e.g. sucrose, xanthan gum, gelatine, etc.) and the rate of area strain, they observed that the fraction of bubbles coalescing (F_c) was dramatically decreased in case of foams made from gelatine even at concentrations as low as 0.01 wt%. Whereas, foams made from other food hydrocolloids showed various stability to coalescence when protein-stabilised bubbles were exposed to a sudden expansion (Murray *et al.*, 2006).

Similarly, to investigate the visualisation of foam microstructure when subject to a pressure change, Heuer *et al.* (2007), utilised a Linkam pressure cell (THMS600) in combination with confocal scanning laser microscopy (CSLM). Pressure drop variation of up to 11 bar absolute was investigated and the resulting changes occurring to foam microstructure captured and quantified. It was found that foam was relatively stable at stationary conditions whereas foam experiencing pressure variation, as normally encountered at industrial processes, brought about changes to the microstructure of the foam. The evolution of the microstructure was linked to

the process of coalescence occurring as a result of the perturbation brought about by variation in pressure drop (Heuer *et al.*, 2007).

As briefly mentioned, foams are complex multiphase dispersion which enjoys numerous industrial applications in a diverse range of industries including in food, oil and gas, mineral transport, firefighting, cosmetics, etc. In most of these industries, the foam is allowed to flow through a pipe, a channel or a narrow constriction and hence knowledge pertaining to its flow behaviour and dynamic stability is crucial for its effective application. Currently, there are very limited amount of empirical studies that investigated the flow and dynamic interaction of foamed viscous shear-thinning fluids with processing equipment. There are no studies that investigated the complex interaction with a narrow orifice constriction. The lack of studies is mainly due to the dynamic behaviour and complex non-linear viscoelastic characteristics, compressibility and wall-slip.

2.6 Rheology

Rheology is the study of flow and deformation of matter. Given enough time, all fluids will eventually flow and the resistance to this flow is known as viscosity. For example, an ideal solid will deform elastically when enough stress is applied, and this is fully recovered once the stress is removed. In comparison, a pure viscous fluid will flow, and the energy of the flow cannot be recovered. The viscosity of a Newtonian fluid is independent of shear rate and a good example is water. In contrast, a non-Newtonian fluid has an apparent viscosity which is dependent on the shear rate and it may or may not be time dependent. If the apparent viscosity decreases as a function of shear rate then it’s called a shear-thinning fluid and if it increases then it’s called

shear-thickening as shown in Fig. 2.18. However, most fluids are viscoelastic meaning they possesses both viscous and elastic properties.

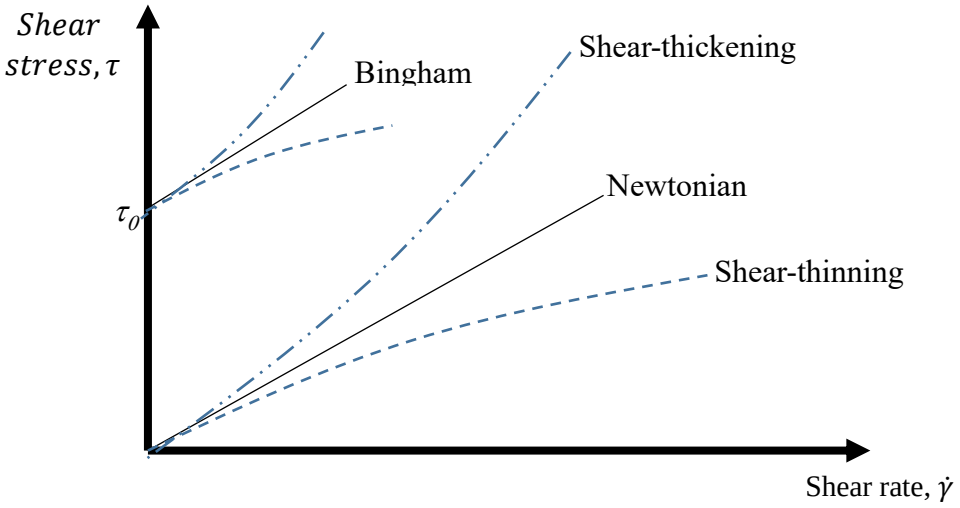

Fig. 2.18: Different types of fluids and their characteristics flow behaviour.

Many empirical rheological models have been proposed to capture and describe the non-Newtonian behaviour of complex fluids including foams. A summary of some of these models are as follows:

Power law	$\eta = k\dot{\gamma}^{n-1}$
Bingham	$\eta = \frac{\sigma_y}{\dot{\gamma}} + \eta_{pl}$
Cross	$\frac{\eta-\eta_\infty}{\eta_0-\eta_\infty} = \frac{1}{1+k\dot{\gamma}^{1-n}}$
Carreau	$\eta = \eta_\infty + \frac{\eta_0-\eta_\infty}{[1+(\lambda\dot{\gamma})^2]^{n/2}}$
Carreau-Yasuda	$\frac{\eta-\eta_\infty}{\eta_0-\eta_\infty} = \frac{1}{[1+(\lambda\dot{\gamma})^a]^{1-n/a}}$

Knowledge pertaining to rheological characteristics of fluids is essential for several industries including food, personal care, pharmaceutical, petrochemical etc. For example, in the food processing industry, the textural and sensorial properties of food is strongly linked to its rheological properties of the product concerned and it also plays a vital role in terms of stability and hence product shelf-life. In addition, the food engineer routinely carries out rheological measurements in order to obtain rheological data for process and product optimisation (Fischer and Windhab, 2011). Whereas, in the oil and gas drilling operations, the understanding of flow in combination with rheological behaviour of drilling fluids (i.e. foams) is of a paramount importance, especially, for pressure drop prediction and for the efficiency of cutting transport (Sherif *et al.*, 2016).

Rotational rheometry is a classical way of determining the rheological properties of the fluids - including bubbly liquids and wet foams. In a rotational rheometer, the sample is sheared between two plates under a controlled shear rate or controlled shear stress. The common geometries are the parallel plate, a cone-plate and concentric cylinder (one rotating and the other stationary) as shown in Fig. 2.19. In addition, Table 2.2 provides a summary of the rheological parameters that can be measured and extracted. The data obtained from these devices can be fitted to various models proposed in the literature to obtain the rheological characteristics (such as viscosity, storage and loss modulus, etc.) of the fluids concerned. The main reason why rheometers are widely employed for rheological measurements lies in the fact that the temperature and humidity level can be easily controlled which can have a significant effect on the experimental results. Furthermore, it can also be used to perform oscillatory tests to determine the viscoelastic nature of the fluids such as bubbly liquids and wet foams. This involves the application of oscillatory shear of angular frequency and simultaneously measuring the harmonic stress response.

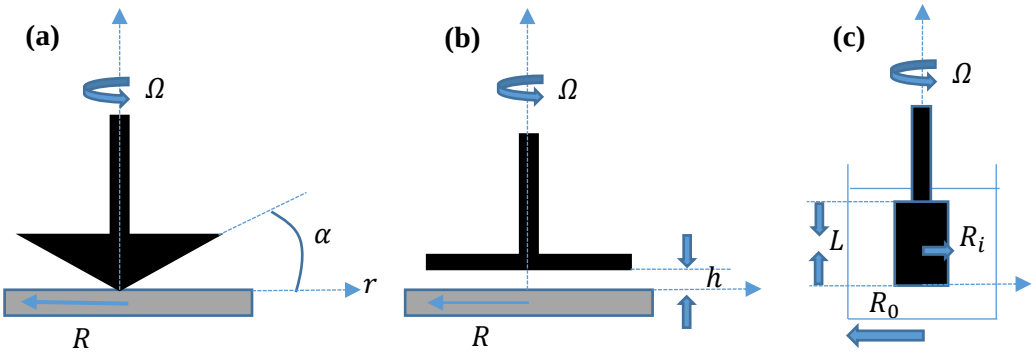

Fig. 2.19: Schematic of commonly used rotational geometries: (a) cone-plate; (b) parallel plate; and (c) concentric cylinder.

Table 2.2: A summary of rheological parameters for commonly used geometries.

Geometry	**Shear stress (τ_{ij}) (Pa)**	**Shear rate ($\dot{\gamma}$) (s^{-1})**	**Viscosity (Pa.s)**
Parallel plate	$\frac{3M}{2\pi R^3}\left[3+\frac{d\ln\left(\frac{M}{2\pi R^3}\right)}{d\ln(\dot{\gamma})}\right]$	$\frac{r\Omega}{h}$	$\frac{M}{2\pi R^3\dot{\gamma}}\left[3+\frac{d\ln\left(\frac{M}{2\pi R^3}\right)}{d\ln(\dot{\gamma})}\right]$
Cone & plate	$\frac{3M}{2\pi R^3}$	$\frac{\Omega}{\alpha}$	$\frac{3M\alpha}{2\pi R^3\Omega}$
Concentric cylinder	$\frac{M}{2\pi R^3 L\frac{R_i}{R_0}}$	$\frac{\frac{R_i}{R_0}\Omega}{1-\frac{R_i}{R_0}}$	$\frac{M\left(1-\frac{R_i}{R_0}\right)}{2\pi R^2 L\left(\frac{R_i}{R_0}\right)^3\Omega}$

When using a rotational rheometer, for the measurement of the rheological properties of complex and structured fluids (such as emulsions, foams, and solid suspensions), it is essential to take into consideration any peculiarities that may arise during the measurement. Wall-slip phenomenon is commonly observed for these fluids which is the migration of the dispersed

phase away from the solid boundary. To minimise this, roughened geometries are often implemented. This can be accomplished by using serrated geometries or by simply attaching an appropriate type sandpaper. In addition, the gap width must be at least 10 times the size of the largest bubble/drop. Shear-induced migration phenomenon can also take place especially when using a parallel plate geometry and when operating under high shear rate. The latter is commonly observed in solid suspension and in 2D foams with non-homogeneous BSD. Finally, shear banding has also been observed as found by the following authors (Lexis and Willenbacher 2014).

Aqueous foams are complex: they are compressible, non-linear viscoelastic materials; their viscosity is much larger than for the liquid constituent, and they often show a high zero-shear viscosity which may be misinterpreted as an apparent yield stress (plasticity). Understanding of foam properties is therefore limited - design and control for applications is more art than science and many issues remain unaddressed/unresolved, e.g. flow dynamics, structural behaviour, stability/metastability, and dependence of rheological properties on structure and physicochemical constitution. Specifically, foams generated from viscous non-Newtonian fluids have received insufficient attention in the literature.

2.7 Conclusion

The above review has briefly outlined and discussed the relevant open literature pertaining to foam formation, structure, flow and dynamic stability. Particular emphasis was placed on foam formation using a commercially available food-grade non-ionic surfactant – polyglycerol ester of fatty acid (PGE 55). The complex mixture of PGE 55 has shown excellent foam stabilisation properties which is mainly due to the formation of uni – and multilamellar vesicles in the bulk and its strong monolayer formed giving rise to resistant against foam drainage, coalescence and coarsening. In addition, foam formation using a mechanically driven continuous rotor-stator devices were highlighted. As well-known, in these devices the hydrodynamical forces are responsible for achieving optimum aeration efficiency and BSD.

Abbreviations

BSD	bubble size distribution
D_{32}	Sauter mean bubble diameter (m)
cmc	critical micelle concentration
G/L	gas-liquid volumetric flowrate ratio
PGE 55	polyglycerol ester of fatty acid
XG	Xanthan gum
X-ray micro-CT	X-ray micro-Computed Tomography

Chapter 3: Foam Imaging – comparison between 2D light microscopy and 3D X-ray micro-Computed Tomography techniques

Summary

A good degree control of a foam texture requires accurate and non-invasive techniques and tools. X-ray micro-Computed Tomography (X-ray micro-CT) is one such technique which has been scarcely implemented. Therefore, in this study, for the first time, a comparison between the traditional 2D light microscopy imaging technique and the non-destructive 3D X-ray micro-CT imaging technique is carried out for wet foams generated using a continuous rotor-stator device. Significant discrepancies can arise between the two techniques especially when non-homogenous and unstable foams are investigated. Using X-ray micro-CT imaging and the image analysis procedure developed in this work, the effects of liquid composition and processing parameters on bubble size distribution (BSD) of wet foams generated using a multi-stage continuous rotor-stator can be clearly distinguished. In addition, provided an accurate image acquisition and processing procedures are implemented, it is found that X-ray micro-CT gives a much more accurate, representative and reliable BSD – important for a wide range of industries especially for food processing.

Keywords: Continuous foaming; non-Newtonian liquid; Foam imaging; 2D light microscopy; X-ray micro-CT. Part of this **chapter published:** Jabarkhyl, S., Zhu, S., Rayment, P., Lloyd, D.M., Rossetti, D., Barigou, M., (2019). Foams generated from viscous non-Newtonian shear-thinning liquids in a continuous multi rotor-stator device. Innovative Food Science and Emerging Technologies, Vol. 59.

3.1 Introduction

Since the 1990's, food manufacturers across the globe have realised the significant potential of aerated food products such as ice cream, mousse, scuffle, meringue, etc. As a result, food aeration is one of the fastest growing unit operations (Campbell and Mougeot, 1999). In the production of aerated products such as whipped cream, ice cream or mousse, it is important to achieve a good degree of control of the air volume fraction and bubble size distribution (BSD) since the stability and the organoleptic properties of the product (creaminess, texture, mouthfeel) are strongly dependent on these critical parameters. For example, small bubbles and uniform BSD impart excellent foam stability and creaminess (Müller-Fischer,Suppiger and Windhab, 2007b, Müller-Fischer and Windhab, 2005).

Presently, there are several techniques for measuring the BSD including conductivity probes, optical fibre technique, light microscopy, freezing and visualising foam cross-sections, X-ray micro-computed tomography (X-ray micro-CT), ultrasonic reflectance spectroscopy and confocal scanning laser microscopy (Kulmyrzaev,Cancelliere and McClements, 2000, Lim and Barigou, 2004, Jang *et al.*, 2005). Each of these techniques have its own advantages and drawbacks. Many of these techniques are intrusive and hence suffer from similar limitations which involve significant tampering with the foam samples which is undesirable. By contrast, X-ray micro-CT is a non-destructive and non-invasive technique that can be employed to image stable foams to reveal their full 3D microstructure with a high degree of accuracy (Lim and Barigou, 2004).

In literature, however, one experimental technique which has been widely adopted to measure the BSD of liquid foams is a 2D light microscopy. This captures two-dimensional images (2D)

through a transparent column or through a sample placed between microscope slides (Gaillard *et al.*, 2015, Gaillard *et al.*, 2017). Light microscopy technique is very simple and cost effective, however, in many cases, the method adopted is not an accurate representation of the bulk foam sample. This is mainly due to the errors associated with the image capturing technique, i.e. planar sampling bias and in some cases the effect of smaller bubbles on larger bubbles at the column wall (Stevenson, 2012). In addition, the method is intrusive, and the procedure is semi-automatic involving the detection of individual bubbles using software such as ImageJ and Matlab. The successful utilisations of these software's also rely on capturing high quality images that are evenly illuminated which can be difficult to obtain in certain industrial and laboratory settings. It is worthy to note that the successful implementation of light microscopy technique requires a statistical representative BSD. Different authors have recommended different sample size. For example, Deshpande & Barigou (2000, 2000a & 2000b) used a sample size of 40 bubbles for coarse texture dry foams and 200 bubbles for fine texture dry foams (Deshpande and Barigou, 2000, Deshpande and Barigou, 2001a, Deshpande and Barigou, 2001). In contrast, Żmudziński *et al.* (2014) and Liszka-Skoczylas, Ptaszek, & Żmudziński (2014) used a sample size of 600 and 3000 bubbles respectively to obtain statistical representative results (Żmudziński *et al.*, 2014, Liszka-Skoczylas,Ptaszek and Żmudziński, 2014).

In foam generation using a continuous rotor-stator device, almost all studies conducted so far, have implemented the traditional 2D light microscopy imaging technique (Müller-Fischer and Windhab, 2005, Mary *et al.*, 2013) with the exception of a study conducted by Balerin et al., (2007) where an online probe sensor was utilised (Balerin *et al.*, 2007). For example, the first study to report the BSD of wet foams generated using a continuous rotor-stator device was by Kroezen and Wassink (1987). In their study, aqueous foam was generated and then allowed to

pass through a camera section where it was visualised through a perspex window using a microscope. The BSD was then obtained by measuring up to 250 bubbles. As mentioned in their study, to correct for the observational error, the de Varies correction factor was utilised (Kroezen and Wassink, 1987). Subsequent studies on foam generation using a continuous rotor-stator utilised the technique of light-microscopy and a bubble detection software (such as BubbleDetect, Semper6P, Matlab, Image ProPlus 4.0, and ImageJ). For example, Hanselmann and Windhab (1998) used an inverse light microscope in combination with a coloured video camera to obtain a number of digital images which was then used to obtain the size of 300 bubbles (Hanselmann and Windhab, 1998). Similarly, Muller-Fischer and Windhab (2005) and Muller-Fischer, Suppiger and Windhab (2007) used a light microscope to obtain five micrographs for each sample investigated, which were then used to obtain the bubble size using in-house software - BubbleDetect. In their study the number of bubbles detected and the size distribution were not reported (Müller-Fischer and Windhab, 2005, Müller-Fischer,Suppiger and Windhab, 2007b).

As briefly summarised above, so far, the use of a 2D light microscopy technique is the rule rather than an exception. The method is cost effective and simple, but for a representative BSD, it is important to take advantage of the non-invasive 3D X-ray micro-Computed Tomography (X-ray micro-CT) technique. Therefore, the main aim of this study is to compare and contrast the 2D light microscopy technique to the 3D X-ray micro-CT technique for the determination of BSD of wet foams generated from model shear-thinning fluids using a continuous rotor-stator device. From the author's knowledge, this is the first extensive study involving the investigation of 3D microstructure of wet foams using X-ray micro-CT technique.

3.2 Materials and methods

3.2.1 Materials

Model fluids 2 and 5 (MF2 and MF5) were used in the experiments, consisting of mixture of polyglycerol fatty acid ester (PGE 55, DuPont, Denmark), xanthan gum (XG, supplied by Unilever), caster sugar (British sugar PLC, obtained from local supermarket) and sodium azide (ReagentPlus, ≥ 99.5%, Sigma Aldrich), all used without prior purification. The composition of these fluids is displayed in Table 3.1.

Table 3.1: Formulation of model fluids.

Model fluid	PGE 55 (wt%)	XG (wt%)	Sugar (wt%)
MF2	0.5	0.50	25
MF5	0.5	0.35	25

3.2.2 Methods

3.2.2.1 Model fluids preparation and foam generation

A Silverson high-shear mixer (Model L4RT, Silverson, UK) was used to mix the ingredients in distilled water held at 80 °C using a water bath, to ensure that the Krafft temperature (58 °C) of PGE 55 was exceeded (Duerr-Auster *et al.*, 2008, Curschellas *et al.*, 2012a). First, polyglycerol fatty acid ester (PGE 55) was added under agitation (6000-7000 rpm) and mixed thoroughly for at least 5 minutes prior to adding sugar and XG. Stirring was continued for another 5 min until all XG was completely dissolved. Sodium azide (0.025 wt%) was added to prevent microbial growth. The model fluids were then stored at 5 °C to degas and mature (hydration of XG) for at least 24 hours, to enable their rheology to fully stabilise (See Chapter 4 for more details).

A pilot-scale continuous rotor-stator device (refer to Chapter 4 for more details) was utilised to generate wet foams from model fluids. Wet foams of various textures were generated by using a combination of air and liquid volumetric flowrates ratio (G/L ratio) and rotor speeds (N) in the range of 500-1750 rpm.

3.2.2.2 Light microscopy

Two techniques were utilised to obtain the foam BSD. The first technique is a well-established method which uses a light microscope (ZEISS, Axiovert 200M) and a digital camera. Foam samples were diluted using the base liquid and then carefully transferred to a viewing chamber according to the protocol described by Gaillard *et al.* (2017) as shown in Fig. 3.1. It consisted of a glass slide (Microscope Slides-Plain, 76×26 mm) on top of which was placed two cover glass (thickness No.1 and 1.5, VWR), spaced apart, to create a chamber in which the diluted foam sample was slowly inserted. After carefully inserting the foam sample in the chamber, it was then covered with a microscope cover glass (thickness No. 1, VWR) as depicted in Fig. 3.1.

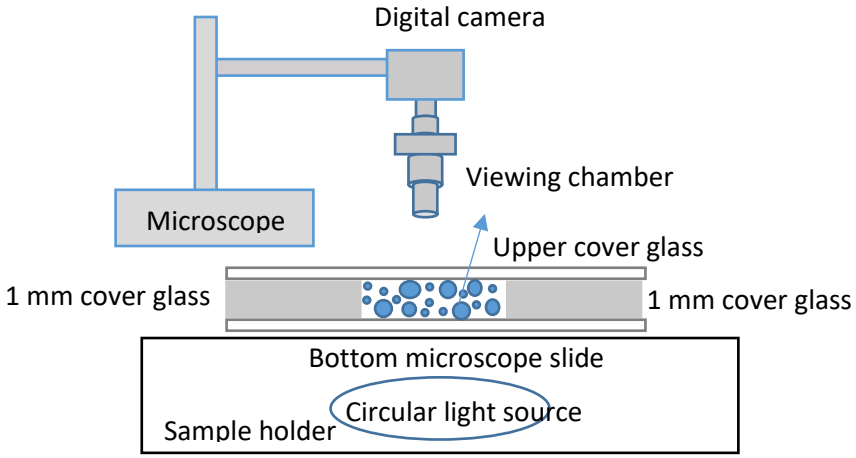

Fig. 3.1: Schematic of light microscopy imaging technique to demonstrate the measurement of a polydispersed foam (not to scale).

The foam sample was then observed through a microscope (ZEISS, Axiovert 200M) using a 5X or a 10X magnification. A digital camera (BASLER, Edmund Optics/Worldwide) was then used to take up to 30 digital images for each sample. Once the required number of images were acquired, it was then manually processed and analysed using the freely available software - ImageJ (https://imagej.nih.gov/ij/index.html). The procedure implemented was as follows:

- Upload the relevant image to ImageJ software (Fig. 3.2a)
- Set the scale using a graticule (1 mm in size)
- Apply the binary function (Fig. 3.2b)
- Remove unwanted bubbles and apply filling holes function (Fig. 3.2c)
- Apply the watershed algorithm and analyse the bubble sizes (Fig. 3.2d)

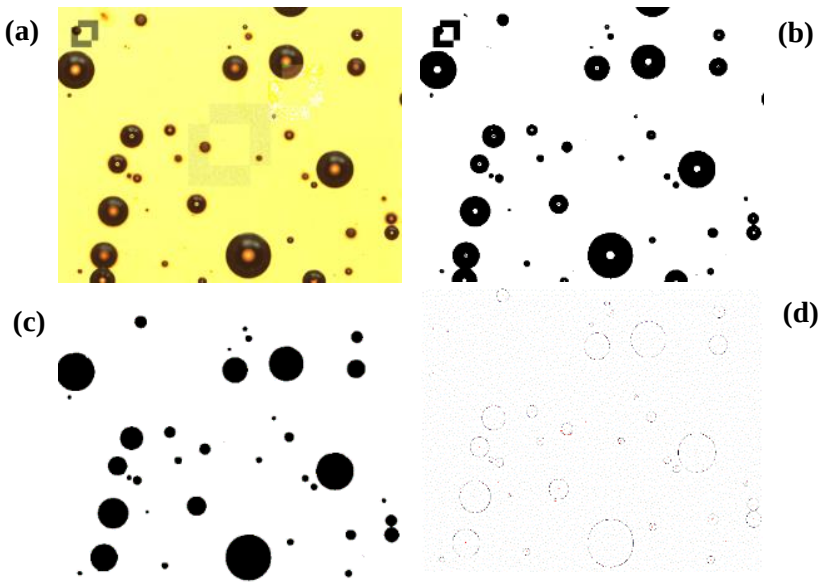

Fig. 3.2: Outline of the procedure used to analyse the bubble size using ImageJ software.

From the BSD, the Sauter mean bubble diameter is obtained:

$$D_{32} = \frac{\sum n_i d_i^3}{\sum n_i d_i^2} \qquad \text{(Eq. 3.1)}$$

where *n* is the number of bubbles of diameter *d* in class size *i*. The BSD was plotted in the form of a histogram. Experimentally measured bubble sizes were grouped into discrete classes (bins) with identical width.

3.2.2.3 X-ray micro-Computed Tomography (X-ray micro-CT)

In contrast to light microscopy, X-ray micro-Computed Tomography (X-ray micro-CT) technique relies on the attenuation (i.e. phase contrast) of X-rays energies after passing through a given object. As noted previously, objects with a high atomic number will completely stop the transmission of X-rays whereas a sample with a lower density and atomic number (i.e. bone) will allow the transmission of X-rays. Therefore, the main principle of X-ray micro-CT is to generate X-rays of various energies, which are then transmitted through the sample held in the centre by a rotatable sample holder. The sample is then rotated by a pre-determined angle over by 180° or 360°. The various intensities of X-rays emitted from the sample are then detected and a digital camera is used to take several shadow images (raw images). A computer is then used to record these images for reconstruction later. The reconstruction is achieved by the principle of filtered back-projection algorithm utilising the method of cone-beam reconstruction. A schematic of the working principle of X-ray micro-CT is shown in Fig. 3.3.

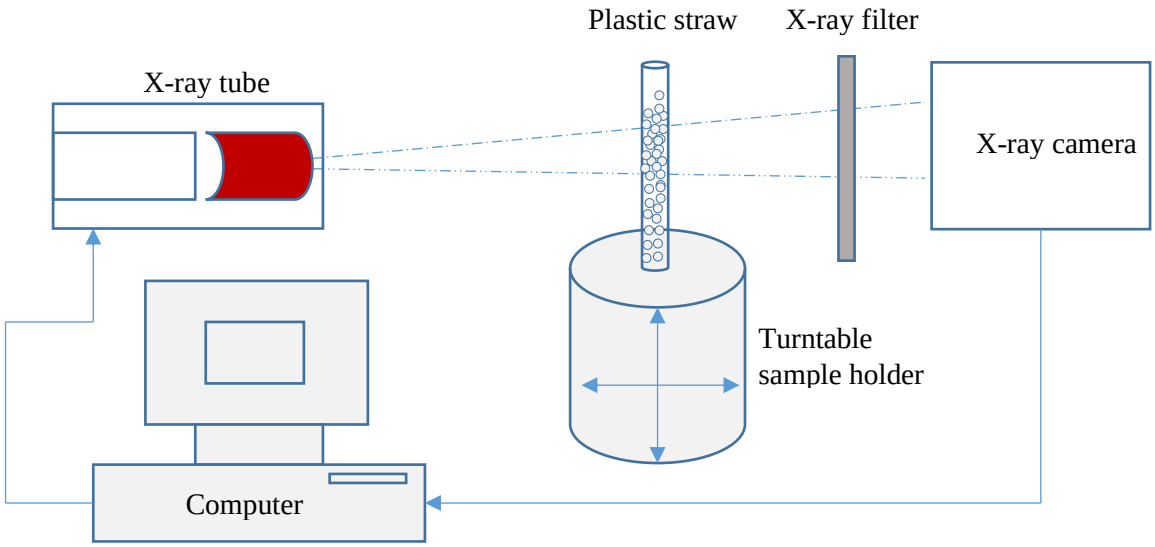

Fig. 3.3 Schematic of working principle of X-ray micro-CT adopted from Barigou and Douaire (2013).

Wet foam samples were carefully transferred to a drinking straw - using a syringe or a pipette. The samples were then taken to X-ray micro-CT (Skyscan, 1072, Bruker, Belgium) for X-ray imaging. Scanning was performed at 80 keV voltage and 100 µA current values and image resolution of 2.43 µm pixel^{-1}, 3.78 µm pixel^{-1} and 5.78 µm pixel^{-1}, respectively. No filter was chosen since the foam consisted of an air and water mixture which are both very low-density materials with a low attenuation coefficient compared to a rock or a bone sample. Each sample was then rotated by 180° with a step size of either 0.4° or 1.0° and frame averaging of 4 to obtain several radiographic raw images. The scanning duration was limited to less than 20 minutes to avoid the process of gravity drainage which can significantly temper with X-ray imaging.

A significant rise in temperature inside the X-ray micro-CT device will lead to foam destabilisation especially gravity driven drainage which must be avoided. Samples which can readily absorb X-ray energies are more liable to such destabilisation process. However, for wet

foam samples investigated in this thesis, the temperature inside the X-ray micro-CT device was well-controlled with the aid of an air-conditioning. In addition, the foam samples consisted mainly of low-density materials, i.e. water and air which does not strongly absorb X-ray energies and hence were much less likely to drain. Furthermore, a few degrees rise in temperature has insignificant effect on the apparent viscosity of the xanthan gum foaming solution since its molecules are strongly resistant to temperature. Similarly, foam samples generated at high rotor speeds and air volume fractions were more liable to foam coarsening. Even though, within the time frame of X-ray scanning < 20 minutes, foams generated in this thesis were stable against foam coarsening, however, any coarsening that did took place was visible and easily removed from imaging analysis procedure. To further check the robustness against foam coarsening, some samples were scanned twice and from negligible to no foam coarsening was observed.

Once scanning was complete, shadow images were then uploaded to a reconstruction N-Recon software (Bruker micro-CT, Belgium) to obtain the equivalent number of virtual cross-sections of the sample. The software allows for the correction of common artefacts arising during imaging acquisition such as: (i) smoothening; (ii) misalignment; (iii) beam hardening; and (iv) ring-artefacts. Depending on the scanning parameters implemented, the reconstruction procedure took approximately 5-10 minutes. Finally, the projection images were then uploaded to a specialised CTan software (Bruker micro-CT, Belgium) for a detailed two- and three-dimensional image analysis.

In CTan, first, a circular region of interest (ROI) is chosen and then applied to a stack of 2D images to eliminate any background noise and objects. The ROI and the new data set are then saved in a separate folder and reloaded. A suitable global thresholding method is then chosen

to binaries the 2D images. Global thresholding is an image binarisation method and it is based on the histogram of the whole set of images. Any pixel corresponding to the given object in study become white (foreground) and the grey levels below the threshold become black (background). It is an appropriate method to utilise when the grey level histogram is bimodal (Leszczyński *et al.*, 2016). The binarsied images were then processed in a custom processing window. In order to isolate the image from the surrounding, an ROI shrink-wrap function in 3D was applied to all the 2D images. After, a bitwise operation (Image and ROI) was performed to distinguish the ROI from the image. In order to remove any unwanted black and white voxel, a despeckle function was applied to all the 2D images. A watershed separation algorithm was then implemented to separate interconnected bubbles. The software establishes a distance map along with local minima through which the bubbles are separated. Similarly, the remove broken object was then used to eliminate broken bubbles – especially at the ROI boundary and failure to remove this can lead to unreliable results (Dalen and Koster, 2012). Subsequently, comparison of individual 2D analysis was performed in CTan and Matlab software. Finally, the bulk volumetric 3D analysis and individual three-dimensional analysis was performed in CTan. The former is useful to render a 3D model from several 2D slices and for obtaining additional parameters such as percentage porosity, degree of anisotropy (DA), cell wall thickness, object surface to volume ratio (OSVR). In contrast, individual 3D analysis is more accurate for obtaining the actual BSD and hence the Sauter mean bubble diameter, D_{32} (Latief,Mohammad and Rarasati, 2019).

3.3 Results and discussion

3.3.1 Light microscopy 2D imaging and analysis

Light microscopy is commonly implemented to determine the BSD of a wide variety of foams and aerated structures (Żmudziński *et al.*, 2014, Liszka-Skoczylas,Ptaszek and Żmudziński, 2014, Müller-Fischer and Windhab, 2005, Mary *et al.*, 2013). The very low cost and operating simplicity are the main reason for its wide usage. The method, however, is 2D and hence significant errors can arise during sample preparation, image capturing and image processing. The number of bubbles analysed to obtain a statistical representative Sauter mean bubble diameter (D_{32}) from this technique has been in the range of 40-3000 bubbles. The most common value, however, reported is 500 bubbles.

In this study, to determine the minimum number of bubbles necessary for statistical representative D_{32}, an analysis was made on 100, 250, 350, 500, 750 and 1000 number of bubbles as depicted in Fig. 3.4b. Typical 2D images for fluid MF2 obtained at ratio of air to liquid volumetric flowrate, G/L, of 1.5 (ϕ_e = 0.62), and rotor speeds of N = 500 - 1750 rpm are shown in Fig. 3.4a. For a G/L ratio of 1.0 (ϕ_e = 0.52), the D_{32} increases with an increase in the number of bubbles analysed – this was especially true for foams generated at a lower N. This is because these foams have a non-homogenous and polydispersed nature. In contrast, all three foam samples generated at G/L ratio of 1.5 showed a similar trend with very little variation in D_{32} with an increase in the number of bubbles analysed. Therefore, due to the uniform bubble size distribution, the number of bubbles analysed had insignificant effect on D_{32}. In addition, it is also important to mention that the bubble size distribution (BSD) varies, sometimes, significantly with the number of bubbles analysed and an example of this for fluid MF2 at G/L = 1.0 and N = 500 rpm is shown in Fig. 3.4. Therefore, for processes where an accurate BSD is

required, it is important to choose an appropriate number of bubbles for accurate and representative BSD results.

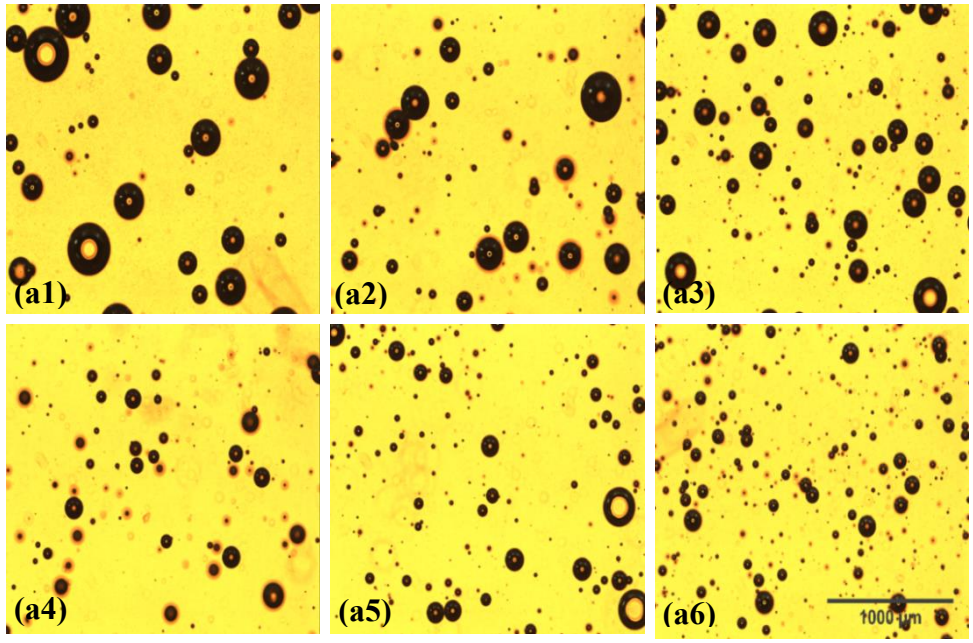

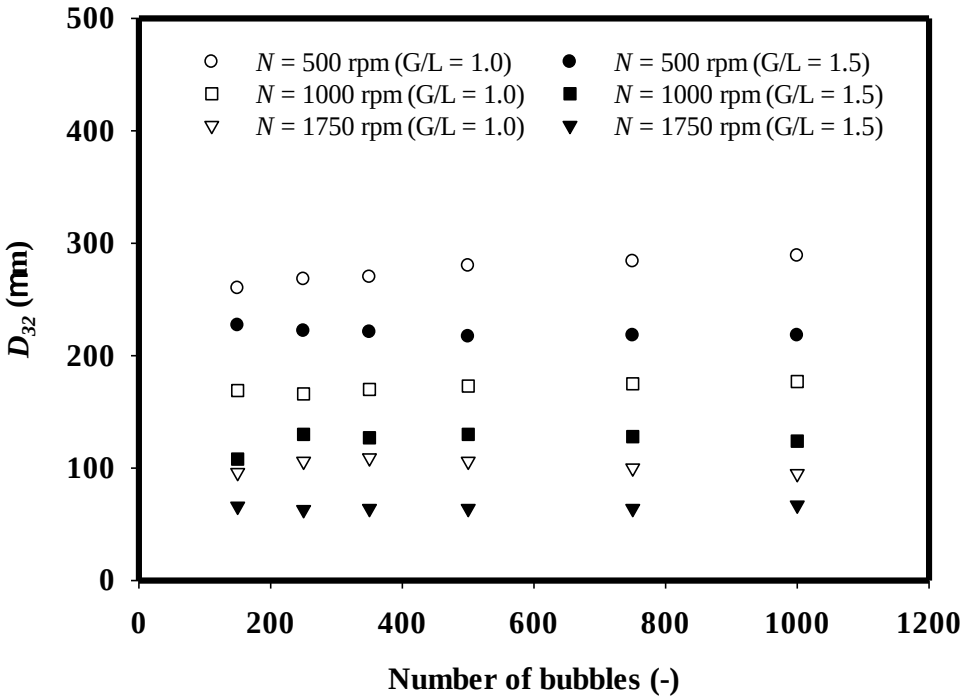

Fig. 3.4: (a) 2D light microscopy images; and (b) effects of number of bubbles analysed on Sauter mean bubble diameter (D_{32}) for foams generated from fluid MF2.

In summary, to obtain a representative BSD and hence D_{32}, from a 2D light microscopy technique, a minimum of 500 bubbles are necessary - as commonly reported in the literature. This is only true, however, for samples with a uniform BSD. Therefore, if the sample is polydispersed or unstable, then it is important to note that the number of bubbles necessary to obtain a statistical representative BSD might be much greater > 1000 bubbles – as expected. The accuracy of this technique is also strongly dependent on the stability of wet foam sample, image acquisition and image processing procedures. The size of the larger bubbles can be significantly underestimated if partially viewed (strongly depends on the depth of the viewing chamber, magnification and polydispersity) or significantly overestimated if larger bubbles are distorted by implementing an incorrect depth of the viewing chamber.

3.3.2 X-ray micro-CT 2D-3D imaging and analysis

In contrast to a 2D light microscopy technique, as outlined above, X-ray micro-CT is a much more powerful and a non-destructive technique. It can be applied to visualise, non-invasively, the complete microstructure of foams and aerated products. In the sections to follow, a bench-top X-ray micro-CT scanner was utilised to carry out a number of systematic studies in order to find the optimum scanning parameters to deduce the full 3D microstructure of a range of wet foams generated using a continuous rotor-stator device. In addition, towards the end of the chapter, a comparison between 2D light microscopy and 3D X-ray micro-CT is also investigated.

3.3.2.1 2D structural analysis using CTan and Matlab software

Wet foams generated from model shear-thinning fluids using a continuous rotor-stator device (as will be outlined in Chapter 4) possessed a range of microstructures with varying static stability. For the X-ray micro-CT scan to be successful, it is essential that no microstructural changes occur during the period of scanning. Any changes, however, that do take place will lead to poor quality images which are difficult to analyse and process automatically. It is therefore crucial to choose appropriate scanning parameters that will yield good contrasted images. Therefore, for the statically stable foams, a scanning duration of 20 minutes was enough to obtain excellent X-ray projection images which were then processed and analysed using CTan software.

For two-dimensional structural analysis using CTan, it is necessary to remove any sources of error that can arise during image processing. One source of error is during image thresholding which needs to be carefully selected. For foam samples generated at N = 500 rpm and 750 rpm, a global thresholding range of 30-250 was chosen and for N > 750 rpm a thresholding range of 80 – 250 was chosen. In addition, a watershed algorithm was implemented in 2D space to separate the interconnected air bubbles as shown in Fig. 3.5. Failure to do this can also give rise to large discrepancy in the results obtained (Saadatfar *et al.*, 2009).

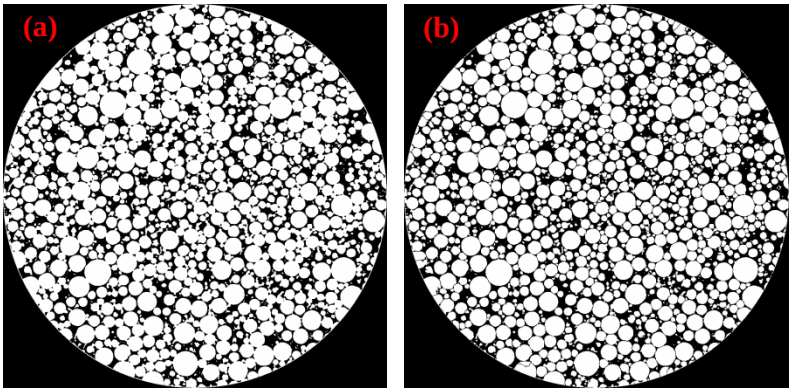

Fig. 3.5: 2D X-ray slices of wet foam generated from fluid MF2 at G/L = 1.5 & N = 1000 rpm: (a) before implementing watershed function; and (b) after.

Similarly, when choosing an appropriate region of interest (ROI), bubbles at the periphery are broken which needed to be removed and this was done using a morphological function of remove broken objects in 2D space. An example of how this is accomplished for a wet foam generated from fluid MF2 at N = 1000 rpm and G/L = 1.5 is shown in Fig. 3.6. As will be outlined, failure to remove these broken bubbles can lead to significant discrepancy between 2D CTan and Matlab results. In addition, it may also significantly under- or over-predict the Sauter mean bubble diameter (D_{32}).

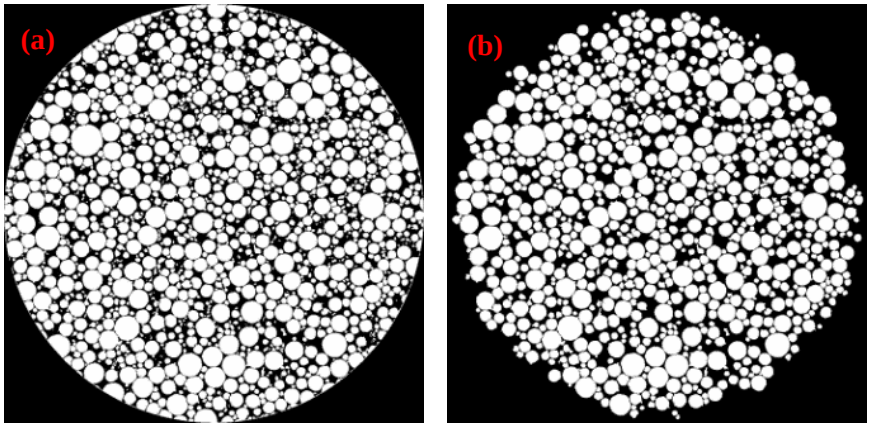

Fig. 3.6: 2D X-ray images of wet foam generated from fluid MF2 at G/L = 1.5 & N = 1000 rpm: (a) before implementing remove broken objects at ROI boundary; and (b) after.

For the wet foams generated from fluid MF5 at N = 500 rpm and G/L = 1.0 and 1.5, however, 2D analysis using CTan was prone to error since the bubbles were slightly distorted at the edges and hence during watershed operation (the separation of interconnected bubbles through finding local minima on a distance map) these bubbles were split into many smaller bubbles – introducing a source of error (refer to Fig. 3.7). Therefore, for samples generated at N = 500 rpm, only Matlab was able to obtain the D_{32}. This was also true for wet foams generated under pressurised conditions since these foams had larger air bubbles and a non-homogenous BSD.

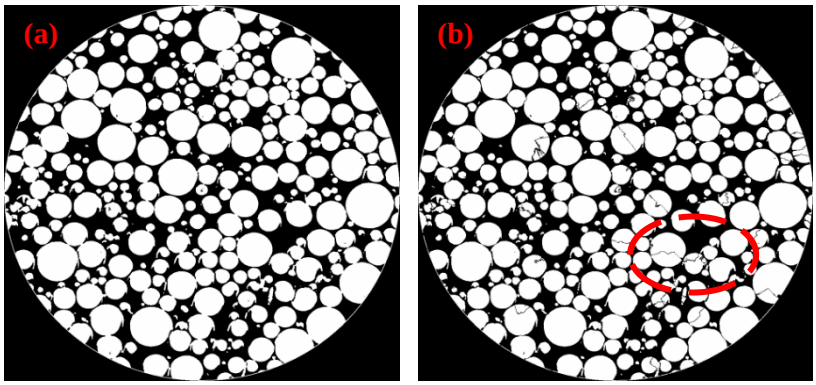

Fig. 3.7: 2D X-ray images of wet foam generated from fluid MF5 showing error arising during image processing: (a) before implementing watershed operation; and (b) after.

Wet foams generated at higher N and G/L ratio were fine textured with a uniform BSD. Therefore, limitations regarding resolution must be known and taken into consideration. This was done by performing X-ray scans on the same sample using three separate resolutions of 2.43 μm pixel^{-1}, 3.78 μm pixel^{-1} and 5.78 μm pixel^{-1} respectively. Fig. 3.8 and Table 3.2 shows the 2D images and cell parameters obtained for foams generated from fluid MF2. As shown, there was insignificant variation in D_{32} with a change in resolution signifying that all three resolutions were sufficient to obtain a representative Sauter mean bubble diameter (D_{32}).

However, in each image, the number of cells identified are slightly greater at 2.43 μm pixel^{-1} resolution as shown in Table 3.2. Consequently, the relative cell area was also slightly greater. This is possibly due to either that at this resolution, X-ray micro-CT was able to identify and resolve more of the smaller bubbles in the range of 20 – 50 μm or it might be due to the noise introduced during global thresholding. In addition, the smaller bubbles resolved at a higher resolution are likely to be introduced during model fluids preparation. The shortcoming, however, of using a higher resolution is a significant increase in scanning time, a lower field of view and an increase in image processing time. The possible side-effects of these are: (i) an increase in scanning time which will lead to gravity drainage; and (ii) a reduction in the field of view meaning that a much smaller volume of foam is X-ray scanned which might not be representative of the bulk foam sample.

Table 3.2: Typical results of comparison of 2D cell parameters of a single slice for foam generated from model fluid MF2 at N = 1000 rpm.

Resolution (μm/pixel)	G/L = 1.0 (ϕ_e = 0.52)			
	Cell count (-)	D_{32} (μm)	Total cell area (mm^2)	Relative area (-)
2.43	736	161	8.88	0.55
3.78	718	162	8.72	0.53
5.78	574	167	7.97	0.51
Resolution (μm/pixel)	G/L = 1.5 (ϕ_e = 0.62)			
	Cell count (-)	D_{32} (μm)	Total cell area (mm^2)	Relative area (-)
2.43	1274	133	10.30	0.65
3.78	1232	135	9.80	0.63
5.78	977	134	8.84	0.62

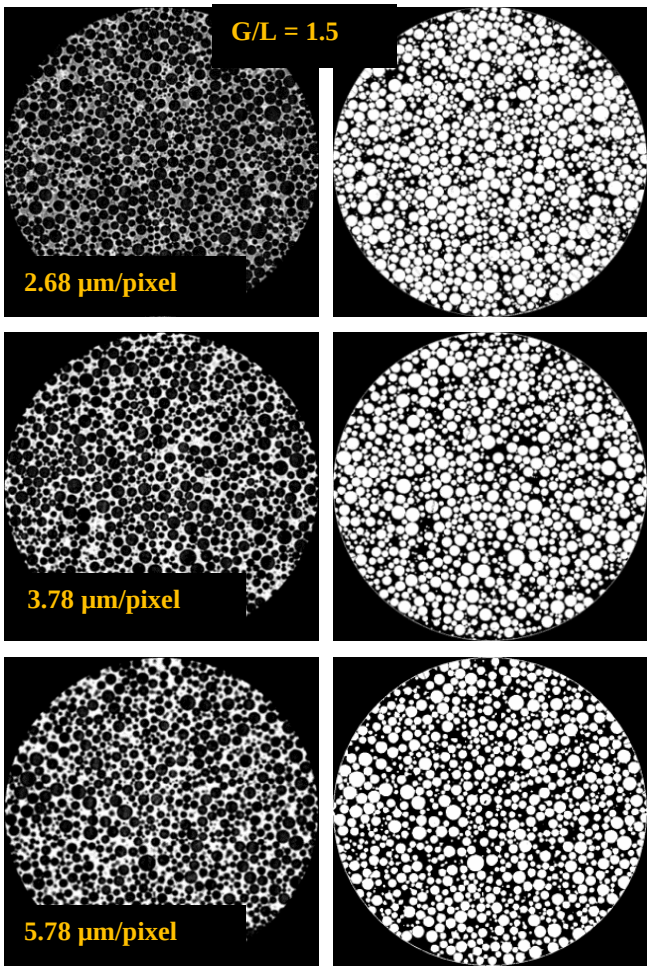

Fig. 3.8: Typical 2D X-ray micro-CT images of wet-foam samples generated from fluid MF2 at N = 1000 rpm.

The corresponding BSD are depicted in Fig. 3.9. As mentioned previously, scanning at a higher resolution enabled the detection of smaller bubbles (< 50 µm), however, these bubbles are likely to be due to noise introduced during image thresholding or it might be bubbles introduced during model fluids preparation.

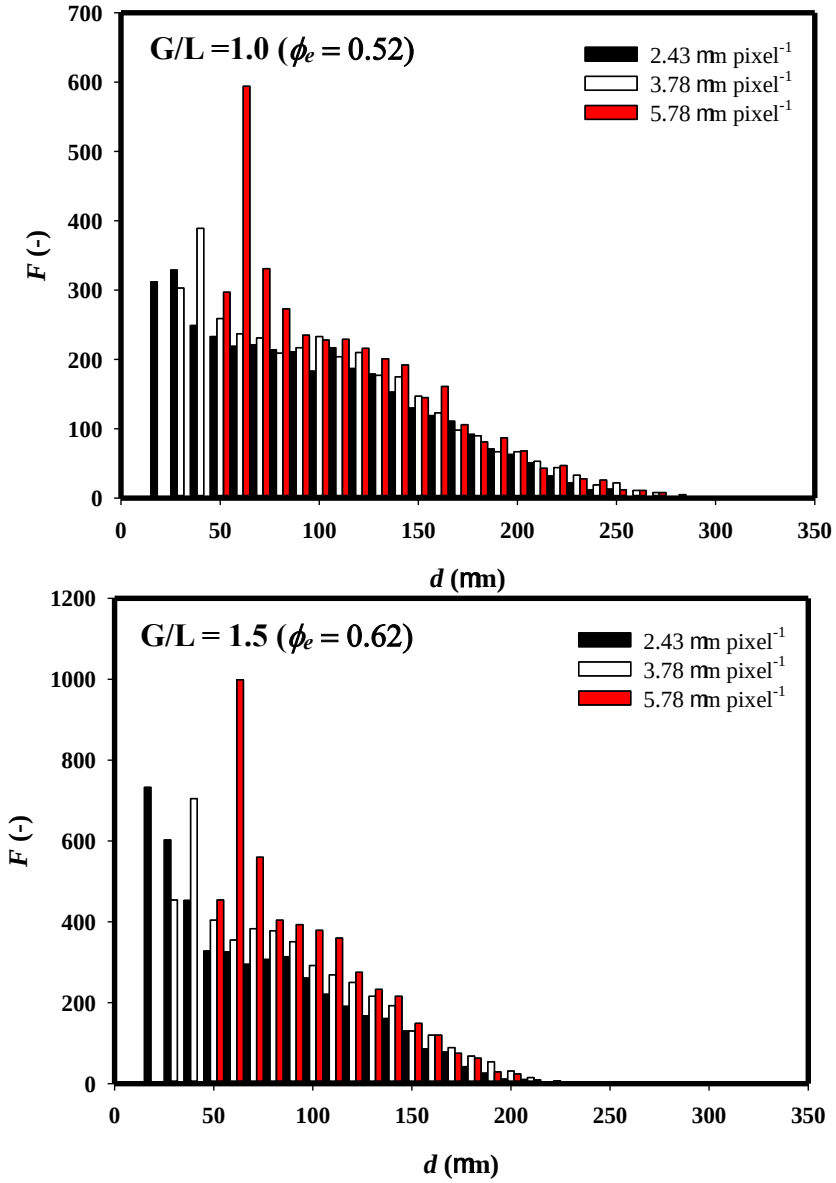

Fig. 3.9: Typical effect of resolution on bubble size distributions (approx. 3500 bubbles) of wet foam samples generated from fluid MF2 at N = 1000 rpm.

For the most unstable foams, however, it was essential to perform the X-ray micro-CT scanning in a short period of time possible since a longer duration lead to complete loss in microstructural details and poor projection images. This was the case for the very wet foams (G/L < 1.0), for foams generated from MF5 at N = 500 rpm and 750 rpm and for samples generated under-pressurised conditions (see Chapter 4 and 5). Fig. 3.10a depicts one scenario where a scanning

duration longer than 10 minutes (rotation step of 0.4°) gave very poor and blurred images that were difficult to analyse automatically using CTan and, in some cases, even manually using ImageJ. Performing the scans, however, at a rotation step of 1.0° took less than 5 minutes and an example of an image from this is displayed in Fig. 3.10b. The image obtained was of a poor quality and hence only Matlab was able to distinguish the individual bubbles. In extreme cases, even Matlab was not able to automatically detect the distorted larger air bubbles (Fig. 3.10) and hence it was necessary to resort to the freely available software – ImageJ. This therefore required the manual tracing of individual bubbles which can be tedious and time consuming. In addition, as will be discussed in Chapter 4 and Chapter 5, the static stability of these wet foams is a strong function of air volume fraction, rotor speed (*N*), xanthan gum (XG) and PGE 55 concentration. As will be outlined and discussed, all these factors led to foams with varying static stability.

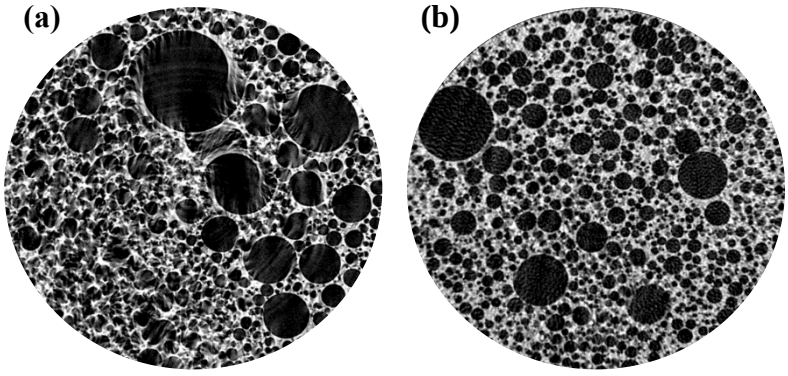

Fig. 3.10: Typical 2D X-ray images of unstable wet foam sample generated from fluid MF2 at G/L = 1.0 & *N* = 1000 rpm when scanned for: (a) 20 minutes; and (b) 5 minutes.

As briefly outlined above, the foam static stability was a function of several variables including the composition of the liquid and processing parameters. The time constant for the destabilisation of the wet foams generated under pressurised conditions (see Fig. 310 and Chapter 5) was very low in the range of 4-7 minutes. These foams also had larger air bubbles

and a non-uniform BSD causing an increase in the rate liquid drainage. In contrast, foams generated under atmospheric conditions were highly stable and little drainage or foam coarsening was observed even when the same sample was scanned twice.

In contrast, wet foams generated from fluid MF2 were more stable and hence typical foam images obtained for fluid MF2 at G/L = 1.5 and N = 500-1750 rpm are displayed in Fig. 3.11. For these highly stable foams a rotation step of 0.4° over a 180°, which took approximately 20 minutes of scanning time, was sufficient to obtain good contrasted 2D X-ray images. To verify the robustness of CTan software, images of the same sample were also independently processed using Matlab script code shown in Appendix 8.1. For each sample, five 2D slices were chosen from a total of 1200 2D slices with each slice 200 slices apart corresponding to 4 mm in vertical distance.

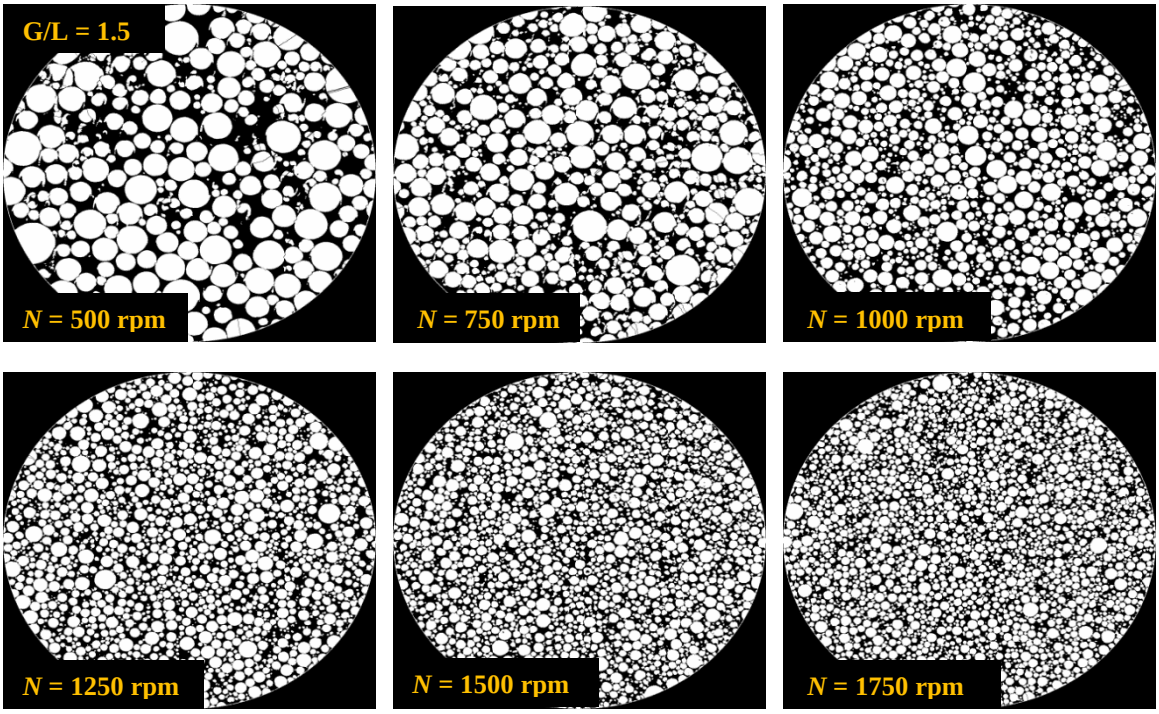

Fig. 3.11: Typical X-ray images of wet foams obtained for fluid MF2 at G/L = 1.5.

The images in Fig. 3.11 above were then independently processed using CTan and Matlab software. Table 3.3 shows the comparison of cell parameters obtained for wet foam samples generated from fluid MF2 at G/L = 1.5 (ϕ_e = 0.62) and at N = 500 rpm, 1000 rpm and 1750 rpm, respectively. Both software predicted similar D_{32} values; but the number of cells identified was slightly greater for CTan. The latter was counterintuitive since during image processing using CTan, the bubbles at the ROI boundary were removed as well as any noise introduced during thresholding and hence CTan was expected to under-predict the number of cells. The slight over-prediction by the CTan, however, can be explained by the fact that a small fraction of bubbles is split into many smaller bubbles during watershed operation.

In addition, there is the likelihood that some noise introduced during thresholding are not eliminated by the despeckle function. Even then, the effects on D_{32} was negligible – as expected. With respect to the relative cell area, Matlab slightly over-predicts the area for wet foams generated at N = 500 rpm and 1000 rpm and this variation can be attributed to the fact that images processed by CTan were binarised and broken bubbles at the edge were removed. In addition, Matlab under-predicts the relative cell area at a higher N and G/L ratio since it failed to distinguish certain bubbles in a given image due to poor image contrast leading to significant underestimation. It is also worthy of mentioning that the relative bubble area predicted by CTan is very close to the actual experimental values.

Table 3.3: Comparison of 2D cell parameters extracted using CTan and Matlab software's for wet foams generated from fluid MF2 at G/L = 1.5 (ϕ_e = 0.62).

Slice number	N = 500 rpm							
	Matlab				CTan			
	Cell count (-)	D_{32} (μm)	Total cell area (mm^2)	Relative area (-)	Cell count (-)	D_{32} (μm)	Total cell area (mm^2)	Relative area (-)
1	250	244	10.15	0.64	260	235	9.59	0.61
2	225	269	10.23	0.65	222	258	9.44	0.60
3	225	264	10.25	0.65	235	250	9.39	0.60
4	281	246	10.41	0.66	258	232	9.51	0.60
5	239	269	10.42	0.66	234	255	9.59	0.61
Slice number	N = 1000 rpm							
	Matlab				CTan			
	Cell count (-)	D_{32} (μm)	Total cell area (mm^2)	Relative area (-)	Cell count (-)	D_{32} (μm)	Total cell area (mm^2)	Relative area (-)
1	1132	135	9.80	0.63	1251	133	9.54	0.61
2	1139	136	9.88	0.63	1307	134	9.62	0.62
3	1145	134	9.75	0.63	1297	132	9.55	0.61
4	1131	135	9.83	0.63	1273	133	9.60	0.62
5	1138	134	9.70	0.62	1286	135	9.62	0.62
Slice number	N = 1750 rpm							
	Matlab				CTan			
	Cell count (-)	D_{32} (μm)	Total cell area (mm^2)	Relative area (-)	Cell count (-)	D_{32} (μm)	Total cell area (mm^2)	Relative area (-)
1	2833	79	9.85	0.61	3344	72	9.86	0.62
2	2746	79	9.70	0.60	3370	70	9.90	0.63
3	2828	76	9.77	0.60	3400	70	9.77	0.62
4	2773	78	9.53	0.59	3490	69	9.67	0.61
5	2762	75	9.35	0.57	3546	68	9.59	0.61

Similarly, typical 2D X-ray images of wet foam generated from fluid MF2 at N = 1000 rpm and G/L = 0.5 (ϕ_e = 0.33), 1.0 (ϕ_e = 0.52), 1.5 (ϕ_e = 0.62) and 2.0 (ϕ_e = 0.67), respectively are shown in Fig. 3.12. These images were also independently processed using CTan and Matlab software and the 2D cell parameters obtained are summarised in

Table 3.4. For the very wet foam (G/L = 0.5), the bubbles were distorted at the edges and hence only Matlab was able to obtain the D_{32}. In addition, as outlined above, CTan slightly over-predicted the number of bubbles; but in both cases the value of D_{32} was the same and hence predicted similar relative cell area.

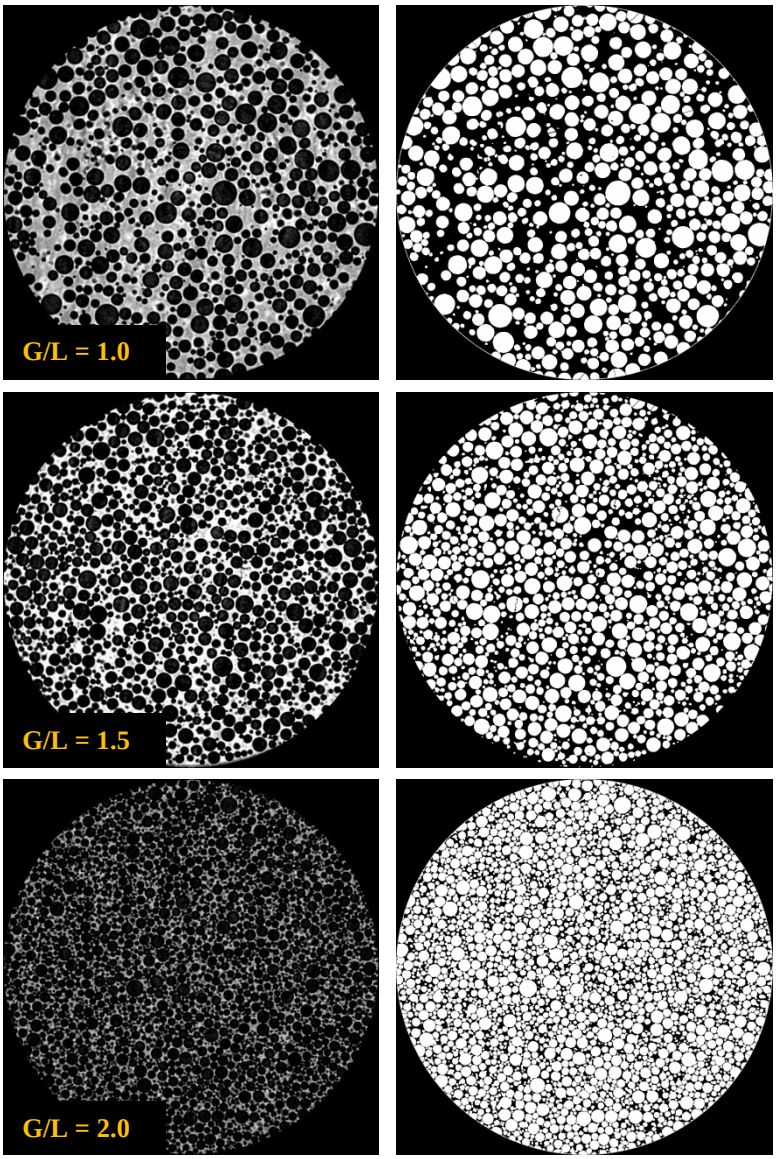

Fig. 3.12: Typical X-ray 2D images of wet foam obtained from fluid MF2 at N =1000 rpm and G/L = 1.0 (ϕ_e = 0.52), 1.5 (ϕ_e = 0.62) and 2.0 (ϕ_e = 0.67).

Table 3.4: Comparison of 2D cell parameters extracted using Matlab and CTan software's for wet foams generated from fluid MF2 at N = 1000 rpm.

Slice number	G/L = 0.5 (ϕ_e = 0.33)							
	Matlab				CTan			
	Cell count (-)	D_{32} (μm)	Total cell area (mm^2)	Relative area (-)	Cell count (-)	D_{32} (μm)	Total cell area (mm^2)	Relative area (-)
1	424	162	7.19	0.32	-	-	-	-
2	442	168	7.48	0.33	-	-	-	-
3	420	176	7.67	0.34	-	-	-	-
4	423	169	7.62	0.34	-	-	-	-
5	424	182	7.23	0.32	-	-	-	-
Slice number	G/L = 1.0 (ϕ_e = 0.52)							
	Matlab				CTan			
	Cell count (-)	D_{32} (μm)	Total cell area (mm^2)	Relative area (-)	Cell count (-)	D_{32} (μm)	Total cell area (mm^2)	Relative area (-)
1	718	162	8.72	0.53	736	161	8.27	0.50
2	729	164	8.65	0.52	745	167	8.41	0.51
3	711	164	8.64	0.52	725	164	8.35	0.51
4	719	166	8.85	0.53	731	163	8.46	0.51
5	731	163	8.72	0.53	742	165	8.52	0.52
Slice number	G/L = 1.5 (ϕ_e = 0.62)							
	Matlab				CTan			
	Cell count (-)	D_{32} (μm)	Total cell area (mm^2)	Relative area (-)	Cell count (-)	D_{32} (μm)	Total cell area (mm^2)	Relative area (-)
1	1132	135	9.80	0.63	1201	133	9.54	0.61
2	1139	136	9.88	0.63	1207	134	9.62	0.62
3	1145	134	9.75	0.63	1197	132	9.55	0.61
4	1131	135	9.83	0.63	1173	133	9.60	0.62
5	1138	134	9.70	0.62	1186	135	9.62	0.62
Slice number	G/L = 2.0 (ϕ_e = 0.67)							
	Matlab				CTan			
	Cell count (-)	D_{32} (μm)	Total cell area (mm^2)	Relative area (-)	Cell count (-)	D_{32} (μm)	Total cell area (mm^2)	Relative area (-)
1	1592	107	10.34	0.62	1687	105	10.10	0.66
2	1764	104	10.08	0.63	1830	100	9.90	0.65
3	1695	105	10.41	0.62	1800	105	10.12	0.67
4	1679	102	10.33	0.63	1797	104	10.04	0.66
5	1677	101	10.15	0.64	1805	102	9.91	0.65

The effects of number of slices on D_{32} and BSD was also investigated and the results for fluid MF2 at N = 500 rpm, 1000 rpm and 1750 rpm and G/L = 1.0 and 1.5 are shown in Fig. 3.13 and Fig. 3.14. At N = 500 rpm, there was some variation in D_{32} with the number of slices analysed, i.e. D_{32} was increased with an increase in number of slices analysed. However, for $N \geq 1000$ rpm, there was negligible variation in D_{32}. In the former scenario, as stated previously, the foam sample is non-homogenous and has larger air bubbles. Whereas at a higher N, the foam sample is fine textured with smaller bubbles and a uniform BSD. The corresponding BSD at G/L = 1.0 and N = 500 rpm, 1000 rpm and 1750 rpm are depicted in Fig. 3.13. In order to ensure that a representative D_{32} was obtained for all foam samples generated under different processing conditions, it was decided to use the maximum number of slices. This corresponded, for G/L = 1.0, to a total of ~ 5000 bubbles at N = 500 rpm and ~ 15000 bubbles at N = 1750 rpm. In addition, the mean and the standard deviation was also plotted against the number of bubbles analysed for foam generated from fluid MF2 at G/L = 1.0 and N = 500, 1000 and 1750 rpm as shown in Fig. 8.1 in Appendix. There was little to negligible variation in both parameters at bubble number greater than 500. As stated previously, 500 number of bubbles are sufficient to obtain statistically significant Sauter mean bubble diameter and BSD.

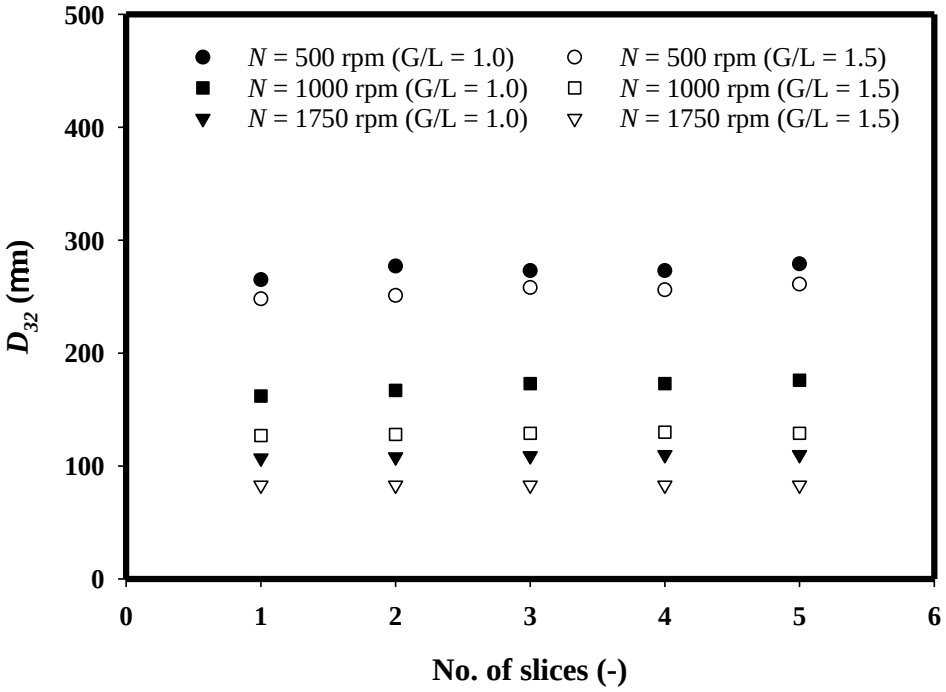

Fig. 3.13: Effects of number of slices on D_{32} for wet foams generated from fluid MF2 at G/L = 1.0 (ϕ_e = 0.52) and 1.5 (ϕ_e = 0.62).

To summarise, for most wet foam samples investigated, the optimum scanning parameters were set to a 3.78 μm pixel^{-1} which took approx. 20 minutes of scanning duration. This yielded excellent 2D contrasted X-ray images from which accurate, reliable and representative BSD's were extracted - without significant effects from gravity drainage. In addition, a well-established and systematic image processing procedure was developed and utilised to reduce any source of error arising. Apart from a representative BSD and Sauter mean bubble diameter, the method is also suitable for obtaining air volume fraction.

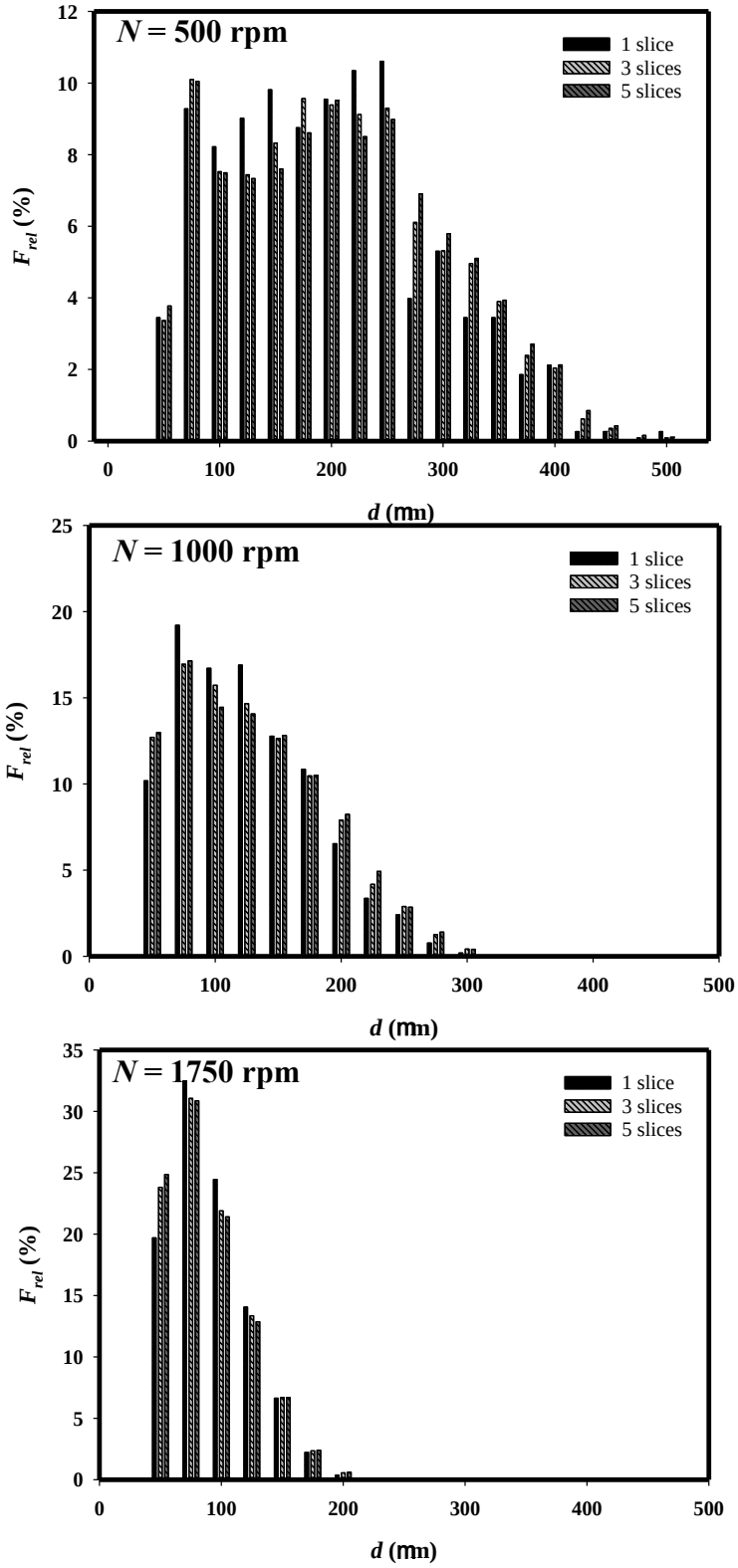

Fig. 3.14: Effects of number of slices on bubble size distributions (BSD) for wet foams generated from fluid MF2 at G/L = 1.0 (ϕ_e = 0.52).

3.3.2.2 3D structural analysis

Although, 2D structural analysis using CTan is useful to extract a reasonable representative BSD and hence D_{32} which is an important parameter for food processing and related industries. The bubble size in 2D, however, may not be representative of the actual 3D objects (Dalen and Koster, 2012). This is because objects observed in 2D space are only an intersection of a plane in the three-dimensional space. Therefore, the true diameters might be significantly under-estimated since the plane might only intersect the objects at one of the poles as shown in Fig. 3.15. Similarly, a given random plane is more likely to intersect larger objects and hence leading to an over-estimation in true diameters. As pointed out by Dalen and Koster (2012), the two might work in opposite directions and hence are likely to cancel each other out. In addition, 2D analysis does not yield the overall complex 3D microstructure and hence mechanical properties.

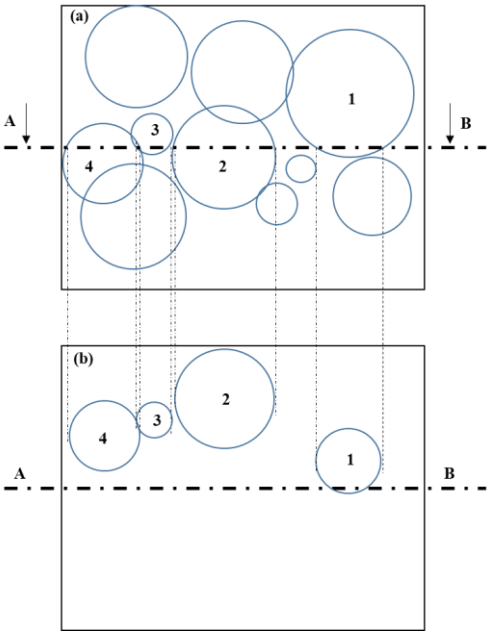

Fig. 3.15: Typical features of spherical objects in 2D and 3D space (adapted from Lim and Barigou (2005)).

3.3.2.2.1 Stereological analysis

Stereology is the science of studying materials in three-dimensional (3D) space using two-dimensional (2D) images obtained from various practical techniques such as X-ray micro-CT techniques. A stack of 2D slices or sections can be processed in order to extract detailed 3D microstructural information such as number, length and volume of the objects. The method is commonly utilised to study biological specimen, metals, ceramics and related objects (Lim and Barigou, 2004). A considerable discrepancy can arise when objects are only analysed in 2D space and a good example is given in Fig. 3.15 which shows a sample of polydispersed foam with a non-uniform bubble size distribution. If a 2D slice of this sample is extracted and analysed one can observe, as shown in Fig. 3.15a, various sizes of circular sections. These 2D sections will correspond to the diameter of these individual objects which might be their true diameter (only possible if the line passes through the centre of the sphere) or it might correspond to their diameter away from the centre. Therefore, to reveal the actual diameter of these spheres, stereological techniques can be applied to construct a 3D model to obtain a detailed microstructural information (Lim and Barigou, 2004).

A common stereological technique for the study of spherical objects is based on a probability function, i.e. what is the likelihood, when random planes are passed through a spherical object (diameter, D), will intersect to give sections of diameter, d. These probability functions are commonly employed to study spherical objects and hence it assumes: (i) all objects are of a spherical nature; and (2) a discontinuous distribution can be used to represent their size distribution. One such method developed is known as Saltykov's analysis (Lim and Barigou, 2004). The method is widely adopted to study spherical objects and it is as follows:

$$(N_v)_j = \frac{1}{D_j}\left[1.6461(N_A)_j - 0.4561(N_A)_{j-1} - 0.1162(N_A)_{j-2} - 0.04151(N_A)_{j-3} - 0.0173(N_A)_{j-4} - 0.0079(N_A)_{j-5} - 0.0038(N_A)_{j-6} - 0.0018(N_A)_{j-7} - 0.0010(N_A)_{j-8} - 0.0003(N_A)_{j-9} - 0.0002(N_A)_{j-10} - 0.002(N_A)_{j-11}\right] \quad \text{(Eq. 3.2)}$$

where, $(N_v)_j$ is the number of bubbles per unit volume of sample in class interval *j*; $(N_A)_j$is the number of circular sections per unit area of the sample cross-section; D_j is the actual diameter of bubble in the class interval j; (see Lim and Barigou 2004 for more details).

To stipulate the circular section of an object, Saltykov's analysis utilises the ratio of an object area to the maximum area (A/A_{max}) of a cell within the population. To obtain the class intervals a logarithmic scale of diameters of factor equal to 0.794 ($10^{-0.1}$) is used. As a result, for the sectional areas, this factor corresponds to 0.631 [$(10^{-0.1})^2$] as tabulated in Table 3.5.

In Saltykove's analysis, the first step involves the determination of cell/bubble size distribution from a stack of 2D images and then identifying the bubble with the maximum diameter (d_{max}) and hence cross-sectional area (A_{max}) across the whole population. This maximum area is then taken as a reference to divide the bubble size distribution into a maximum of 12 class intervals and then to locate the number of bubbles in each class interval. For example, foam sample obtained from fluid MF2 generated at G/L = 1.0 and N = 500 rpm was scanned and reconstructed into 1200 2D slices. From this set of data 20 slices (spacing of 0.095 mm) was then analysed using MATLAB. Across all the slices, the bubble with a maximum area A_{max} equal to 0.255 mm^2 and hence a d_{max} equal to 0.57 mm was identified. These values along with a scaling factor of 0.631 (outlined above) was then set as a reference to identify the class intervals for all the remaining bubble sizes within the population as tabulated in Table 3.5.

Table 3.5: Size distribution of circular bubble sections measured from a total of 21 reconstructed 2D slice images of wet foam generated from fluid MF2 at G/L = 1.0 and N = 500 rpm.

j (-)	A/A_{max} (-)	d_j (μm)	N_j (bubbles)	$(N_A)_j$ (bubbles/cm^2)
1	1.000 – 0.631	569.83 – 452.63	66	20
2	0.631 – 0.398	452.63 – 359.54	327	99
3	0.398 – 0.251	359.54 – 285.59	625	190
4	0.251 – 0.158	285.59 – 226.85	553	168
5	0.158 – 0.100	226.85 – 180.20	402	122
6	0.100 – 0.063	180.20 – 143.13	304	92
7	0.063 – 0.040	143.13 – 113.70	266	81
8	0.040 – 0.025	113.70 – 90.31	231	70
9	0.025 – 0.016	90.31 – 71.73	218	66
10	0.016 – 0.010	71.73 – 56.93	124	38
11	0.010 – 0.006	56.93 – 45.26	70	21
12	0.006 – 0.004	45.26 – 35.95	40	12
		Total	3226	

After following the above procedure, subsequently Eq. 3.2 can then be used to convert the 2D bubble sizes into 3D bubble size distribution as follows:

$$(N_v)_1 = \frac{1}{D_1}\,[1.6461(N_A)_1] = \frac{1}{0.057}[1.6461(20)] = 577 \qquad \text{(Eq. 3.3)}$$

To obtain the 3D distribution for the remaining smaller class intervals, a similar procedure is utilised but the area contribution from the previous sections needs to be subtracted as follows:

$$(N_v)_2 = \frac{1}{D_2}\,[1.6461(N_A)_2 - 0.4561(N_A)_1]$$

$$= \frac{1}{0.045}[1.6461(99) - 0.4561(20)] = 3418 \qquad \text{(Eq. 3.4)}$$

The above procedure is then extended to determine the class intervals of the remaining bubble size until all of them are taken into consideration and the 3D bubble size distribution determined as tabulated in Table 3.6.

Table 3.6: 3D cell size distribution in wet foam generated from fluid MF2 at G/L = 1.0 and *N* = 500 rpm obtained using Saltykov's area analysis.

j (-)	D_j (mm)	D_j (cm)	$1/D_j$ (cm)	$(N_v)_j$ (bubbles/cm^3)	f_j (-)
1	0.570	0.057	18	577	0.012
2	0.453	0.045	22	3418	0.076
3	0.360	0.036	28	7371	0.164
4	0.286	0.029	35	6220	0.138
5	0.227	0.023	44	4316	0.096
6	0.180	0.018	55	3722	0.083
7	0.143	0.014	70	4584	0.102
8	0.114	0.011	88	5107	0.113
9	0.090	0.009	111	6582	0.146
10	0.072	0.007	139	2321	0.052
11	0.057	0.006	175	719	0.016
12	0.045	0.005	221	112	0.002
			Total	45037	

The air volume fraction predicted by the Saltykove's analysis is 0.53 which is close to the experimental value of 0.52 but slightly lower than predicted by the CTan software 0.57. The approximately 8% discrepancy is possibly due to the noise introduced during image thresholding using CTan. In addition, a comparison of D_{32} values obtained shows a similar

trend, but with CTan predicting a smaller value of 296 μm in comparison to 360 μm from 2D analysis and 346 μm using Saltykove's analysis. The under-prediction by the CTan was not surprising since during image processing some of the larger air bubbles were split into many smaller bubbles as described in section 3.3.2.1. In addition, the degree of discrepancy is expected to be much lower for samples generated at higher rotor speed and G/L ratio.

3.3.2.2.2 3D analysis using CTan

As mentioned in the materials and methods section, three-dimensional structural analysis (3D) in CTan can be achieved in two main ways: (i) individual 3D analysis; and (ii) bulk volumetric 3D analysis. In both cases, to determine the 3D structural parameters using CTan, the selection of a suitable volume of interest (ROI) in 3D space is required. In addition, the image processing procedure found for 2D analysis was implemented except some of the morphological functions were applied in 3D space. Depending on the nature of the foam sample, the number of 2D slices necessary and analysed ranged from approximately 600 to 1200 with each slice being 0.002 mm apart. As stated previously, an increase in the number of 2D slices, of course, led to an increase in image processing time.

Therefore, individual 3D analysis in CTan was performed on 600 and 1200 2D slices for wet foams generated from fluid MF2 at N = 1000 rpm and G/L = 1.0 and 1.5. The BSD results are depicted in Fig. 3.16. As shown, there was negligible variation in D_{32} meaning 600 2D slices were sufficient to obtain a representative BSD and hence D_{32}. It should also be stated that the image processing time reduces significantly with a reduction in the number of 2D slices analysed, i.e. it takes approximately 30 minutes to process 600 2D slices in comparison of up to 60 minutes for 1200 2D slices. Therefore, for all conditions investigated, 600 2D slices were

analysed which yielded reliable and representative BSD. This was also true for foam samples generated at other experimental conditions, but except for some samples generated at N = 500 rpm; for the very wet foams (G/L < 1.0); and for samples produced under-pressurised conditions for which 3D analysis was not possible.

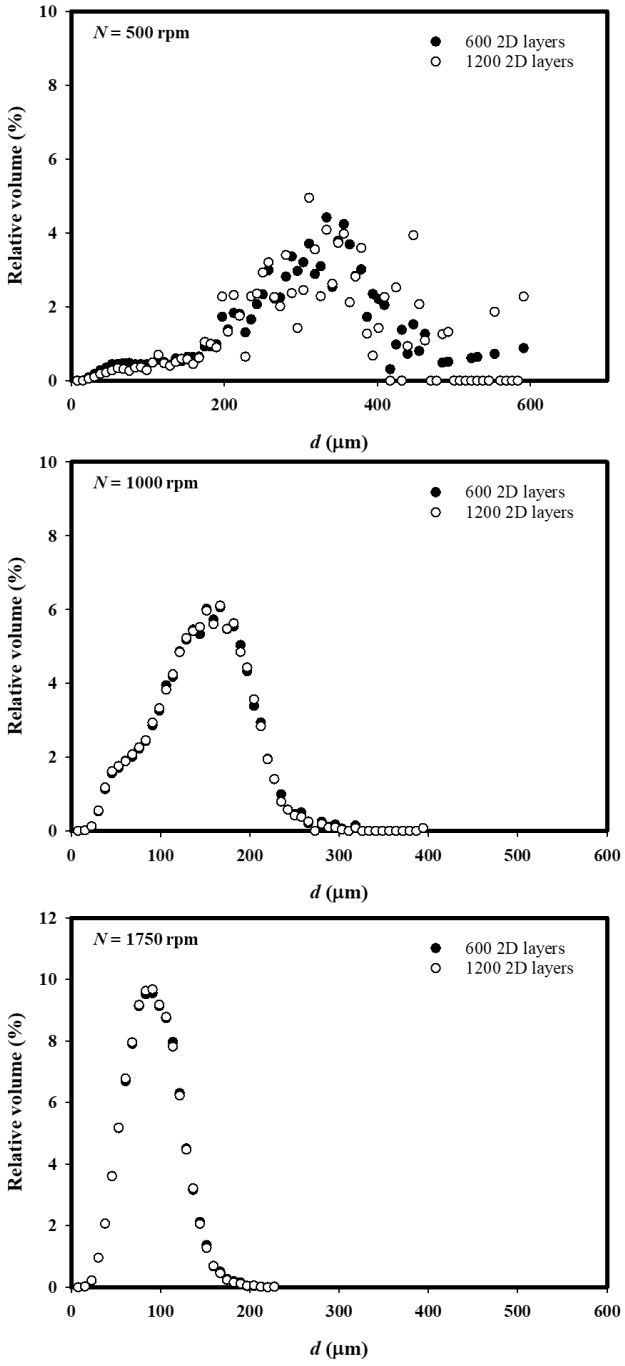

Fig. 3.16: Comparison of volume-weighted bubble size distributions of wet foams generated from fluid MF2 at G/L = 1.5 (ϕ_e = 0.62).

Individual 3D analysis is essential for determining the BSD and hence the D_{32}, but it does not yield a rendered 3D model of the foam sample and for obtaining additional parameters such as the degree of anisotropy (*DA*). Typical 3D images obtained by reconstructing a stack of 1200 2D slices for foam samples generated from fluid MF2 at G/L = 1.0 and 1.5 and N = 500 rpm, 1000 rpm and 1750 rpm are depicted in Fig. 3.17.

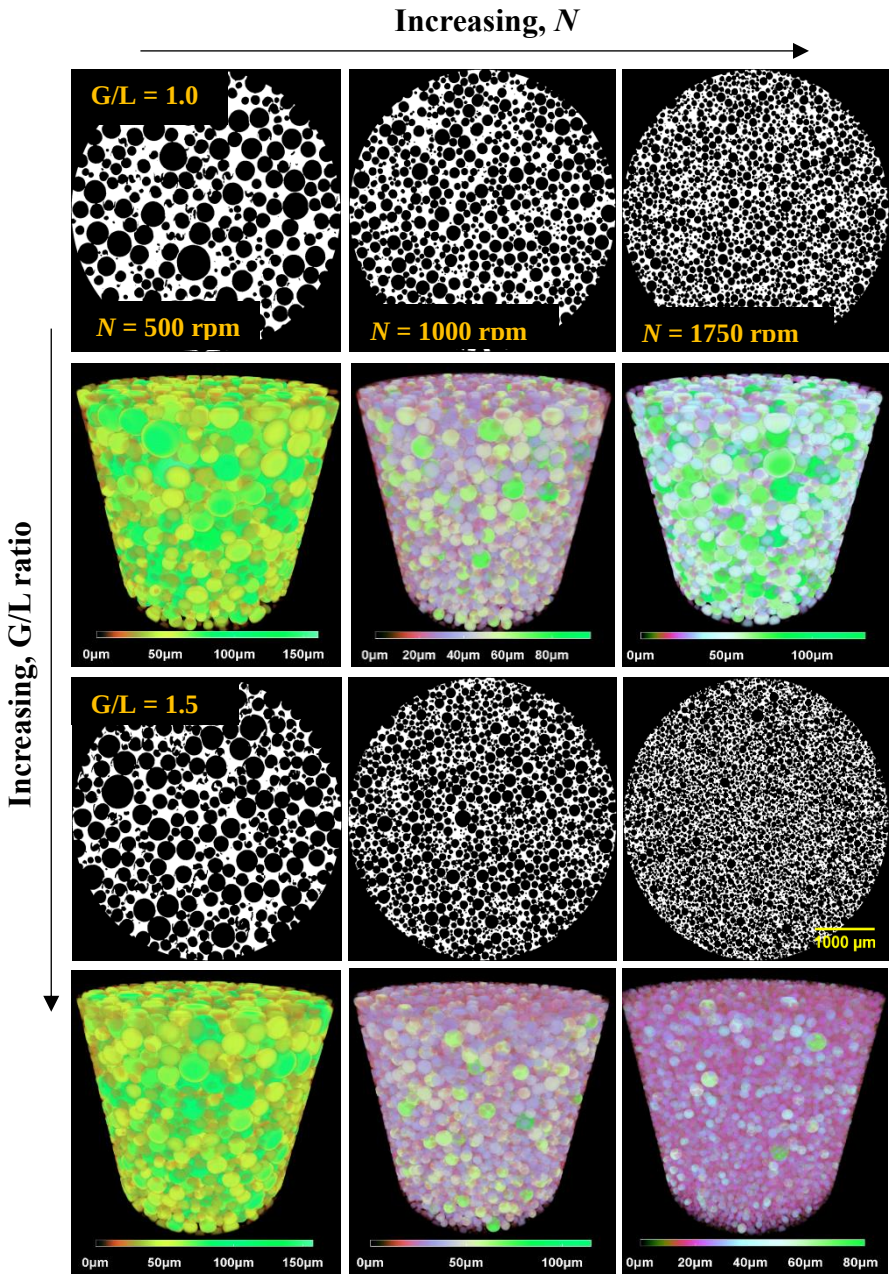

Fig. 3.17: Rendered 3D X-ray micro-CT model of foam generated from MF2 numerically cut to reveal its inner structure.

Apart from the average bubble size, one of the parameters that can be extracted during bulk volumetric 3D structural analysis is the degree of anisotropy (*DA*) which is related to microstructural symmetry (Lim and Barigou, 2005). A value of 1.0 corresponds to a total anisotropy whereas a value of 0 indicates a total isotropy. The values of *DA* obtained for wet foam samples generated from fluid MF2 at G/L = 1.0, 1.5 and 2.0 and N = 500 – 1750 rpm are tabulated in Table 3.7 and Table 3.8 respectively. These samples possessed a good degree of isotropy meaning there was little variation in the bubble size across the sample. The percentage of porosity is also determined and the results shown in Table 3.7 and Table 3.8. Similarly, a good correspondence was obtained between both techniques, however, there was some discrepancy between the experimentally derived and values obtained from the CTan software especially for samples generated at lower N. These can be attributed to several factors including errors arising during image processing including thresholding and the fact that a much smaller sample size, 2-5 ml, is analysed in CTan in contrast to a 250 ml measured experimentally. Nevertheless, both methods seem to give a reasonably accurate value of porosity especially for foams generated at a higher G/L ratio and N.

Table 3.7: Geometric parameters (extracted from CTan software using bulk volumetric 3D analysis) of foam samples generated from fluid MF2 at G/L = 1.5 (ϕ_e = 0.62) for 1200 2D layers.

N (rpm)	*OSVR* (-)	Average diameter (μm)	*DA* (-)	Porosity (%)
500	0.035	237	0.42	66.6
750	0.047	169	0.36	65.6
1000	0.052	129	0.17	63.6
1250	0.061	105	0.15	62.7
1500	0.074	91	0.17	61.7
1750	0.085	73	0.13	61.2

Table 3.8: Geometric parameters (extracted from CTan software using bulk volumetric 3D analysis) of foam samples generated from MF2 at N = 1000 rpm for 1200 2D layers.

Air volume fraction (-)	*OSVR* (-)	Average diameter (μm)	*DA* (-)	Porosity (%)
1.0 (ϕ_e = 0.52)	0.041	151	0.26	57.0
1.5 (ϕ_e = 0.62)	0.052	129	0.17	63.6
2.0 (ϕ_e = 0.67)	0.078	93	0.11	66.6

Likewise, a detailed cell wall thickness distribution can also be extracted during bulk volumetric 3D structural analysis. Typical 3D cell wall thickness images obtained for fluid MF2 at G/L = 1.5 and N = 500 rpm, 1000 rpm and 1750 rpm are shown in Fig. 3.18. The corresponding cell wall thickness distributions are depicted in Fig. 3.19.

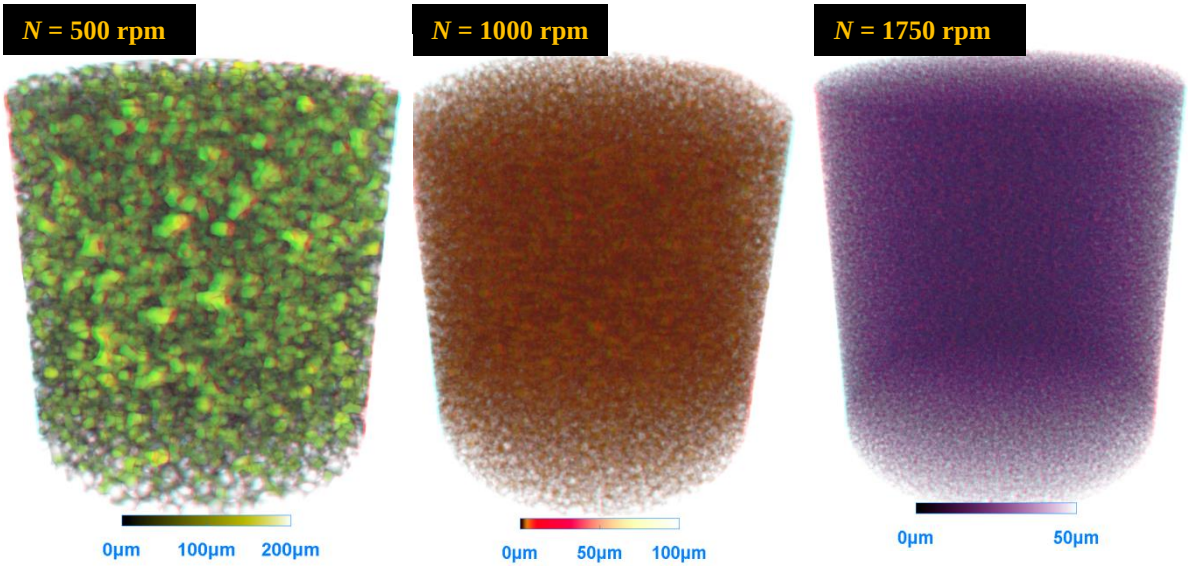

Fig. 3.18: Typical 3D images of cell wall thickness of wet foams generated from fluid MF2 at G/L = 1.5 (ϕ_e = 0.62).

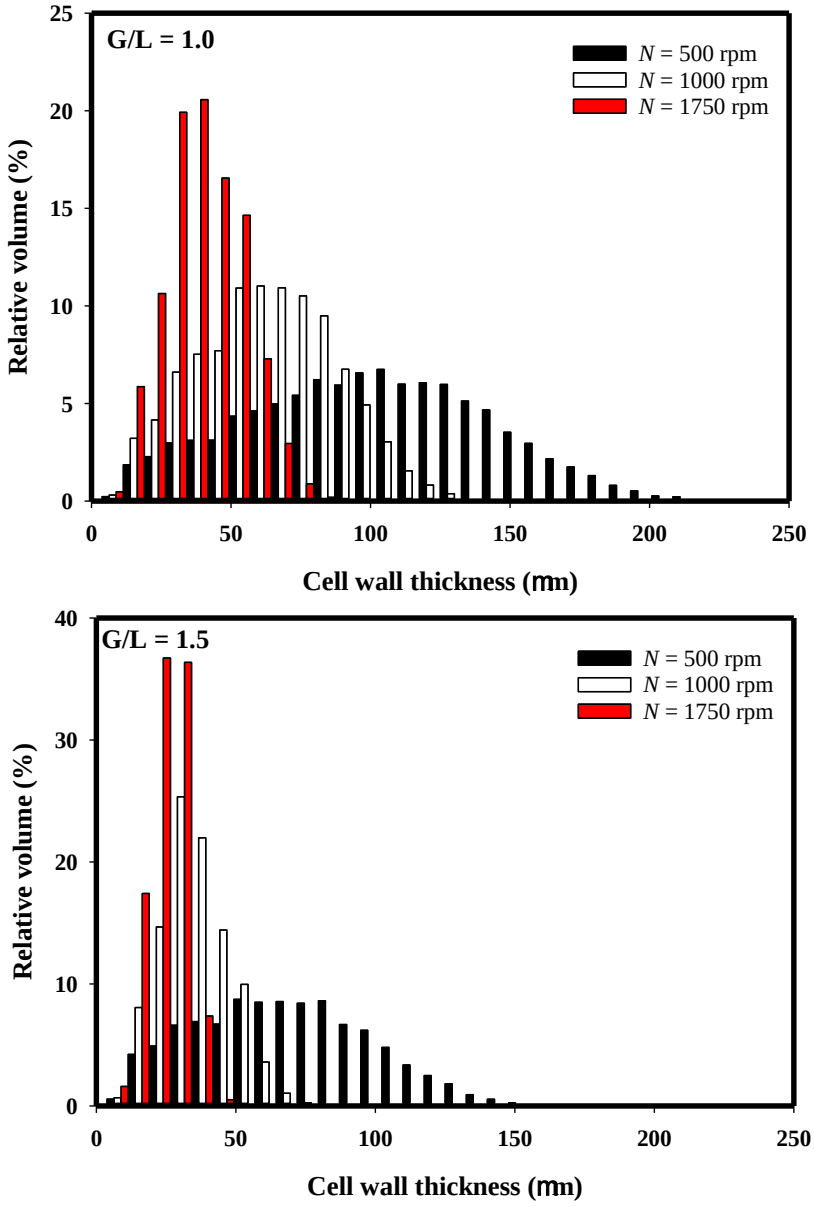

Fig. 3.19: Corresponding typical cell wall thickness distributions of wet foams generated from fluid MF2 at G/L = 1.0 (ϕ_e = 0.52) and 1.5 (ϕ_e = 0.62).

3.3.2.3 Comparison between 2D and 3D structural analysis

3.3.2.3.1 Comparison of individual 2D and 3D structural analysis using CTan

A comparison of BSD made using CTan individual 2D and 3D structural analysis was also performed. The results for wet foams generated from fluid MF2 at G/L = 1.5 and N = 500 rpm,

1000 rpm and 1750 rpm respectively are presented in Table 3.9 and Fig. 3.20. As shown, depending on the wet foam sample, from negligible to large variation in BSD's was observed. The degree in variation was a strong function of foam microstructure and hence it was the largest for wet foams generated at lower *N* and G/L ratio since these foams had larger air bubbles and a non-uniform BSD. The discrepancy between 2D and 3D, however, become much smaller for foam generated at *N* = 1000 rpm. This was not expected, but it can be explained as follows. As mentioned previously, the true diameters in 2D space can be either over- or under-predicted or the two might work in opposite direction and hence cancel each other out (Dalen and Koster 2012). This seems to be the case for the wet foams generated at G/L = 1.5 and *N* = 1000 rpm. In contrast, for foams generated at *N* = 500 rpm and 1750 rpm, the D_{32} seems to be under-estimated by 2D analysis. In addition, as shown in Fig. 3.20, there is significant noise associated with sample generated at *N* = 500 rpm which can be attributed to the image processing in 3D. The larger air bubbles are likely to be distorted at the edges which are then broken down into smaller bubbles during watershed operation (as described above). Therefore, any change in the number of larger air bubbles can have a significant effect on the relative percentage volume.

Table 3.9: Comparison of 2D and 3D structural parameters extracted using CTan for wet foams generated from fluid MF2 at G/L = 1.5 (ϕ_e = 0.62).

N (rpm)	D_{32} (μm)	
	2D	3D_individual
500	246	264
1000	133	128
1750	70	81

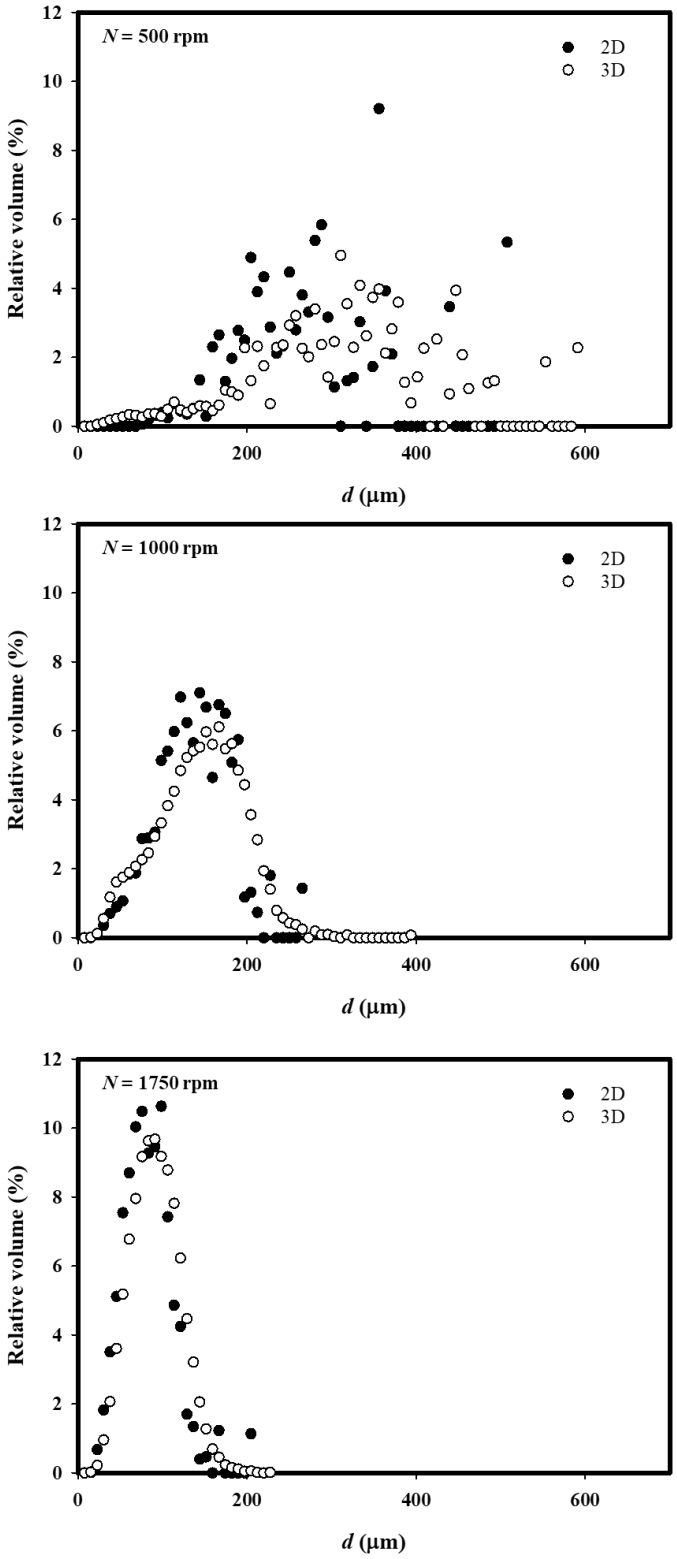

Fig. 3.20: Comparison of 2D and 3D volume-weighted bubble size distributions of wet foams generated from fluid MF2 at G/L = 1.5 (ϕ_e = 0.62).

3.3.2.3.2 Comparison between 2D light microscopy and 3D CTan

A set of 2D foam images produced from MF5 using light microscopy and X-ray micro-CT, described above, are shown in Fig. 3.21. The corresponding Sauter mean bubble diameter (D_{32}) data are plotted in Fig. 3.22 for G/L = 1.5. These images have been selected to illustrate the degree of discrepancy that can exist between the results yielded by the two techniques. Light microscopy is a 2D technique which suffers from a number of shortcomings including: (i) out-of-focus bubbles have to be manually detected and removed; any out-of-focus bubbles not filtered out may introduce errors; (ii) bubbles larger than the gap of the viewing cell are distorted, thus, giving rise to errors; and (iii) the size of bubble sample analysed (~500–1000) is limited by the slow and tedious semi-automatic image processing. In comparison, X-ray micro-CT is a non-invasive technique which yields the full 3D structure of the foam which can then be sliced and examined along any plane. The number of 3D bubbles analysed in X-ray micro-CT is much greater (~5000–15,000) and the analysis is fully automated.

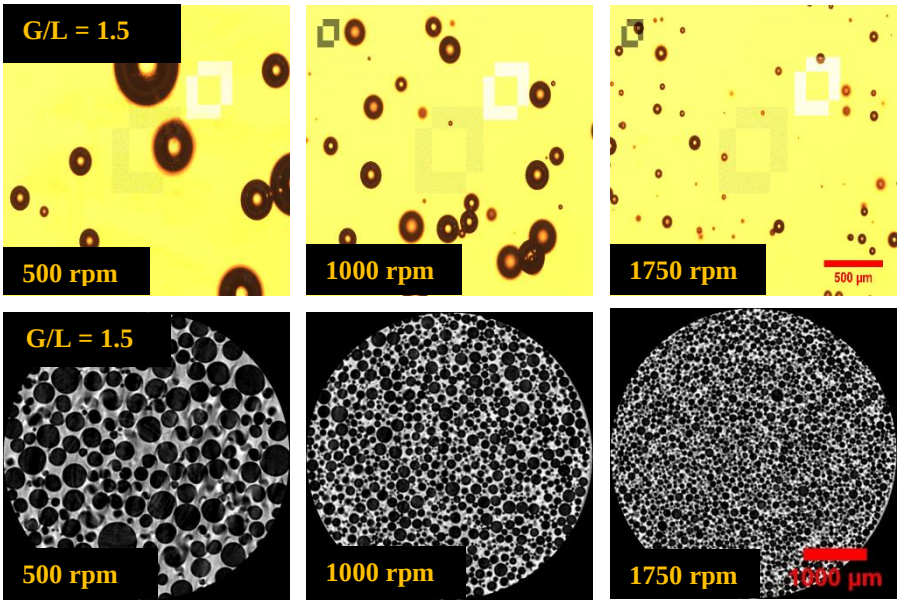

Fig. 3.21: Foam images obtained for MF5 using: a digital microscope (top); and X-ray micro-CT technique (2D slices) (bottom).

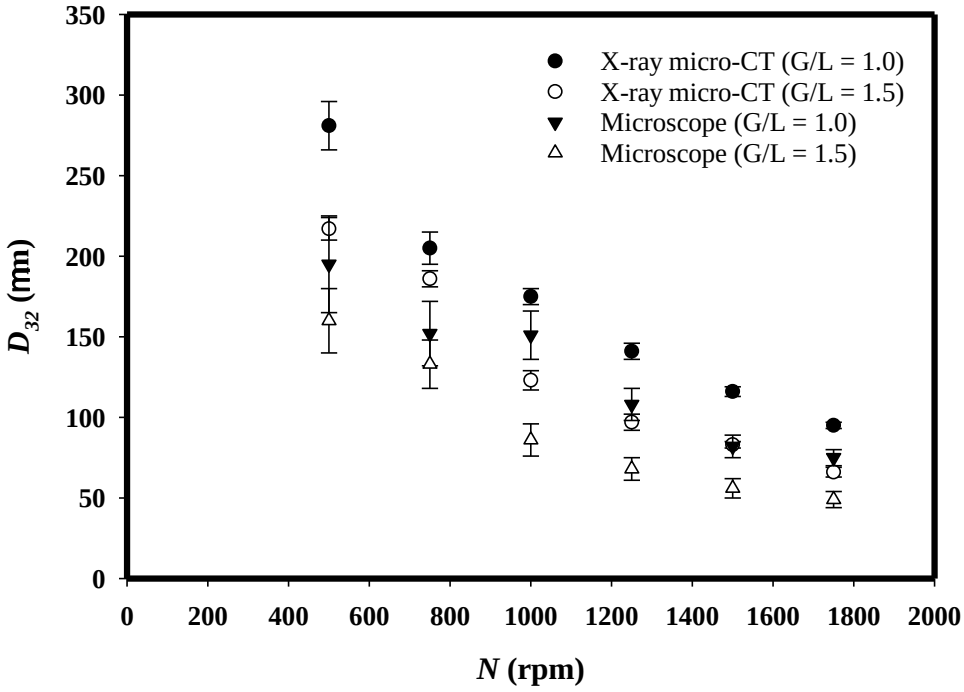

Fig. 3.22: Comparison of D_{32} obtained from light microscopy and X-ray micro-CT techniques for foam generated from fluid MF5.

Similarly, a comparison between 2D light microscopy and 3D X-ray micro-CT for wet foam samples generated from fluid MF2 was also performed and the results shown in Fig. 3.22. In this scenario, a reasonably good correspondence was found between the two techniques signifying that both techniques were reliable to obtain a representative D_{32}. The number of bubbles analysed, however, was much greater for X-ray micro-CT technique up to 14000 bubbles were analysed for a single sample in contrast to 500 bubbles for light microscopy. A comparison in terms of BSD is depicted in Fig. 3.23. The extent of error arising between the two techniques increases significantly for polydispersed foams, blurred and poor-quality images and for implementing poor image processing procedure. In addition, it should also be noted that the degree of discrepancy between the 2D and 3D analysis increases significantly for non-homogenous samples with a non-uniform bubble size distribution. As outlined above, this was also true when the BSD was obtained using the 2D light microscopy technique.

As shown in Fig. 3.23, the error between 2D light microscopy and 3D X-ray micro-CT can be significantly reduced provided the foam sample being analysed is stable with smaller bubble size and a uniform BSD. In addition, it is important to choose the correct chamber depth so that larger air bubbles are not distorted (leading to overestimation) or partially viewed (leading to underestimation) as previously identified by Chesterton et al., (2013) and Gillard et al., (2007). Furthermore, 2D light microscopy is also prone to errors arising during semi-automatic image processing.

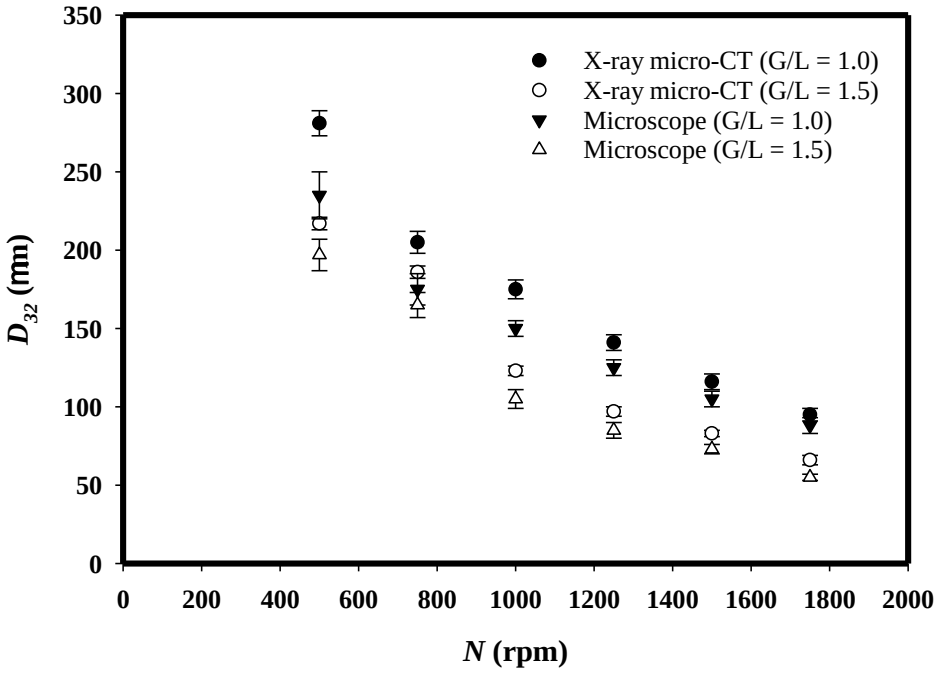

Fig. 3.23: Comparison of D_{32} obtained from light microscopy and X-ray micro-CT techniques for foam generated from fluid MF2.

3.4 Conclusion

The traditional 2D light microscopy imaging technique is a reasonably accurate and reliable method for determining the Sauter mean bubble diameter of wet foam samples, but it does not always yield a reliable bubble size distribution and does not give detailed microstructural details and properties. In addition, as discussed, the method also has several shortcomings: (i) it is intrusive and hence requires significant sample tempering; it's only a 2D technique; extremely laborious; and it can significantly under- or over-predict the bubble size distribution. In this study, a minimum of 500 bubbles were necessary to obtain a reasonable accurate Sauter mean diameter.

In contrast, X-ray micro-CT imaging technique is non-intrusive and hence extremely powerful for the determination of bubble size distribution in 3D and it gives a full and detailed 3D microstructural feature of the sample in study. The method also allows for the visualisation of aerated products in 3D space and along any plane which can be of a huge advantage especially when considerable non-homogeneity of the bubble size distribution exist. The image acquisition technique and image processing technique developed in this work are of a huge benefit to several processing industry especially food processing. In this study, for statically stable wet foams, a scanning duration of 20 minutes was sufficient to obtain good quality images from which a number of 2D and 3D structural parameters were extracted using CTAn software. The accuracy and reliability of CTAn software was confirmed by independently analysing foam images from the same sample using a Matlab software. A good correspondence was found between the two and hence either of them could be used to determine the 2D bubble size distribution. CTan, however, slightly over-predicted the number of cells in a given image

and this was attributed to the fact that some bubbles were split into many smaller bubbles as a result of image processing.

Three-dimensional analysis, and in certain cases automatic 2D analysis, using CTAn and Matlab software was not possible for the very wet foams; for foams generated at $N < 750$ rpm; and for foams generated under-pressurised conditions. These foams were more likely to drain during X-ray imaging and hence the 2D images contained bubbles that were distorted. The distorted bubbles were liable to be split into many smaller bubbles during watershed operation and hence leading to significant error. In extreme cases, a scanning duration of more than 8 minutes led to poor quality images from which it was difficult to distinguish individual bubbles and hence automatic image analysis was not possible. For these foams, a scanning duration of 5 minutes was adopted. In addition, for the highly statically stable and fine-textured foams with smaller and a uniform bubble size distribution, 2D and 3D analysis using CTAn yielded similar bubble size distribution and hence Sauter mean bubble diameter.

In summary, this study has shown that X-ray micro-CT is useful in obtaining detailed 3D microstructural details which is important for a wide range of industries including food processing. Such information, for example, can be used to relate the microstructure to flow and rheological properties.

Notation

F_{rel}	relative bubble number frequency (%)
D_{32}	Sauter mean bubble diameter (m)
d	bubble diameter (m)
N	rotor speed (rpm)

Abbreviations

BSD	bubble size distribution
DA	degree of anisotropy (-)
G/L	ratio of air and liquid volumetric flowrate
MF2	model fluid 2
MF5	model fluid 5
OSVR	object surface to volume ratio
PGE 55	polyglycerol ester of fatty acid
ROI	region of interest
XG	Xanthan gum
X-ray micro-CT	X-ray micro-Computed Tomography

Greek symbols

ϕ	air volume fraction (-)
ϕ_e	experimental air volume fraction (-)
ρ	density (kg m^{-3})

Chapter 4: Foams generated from viscous non-Newtonian shear-thinning liquids in a continuous multi rotor-stator device

Whilst aeration is ubiquitous in the food industry, little work has been done on foams generated from viscous non-Newtonian liquids. This study examines the production of foams from viscous shear-thinning liquids containing a non-ionic food grade surfactant (PGE 55), xanthan gum and caster sugar, using a continuous pilot-scale device having twelve rotor-stator pairs. The effects of process parameters (rotor speed, gas-liquid volumetric flowrate ratio (G/L)) and liquid composition (surfactant concentration, xanthan gum concentration) on foam gas volume fraction and bubble size distribution are elucidated. X-ray micro-Computed Tomography is employed to characterise the 3D microstructure of the foams. Rotor speed and G/L ratio are the dominant factors in determining the gas volume fraction and bubble size distribution. The foams produced exhibit smaller bubble size and a uniform bubble size distribution with high static stability. For a given energy input in turbulent flow, a higher G/L ratio results in a higher gas fraction and a smaller bubble size.

Keywords: Continuous foaming; non-Newtonian liquid; X-ray micro-CT; Rheology; Bubble size distribution. **Chapter published:** Jabarkhyl, S., Zhu, S., Rayment, P., Lloyd, D.M., Rossetti, D., Barigou, M., (2019). Foams generated from viscous non-Newtonian shear-thinning liquids in a continuous multi rotor-stator device. Innovative Food Science and Emerging Technologies, Vol. 59.

4.1 Introduction

Over the last 30 years, aerated food products have become increasingly popular since the inclusion of air bubbles gives rise to a variety of microstructures which exhibit better textural and sensorial properties (Indrawati and Narsimhan, 2008, Campbell and Mougeot, 1999, Guo *et al.*, 2017). Depending on the gas volume fraction (ϕ), aerated food products can be classified as wet foam ($\sim 0.50 > \phi < 0.95$) or dry foam ($\sim \phi > 0.95$). A foam consists of a continuous liquid phase in the form of a network of thin lamellae and a dispersed gas phase in the form of bubbles ranging from microns to millimetres in size (Bikerman, 1973, Walstra, 1989). Foams are thermodynamically unstable structured fluids (Germain and Aguilera, 2014, Curschellas *et al.*, 2012a, Curschellas *et al.*, 2012b-a). They are subject to three distinct destabilisation mechanisms: liquid drainage, bubble coalescence and disproportionation (Kroezen and Wassink, 1987, Cox,Aldred and Russell, 2009).

In the production of aerated products such as whipped cream, ice cream or mousse, it is important to achieve a good degree of control of the air volume fraction and bubble size distribution since the stability and the organoleptic properties of the product (creaminess, texture, mouthfeel) are strongly dependent on these critical parameters. For example, small bubbles and uniform bubble size distribution impart excellent foam stability and creaminess (Müller-Fischer,Suppiger and Windhab, 2007b, Müller-Fischer and Windhab, 2005).

Food foams are generated using a number of different techniques including mechanical whipping, membrane foaming, gas sparging (Pugh, 2016b). At pilot and industrial scales, mechanical whipping devices are preferred as they are more amenable to continuous large-scale production and better process control. In this respect, continuous rotor-stator devices are

popular especially when processing viscous and non-Newtonian liquids (Hanselmann and Windhab, 1998, Kroezen and Wassink, 1987, Kroezen,Groot Wassink and Bertlein, 1988b, Müller-Fischer,Suppiger and Windhab, 2007b, Narchi *et al.*, 2011, Nicorescu *et al.*, 2010, Mary *et al.*, 2013, Mezdour *et al.*, 2017).

In-line or continuous rotor-stator devices are widely employed in a number of energy intensive industries such as food processing, chemicals and personal and healthcare. The specific geometry of the device can vary drastically from one design to another but the narrow gap between the rotor-stator unit is a common feature among all of them. In addition, these devices are also capable of operating at higher rotor speeds which enables high level of local stresses and energy dissipation important for achieving a fine and well-dispersed system. For process design, optimisation and scale-up, it is critical to control the bubble size distribution and to minimise energy consumption as much as possible (Wu *et al.*, 2014). Therefore, knowledge pertaining to power characteristics is crucial for the aforementioned variables. Due to the wide variety of designs, to date a well-established correlation for assessing the power characteristics of these devices does not exist (Özcan-Taşkın,Kubicki and Padron, 2011). To determine and assess power characteristics, however, several correlations have been developed. For example, using a multi-stage rotor-stator, Krozen, Groot Wassink and Bertlein (1988b) were able to derive a generalised Power number (P_o) and Reynolds number (*Re*) relationship independent of mixer geometry. They found that in the laminar flow regime, P_0 was inversely proportional to the *Re* and in turbulent flow regime P_0 was found to be constant (Kroezen,Groot Wassink and Bertlein, 1988b).

The first study using a continuous rotor-stator device was by Krozen and Wassink (1988). Smaller bubbles were obtained at higher rotational speeds and lower air volume fractions. In

addition, air inclusion was found to be good in the turbulent flow regime, poor in transitional flow and moderate in laminar flow. A number of studies then followed which studied the effects of liquid mix properties (density, viscosity and surface tension) and processing parameters (rotor speed, air volume fraction, power input, residence time, static pressure and temperature in the mixing-head chamber). For example, using a single non-Newtonian fluid and a fixed twelve rotor-stator geometry operating at a single speed, Muller-Fischer and Windhab (2005) found that bubble size increased as the gas-liquid ratio inside the mixing-head chamber was increased (G/L = 0.5 – 3.5) covering laminar to transitional flow, and this was attributed to bubble coalescence. Nicorescu *et al.* (2010), on the other hand, using a fixed seven rotor-stator geometry, a fixed non-Newtonian fluid and a single G/L ratio of 2.0, investigated the effects of rotor speed and residence time on aeration efficiency and bubble size. Rotor speed was found to be the main processing parameter affecting bubble size, but no reference was made to the flow regime and how it influences bubble size and aeration efficiency (Nicorescu *et al.*, 2010). Narchi *et al.* (2011) also investigated the effects of rotor speed on bubble size for a fixed Newtonian and a fixed non-Newtonian medium under laminar conditions. For both fluid systems, bubble size was found to decrease with rotor speed. For the Newtonian fluid, bubble size also decreased as a function of G/L ratio, but no explanation was given. This effect was not investigated for the non-Newtonian system (Narchi *et al.*, 2011).

So far there is no study reported on the combined effects of liquid composition (surfactant concentration, thickener concentration) and processing parameters (rotor speed, G/L ratio) for non-Newtonian media which are most relevant to the production of food foams. In the present investigation, a first extensive study of wet foams generated from viscous non-Newtonian shear-thinning liquids using a continuous multi rotor-stator device is conducted. A range of experimental conditions are investigated to determine the effects of liquid formulation and

processing conditions on foam bubble size distribution, gas volume fraction and static stability. Foaming is carried out under atmospheric conditions to avoid foam expansion which can bring about drastic changes in foam microstructure which is uncontrollable and undesirable (Müller-Fischer,Suppiger and Windhab, 2007b). An advanced X-ray micro-CT technique is used to non-invasively visualise and analyse the 3D microstructure of the foams.

4.2 Materials and methods

4.2.1 Model fluids preparation and characterisation

The model fluids employed in the experiments consisted of a mixture of polyglycerol fatty acid ester (PGE 55, DuPont, Denmark), xanthan gum (XG, supplied by Unilever), caster sugar (British sugar PLC, obtained from local supermarket) and sodium azide (ReagentPlus, ≥ 99.5%, Sigma Aldrich), used without prior purification. A Silverson high-shear mixer (Model L4RT, Silverson, UK) was used to mix the ingredients in distilled water held at 80°C using a water bath, to ensure that the Krafft temperature (58°C) of PGE 55 was exceeded (Duerr-Auster *et al.*, 2008, Curschellas *et al.*, 2012a). First, polyglycerol fatty acid ester (PGE 55) was added under agitation (6000 – 7000 rpm) and mixed thoroughly for at least 5 minutes prior to adding sugar and XG. Stirring was continued for another 5 min until all XG was completely dissolved. Sodium azide (0.025 wt%) was added to prevent microbial growth. The model fluids were then stored at 5°C to degas and mature (hydration of XG) for at least 24 hours, to enable their rheology to fully stabilise. In order to check that the high-shear processing used did not affect the rheology of the fluids, we also prepared smaller volumes of such liquids using gentle mixing provided by a magnetic stirrer. There was no significant difference between the liquids obtained.

The equilibrium surface tension of the fluids was measured at 25°C using a Wilhelmy plate method (Sigma 701 Force Tensiometer). Dynamic surface tension measurements were obtained using a pendant drop method (PAT1P Tensiometer, Sinterface, Germany). Prior to any measurement, solutions were centrifuged for 4 minutes at a rotational speed of 2800 rpm to remove entrapped air bubbles. Each measurement was repeated at least three times and an average taken (SD = 1.5 mN m^{-1}).

Table 4.1 summarises the composition of the model fluids and their physical properties. The presence of caster sugar and XG, had negligible effects on the surface tension as the surface activity of PGE 55 is much greater than both caster sugar and XG. For all model fluids tested, surface tension was shown to evolve with respect to time, with a rapid initial reduction followed on by a gradual decline tending towards an equilibrium value. Equilibrium values of surface tension are given in Table 4.1. As shown and expected, surface tension kinetics was found to be a function of PGE 55 and XG concentration.

Table 4.1: Model fluids composition and properties.

Model fluid	PGE 55 (wt%)	XG (wt%)	Sugar (wt%)	σ_e (mN m^{-1})	η_o (Pa.s)	η_∞ (Pa.s)	λ (s)	n (-)	R^2 (-)
MF1	0.2	0.50	25	39	80	0.007	30	0.20	0.999
MF2	0.5	0.50	25	38	100	0.007	35	0.20	0.999
MF3	1.0	0.50	25	38	135	0.007	40	0.20	0.999
MF4	0.5	0.25	25	38	9	0.007	15	0.30	0.998
MF5	0.5	0.35	25	38	35	0.007	30	0.30	0.998

A controlled stress/strain rheometer (Discovery HR-2, Hybrid Rheometer, TA, USA) equipped with a 40 mm parallel plates geometry was used to characterise the rheology of the model fluids. No slip was detected as measurements conducted using different plate gaps yielded similar results; thus, a 0.5 mm gap was adopted throughout. Complete flow curves were obtained at controlled strain rate by varying the shear rate in the range of 0.001 – 8000 s^{-1} and were well fitted by the Cross rheological model (coefficient of determination, $R^2 \sim 0.999$). The cross model incorporates both the upper and limiting viscosities, η_o and η_∞, corresponding, respectively, to the upper and lower Newtonian regions, and is given by:

$$\eta = \eta_\infty + \frac{\eta_0 - \eta_\infty}{1 + (c\dot{\gamma})^m} \qquad \text{(Eq. 4.1)}$$

where η is the apparent viscosity, $\dot{\gamma}$ is the shear rate, and c and m are the Cross time constant and rate constant, respectively. This model can be reduced to the power law model in the region where $\eta << \eta_o$ and $\eta >> \eta_\infty$, which will be useful for the definition of a modified Weber number, as discussed further below.

4.2.2 Foam generation

A pilot-scale continuous rotor-stator (Megatron FM 12 – 50/2 HR), shown in Fig. 4.1, was used to aerate the model fluids and continuously generate foam. The device consists of 12 rotor-stator pairs in series where the rotor and stator have diameters of 50 and 52 mm each. Every rotor and stator has 13 pins (4.7 × 4.6 × 2.5 mm) with square ends and the gap between the rotor and stator is 1.0 mm. The geometrical dimensions of the rotor-stator pairs are provided in Table 4.2.

A progressive cavity pump is utilised to continuously pump the liquid at a controlled flowrate to the mixing-head chamber which has a free volume of approximately 85 mL. Simultaneously, a controlled amount of air is also introduced into the feed line from a gas cylinder, which combines with the liquid upon entering the mixing-head chamber. Foam was generated at atmospheric pressure using rotor speeds in the range 500 – 1750 rpm. A Julabo F-25 cooler (JULABO GmbH, Germany) was used to dissipate the heat generated during operation and control the mixing-head temperature, so that the exit foam temperature was maintained approximately equal to the liquid feed temperature at 25°C ± 3°C, which kept the effects on fluid rheology and surfactant kinetics minimal.

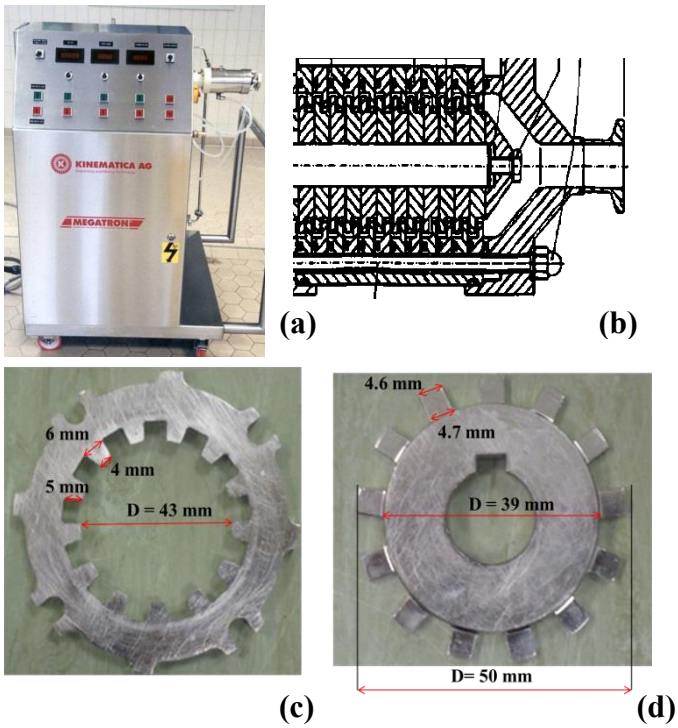

Fig. 4.1: Foam generator: (a) pilot-scale continuous rotor-stator unit; (b) schematic of mixing-head chamber; (c) stator; and (d) rotor.

Table 4.2: Geometrical dimensions of continuous rotor-stator device.

Parameter	Symbol (unit)	Value
Diameter of annulus mixing space	*L* (mm)	5.00
Number of pins on rotor	*I* (-)	13.00
Number of rotor-stator pairs	*h* (-)	12.00
Distance between rotor-stator	*s* (mm)	1.00
Height of rotor/stator pin	*q* (mm)	2.50
Width of rotor pin	*o* (mm)	4.70
Rotor diameter	*D* (mm)	50.00
Distance between rotor pins	*z* (mm)	12.08

Experiments were conducted to generate foams with varying microstructure by using combinations of liquid flowrate values within the range 3.46 – 6.67 $Lh^{-1}$and air flowrate values within the range 5.0 – 10.1 Lhr^{-1}. These experiments showed a high degree of reproducibility in terms of foam gas volume fraction and mean bubble size, i.e. within 5% at the lowest rotor speed and within 1% at the highest speed.

4.2.3 Foam characterisation

4.2.3.1 Air volume fraction

The air volume fraction in the foam is theoretically defined as:

$$\phi_{th} = \frac{Q_G}{Q_G + Q_L} \qquad \text{(Eq. 4.2)}$$

where Q_G and Q_L are, respectively, the air and liquid volumetric flowrate. This was experimentally measured by collecting foam samples at the exit of the rotor-stator device and determining the average mass of base liquid and foam that fill the same volume. The

experimentally measured ϕ_e value cannot be greater than the theoretical value (ϕ_{th}) and an efficient foaming process will aim to maximise ϕ_e:

$$\phi_e = \frac{\frac{OR}{100}}{\frac{OR}{100} + 1} \quad \text{(Eq. 4.3)}$$

where ρ_f is the density of the foam, ρ_L is the density of the base liquid and *OR* is the overrun experimentally determined, thus:

$$OR = \frac{\rho_L - \rho_f}{\rho_f} \times 100 \quad \text{(Eq. 4.4)}$$

4.2.3.2 Bubble size distribution

A desktop X-ray micro-CT (Skyscan 1172, Bruker, Belgium) was used to scan and visualise, non-invasively, the full 3D microstructure of the foam samples (3.8 µm resolution, see Chapter 3 for more details). A 2 – 5 mL foam sample was placed inside a drinking straw and sealed prior to scanning (Lim and Barigou, 2004, Barigou and Douaire, 2013). From the bubble size distribution, the Sauter mean bubble diameter was obtained:

$$D_{32} = \frac{\sum n_i d_i^3}{\sum n_i d_i^2} \quad \text{(Eq. 4.5)}$$

where *n* is the number of bubbles of diameter *d* in class size *i*.

4.2.3.3 Foam static stability

Foam stability is determined by liquid drainage, bubble coalescence and Ostwald ripening. Foam drainage was measured over a period of many weeks by monitoring a 50 mL foam sample collected at the outlet of the continuous rotor-stator and stored at a constant temperature of 5°C, 25°C and 50°C. Thus, transients of drained liquid were obtained for all experimental conditions investigated. Foam collapse was measured by monitoring the height of standing foams. Foam coarsening which is a consequence of bubble coalescence and Ostwald ripening was investigated using X-ray micro-CT, by scanning foam samples also stored at constant temperature (25°C) on a weekly basis over a period of several weeks. The schematic of the experimental set-ups is shown in Fig. 4.2.

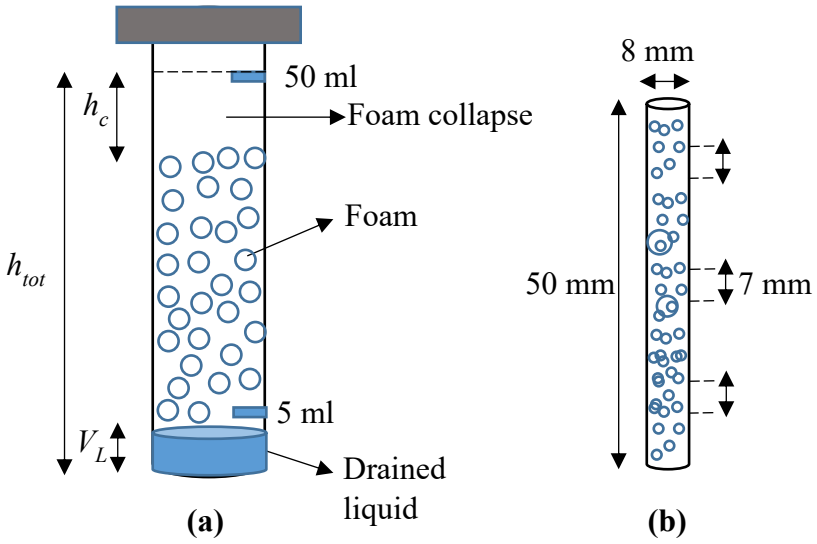

Fig. 4.2: Schematic showing set-up of: (a) liquid drainage and collapse; and (b) foam coarsening.

Foam decay rate was plotted in terms of percentage of total height collapse, thus:

$$h_L = \frac{h_c}{h_{tot}} \times 100 \qquad \text{(Eq. 4.6)}$$

where h_c is foam collapse in time t and h_{tot} is the total height of the sample bottle. Liquid drained rate can be modelled using the following empirical equation:

$$h_s = \frac{v_0 t}{1 + kt} \quad \text{(Eq. 4.7)}$$

where v_0 is the initial rate of liquid drained and k is a constant.

4.2.4 Theory

4.2.4.1 Foam hydrodynamics inside mixing-head chamber

The hydrodynamics inside the mixing-head chamber play a crucial role in the production of homogenous foams. The pertinent parameters are the Power number and the Reynolds number. The Power number is the dimensionless form of the power input (P):

$$P_o = P/\rho_f N^3 D^5 \quad \text{(Eq. 4.8)}$$

where N is the rotor speed and ρ_f is the density of the gas-liquid dispersion measured at the outlet of the rotor-stator device. The Power number is in turn dependent on the value of Reynolds number (Re) defined as follows:

$$P_o = f(Re) \quad \text{(Eq. 4.9)}$$

where Re is given by:

$$Re = \rho_f N D^2/\eta(\dot{\gamma}) \quad \text{(Eq. 4.10)}$$

where $\eta(\dot{\gamma})$ is the apparent foam viscosity at shear rate $\dot{\gamma}$.

Krozen and Wassink (1988) were the first to derive via an extensive study the empirical relationship $P_o = f(Re)$ for a continuous rotor-stator device, by experimenting with different geometries and a wide range of water-glycerol mixtures. Such a relationship was based on a generalised Power number:

$$P_o^* = Pz/\rho_F D^4 N^3 hLq \quad \text{(Eq. 4.11)}$$

and a generalised Reynolds number:

$$Re^* = \rho_F NDs/(f \times \eta(\dot{\gamma})) \quad \text{(Eq. 4.12)}$$

both of which are independent of rotor-stator device geometry. The correlation factor *f* in Eq. 4.12 is defined as:

$$f = 71o/q + 553s/\sqrt{Dq} \quad \text{(Eq. 4.13)}$$

and the geometrical dimensions *h*, *L*, *q*, *o* and *s* are defined in Table 4.2. In the laminar flow regime ($Re^* < 0.01$), the Power number was found to be inversely proportional to the Reynolds number, whereas in the turbulent regime ($Re^* > 0.1$), P_o^* was found to be constant (equal to 17). It should be noted that the equations derived above does not taken into account foam compressibility and elasticity which is likely to contribute to power consumption. Therefore, it is only used to estimate approximately the net power consumption within the multistage rotor-stator device. For the actual power consumption, it is pertinent to obtain the corresponding values experimentally which can be difficult for shear-thinning fluids (Özcan-Taşkın,Kubicki and Padron, 2011).

4.2.4.1.1 Energy dissipation inside mixing-head chamber

The energy consumption in foaming experiments was estimated using the above empirical relationship $P_o = f(Re)$ developed by Krozen and Wassink (1988). This initially involved the identification of the flow regime using the definition of *Re** (Eq. 4.12) and *f* (Eq. 4.13)), the dimensions of the rotor-stator geometry (Table 4.2) and the function $\mu(\dot{\gamma})$. For all experimental conditions investigated, *Re** was found to be in the range of 0.02 – 5.7, i.e. corresponding in the vast majority to turbulent flow where, as indicated above, P_o^* is constant and equal to 17. The net mechanical power input per unit volume (P_v) is defined as:

$$P_v = \frac{P}{V} \qquad \text{(Eq. 4.14)}$$

where *V* is the volume of the mixing-head chamber (85 mL). The shear rate ($\dot{\gamma}$) inside the mixing-head chamber is the maximum shear rate at the tip of the rotor (Müller-Fischer,Bleuler and Windhab, 2007a):

$$\dot{\gamma} = \frac{\pi DN}{s} \qquad \text{(Eq. 4.15)}$$

Another method based on the Metzner-Otto approach (Metzner and Reed, 1955) uses an average values of the shear rate (Balerin *et al.*, 2007, Wu *et al.*, 2014). This approach would lead to the prediction of laminar rather than turbulent flow inside the mixing-head chamber. Using Eq. 4.15, the viscosity function of the foam $\eta(\dot{\gamma})$ is obtained by determining the rheological flow curve of foam samples taken at the outlet of the rotor-stator device using the rheometer described above. Finally, the net volumetric energy input (E_V) can be determined, thus:

$$E_V = \tau P_v \quad \text{(Eq. 4.16)}$$

where τ is the average residence time of both the gas and liquid in the mixing-head chamber, at atmospheric conditions, is given by:

$$\tau = \frac{V}{V_{foam}} = \frac{V}{Q_L + Q_G} \quad \text{(Eq. 4.17)}$$

where V_{foam} is the volumetric flowrate of foam and Q_L and Q_G are the liquid and air volumetric flowrate, respectively.

4.3 Results and discussion

4.3.1 Preliminary trials

In the literature, it is widely known that rotor speed (N), static pressure (P_{static}), temperature (T) and the residence time (τ) inside the mixing-head chamber are the main processing parameters of a continuous rotor-stator device that affects the aeration efficiency and bubble size distribution. All the experimental studies conducted using a continuous rotor-stator device have reported that N is the most influential processing parameter affecting the aeration efficiency and bubble size distribution. The effects, however, of static pressure (P_{static}), G/L ratio (ratio of volumetric flowrate of gas to liquid) and residence time (τ) on bubble size distribution is still unclear and hence requires further investigation. In addition, there are very limited amount of studies that investigated model fluids with viscous shear-thinning properties suitable for the manufacture of food foams such as ice cream, mousse, scuffle, etc. Continuous phase viscosity (η), surfactant type and surface tension kinetics have been found to be the major liquid properties influencing the bubble size distribution using a continuous rotor-stator device.

In this thesis, the rotor-stator geometry (consisting of 12 rotor-stator pairs with a 1.0 mm shearing gap) was fixed and hence it was not investigated. Similarly, all foaming operation in this study was conducted under ambient conditions and hence the effects of static pressure (P_{static}) on aeration efficiency and bubble size distribution was not investigated. Therefore, stable and fine-textured foams were obtained by varying the processing conditions (rotor speed, G/L ratio) and liquid properties (surfactant concentration and XG concentration). Prior to any detailed investigation onto the effects of processing parameters and liquid formulation on aeration efficiency and bubble size distribution, it was necessary to identify the desirable operating conditions for obtaining the required specification of foams (air volume fraction in the range of 0.33 – 0.72 and bubble size in the range of 60 – 300 μm).

Therefore, initial trials were conducted using model fluid 2 (MF2) by varying the values of N in the range of 500 – 4000 rpm and G/L ratios of 0.5, 1.0, 1.5 and 2.0 respectively. For all the conditions investigated, it was decided to maintain the foam outlet temperature at 25°C using water as the cooling medium. This was necessary because, during the process of shearing, vast amount of dissipative heat is generated inside the mixing head-chamber especially when operating at higher rotor speeds (N) - as previously observed by (Müller-Fischer and Windhab, 2005). This has been shown to affect the continuous phase viscosity and hence aeration efficiency and bubble size distribution.

Aeration efficiency is an important feature of the foam generation process which indicates the ability to incorporate all of the available gas into the foaming liquid to make a homogeneous

foam. Thus, optimum aeration is achieved when the theoretical and experimental values of volume gas fraction (ϕ) are equal (Eq. 4.2). Independent of residence time (τ), theoretical aeration efficiency (ϕ_{th}) was achieved at all rotor speeds (N) when G/L was set to 0.5 and 1.0. However, ϕ_{th} was not achieved at G/L = 1.5 when N = 3500 and N = 4000 rpm. Similarly, it was not achieved at G/L = 2.0 for N = 500 rpm, 3000 rpm, 3500 rpm and 4000 rpm. A possible explanation for this significant drop in aeration efficiency at higher N might be due to the occurrence of over-beating phenomena as commonly observed during batch aeration (Jakubczyk and Niranjan, 2006a). In addition, it was difficult to control the foam outlet temperature at N > 2000 rpm and hence a significant rise in foam outlet temperature was observed. Furthermore, the rate of coalescence inside the mixing-head chamber is likely to increase with an increase in rotor speeds (N > 2000 rpm) and G/L values.

Therefore, to quantify the degree of dissipative heating, it was decided to measure the foam outlet temperature using a sensitive digital thermometer. With an increase in N, the foam outlet temperature was shown to increase due to the significant amount of dissipative heating that was generated as a result of the viscous nature of the foaming liquid. This was apparent once it was decided to measure the foam outlet temperature using a sensitive temperature sensor. The foam outlet temperature was shown to increase from 20°C to almost 35°C once N was increased from 500 to 4000 rpm respectively. Locally, the temperature gradient inside the small gap (1.0 mm) of the rotor-stator is expected to be even greater but this is difficult to measure and control.

Bubble size distribution was also measured and the Sauter mean bubble diameter (D_{32}) at different N and G/L ratios are summarised in Fig. 4.3. There was a significant drop in D_{32} with

an increase in N as widely observed in the literature. The reduction in D_{32} was exponential between N = 500 – 2000 rpm and then a much smaller and linear reduction was obtained at $N \geq$ 2000 rpm. There are several possible reasons why at a higher N, the D_{32} approaches an asymptote as shown in Fig. 4.3. First of all, there is a competition between bubble breakage and coalescence and it seems that at a higher N the rate of bubble coalescence approaches that of a bubble breakage, i.e. an equilibrium is established. Secondly, as mentioned above, there is a significant rise in local temperature inside the small gap of the rotor-stator device which can have an effect on the hydrocarbon chain fluidity of the emulsifier – PGE 55. As pointed out by Natalie Dürr-Auster, the mobility of the PGE vesicles is increased as the temperature of the solution approaches the Kraft temperature (defined as the temperature at which the hydrocarbon chain melts) inside the mixing-head chamber. This is especially true for the monolayer on the bubble surface which becomes fluid-like and hence can be easily rearranged or altered at temperature lower than the chain-melting temperature of the bilayer in the bulk fluid (Dürr-Auster, 2008).

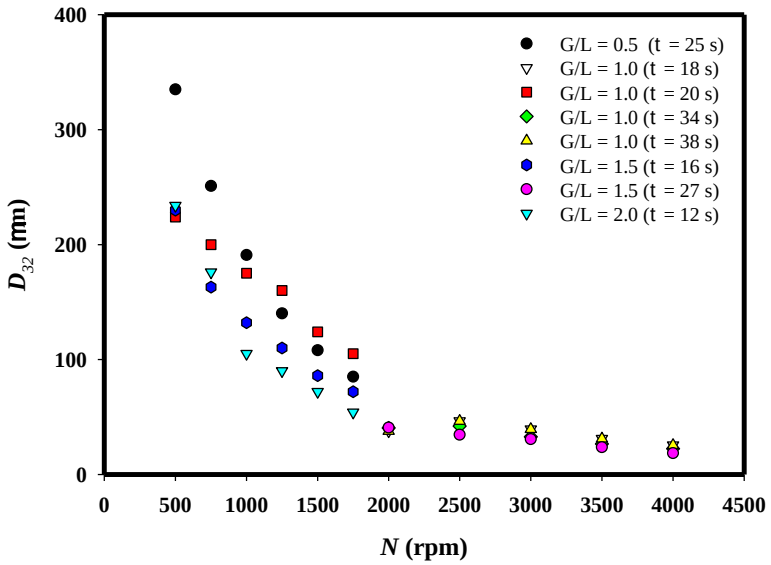

Fig. 4.3: Preliminary trials results of D_{32} of wet foams generated from fluid MF2.

Overall, it can be concluded that at a higher rotor speeds (N > 1750 rpm), dissipative heating inside the mixing-head chamber is likely to affect the aeration efficiency and the corresponding bubble size distribution. In addition, it is difficult to control the rate of coalescence inside the mixing-head chamber when operating at a higher N and G/L ratios. Therefore, to eliminate the effects of temperature (T), it was decided to limit the maximum N to 1750 rpm. Operating at and below 1750 rpm always guaranteed that the foam outlet temperature was maintained at 25°C ± 3°C.

In the sections to follow, a detailed study was conducted to investigate the effects of processing parameters (rotor speed, air and liquid volumetric flowrates) and liquid properties (surfactant PGE 55 content and xanthan gum concentration).

4.3.2 Aeration efficiency

As noted previously, aeration efficiency is an important feature of the foam generation process which indicates the ability to incorporate all of the available gas into the foaming liquid to make a homogeneous foam. Thus, optimum aeration is achieved when the theoretical and experimental values of volume gas fraction (ϕ) are equal (Eq. 4.2). The effects on the incorporated gas volume fraction of the processing parameters (rotor speed, air and liquid volumetric flowrates) and the physical properties of the liquid (dynamic surface tension, liquid viscosity) were studied. In the first set of experiments, the liquid flowrate was set to 5 L hr^{-1} and the air flowrate was varied between 5.0, 7.5 and 10.0 L hr^{-1} to achieve foams with ϕ_{th} values in the range of 0.50 – 0.67. When the G/L ratio (ratio of air to liquid volumetric flowrate) was set to 1.0, all model fluids were able to achieve maximum aeration, i.e. $\phi_e = \phi_{th}$, over the range

of rotational speed 500 – 1750 rpm, independent of the residence time (τ) and the composition of the liquid used, as shown in Table 4.3.

However, when the G/L ratio was increased to 1.5, a 'blow-by' phenomenon was observed for MF1 at rotational speeds of 500 and 750 rpm and this was also independent of τ. The term 'blow-by' was initially coined by Kroezen and Wassink (1988) who observed a large pocket of undispersed gas (slug flow regime) at the outlet of the continuous rotor-stator, which is undesirable. The moderate concentration of PGE 55 (0.2 wt%) seems to limit the incorporation of air in liquid MF1 at these particular rotational speeds. This phenomenon may be attributed to bubble coalescence inside the mixing-head chamber due to insufficient surfactant, as previously observed in turbulent emulsification (Tcholakova *et al.*, 2011). As G/L was increased, 'blow-by' occurred at higher and higher rotational speeds and no homogeneous foam could be produced at any speed within the range studied when G/L ~ > 2.5. Fluids MF2 and MF3, with a higher PGE 55 content (0.5 wt% and 1 wt%, respectively), were in fact able to achieve maximum air volume fraction at all rotational speeds investigated when G/L = 1.5. 'Blow-by' was observed, however, for both fluids regardless of residence time when G/L = 2.0 at rotational speeds of 500 and 750 rpm, and at G/L ~ > 2.5 it occurred at all rotational speeds. Thus, a doubling in PGE 55 concentration between MF2 and MF3 had no influence on the onset of 'blow-by'. Fluids M4 and M5 have the same surfactant concentration as fluid MF2 but a lower xanthan gum concentration (Table 4.3); they exhibit 'blow-by' under the same conditions as MF2 but their foam stability, bubble size distribution and rheological properties are significantly different. These results seem to suggest that beyond a certain concentration, the aeration process is no longer determined by surfactant content or the hydrodynamics of the process.

Table 4.3: Effects of experimental conditions on experimental gas volume fraction (Sample ϕ_e data shown here for cases where Q_L = 5 L hr^{-1} and Q_G = 5.0, 7.5 and 10.0 L hr^{-1}).

***N* (rpm)**	**MF1**		**MF2**			**MF3**		**MF4**		**MF5**	
	G/L = 1.0 (τ = 31 s)	G/L = 1.5 (τ = 25 s)	G/L = 1.0 (τ = 31 s)	G/L = 1.5 (τ = 25 s)	G/L = 2.0 (τ = 20 s)	G/L = 1.0 (τ = 31 s)	G/L = 1.5 (τ = 25 s)	G/L = 1.0 (τ = 31 s)	G/L = 1.5 (τ = 25 s)	G/L = 1.0 (τ = 31 s)	G/L = 1.5 (τ = 25 s)
500	0.52	blow-by	0.52	0.62	blow-by	0.51	0.61	0.51	0.61	0.52	0.62
750	0.53	blow-by	0.52	0.63	blow-by	0.51	0.61	0.52	0.61	0.52	0.62
1000	0.53	0.63	0.52	0.63	0.69	0.51	0.61	0.51	0.61	0.52	0.62
1250	0.53	0.63	0.52	0.63	0.69	0.52	0.61	0.52	0.61	0.52	0.62
1500	0.54	0.63	0.52	0.63	0.69	0.53	0.61	0.52	0.62	0.53	0.63
1750	0.54	0.63	0.52	0.63	0.69	0.53	0.61	0.53	0.62	0.52	0.63

4.3.3 Effects of processing parameters and physical properties of foaming solution on bubble size

4.3.3.1 Effects of G/L ratio and residence time

The effects of varying the rotor speed on the Sauter mean bubble diameter of the foam are shown in Fig. 4.4 for fluids MF1, MF2 and MF3 at different G/L ratios. Irrespective of the model fluid and G/L ratio, increasing *N* leads to a sharp reduction in bubble size as widely reported in the literature where similar rotor-stator devices were used (Balerin *et al.*, 2007, Seguineau De Preval *et al.*, 2014a, Narchi *et al.*, 2011, Nicorescu *et al.*, 2010, Mary *et al.*, 2013, Seguineau De Preval *et al.*, 2014b, Müller-Fischer,Suppiger and Windhab, 2007b). This reduction is mainly due to the increased shear, elongation and inertia forces acting inside the mixing-head chamber which break down larger air bubbles into smaller bubbles (Müller-Fischer,Suppiger and Windhab, 2007b). In addition, increasing *N* leads to a narrower and more uniform bubble size distribution, as shown in Fig. 4.4.

For a given fluid and a given rotational speed, increasing the G/L ratio results in a considerable reduction in bubble size (D_{32}), as shown in Fig. 4.4. This result is counter-intuitive since an increase in G/L reduces the foam residence time (Table 4.3) in the mixing-head chamber, thus, leading to less shearing of the gas-liquid dispersion. Over the range of rotor speeds studied (500 – 1750 rpm), *N* does not affect the residence time (τ). The residence time inside the mixing-head chamber which has a fixed volume and a fixed number of rotor-stator pairs (12) can be varied only by changing the G/L ratio (Eq. 4.17). As shown by the data in Fig. 4.4 and Table 4.3, for a fixed liquid flowrate, varying the gas flowrate leads to a different G/L ratio and, hence, a different residence time.

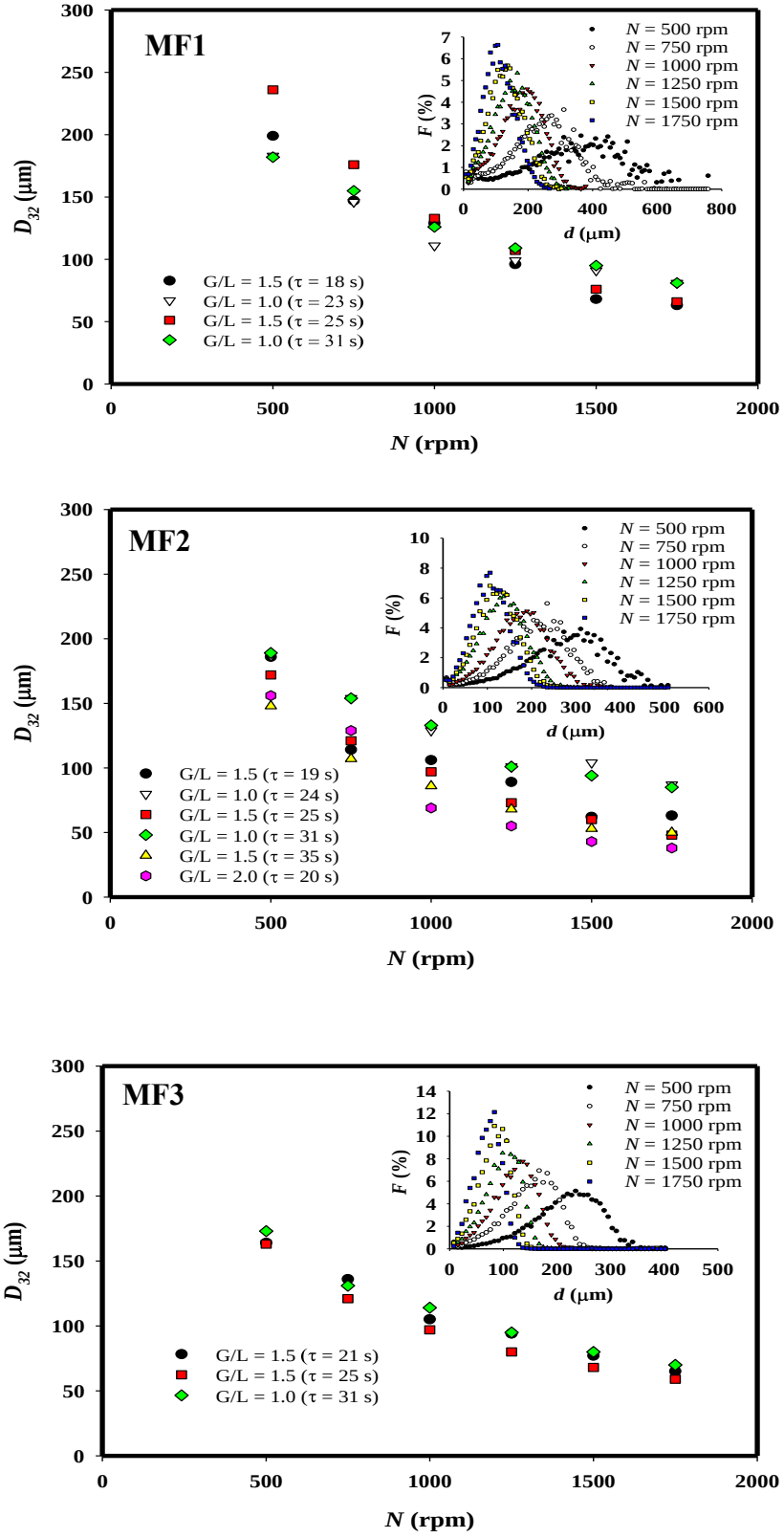

Fig. 4.4: Effects of rotational speed and G/L ratio on D_{32}.

Other authors found it hard to interpret the effects of τ on bubble size because this cross-influence between G/L and τ was not taken into account. In our case, the reduction in bubble size caused by increasing the G/L ratio, however, can be explained by the significant rise in the apparent viscosity of the dispersion inside the mixing-head chamber when the G/L ratio is increased, as shown in Fig. 4.5. The shear rate inside the mixing-head chamber was estimated using Eq. 4.15 and used to predict the apparent viscosity of the model fluids and gas-liquid dispersion using Eq. 4.1. An increase in apparent viscosity enhances the shear stresses acting on the bubbles leading to a reduction in bubble size (Indrawati and Narsimhan, 2008). As shown in Fig. 4.6, foam generated from MF2 at G/L = 1.5 exhibits a much more uniform bubble size distribution compared to foam generated at G/L = 1.0. Muller-Fischer *et al.* (2007a), using a dynamically enhanced membrane foaming technique, found that an increase in air volume fraction led to a reduction in bubble size which they attributed to an increase in dispersion viscosity. Similarly, increasing the disperse phase volume fraction in emulsions has also been reported to lead to a reduction in droplet size and polydispersity in the turbulent flow regime (Tcholakova *et al.*, 2011, Vankova *et al.*, 2007).

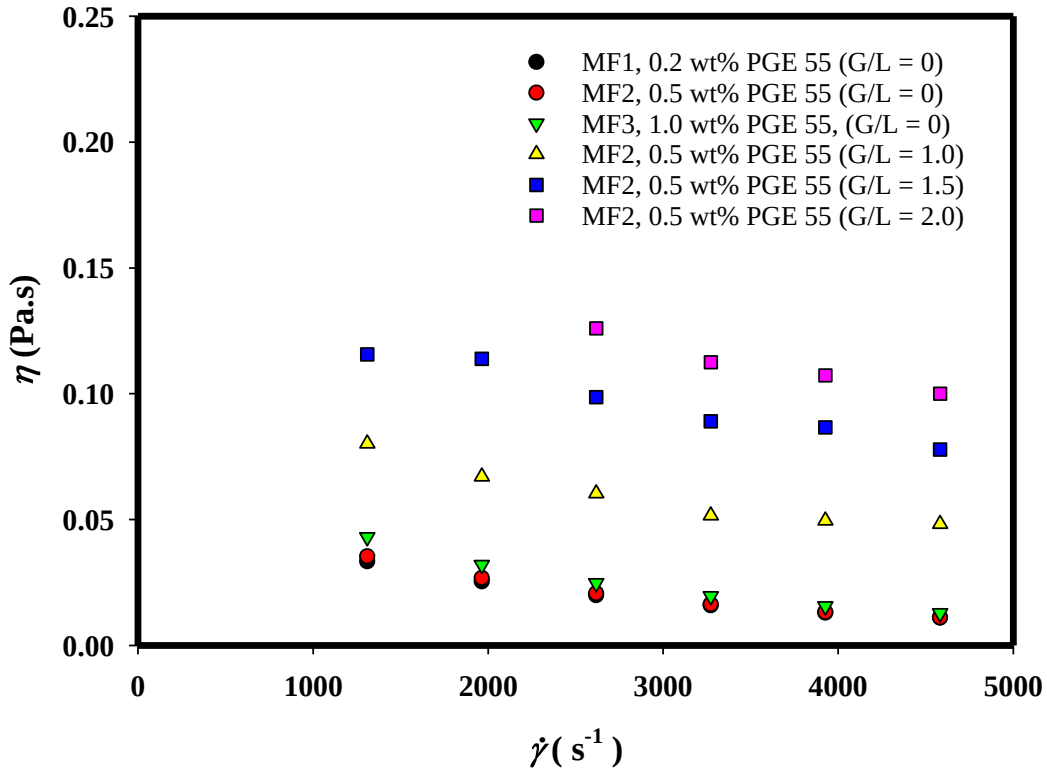

Fig. 4.5: Variation of apparent viscosity (Eq. 4.1) of gas-liquid dispersion inside mixing-head chamber and model fluids under the same process conditions of shear (Eq. 4.15).

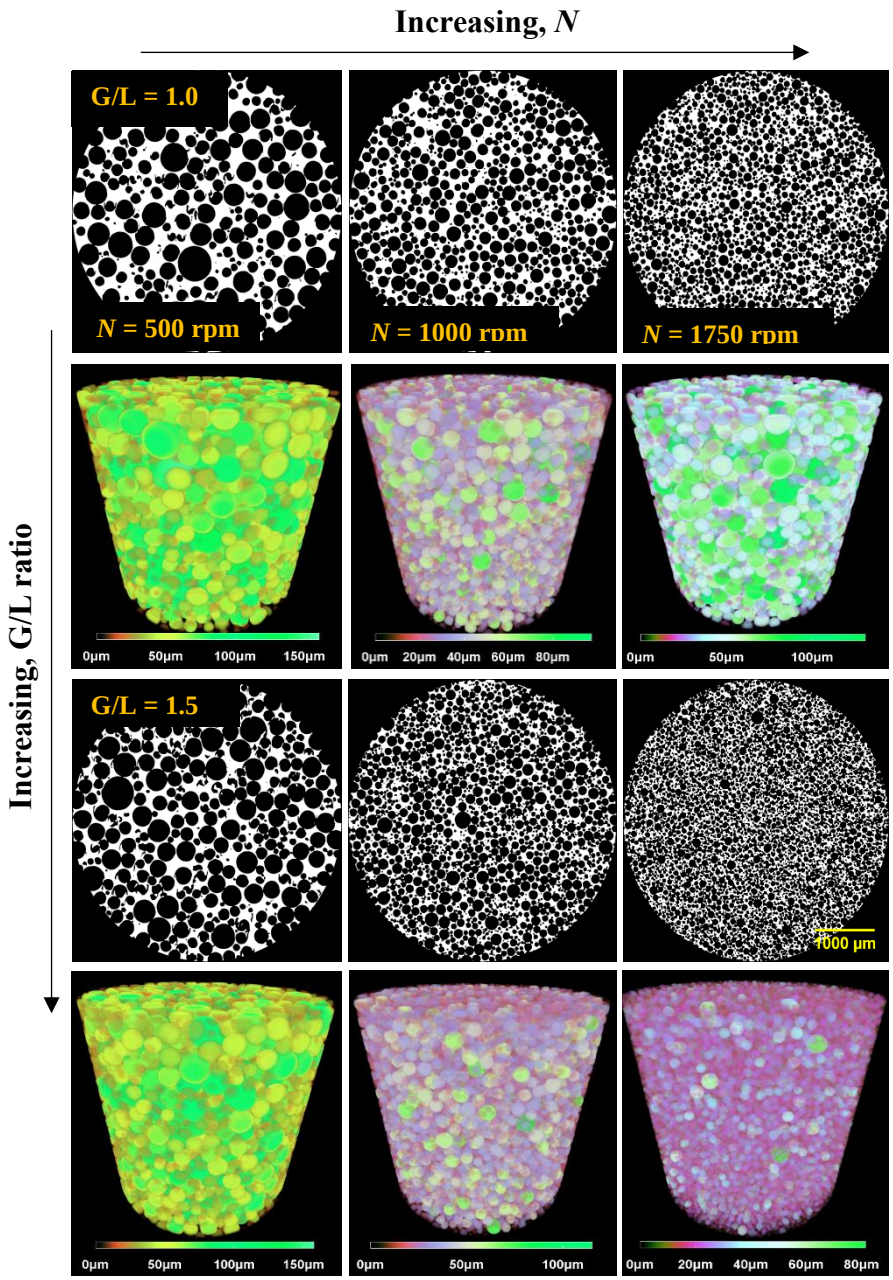

Fig. 4.6: Rendered 3D X-ray micro-CT model of foams generated from MF2 numerically cut to reveal its inner structure.

4.3.3.2 Effects of surfactant concentration

The effects of surfactant concentration on foam bubble size are depicted in Fig. 4.7. Fluids MF1, MF2 and MF3 are identical except for their different surfactant content. For G/L = 1.0, a higher concentration of PGE 55 from MF1 to MF2, to MF3 does not result in significant difference in mean bubble size. At higher G/L values, e.g. G/L = 1.5, a higher surfactant concentration initially leads to a much smaller bubble size (MF1 and MF2) but no further effect is observed beyond a certain concentration; MF2 and MF3 have concentrations of 0.5 wt% and 1.0 wt%, respectively, but exhibit the same mean bubble size at all rotational speeds. These effects are visualised in Fig. 4.8 showing sample X-ray micro-CT images of the different foam microstructures. This bubble size behaviour has previously been reported for Newtonian fluids (Seguineau De Preval *et al.*, 2014a, Seguineau De Preval *et al.*, 2014b). The same trend was followed by the volume gas fraction, as discussed above.

It is estimated (see Appendix 8.3 for detailed calculation) that to fully stabilise a 200 ml of 60% air volume fraction dispersion will require approximately 0.012 grams of PGE 55. The concentration added to the model fluids is much greater corresponding to 0.066 g for MF1, 0.164 g for MF2 and 0.328 g for MF3. This implies that there is sufficient PGE 55 available to fully stabilise the required air-water interface. It is therefore likely that other mechanisms are responsible for the change in bubble size behaviour instead of surfactant dynamics. The excess PGE 55 is likely to alter the bulk and interfacial rheological properties which may result in smaller bubble size as observed for model fluids with a higher surfactant content.

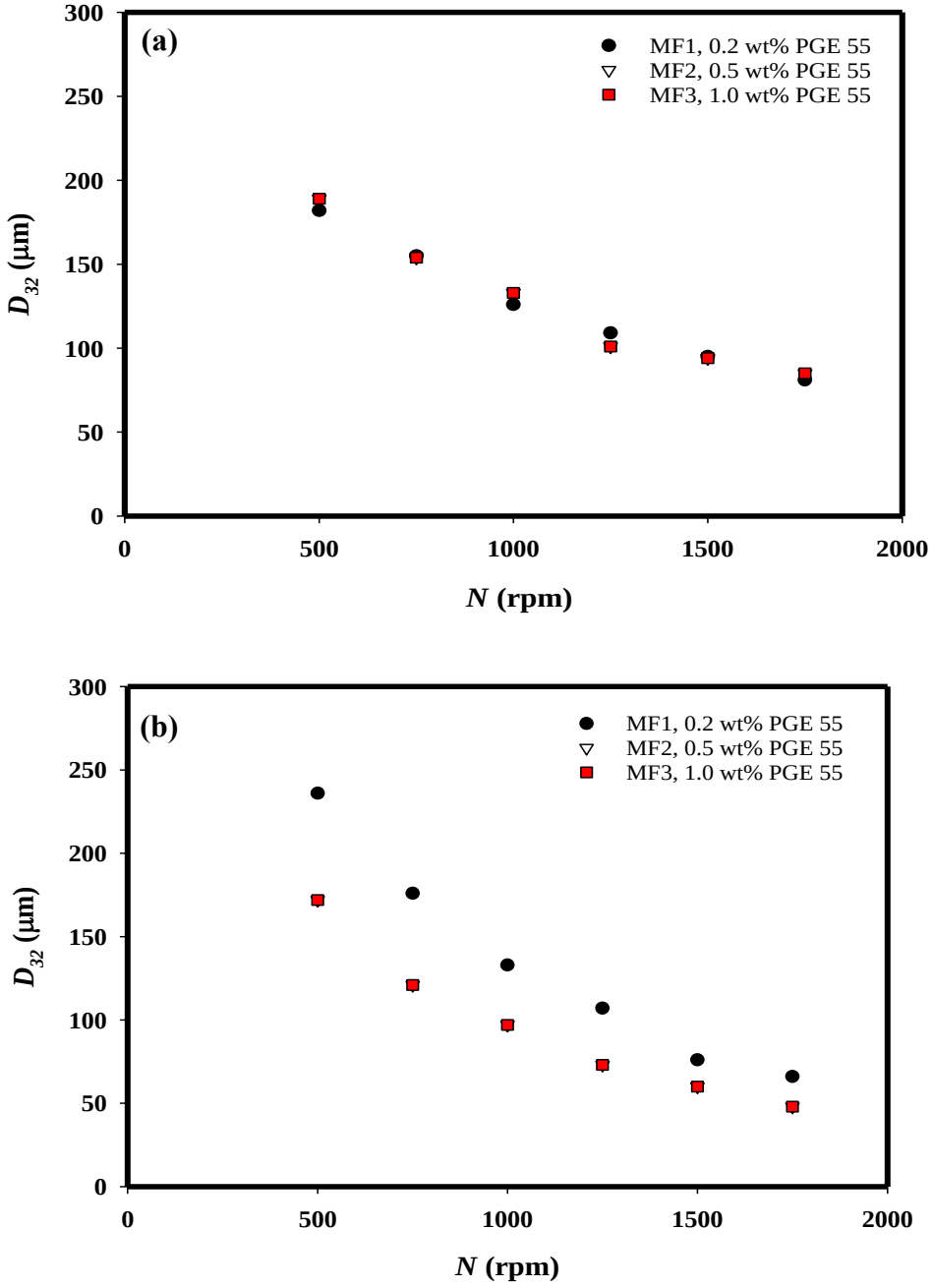

Fig. 4.7: Effects of surfactant concentration on D_{32}: (a) G/L = 1.0; (b) G/L = 1.5.

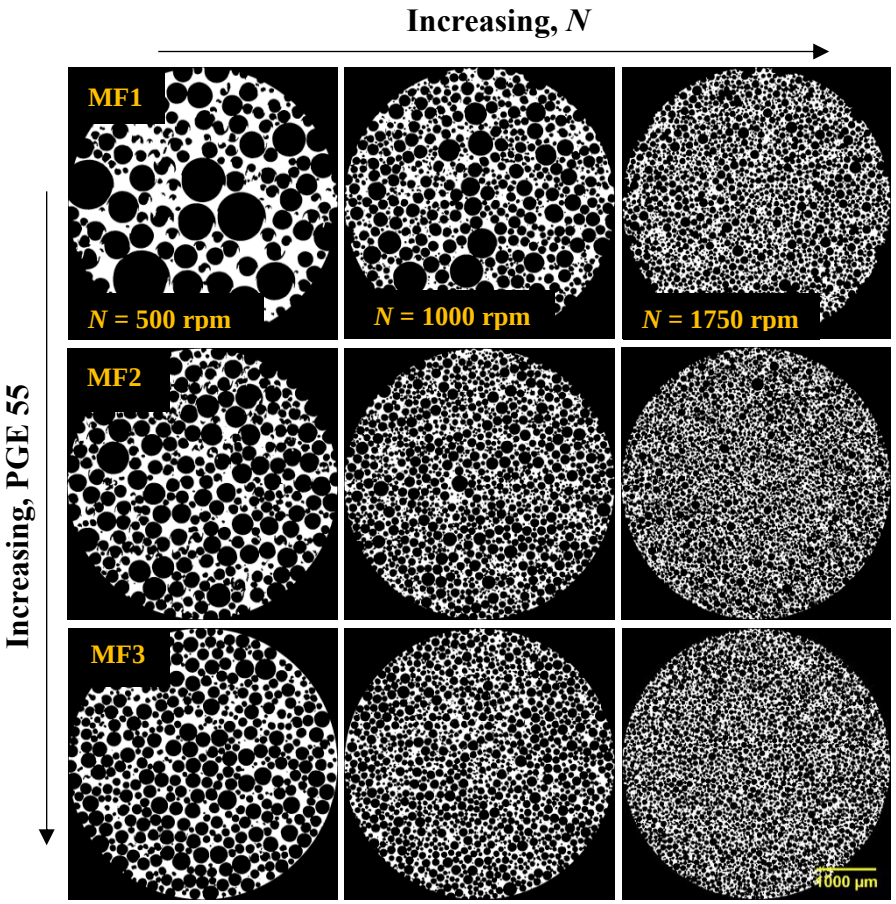

Fig. 4.8: X-ray micro-CT images of foam samples generated from MF1, MF2 and MF3 at G/L = 1.5.

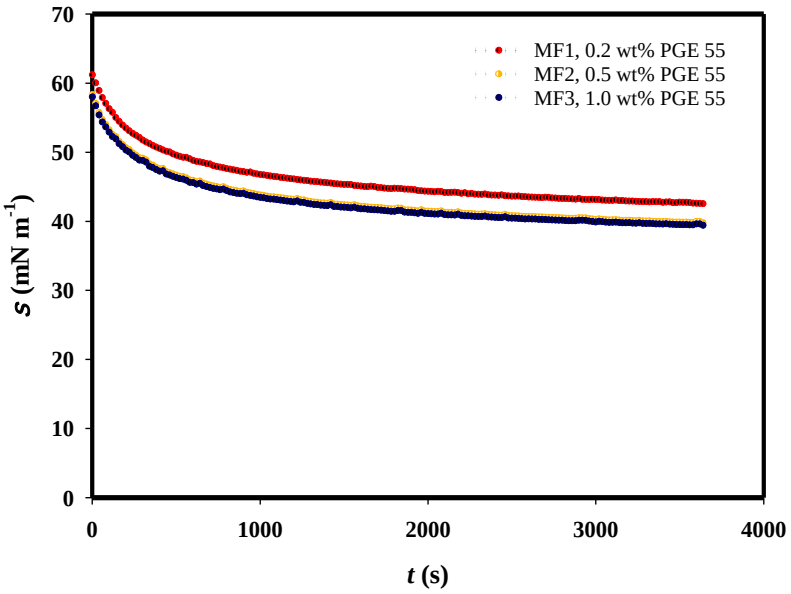

Fig. 4.9: Dynamic surface tension isotherm of model fluids.

As shown in Fig. 4.9, changing the surfactant concentration alters the surface tension kinetics especially at short time scales similar to the processing times (< 100 s). At higher PGE 55 concentrations up to ~ 0.5 wt%, the higher availability of surfactant molecules and their ability to diffuse faster to the air-water interfaces leads to the formation of smaller bubbles. Thereafter, the solution is saturated with surfactant and more PGE 55 produces no effect on surface tension kinetics and, hence, bubble size.

4.3.4 Effects of xanthan gum concentration

A higher XG concentration leads to a reduction in foam bubble size at all rotor speeds, but beyond a certain value the effect becomes negligible, as visualised in the images of Fig. 4.10 and represented in the mean bubble size plots in Fig. 4.11a. This has also been previously observed for foams generated from Newtonian fluids (Mary *et al.*, 2013, Seguineau De Preval *et al.*, 2014b, Seguineau De Preval *et al.*, 2014a) and non-Newtonian shear-thinning fluids (Balerin *et al.*, 2007, Indrawati and Narsimhan, 2008, Hanselmann and Windhab, 1998).

There are two competing factors which are affected by changing the XG concentration, namely the apparent viscosity and the surface tension kinetics, as shown in Fig. 4.11b and Fig. 4.11c, respectively. As discussed above, a higher dispersion viscosity arising from a higher XG content can, up to a point, lead to a finer foam texture in the mixing-head chamber due to higher shear stresses which produce smaller bubbles and slower drainage which prevents bubble coalescence (Indrawati and Narsimhan, 2008). At the same time, the slower surface tension kinetics arising from a higher XG content, up to a point, lead to the formation of larger bubbles since the surfactant diffuses more slowly to air-water interfaces. The results obtained here indicate that the viscosity effects are predominant.

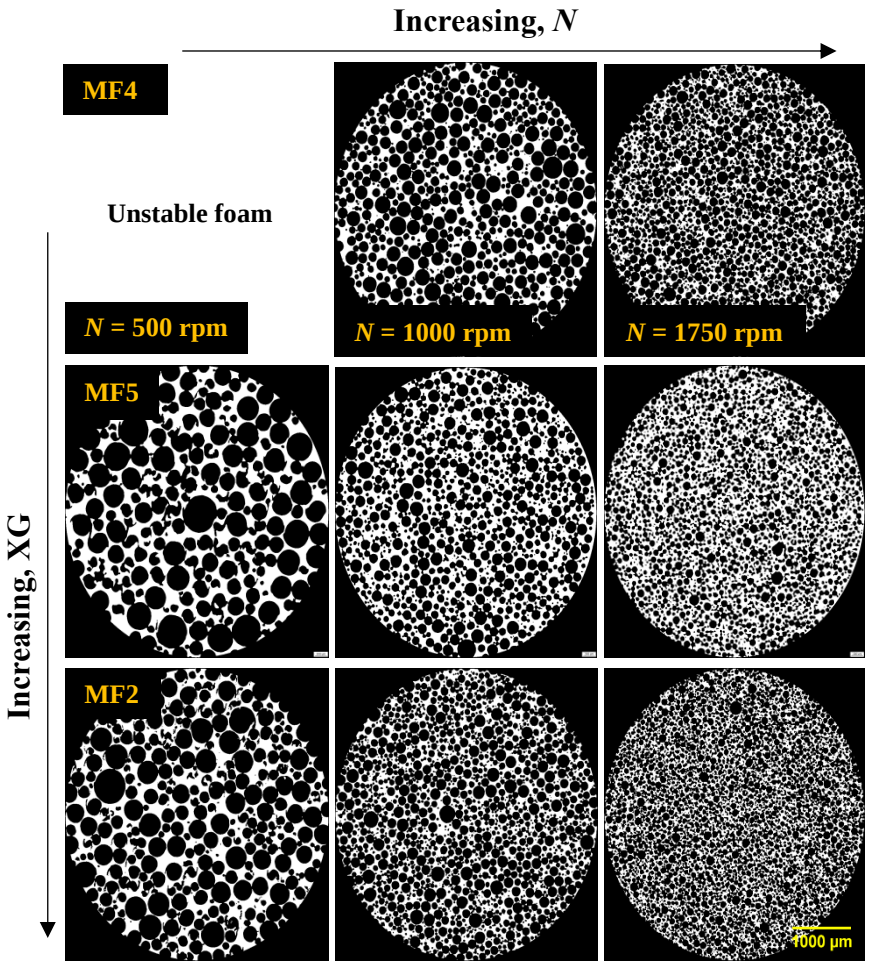

Fig. 4.10: X-ray micro-CT images of foam samples generated from MF2, MF4 and MF5 at G/L = 1.5.

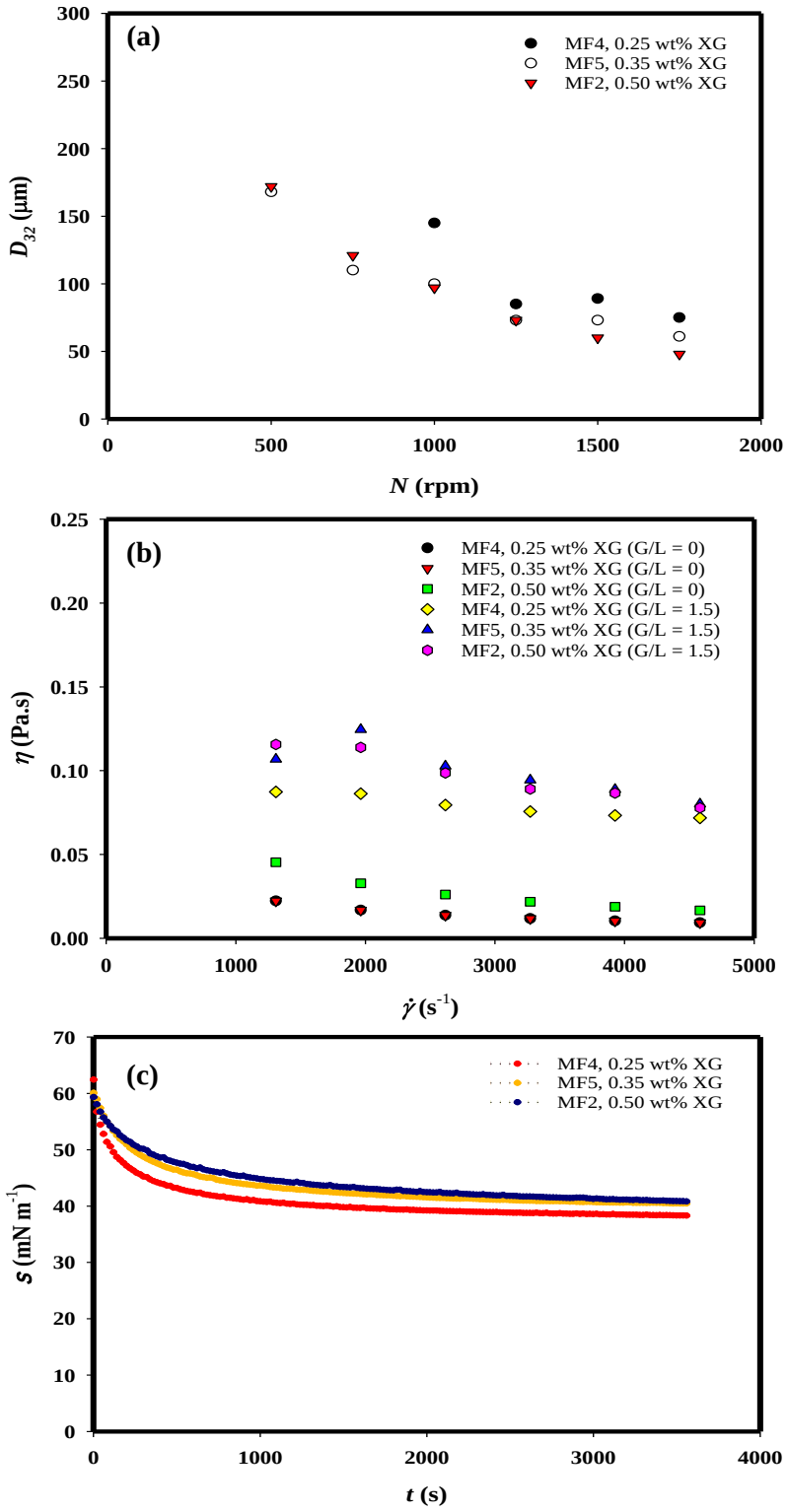

Fig. 4.11: Effects of xanthan gum concentration: (a) mean bubble size; (b) apparent dispersion viscosity; and (c) dynamic surface tension.

4.3.5 Theoretical analysis

4.3.5.1 Data reduction for interpretation of bubble size

The above results can be generalised by interpreting the data in terms of the Weber number, a ratio of shear forces to capillary pressure acting on the bubble. Typical apparent viscosity curves of the model fluids used and the foams produced are represented in Fig. 4.12. As pointed out above, the Cross model (Eq. 4.1) used to represent the apparent viscosity curves of the foam can be reduced in the central shear-thinning region ($\eta_\infty << \eta << \eta_o$) which covers the entire experimental conditions of this study to the much simpler two-parameter power law model:

$$\eta = k\dot{\gamma}^{n-1} \qquad \text{(Eq. 4.18)}$$

where *k* is the consistency index, *n* is the flow behaviour index. This facilitates the definition of a modified Weber number (Thakur,Vial and Djelveh, 2003), thus:

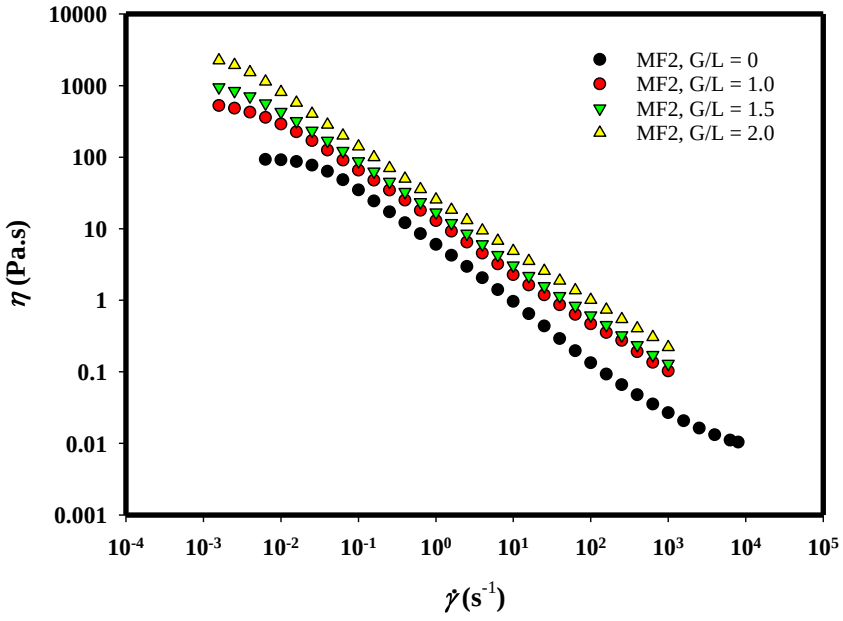

Fig. 4.12: Typical apparent viscosity curves of fluid MF2 and associated foam generated at *N* = 1000 rpm and different G/L ratios.

$$We = \frac{k(ND)^n}{\sigma_e s^{n-1}} \qquad \text{(Eq. 4.19)}$$

where σ_e is the equilibrium surface tension value reached after at least one hour (Fig. 4.9). The Reynolds number (*Re*) was computed using Eq. 4.10 above, and values in the range of $0.05 \geq Re \leq 5.7$ was found which corresponds to the majority of cases to turbulent flow regime (Kroezen,Groot Wassink and Bertlein, 1988b).

Different authors have adopted different definitions of *We* for foam taking into consideration the geometrical dimensions of the foam generating device, the hydrodynamics and liquid composition. A constant value of 0.24 – 0.60 is commonly reported for the critical Weber number at which bubbles rupture (Kroezen,Groot Wassink and Bertlein, 1988b, Thakur,Vial and Djelveh, 2005, Balerin *et al.*, 2007). Thakur *et al.* (2003), however, using time and shear rate dependent non-Newtonian liquids in a mechanical agitator device, found that *We* increased as a function of rotor speed. Similarly, using a continuous rotor-stator device and Newtonian media, Balerin *et al.* (2007) reported the same result; the increase in this case was attributed to a rise in local heat dissipation at higher rotor speeds.

The variations of foam mean bubble size are plotted in Fig. 4.13 as a function of *We* for the various experimental conditions investigated including all G/L ratios. The data follow the same general trend showing D_{32} decreasing with *We* (Fig. 4.13a). The best line fitted through the data shows, however, a significant amount of scatter (± 20 %). When the data are plotted for $G/L \geq 1.5$ only, in Fig. 4.13b, the data collapse on a single line with much little scatter (± 10 %). This can be explained by the fact that data for G/L = 1.0 correspond to an inertial turbulent flow regime where the eddy scale is smaller than the bubble size and, hence, do not fit in with data

for G/L > 1.5 which correspond to a viscous turbulent flow regime where the eddies are larger than the bubble size. It is interesting to note that if the results for MF2, MF4 and MF5 at G/L = 1.5, with the same surfactant concentration but a lower XG concentration, are plotted separately (Fig. 4.13c), the data collapse on a single line with little scatter (± 5 %). Indrawati and Narsimhan (2008) reported similar observations using a mechanically agitated vessel to generate their foam, but this result is hard to explain (Indrawati and Narsimhan, 2008).

Overall, these findings show that a general (approximately) unified curve can be obtained with such complex systems which, when produced for one fluid formulation, could be used to interpret data of foams in different non-Newtonian media. This result should simplify the prediction of foam texture.

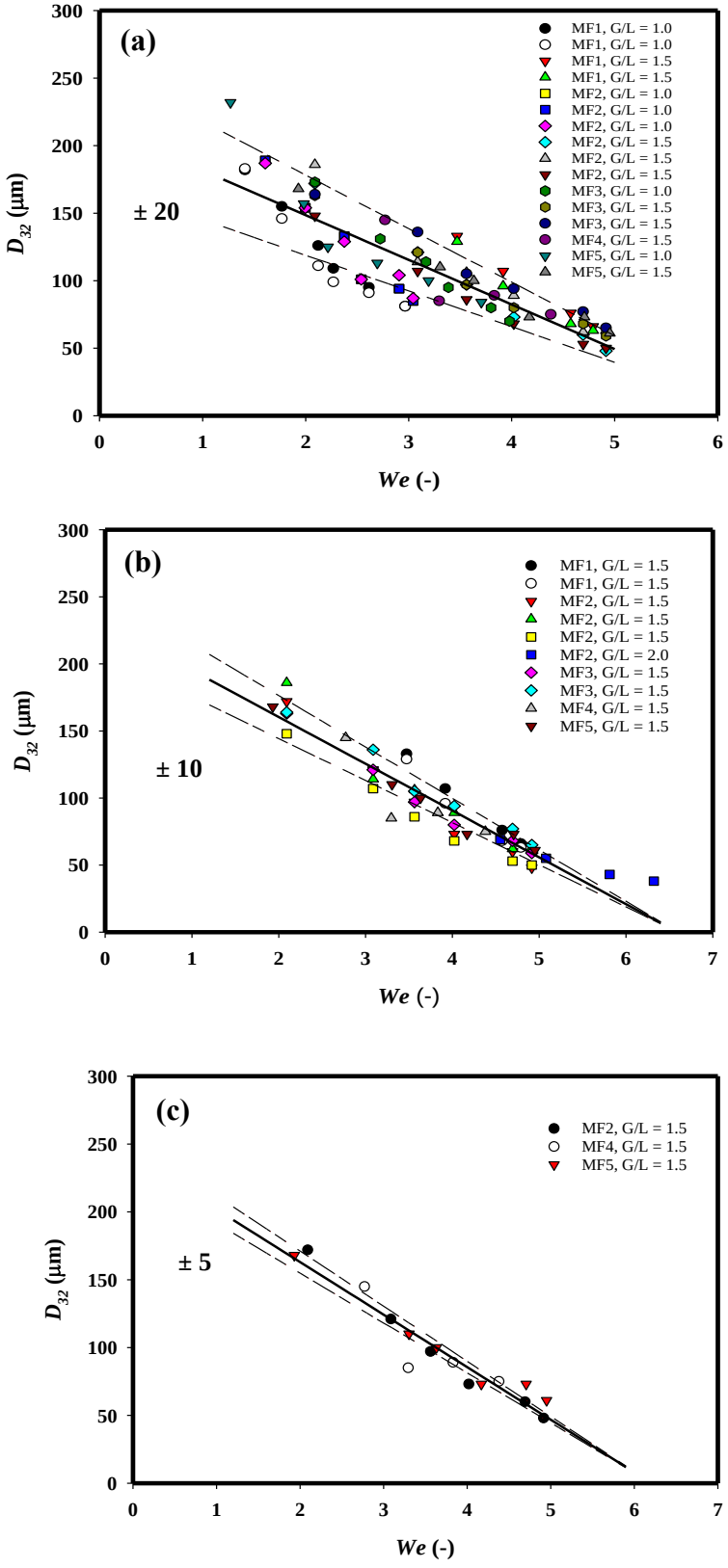

Fig. 4.13: Variation D_{32} as a function of *We* for: (a) MF1 – MF5 at G/L = 1.0 – 2.0; (b) MF1 – MF5 at G/L = 1.5, 2.0; (c) MF2, MF4 and MF5 at G/L = 1.5.

4.3.5.2 Effects of energy input on foam microstructure

The energy input during the production of foam using a continuous rotor-stator is an important parameter for process design and optimisation (Wu *et al.*, 2014). For a given fluid formulation and a fixed rotor-stator geometry, energy dissipation inside the mixing-head chamber can be controlled by either changing the rotational speed or the G/L ratio (Müller-Fischer,Suppiger and Windhab, 2007b). The rotor speed affects the shear stresses acting within the mixing-head chamber, whereas G/L ratio controls the residence time (τ), and both parameters impact the bubble size distribution and, hence, the microstructure of the foam. Thus, the effects of N and G/L on gas volume fraction and bubble size distribution were investigated.

Typical variations of the net volumetric energy input (E_v) with N and G/L ratio are depicted in Fig. 4.14 for foams produced from fluid MF2. As expected, for a given G/L ratio, E_v increases as a function of N. The increase in E with an increase in N is not linear but exponential since the power input is proportional to the cubed power (see Eq. 4.8). Similarly, E also increases with an increase in G/L ratio since the air volume fraction and hence the apparent viscosity of the dispersion increases inside the mixing-head chamber. Conversely, for a fixed liquid flowrate, E decreases as gas flowrate increases since the residence time decreases (see Eq. 4.16 & 4.17). In addition, it is possible that with an increase in G/L ratio, the size of the undispersed gas zone at the inlet of the mixing-head chamber increases and hence the value of E decreases as stated for conventional mechanical agitators (Nagata, 1975). Also, it is to be noted that there is the possibility that additional forces exist inside the mixing-head chamber which are not taken into account such as foam compressibility and elasticity. This is likely to contribute to power input.

In summary, the determination of energy dissipation rate inside the multi-stage rotor-stator device is pertinent for process optimisation and scale-up. Indeed, it is difficult to determine experimentally and theoretically the exact amount of energy consumption rate especially for complex shear-thinning fluids such as wet foams generated in this thesis. More experimental work is required to elucidate the exact mechanism and forces responsible for the energy dissipation rate inside the multi-stage rotor-stator device.

Bubble size, on the other hand, follows an exponential decay as more energy is dissipated inside the mixing-head chamber (Fig. 4.15). As previously pointed out, increasing the G/L ratio increases the apparent viscosity of the dispersion which enhances the shear forces inside the mixing-head chamber to break down larger air bubbles into smaller bubbles. Thus, for a given amount of energy dissipation, a higher G/L ratio leads to a smaller bubble size. Hence, for a given E_v, a higher G/L ratio results in a higher gas fraction and a smaller bubble size, i.e. a richer foam with a finer texture.

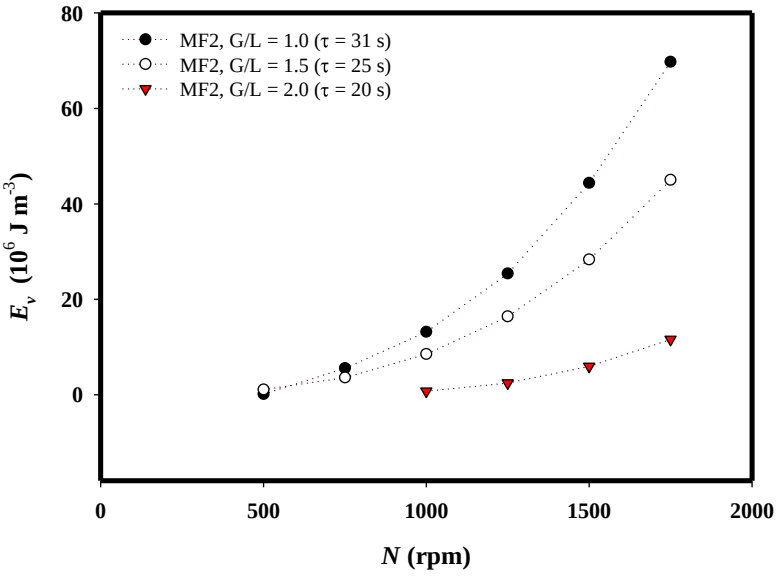

Fig. 4.14: Effects of rotor speed and G/L ratio on net volumetric energy input.

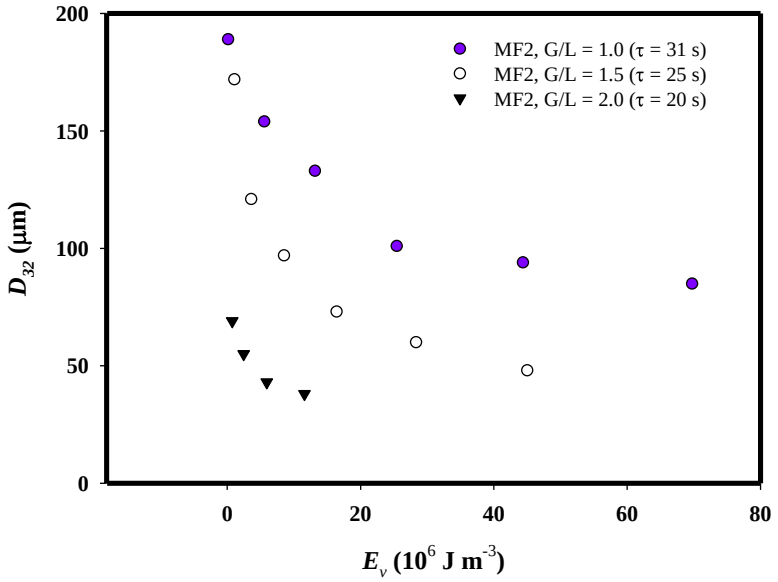

Fig. 4.15: Typical variation of D_{32} as a function of E_v..

4.3.6 Foam static stability

4.3.6.1 Foam gravity drainage and collapse

4.3.6.1.1 Effects of air volume fraction

Foam static stability is governed by the combined effects of gravity drainage, collapse and coarsening. Foam drainage and collapse were measured over a long period of time (up to ~ 600 hr) by monitoring foam samples collected at the outlet of the rotor-stator device and stored in a controlled environment of 50°C. Typical foam drainage and collapse profiles are shown in Fig. 4.16a and Fig. 4.16b for MF2 at N = 1000 rpm and G/L = 0.5, 0.6, 0.8, 1.0, 1.5 and 2.0 corresponding to ϕ_e = 0.33, 0.38, 0.48, 0.52, 0.62 and 0.67. In general, both drainage and collapse are very slow indicating that the foams are very stable.

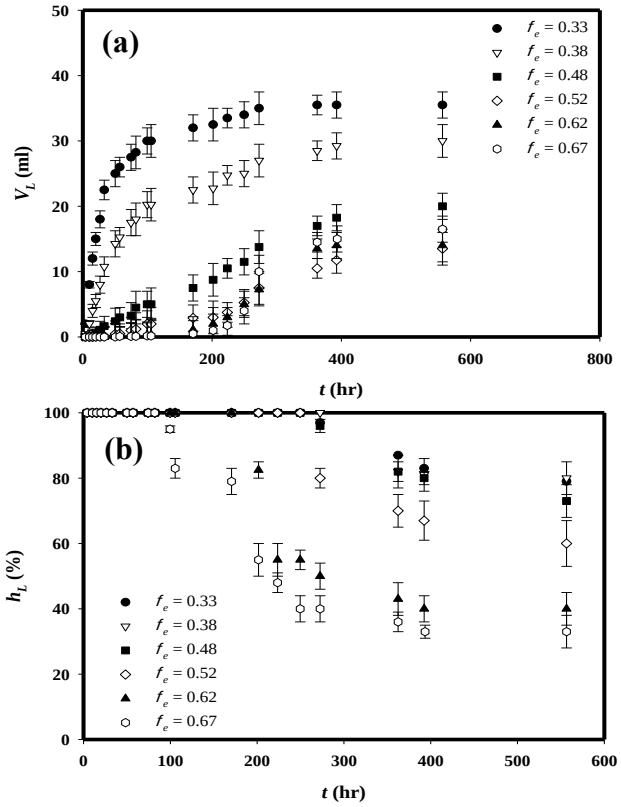

Fig. 4.16: Fluid MF2, N = 1000 rpm, G/L = 0.5 – 2.0 ($0.33 \leq \phi \leq 0.67$) and T = 50°C: (a) foam drainage transient; and (b) foam decay.

For the very wet foams generated at ϕ_e = 0.33, 0.38 and 0.48 gravity drainage were the predominant mechanism as shown in Fig. 4.16 and foam collapse was only observed after ~ 250 hr of storage time. This was also confirmed during coarsening study carried out using X-ray micro-CT technique as will be discussed below. In contrast, for foams generated at ϕ_e = 0.62 and 0.67, there is very little drainage until ~ 200 hours storage time was reached after which there is a rapid increase as shown in Fig. 4.16a. This is possibly due to the rapid foam collapse causing an increase in the rate of drainage as shown in Fig. 4.16b. At this time frame, the rate of foam coarsening and hence collapse is the predominant mechanism. This can also be confirmed by looking at the interior of the foams from the coarsening study carried out using X-ray micro-CT (see below). Furthermore, increasing the G/L ratio, as discussed above, increases the air

volume fraction which reduces the liquid contained within the foam (Plateau borders and lamellae) and the foam stability is enhanced. For example, at G/L = 1.5 and 2.0, the rate of drainage is slowed down by an order of magnitude and no foam collapse is observed within 200 hr of storage time.

4.3.6.1.2 Effects of rotor speed

Foams produced at higher rotor speeds (N) exhibit slower drainage. Increasing N leads to a significant reduction in bubble size and a narrower bubble size distribution (as previously discussed). This results in an increase in foam stability due to the higher liquid flow resistance through the thinner lamellae and Plateau borders network (Nicorescu *et al.*, 2010). Typical results for fluid MF2 at G/L = 1.0, T = 50°C, and N = 500, 1000 and 1750 rpm are shown in Fig. 4.17.

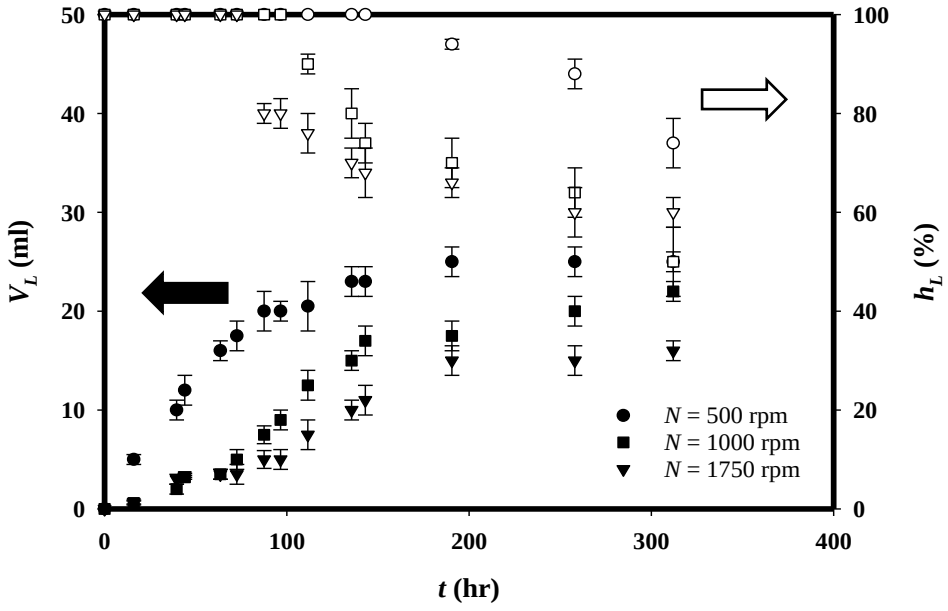

Fig. 4.17: Transient foam drainage and collapse for fluid MF2, G/L = 1.0 (ϕ_e = 0.52), N = 500, 1000 and 1750 rpm and T = 50°C.

4.3.6.1.3 Effects of storage temperature

The effects of storage temperature on foam liquid drainage and collapse were also investigated and the results are shown in Fig. 4.18. Foam liquid drainage was significantly increased as the storage temperature was increased in the range of 5-50 °C. Since temperature has very little effect on the rheology of XG, it is postulated that temperature affects the viscosity of the sucrose solution and may also affect confirmation of PGE 55 vesicles. Patino, Dolores Naranjo Delgado and Linares Ferna (1995) found that protein foam stability was independent of temperature in the range of 2-20°C (Rodríguez Patino,Dolores Naranjo Delgado and Linares Fernández, 1995), but this was not the case for wet foams generated in this study. In addition, foam collapse and hence coarsening were found to be much greater at a higher storage temperature. This is because the rate of liquid drainage is greater causing a faster thinning of the film separating the neighbouring bubbles. This allows easier diffusion of gas and a higher probability of bubble coalescence.

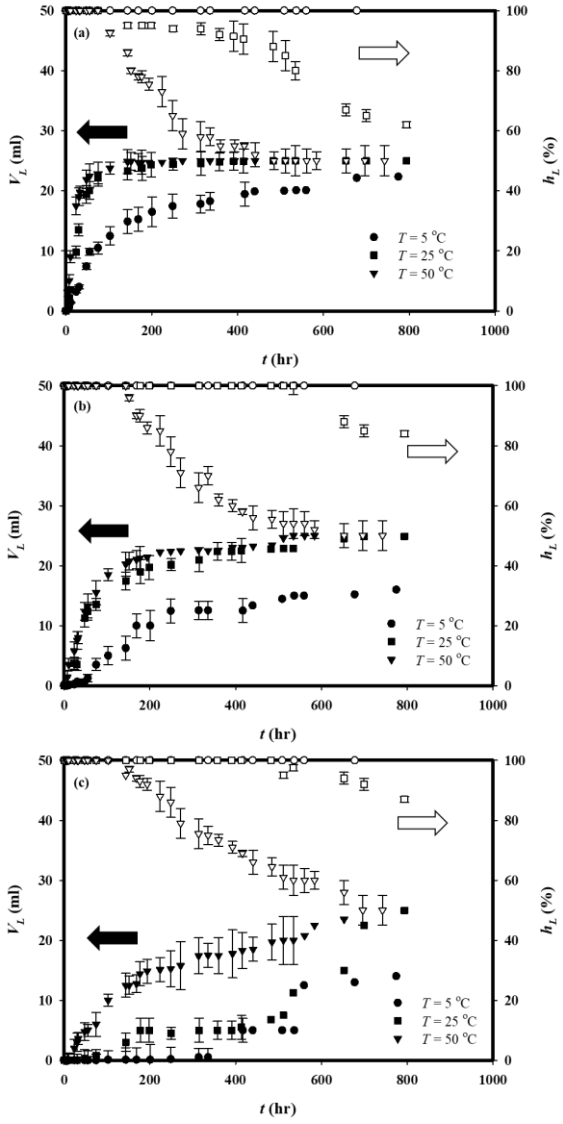

Fig. 4.18: Transient foam drainage and collapse for fluid MF5, G/L = 1.0 (ϕ_e = 0.52) and T = 5°C, 25°C and 50°C: (a) N = 500 rpm; (b) N = 1000 rpm; and (c) N = 1750 rpm.

4.3.6.1.4 Effects of PGE 55 concentration

It is known that PGE 55 can form multilamellar vesicles in the liquid which can significantly hinder liquid drainage by obstructing the Plateau borders (Curschellas *et al.*, 2013, Curschellas *et al.*, 2012b-b, Curschellas *et al.*, 2012a). Therefore, higher PGE 55 concentrations improve foam stability. Typical results for fluid MF1 (0.2 wt% PGE 55) and MF2 (0.5 wt% PGE 55) at G/L = 1.0 and N = 500, 1000 and 1750 rpm respectively are shown in Fig. 4.19. MF3 was not

investigated since it was difficult to judge and record the liquid drainage rate since the liquid was very opaque.

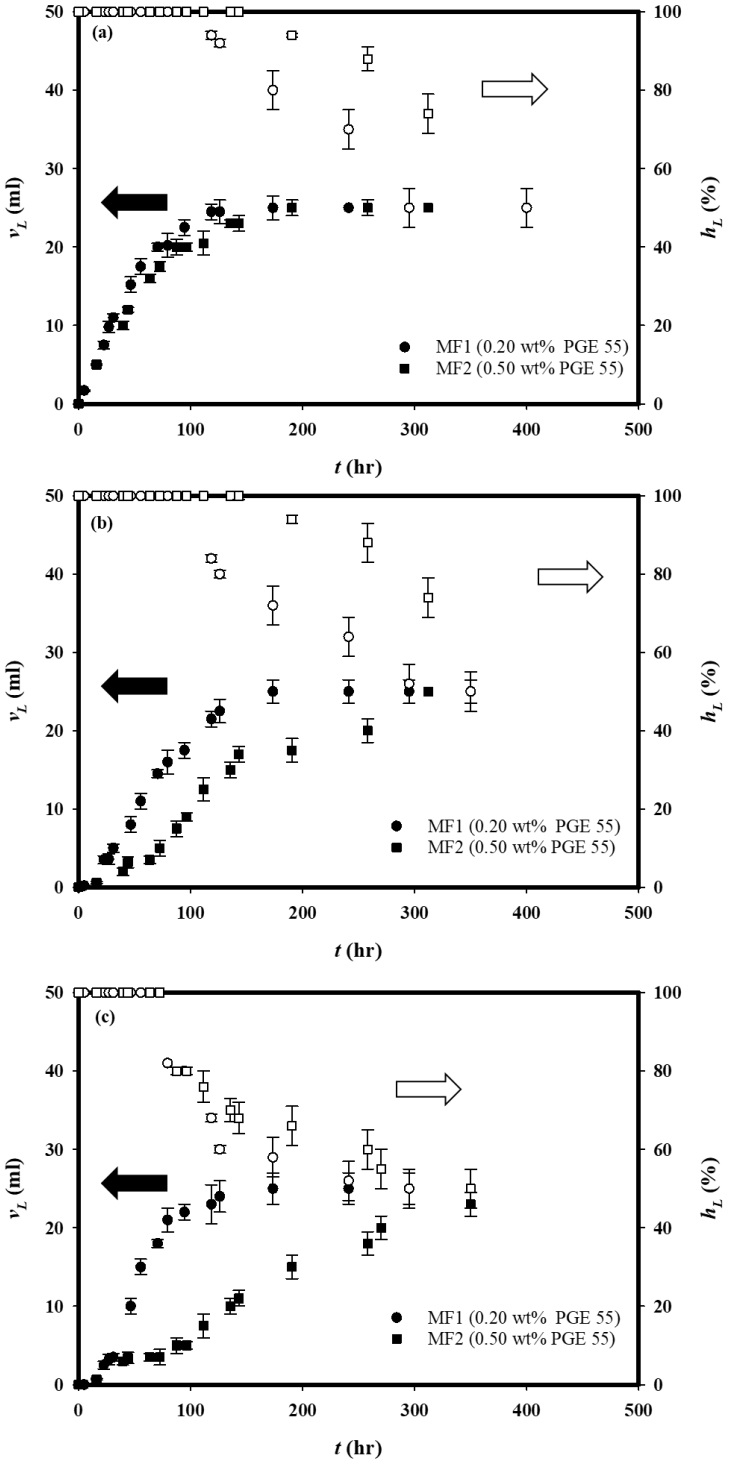

Fig. 4.19: Transient foam drainage and collapse for fluid MF1 and MF2, G/L = 1.0 (ϕ_e = 0.52) and T = 50°C: (a) N = 500 rpm; (b) N = 1000 rpm; and (c) N = 1750 rpm.

At all rotor speeds, fluid MF2 containing a higher PGE 55 concentration are more stable against gravity drainage and collapse and the effects become greater as *N* increases. A possible reason for this might be due to the much thinner films which are more likely to get clogged by the higher concentration of PGE multilamellar vesicles.

4.3.6.1.5 Effects of xanthan gum concentration

The use of XG imparts non-Newtonian characteristics to the continuous phase including a high zero-shear Newtonian viscosity (Fig. 4.12; sometimes confused in the literature with the existence of a yield stress) which counters gravitational drainage and gives high stability to the foam. Typical results for fluid MF4 (0.25 wt% XG), MF5 (0.35 wt% XG) and MF2 (0.5 wt% XG) at G/L = 1.0 and *N* = 500, 1000 and 1750 rpm respectively are depicted in Fig. 4.20. As shown, foam drainage curve can be divided into three distinct regions. First, there is a fast drainage rate due to the high liquid content of the wet foam and it is much greater for samples containing a lower XG content – as expected. In the second part of the curve, the rate of drainage is slower as the samples are depleted of the liquid content and the bubbles are much closer to each other. Finally, a plateau region is reached at which point all the samples are drained of the liquid and the dry foam is much more prone to coarsening and hence collapse. In contrast, foam collapse rate followed the opposite trend since samples containing a higher XG content had smaller bubbles possessing thinner film leading to a much faster coarsening and hence collapse rate.

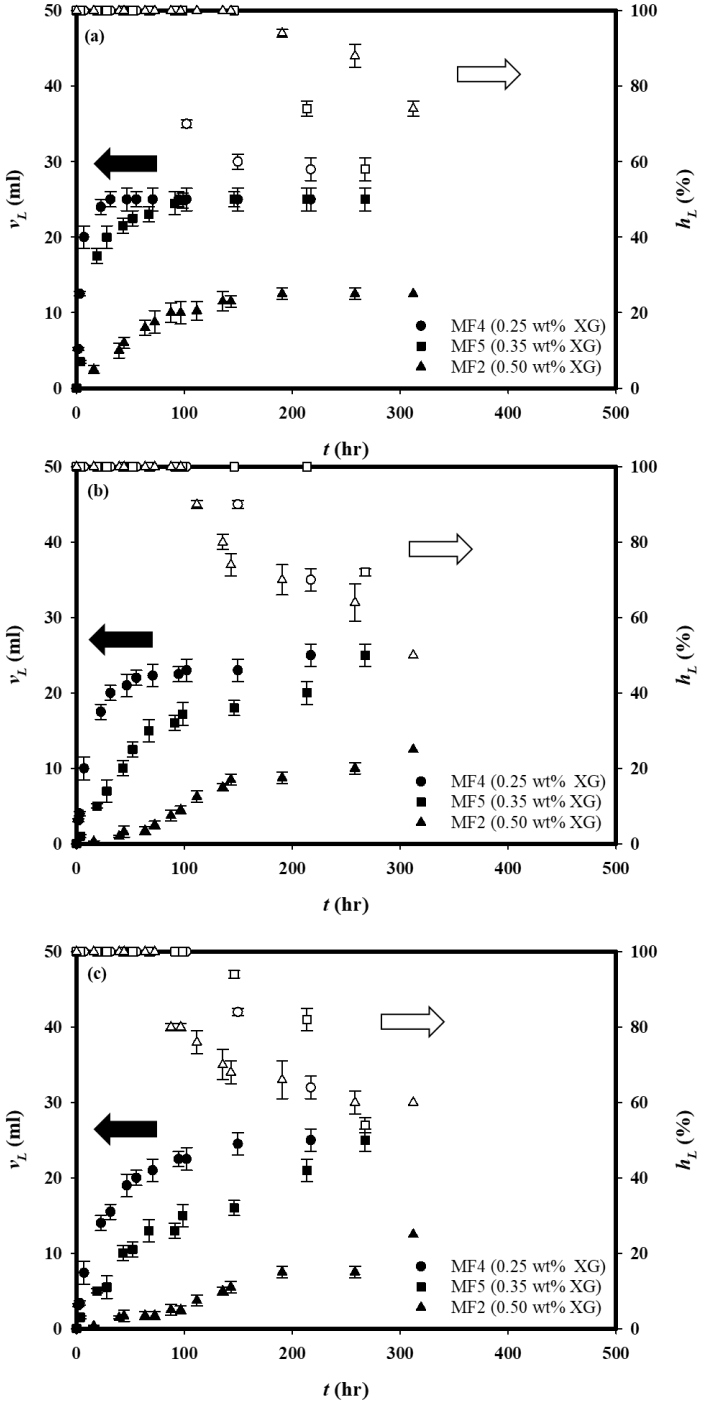

Fig. 4.20: Transient foam drainage and collapse for fluid MF4, MF5 and MF2, G/L = 1.0 (ϕ_e = 0.52) and T = 50°C: (a) N = 500 rpm; (b) N = 1000 rpm; and (c) N = 1750 rpm

4.3.6.2 Foam coarsening

Foam coarsening was assessed over several weeks via X-ray micro-CT using similar foam samples described above. Typical foam coarsening behaviour for foams generated from fluid MF2 at G/L = 1.5 and N = 500, 1000 and 1750 rpm is shown in Fig. 4.21. The use of the non-ionic surfactant PGE 55 provided excellent resistance to bubble coarsening as its multilamellar vesicles irreversibly adsorb at air-water interfaces (Curschellas *et al.*, 2013). Foam coarsening was found to be generally slow especially when foams were freshly generated.

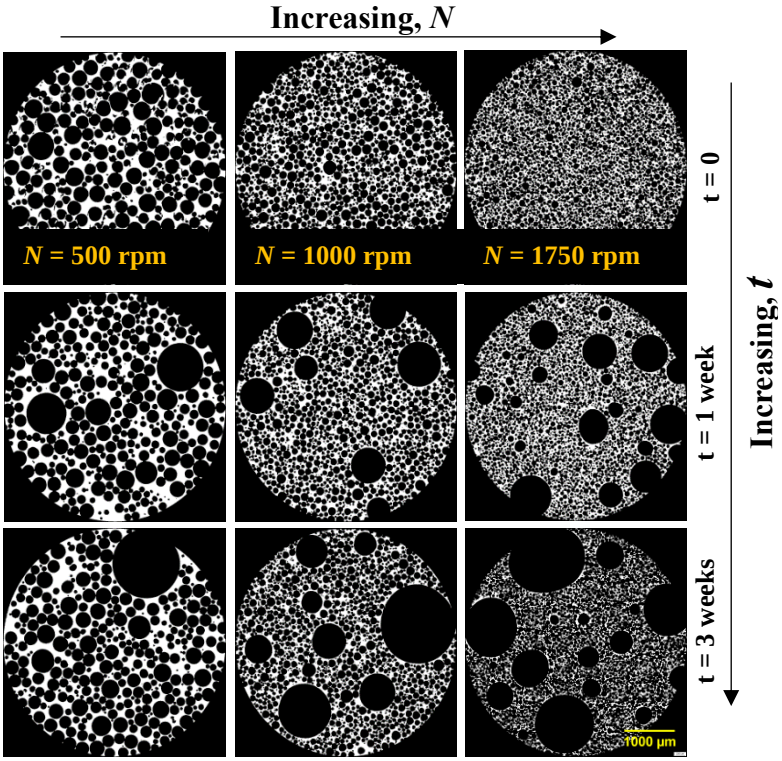

Fig. 4.21: Typical foam coarsening behaviour observed using X-ray micro-CT images of MF2 foams at G/L = 1.5 (ϕ_e = 0.62).

Foams generated at higher rotor speeds had finer bubbles (i.e. faster air diffusion and disproportionation) and thinner foam lamellae which led to faster foam coarsening. This is because smaller bubbles possess a higher Laplace pressure and therefore the rate of air diffusion

is much greater in comparison to larger bubbles. As the bubbles become smaller, the Laplace pressure inside them increases which in turn increases the gas (i.e. air) solubility in the continuous phase. This process continues until the smaller bubbles completely disappears (Ellis and Lazidis, 2018). Similarly, whilst high G/L ratios lead to slower drainage and collapse, they undergo faster coarsening due to their thinner lamellae separating the neighbouring bubbles as shown in Fig. 4.22. It is also known that PGE 55 can irreversibly adsorb to an air-water interface and hence provide steric stabilisation against bubble coalescence (Duerr-Auster *et al.*, 2009). Note also that the rate of coarsening does not just leads to the disappearing of smaller bubbles, but it also has a significant influence on the rate of liquid drainage and coalescence.

To assess the foam coarsening rate further, foam samples were generated from fluid MF2 at N = 1000 rpm and G/L = 1.5 and 2.0. The corresponding foam coarsening images obtained from X-ray micro-CT and the evolution of the BSD and hence D_{32} is depicted in Fig. 4.22a and Fig. 4.22b respectively. The rate of liquid drainage for these foams was found to be very low (as shown in the previous section) due to the high zero-shear viscosity imparted by the XG solution. However, as expected, the rate of coarsening was found to be a function of time and G/L ratio. Increasing the G/L ratio led to smaller bubbles (possessing higher Laplace pressure) and a more packed bubbles matrix. The former increases the rate of air diffusion due to higher gas solubility and the later decreases the diffusion length. Moreover, for these wet foams, the rate of coarsening was predominant in contrast to liquid drainage. Generally, for dry foams, the rate of coarsening is found to follow xx law. The foams assessed in this study did not satisfy this law possibly due to the combined influence of liquid drainage and bubble coalescence.

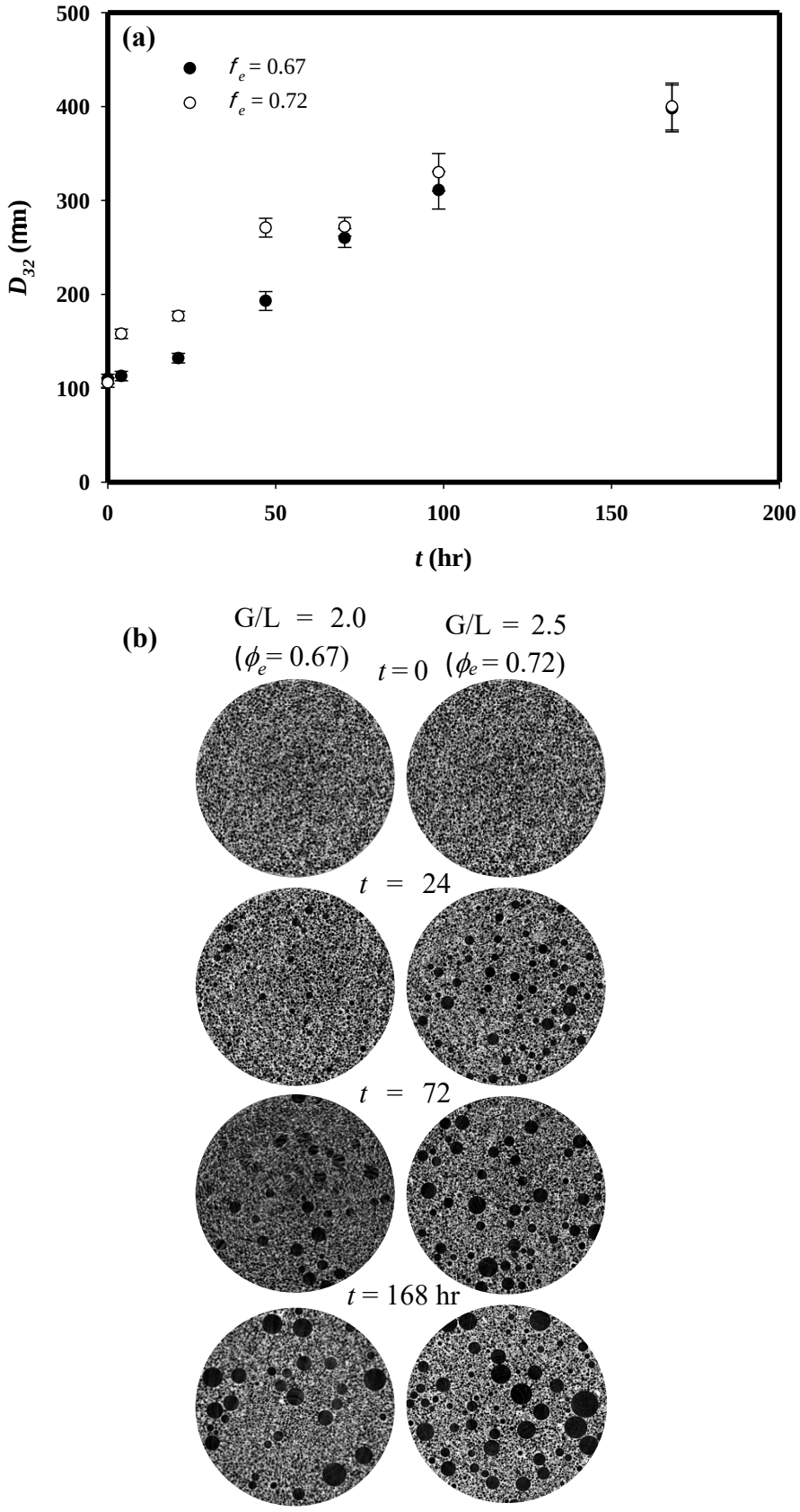

Fig. 4.22: Coarsening for foam generated from fluid MF2 at room temperature: (a) evolution of bubble size (D_{32}); and (b) corresponding foam images.

4.4 Conclusion

This study focused on the production of foams from viscous shear-thinning liquids using a pilot-scale continuous multi rotor-stator device operating at atmospheric pressure. The effects of process parameters (rotor speed, G/L ratio) and liquid formulation (surfactant concentration, xanthan gum concentration) on foam gas volume fraction and bubble size distribution were studied. Rotor speed and G/L ratio were the dominant factors in determining the gas volume fraction and bubble size distribution. Higher rotor speed (N >1000 rpm) which implies higher energy input, led to finer texture foams.

Energy consumption is a pertinent parameter for process optimisation and scale-up. Determining the exact power consumption is indeed difficult for multi-stage rotor-stator device and for complex shear-thinning fluids such as wet foams investigated in this thesis. However, a theoretical correlation developed by Krozen and Wassink (1988) was utilised to estimate the power consumption. The shear rate was estimated based on the tip speed of the rotor and for the majority of experimental conditions investigated turbulent flow regime was found. Higher energy input is undesirable both in terms of energy efficiency and in terms of product microstructure. Operating at N > 2000 rpm, the local temperature rise inside the small gap of the rotor-stator device can approach that of the chain-melting temperature of the bubble monolayer leading to increased hydrocarbon chain mobility and hence to bubble coalescence. As a result, an equilibrium seems to be reached between bubble breakage and coalescence.

Increasing the G/L ratio led to a reduction in average residence time but, counter-intuitively, reduced foam bubble size and polydispersity. This was attributed to an increase in the apparent viscosity of the dispersion which in turn enhances the shear forces inside the mixing-head

chamber to break down larger air bubbles into smaller bubbles. Hence, for a given energy input, a higher G/L ratio in turbulent results in a higher gas fraction and a smaller bubble size, i.e. a richer foam with a finer texture.

A detailed foam drainage, collapse and coarsening study was also conducted. Generally speaking, foams generated from a commercially available non-ionic surfactant (PGE 55), in a viscous xanthan gum and sucrose solution, possesses excellent static stability, i.e. half-life consisting of several weeks. Both the processing conditions (rotor speed and G/L ratio) and the bulk liquid properties (PGE 55 and XG concentration) had a strong influence on the rate of liquid drainage, foam collapse and coarsening. For the very wet foams (G/L $\leq$ 1.0) and for foams generated at lower rotor speed ($N \leq$ 1000 rpm), the rate of liquid drainage was predominant and foam coarsening only took place after a prolong storage time. The presence of XG in the bulk liquid and the multilamellar vesicles of PGE 55 in the Plateau borders significantly reduces the rate of liquid drainage. In addition, increasing the XG and PGE 55 concentration led to improved static stability. The former imparts high zero-shear viscosity to the bulk fluid which can resist drainage due to gravity. The latter is able to impart strong viscoelastic interfacial layer which can resist bubble coalescence and coarsening. Moreover, foam liquid drainage and collapse was significantly enhanced when stored at low temperature (5 °C) In contrast, foams generated at a higher gas/liquid volumetric flowrate ratio (G/L $\geq$ 1.5) and at a higher rotor speed ($N \geq$ 1000 rpm) were more stable against liquid drainage, but were more susceptible to foam coarsening. The combined influence of higher internal Laplace pressure associated with smaller air bubbles, gas solubility and a more packed bubbles matrix were the main drivers for increasing the rate of foam coarsening.

Notation

D	rotor diameter (m)
d	bubble diameter (m)
D_{32}	sauter mean diameter (m)
E_V	specific energy per m^3 of foam processed (J m^{-3})
f	correlation factor (-)
F	relative bubble volume frequency (%)
h	number of rotor-stator pairs (-)
h_f	foam collapse (m)
I	number of pins on rotor (-)
k	consistency index (Pa $s^{n'}$)
L	diameter of annulus mixing space (m)
N	rotational speed (s^{-1})
n	flow behaviour index (-)
n_i	number of bubble with diameter i (-)
o	width of rotor pin (m)
$P_{v,diss}$	net volumetric power input (J s^{-1} m^{-3})
P_0	Power number (-)
P^*_0	generalised Power number (-)
q	height of rotor/stator pin (m)
Q_L	liquid volumetric flowrate (m^3 s^{-1})
Q_G	gas volumetric flowrate (m^3 s^{-1})
Re	Reynolds number (-)
Re^*	generalised Reynolds number (-)
s	distance between rotor-stator (m)
V	volume of mixing-head chamber (m^3)
v_L	liquid drained (m^3)
We	Weber number (-)
$z = \frac{\pi D}{I}$	distance between rotor pins (m)

Abbreviations

BSD	bubble size distribution
G/L	ratio of air and liquid volumetric flowrate
MF1	model fluid 1
MF2	model fluid 2
MF3	model fluid 3
MF4	model fluid 4
MF5	model fluid 5
PGE 55	polyglycerol ester of fatty acid
XG	Xanthan gum
X-ray micro-CT	X-ray micro-Computed Tomography

Greek symbols

τ	average residence time (s)
η	apparent viscosity (Pa.s)
ρ	density (kg m^{-3})
σ	surface tension (N m^{-1})
ϕ	air volume fraction (-)
ϕ_e	experimental air volume fraction (-)
ϕ_{th}	theoretical air volume fraction (-)
$\dot{\gamma}$	shear rate (s^{-1})

Chapter 5: Dynamic interactions of foamed viscous shear-thinning fluids with an orifice flow constriction

Foam flow through processing equipment tends to affect the structure of the foam and its properties. In the design of a food foam formulation and its flow system, it is therefore important to consider the possible effects on the end-of-pipe structure and, hence, quality attributes of the foam. These effects may have serious practical implications and must be carefully considered as preservation of product structure and quality is important. This study examines the flow of wet foams, generated in a continuous multi rotor-stator device using complex formulations of viscous non-Newtonian fluids, through a straight pipe with and without the presence of a narrow orifice plate. The effects of fluid formulation, gas-liquid ratio, rotor speed and orifice aperture size, are investigated. The original foams exhibit a fine texture and a long shelf life which remain unaffected during flow in a short straight pipe with no significant pressure drop. At low pressure drops, foams are able to squeeze through a narrow orifice constriction without incurring significant structural transformations. At higher pressure drops, flow through the constriction causes significant bubble coalescence and, in some cases, loss of air volume leading to much coarser and much less stable foam. Increased surfactant content, liquid viscosity and rotor speed reduce bubble coalescence and help preserve foam structure during dynamic interaction with a flow constriction.

Keywords: foam flow; flow constriction; pressure drop; wet foam; non-Newtonian liquid.

Chapter submitted to Food Engineering Journal: Jabarkhyl, S., Barigou, M., Zhu, S., (2020). Dynamic interactions of foamed viscous shear-thinning fluids with an orifice flow constriction

5.1 Introduction

Foams are complex multi-component structures which enjoy many applications in a wide range of industries including in food, pharmaceuticals, mineral transport, oil and gas. Dry foams are structured two-phase fluids in which polyhedral gas bubbles are separated by interconnecting thin liquid films and Plateau borders which denote the regions of intersection of the thin films, whilst wet foams including food foams tend to be bubbly liquids with spherical bubbles. Foams represent an important class of structured fluids possessing a complex rheology and flow behaviour strongly dependent upon local structure and chemical composition. The nature of the foam, i.e. its texture and stability, and its overall rheological and flow properties can determine both the economic and technical successes of the industrial process concerned. For example, some aerated products possessing a smaller bubble size and a uniform bubble size distribution have a much longer shelf life and better consumer perception because of their better creaminess (Müller-Fischer,Suppiger and Windhab, 2007b, Müller-Fischer and Windhab, 2005). Information on both the static as well as dynamic behaviour of foams is of direct value to the manufacture of a wide range of foods. Foam flow through processing equipment usually affects the structure of the foam and its properties. In the design of a food foam formulation and its flow system, it is therefore important to consider the possible effects on the end-of-pipe structure and, hence, quality attributes of the foam. These effects may have serious practical implications and have to be carefully considered as preservation of product structure and quality during processing is important.

Effective stabilisation of a food foam is critical since bubble coalescence can lead to loss of microstructure and hence its organoleptic properties such as texture and taste. Food foams are often stabilised with protein molecules (β-lactoglobulin, casein, albumin and whey protein

isolate) commonly derived from milk and egg (Zayas, 1997). Protein molecules drastically alter the interfacial rheological properties providing a strong mechanical barrier against bubble coalescence (Murray *et al.*, 2006). More recently, however, non-ionic surfactants such as polyglycerol fatty acid ester, PGE 55, hydrophobins and food-grade particles (agar gel particles) have attracted enormous attention (Curschellas *et al.*, 2013, Cox,Aldred and Russell, 2009, Ellis *et al.*, 2017, Dickinson, 2010), as they have been shown to have excellent foam stabilisation properties (Duerr-Auster *et al.*, 2007, Duerr-Auster *et al.*, 2008, Curschellas *et al.*, 2013b). The irreversible adsorption of PGE 55, once exposed to heat above its Kraft temperature (58℃), can significantly reduce the rate of coalescence. In addition, the presence of multilamellar vesicles, formed as a result of its very low critical aggregation concentration (cac), in films and Plateau borders greatly improves stabilisation against drainage (Curschellas *et al.*, 2013). Likewise, the addition of food hydrocolloids such as guar gum, xanthan gum and low-molecular weight viscosity-enhancing sucrose can drastically reduce foam drainage. Inclusion of hydrocolloids tends to also improve foam texture and smoothness in products such as ice cream (Murray *et al.*, 2006). In the case of proteins, inclusion of these viscosity modifying ingredients may lead to synergistic interaction, however, but this is not the case with PGE 55.

Any process where significant deformation of the air-water interface is likely to occur may lead to bubble coalescence. Such processes include the flow of aerated products through nozzles, pipes, pipe fittings and pumps. In addition, in the food industry, aeration is predominantly performed under pressurised conditions (typically, 2 – 3 bar) to decrease the effective air volume fraction inside the mixing-head chamber of the foam generator and, hence, reduces the probability of bubble collision and recoalescence during foam generation. However, once the foam is discharged to atmosphere, such an operation leads to two undesirable side effects

downstream: (i) the bubbles expand as a result of the pressure drop and are more likely to collide with each other, hence, increasing the rate of recoalescence; (ii) an over-beating phenomenon can take place as a result of increased residence time because of the reduced gas flowrate inside the mixing-head chamber.

Operations involving rapid pressure drop (e.g. flow from a nozzle), steady and elongation shear (e.g. flow through a pipe) can lead to a severe loss of foam attributes. Much of the current understanding of these effects stems from the engineering literature. Calvert (1987; 1988) was the first to examine the effects of geometric constrictions (commercial diaphragm, global and ball valves) on firefighting foams. It was found that a flow constriction (global valve) with an intricate flow path (high shear rates) and a high residence time led to a complete loss of foam microstructure in contrast to a diaphragm or ball valve. Deshpande and Barigou (2000; 2001ab) examined the flow of dry and wet detergent-stabilised foams in straight pipes fitted with a variety of flow constrictions (expansion, contraction, orifice plate, perforated plate, bend, elbow). They found that foam flow through pipe fittings is characterised by complex phenomena which influence foam structure, liquid holdup and flow regime. In general, the liquid holdup decreases substantially downstream of a fitting, which results in intense recirculation flow patterns upstream and a much drier foam downstream. A sudden expansion can lead to a complete breakdown of the foam. Thus, pipe fittings can have serious effects on the end-of-pipe structure of a foam, hence, resulting in important practical implications for the preservation of product structure. However, little is known about the flow behaviour of food foams which have a more complex composition and, thus, a more complex rheology.

Dickinson *et al*., (2002) and Murray *et al*., (2006) developed an apparatus for the direct visualisation of foam microstructure under rapid pressure drop. One major finding from their study was that foam made from gelatine was less likely to undergo coalescence when exposed to rapid pressure drop (Dickinson *et al.*, 2002, Murray *et al.*, 2006). Similarly, Heuer et al. (2007) reported the effects observed on the microstructure of a model food foam, using a Linkam pressure cell to pressurise the foam to different levels from atmospheric pressure up to 11 bar and then releasing the pressure at varying rates. The setup was also used to study the effects of disproportionation and single and multiple pressure cycles on the resultant foam. Significant pressure drops were quite destructive, with most coalescence seen at 2 bar pressure down to 1 bar absolute. Surprisingly, however, no coalescence was observed from 11 bar, the starting pressure, down to 2 bar absolute. Startling effects were seen when the pressure release rates were varied. Slow pressure release rates (2 min per bar released) had the effect of causing increased coalescence events, when compared to very quick release rates (Heuer *et al.*, 2007). Other studies on continuous foaming of Newtonian and non-Newtonian model liquid food formulations using a rotor-stator device all agree on the fact that an increase in rotor speed leads to a significant reduction in bubble size (Müller-Fischer,Suppiger and Windhab, 2007b, Mary *et al.*, 2013, Jabarkhyl *et al.*, 2019). However, there are conflicting reports on the effects of static pressure and residence time which hitherto remain unclear and hence need further investigation (Balerin *et al.*, 2007, Mary *et al.*, 2013).

In Chapter 4, the continuous foaming of viscous non-Newtonian shear-thinning model food liquids in a pilot-scale multi rotor-stator high-shear device was investigated (Jabarkhyl *et al*., 2019), and the effects of processing parameters including rotor speed, gas-liquid ratio, surfactant and xanthan gum concentration. Furthermore, in chapter 6, a detailed study of steady-

shear as well as viscoelastic rheological properties of the various wet foams thus generated is examined (Jabarkhyl *et al.,* 2020). As will be shown, the foams exhibited high static stability and resistance to steady shear with no bubble breakage observed when the foams were sheared between parallel-plates on a rheometer. In the present chapter, the flow of these wet model food foams and their dynamic stability as they flow through a straight pipe and interact with a narrow orifice plate is conducted. Narrow orifices are used to generate significant pressure drops on a lab scale which would mimic the flow of such foams through nozzles and pipe fittings in industrial setups. The effects of fluid formulation, gas-liquid ratio, rotor speed and orifice aperture size, are investigated.

5.2 Materials and methods

5.2.1 Model fluids and foam generation

The materials and methods used are based on our recent related work which studied the continuous production of foams from complex viscous shear-thinning fluids in a multi rotor-stator device and their rheological properties (Jabarkhyl *et al.,* 2019; Jabarkhyl *et al.,* 2020). Five model complex non-Newtonian fluid formulations of shear-thinning rheology consisting of a mixture of polyglycerol fatty acid ester (PGE 55), xanthan gum (XG), caster sugar and sodium azide, denoted MF1, MF2, MF3, MF4 and MF5 whose composition and physical properties are summarised in Table 5.1.

Foams were generated by aerating the model fluids in a pilot-scale continuous multi rotor-stator unit (Megatron FM 12 – 50/2 HR) depicted in Fig. 5.1. The geometrical dimensions of the 12 rotor-stator pairs positioned in series inside the foam generator are provided in Table 5.2. A

Julabo F-25 cooling system enabled the foam temperature at the outlet of the foaming unit to be kept approximately equal to the inlet feed temperature (25 °C). Foams of different textures were obtained by using combinations of liquid and air flowrates within the range 2.5 – 5.0 L $h^{-1}$and 0.1 – 12.5 L hr^{-1} respectively. Further details of the protocols adopted for the preparation of the model fluids and foams can be found in Chapter 4. As previously found, the density of all the fluids was 1080 kg m^{-3} and the equilibrium surface tension measured by a Wilhelmy plate method was 38.0 ± 2 mN m^{-1}.

Table 5.1: Model fluids composition and properties.

Model fluid	PGE 55 (wt%)	XG (wt%)	Sugar (wt%)	σ_e (mN m^{-1})	η_o (Pa.s)	η_∞ (Pa.s)	λ (s)	n (-)	R^2 (-)
MF1	0.2	0.50	25	39	80	0.007	30	0.20	0.999
MF2	0.5	0.50	25	38	100	0.007	35	0.20	0.999
MF3	1.0	0.50	25	38	135	0.007	40	0.20	0.999
MF4	0.5	0.25	25	38	9	0.007	15	0.30	0.998
MF5	0.5	0.35	25	38	35	0.007	30	0.30	0.998

Table 5.2: Geometrical dimensions of continuous rotor-stator device.

Parameter	Symbol (unit)	Value
Diameter of annulus mixing space	L (mm)	5.00
Number of pins on rotor	I (-)	13.00
Number of rotor-stator pairs	h (-)	12.00
Distance between rotor-stator	s (mm)	1.00
Height of rotor/stator pin	q (mm)	2.50
Width of rotor pin	o (mm)	4.70
Rotor diameter	D (mm)	50.00
Distance between rotor pins	z (mm)	12.08

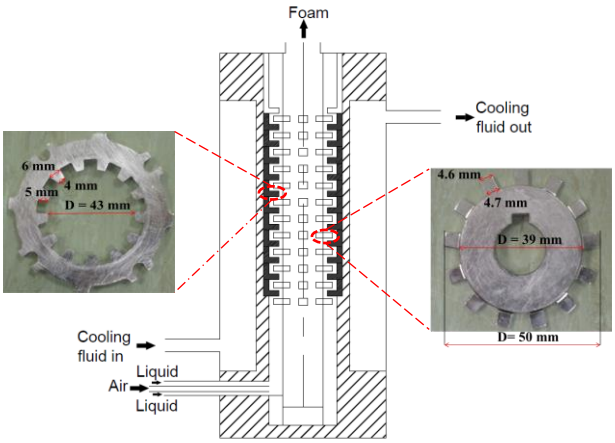

Fig. 5.1: Foam generator: (a) pilot-scale continuous rotor-stator unit; (b) schematic of mixing-head chamber; (c) stator; (d) rotor. The device consists of 12 rotor-stator pairs in series where, respectively, the rotor and stator have diameters of 50 and 52 mm each. Every rotor and stator has 13 pins (4.7 × 4.6 × 2.5 mm) with square ends and the gap between the rotor and stator is 1.0 mm.

5.2.2 Foam characterisation

5.2.2.1 Air volume fraction

The foam air fraction (ϕ_e) was experimentally determined by collecting foam samples of known volume at the outlet of the foam generator and measuring the mass of liquid within. The foaming process aims to maximise ϕ_e and achieve the maximum theoretical value, defined in terms of the pressure-dependent volumetric air flowrate and liquid volumetric flowrate Q_L, as:

$$\phi_{th}{}^{(P)} = \frac{Q_G{}^{(P)}}{Q_G{}^{(P)} + Q_L} \qquad \text{(Eq. 5.1)}$$

The ideal gas law can be used to relate $\phi_{th}{}^{(P)}$ at pressure P to an equivalent air volume fraction, $\phi_{th}{}^{(P_{atm})}$, at atmospheric pressure P_{atm}, thus:

$$T_f = \phi_{th}^{(P_{atm})} \left(\frac{P_{atm}}{P}\right) \qquad \text{(Eq. 5.2)}$$

where F_E is the foam expansion rate dependent on pressure, air and liquid flowrate in the mixing-head chamber. Another important parameter is the average residence time, τ, inside the mixing-head chamber of the foam generator (Fig. 5.1) which can be estimated using the foam volumetric flowrate (V_{foam}) and the volume of the mixing-head chamber (V = 85 mL), thus:

$$\tau = \frac{V}{V_{foam}} = \frac{V}{Q_L + Q_G^{(P)}} \qquad \text{(Eq. 5.3)}$$

where V_{foam} is the volumetric flowrate of foam and V is the volume of the mixing-head chamber (85 mL).

5.2.2.2 Measurement of bubble size distribution

Foam bubble size distribution was measured using an X-ray micro-Computed Tomography (Skyscan 1172, Bruker, Belgium) with a 5.78 μm resolution. A foam sample of about 5 ml was placed inside a plastic straw and sealed prior to scanning. The technique provides non-invasively a high-resolution 3D model of the microstructure of a stable foam, from which the bubble size distribution and various descriptive statistics are derived including the Sauter mean bubble diameter (D_{32}) defined as:

$$D_{32} = \frac{\sum n_i d_i^3}{\sum n_i d_i^2} \qquad \text{(Eq. 5.4)}$$

where n is the number of bubbles of diameter d in class size i. The bubble size distribution was plotted in the form of a histogram. Experimentally measured bubble sizes were grouped into discrete classes (bins) with identical width. For foam generated without a flow constriction, up

to 10000 bubbles were analysed. Foam generated in the presence of a flow constriction, up to 4000 smaller bubbles and up to 500 larger bubbles were analysed.

5.2.2.3 Rheological properties of model fluids and foams

The steady-shear rheology of the model fluids was characterised using a 40 mm parallel-plate geometry with a gap of 2.0 mm fitted on a controlled stress/strain rheometer (Discovery HR-2, Hybrid Rheometer, TA, USA). Using the same set-up, amplitude sweep tests with % strain varying in the range 0.01 to 1000% were conducted at 1 Hz frequency to determine the viscoelastic moduli) of the foams studied. The use of roughened plates (58 μm equivalent grit size) enabled the elimination of slip. More details on the rheometry procedures adopted can be found in Chapter 6.

5.2.2.4 Foam flow through an orifice constriction

The foam flow rig consisted of two lengths of acrylic pipe of 30 mm diameter and 0.5 m length connected by bolted flanges, as schematically represented in Fig. 5.2. Digital pressure transducers (Druck, UK) connected to a computer via a data logger (PicoLog 1000 Series), were installed along the flow pipe including at the inlet and at the exit of the constriction for pressure drop measurements. A thin stainless-steel orifice plate (1.5 mm thick) was inserted between the two flanges to act as a constriction to the foam flow. The orifice sizes investigated were: D_o = 0.4, 0.5, 0.6, 0.8 and 1.8 mm diameter corresponding, respectively, to orifice-pipe area ratios of A_o/A = 0.00020; 0.00032; 0.00046; 0.00082; 0.00413). A foam sampling point was fitted at the exit of the constriction.

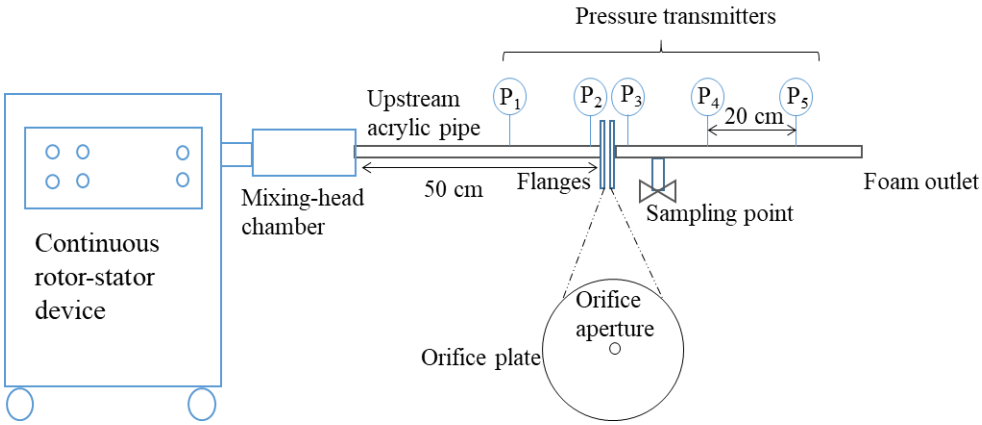

Fig. 5.2: Schematic of foam flow rig.

In a typical experiment, foam generated by the continuous rotor-stator device is fed directly into the flow pipe. Foam samples are collected at the exit of the constriction for off-line analysis using an X-ray micro-CT technique to determine the bubble size distribution. At this point, the foam pressure would have dropped to nearly atmospheric and sampling at the wall does not introduce any significant effects on the foam microstructure. Upstream of the constriction, however, the foam pressure is high and wall sampling would cause expansion of the foam. Hence, the foam is photographed in-situ at the pipe wall using a digital camera fitted onto a Leica microscope with a variable zoom lens, and the bubble size distribution determined via image analysis using ImageJ software. Typically, a sample of at least 500 bubbles is used and only bubbles in the centre of an image are analysed to avoid curvature effects. It should be pointed out, however, that imaging at the wall does not yield accurate information on the full 3D microstructure of the foam and is only used as a rough indication of the bubble size when other means of visualisation are not possible (Deshpande and Barigou, 2000, Deshpande and Barigou, 2001a, Deshpande and Barigou, 2001b). Before taking measurements, the foam is allowed to flow through the constricted pipe for up to 20 min until steady state conditions are

reached, i.e. when pressure readings and volume fraction of the foam collected at the exit of the pipe stabilise.

5.2.3 Foam static stability

Foam static stability was determined by monitoring, at a constant temperature of 50°C over a period of several weeks, liquid drainage in 50 mL samples collected at relevant points of the flow system. Thus, transients of drained liquid were obtained for all experimental conditions investigated.

5.2.4 Statistical analysis

All measurements were performed in triplicate. A one-way analysis of variance (ANOVA) was conducted using the well-known Minitab statistical software, and Tukey's pairwise comparison was performed to find statistically significant results (i.e. $p < 0.05$). Results are reported as mean values ± standard deviation in Tables 5.3 – 5.8.

5.3 Results and discussion

5.3.1 Aeration efficiency

Aeration efficiency ($\eta = \phi_e/\phi_{th}^{(P_{atm})}$) is an important feature of the foam generation process which indicates the ability to incorporate all of the available gas into the foaming liquid to make a homogeneous foam. Thus, optimum aeration is achieved when the theoretical and experimental values of volume gas fraction are equal (Eq. 5.2). At atmospheric pressure, i.e. when the foam flow rig is not connected to the rotor-stator device, maximum aeration efficiency

was achieved for all model fluids at most rotor speeds when the G/L ratio (ratio of air to liquid volumetric flowrate) was set to 1.0, 1.5 and 2.0, corresponding to $\phi_{th}^{(P_{atm})} = 0.50, 0.60$ and 0.67. These conditions were also achieved when the foam flow rig was connected to the foam generator unit and flow took place through the short straight pipe without a constriction; in this case the pressure inside the mixing-head chamber was close to atmospheric given that the linear pressure drop in the pipe was small (~ 0.01 bar), as shown in Table 5.4. Such a low pressure drop along the pipe did not have any significant effects on the microstructure of the flowing foam including bubble size and gas holdup.

In the presence of a flow constriction, maximum aeration efficiency was only achieved when the pressure drop ΔP_c across the constriction was below 1.0 bar, independent of the G/L ratio used (Table 5.4). The reduction in aeration efficiency with increasing pressure drop may be attributed to the relatively large increase in bubble size across the constriction caused by bubble coalescence - note that bubble expansion through the constriction accounts for only a relatively small part (~ 20%) of this increase in bubble size.

5.3.2 Effects of processing parameters on bubble size distribution

5.3.2.1 Effects of residence time

Whilst it is well-known that increasing the rotor speed reduces bubble size (Jabarkhyl *et al*., 2019; Mary *et al*., 2013; Muller-Fischer & Windhab 2007), the effects of residence time and G/L ratio are not always clearly identified. For example, Muller-Fischer & Windhab (2007) reported that a longer residence time led to a smaller bubble size, whereas Mary *et al*., (2013) did not observe a clear trend. Such conflicting reports may be due to differences in foaming solutions (Newtonian, non-Newtonian), processing parameters and different hydrodynamic

conditions (rotor speed, pressure and G/L ratio, laminar flow, turbulent flow), imaging procedures (online, off-line) different and rotor-stator geometry; in addition, the cross-influence of residence time and dispersion viscosity is not taken into account in most cases.

In this study, for a fixed G/L ratio, doubling the residence time led to a significant reduction in bubble size, as shown in Fig. 5.3, the extent of reduction being a function of G/L ratio and N. The smaller the G/L ratio, the greater the influence of residence time on the bubble size distribution (BSD) and, hence, D_{32}. Increasing the G/L ratio (i.e. increasing ϕ) and τ leads to a narrower more uniform BSD; the effects of τ reduce as the G/L ratio and N increase. These observations can be explained in terms of bubble breakage and coalescence frequency inside the mixing-head chamber. At smaller G/L ratios, the probability of bubble coalescence is low and bubble breakage is predominant and, hence, a longer residence time results in a smaller bubble size. At higher G/L ratios, the larger bubble number density leads to an equilibrium between bubble breakage and coalescence, which reduces the effect of τ. Under all conditions, the effect of τ diminishes with increasing N. It should also be pointed out that substantial variations in τ are required to generate any noticeable effects on bubble size.

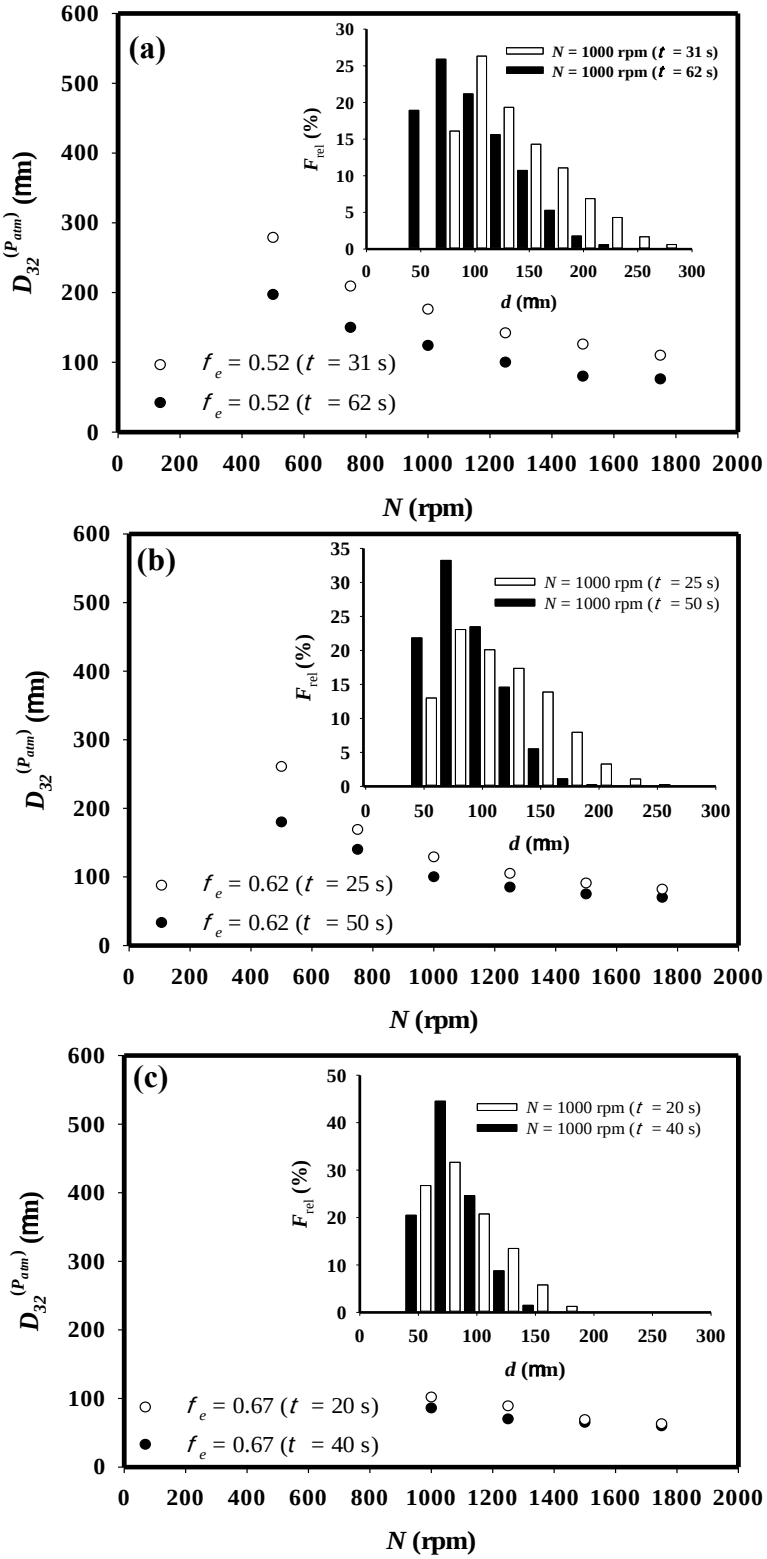

Fig. 5.3: Effects of residence time on bubble size of foams generated from fluid MF2: (a) G/L = 1.0 ($\phi_{th}^{(P_{atm})}$ = 0.50); (b) G/L = 1.5 ($\phi_{th}^{(P_{atm})}$ = 0.60); and (c) G/L = 2.0 ($\phi_{th}^{(P_{atm})}$= 0.67).

5.3.2.2 Effects of air volume fraction

Typical results depicting the effects of air volume fraction on bubble size for a fixed residence time (τ = 40 s) are shown in Fig. 5.4. The BSD is the same for G/L $\leq$ 1.0, however, the BSD becomes much narrower and more uniform for G/L $\geq$ 1.5. The data fall into two distinct regions: (i) a region of constant D_{32} corresponding to low and medium ϕ values; and (ii) a region of sharp decline in D_{32} at higher gas volume fractions. Müller-Fischer, Suppiger, *et al*. (2007) using a similar rotor-stator device, but a different non-Newtonian fluid formulation and operating at much higher rotor speeds and a much shorter residence time, reported the same plateau region beyond which, however, D_{32} increases sharply as a function of ϕ. The rise in bubble size was attributed to the increased coalescence rate because of the higher rotor speeds and the higher ϕ values they used as well as the significant time lag between foam sampling and bubble size measurement using a light microscope. The latter effect was obviated here because of the high stability of the foams (Jabarkhyl *et al.*, 2019) and the use of fast X-ray micro-CT analysis. There is no significant effect on BSD for G/L < 1.0; however, the BSD becomes much more uniform for G/L $\geq$ 1.5.

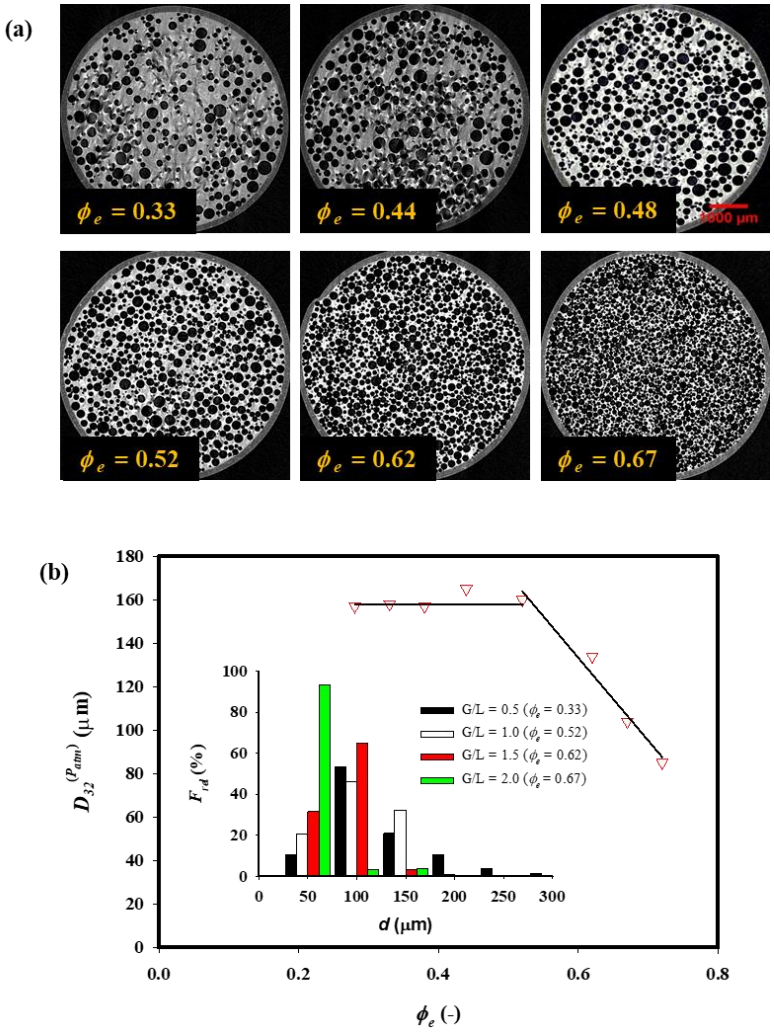

Fig. 5.4: Effects of air volume fraction on bubble size of foams generated from fluid MF2: N = 1000 rpm; τ = 40 s.

5.3.3 Foam flow through a straight pipe

Initial foam flow experiments were conducted through a short straight pipe without constriction. Using foams generated from the different model fluids (Table 5.1), varying the foam flowrate in the range 5.0 – 10.0 L hr^{-1} by varying the G/L ratio from 1.0 to 2.0, engendered a maximum pressure drop along the pipe of about ~ 0.01 bar. Such a pressure drop was too low to cause any significant effects in the foam microstructure along the pipe. These foams exhibit high static and quasi-static stability (Jabarkhyl *et al.*, 2019). Fig. 5.5 shows the gauge pressure along the

length of a 1.0 m horizontal flow pipe for foam generated from fluid MF2 at N = 1000 rpm and G/L = 1.0, 1.5 and 2.0 respectively. As expected, for a fully developed laminar flow, a linear drop in pressure was observed along the flow pipe at all flowrates investigated. The gradient of pressure drop increased with an increase in G/L ratio since at higher air volume fractions bubbles are much closer to each other, even though packing transition is not reached and, hence, the bubble matrix is more likely to undergo significant deformation under shearing. A finer foam texture should offer more resistance to deformation than a coarser foam because of the more complex thin liquid film network and the higher internal Laplace bubble pressure. Table 5.3 shows a summary of the aeration efficiency and bubble size for foams generated with and without a straight pipe. As shown, there was no variation in bubble size and hence the effects of ~ 0.01 bar linear pressure drop was not significant to cause changes to foam microstructure – as expected.

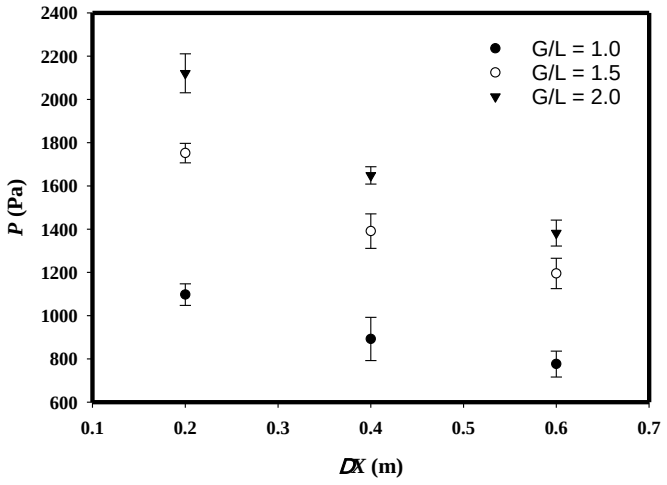

Fig. 5.5: Linear pressure drop profile along horizontal pipe for wet foams generated from fluid MF2 at N = 1000 rpm.

As mentioned above, the flow inside the pipe is laminar due to the low *Re* as a result of thecombined effects of large pipe diameter, low flowrate and a high apparent viscosity of the

foam. In addition, the wall effects on flow pattern with pipe radius is expected to be much lower mainly due to the relative larger conduit diameter and lower shear rate, (Deshpande and Barigou, 2000).

Table 5.3: A summary of pressure drop, bubble size and aeration efficiency in presence and absence of a straight pipe at G/L = 1.0 ($\phi_{th}^{(P_{atm})}$ = 0.50); (b) G/L = 1.5 ($\phi_{th}^{(P_{atm})}$ = 0.60); and (c) G/L = 2.0 ($\phi_{th}^{(P_{atm})}$= 0.67). Values followed by different subscript letters in the same column are significantly different (p < 0.05).

Sample	ΔP_c (kPa)	τ (s)	$D_{32}^{(P)}$ (μm)	$D_{32}^{(P_{atm})}$ (μm)	$\phi_{th}^{(P)}$ (-)	$\phi_{th}^{(P_{atm})}$ (-)	ϕ_e (-)	$\eta = \phi_e/\phi_{th}^{(P_{atm})}$ (-)
G/L = 1.0	without pipe	31	–	$147^a \pm 3$	**0.500**	**0.500**	**0.500**	**1.00**
	0.5	31	$147^a \pm 10$	$149^a \pm 3$	0.495	0.500	0.500	1.00
G/L = 1.5	without pipe	25	–	$130^b \pm 3$	**0.600**	**0.600**	**0.600**	**1.00**
	0.7	25	$130^a \pm 10$	$132^b \pm 3$	0.593	0.600	0.600	1.00
G/L = 2.0	without pipe	20	–	$113^c \pm 3$	**0.670**	**0.670**	**0.670**	**1.00**
	1.0	20	$113^a \pm 10$	$114^c \pm 3$	0.662	0.670	0.670	1.00

5.3.4 Foam flow through a straight pipe with an orifice constriction

5.3.4.1 Effects of G/L ratio

The diameter of the orifice constriction was varied in the range 0.5 – 1.8 mm to achieve different pressure drops in the foam flow (Table 5.4). X-ray micro-CT images showing the microstructure of foams generated from MF2 flowing with and without a flow constriction are depicted in Fig. 5.6. In the absence of a flow constriction, the foams exhibit a fine texture characterised by a narrow BSD with a peak at 100 μm and the vast majority of bubbles being less than 200 μm. In contrast, in the presence of a flow constriction the BSD is much wider and the foam texture much coarser with bubble sizes up to 600 μm being observed. Though the relative frequency of the larger bubbles is small, they do contribute significantly to the Sauter mean diameter (D_{32}), as shown in Fig. 5.7.

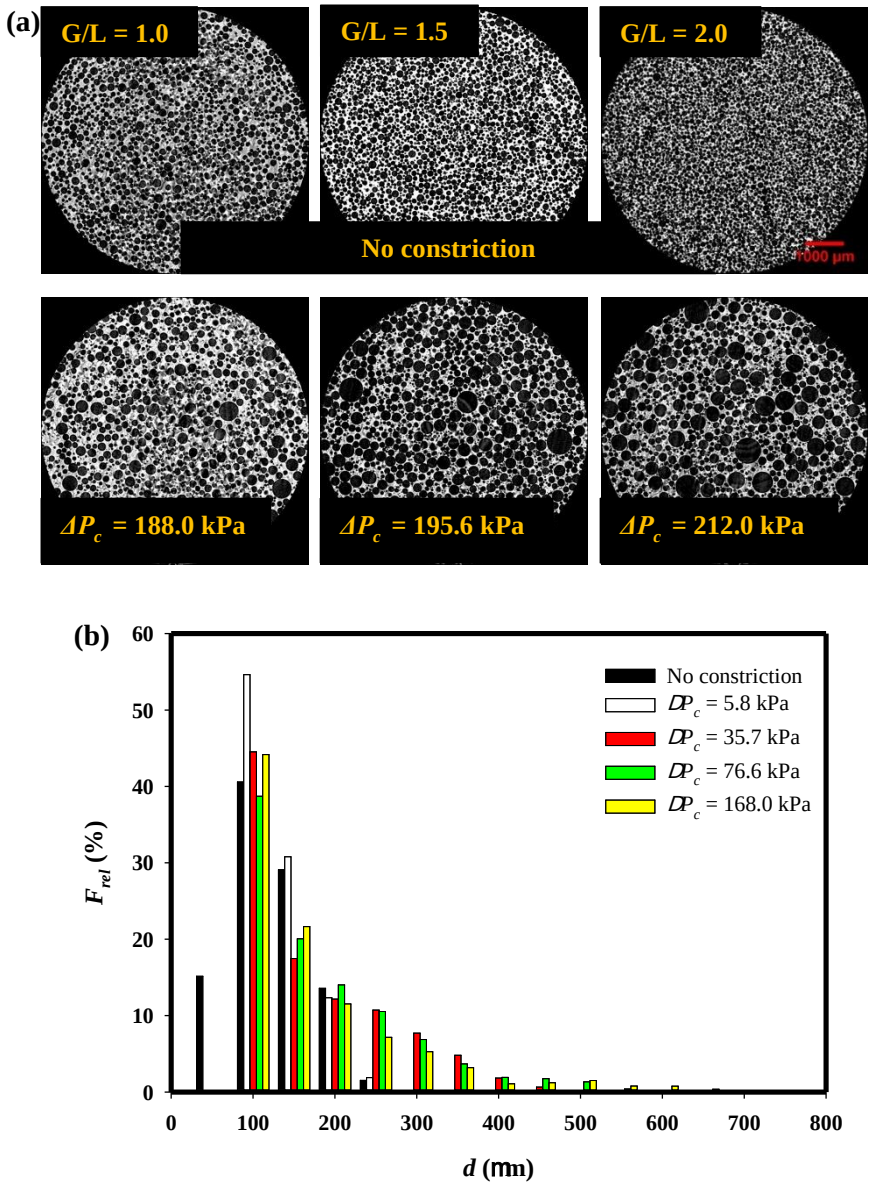

Fig. 5.6: Effects of pressure drop across constriction on foam microstructure generated from fluid MF2 N = 1000 rpm; Q_L = 5.0 L hr^{-1}; $Q_G^{(P_{atm})} = 5.0\ (\phi_{th}^{(P_{atm})} = 0.50), 7.5\ (\phi_{th}^{(P_{atm})} = 0.60)$and 10.0 L hr^{-1}$(\phi_{th}^{(P_{atm})} = 0.67)$.: (a) Typical X-ray micro-CT foam images; and (b) bubble size distributions.

Table 5.4: Typical results of aeration efficiency and mean foam bubble size for different flow conditions obtained with fluid MF2 at N = 1000 rpm; Q_L = 5.0 L hr^{-1}; $Q_G^{(P_{atm})} = 5.0, 7.5$ and 10.0 L hr^{-1}. Values followed by different subscript letters in the same column are significantly different ($p < 0.05$).

Sample	ΔP_c (kPa)	τ (s)	$D_{32}^{(P)}$ (μm)	$D_{32}^{(P_{atm})}$ (μm)	$\phi_{th}^{(P)}$ (-)	$\phi_{th}^{(P_{atm})}$ (-)	ϕ_e (-)	$\eta = \phi_e/\phi_{th}^{(P_{atm})}$ (-)
G/L = 1.0	No constriction	31	–	$147^{h} \pm 3$	**0.500**	**0.500**	**0.500**	**1.00**
D_o = 1.8 mm	4.7	32	$147^{a} \pm 3$	$157^{g} \pm 5$	0.477	0.500	0.500	1.00
D_o = 0.8 mm	30.0	38	$147^{a} \pm 5$	$200^{f} \pm 5$	0.385	0.500	0.500	1.00
D_o = 0.6 mm	66.6	45	$147^{a} \pm 7$	$230^{e} \pm 10$	0.266	0.500	0.500	1.00
D_o = 0.5 mm	145.0	49	$147^{a} \pm 13$	$323^{c} \pm 20$	0.204	0.500	0.460	0.92
G/L = 1.5	No constriction	25	–	$130^{i} \pm 3$	**0.600**	**0.600**	**0.600**	**1.00**
D_o = 1.8 mm	5.8	27	$130^{b} \pm 5$	$138^{h} \pm 5$	0.567	0.600	0.600	1.00
D_o = 0.8 mm	35.7	34	$130^{b} \pm 5$	$227^{e} \pm 10$	0.442	0.600	0.600	1.00
D_o = 0.6 mm	76.6	43	$130^{b} \pm 11$	$300^{c} \pm 20$	0.307	0.600	0.600	1.00
D_o = 0.5 mm	168.0	48	$130^{b} \pm 13$	$447^{b} \pm 50$	0.224	0.600	0.560	0.93
D_o = 0.4 mm	250.0	54	$130^{b} \pm 10$	$580^{a} \pm 50$	0.171	0.600	0.540	0.90
G/L = 2.0	No constriction	20	–	$113^{j} \pm 3$	**0.670**	**0.670**	**0.670**	**1.00**
D_o = 1.8 mm	6.9	23	$113^{c} \pm 5$	$127^{i} \pm 5$	0.627	0.670	0.670	1.00
D_o = 0.8 mm	41.7	32	$113^{c} \pm 5$	$251^{d} \pm 5$	0.473	0.670	0.670	1.00
D_o = 0.6 mm	85.6	42	$113^{c} \pm 13$	$320^{c} \pm 20$	0.316	0.670	0.640	0.96
D_o = 0.5 mm	179.0	47	$113^{c} \pm 10$	$590^{a} \pm 50$	0.236	0.670	0.610	0.91

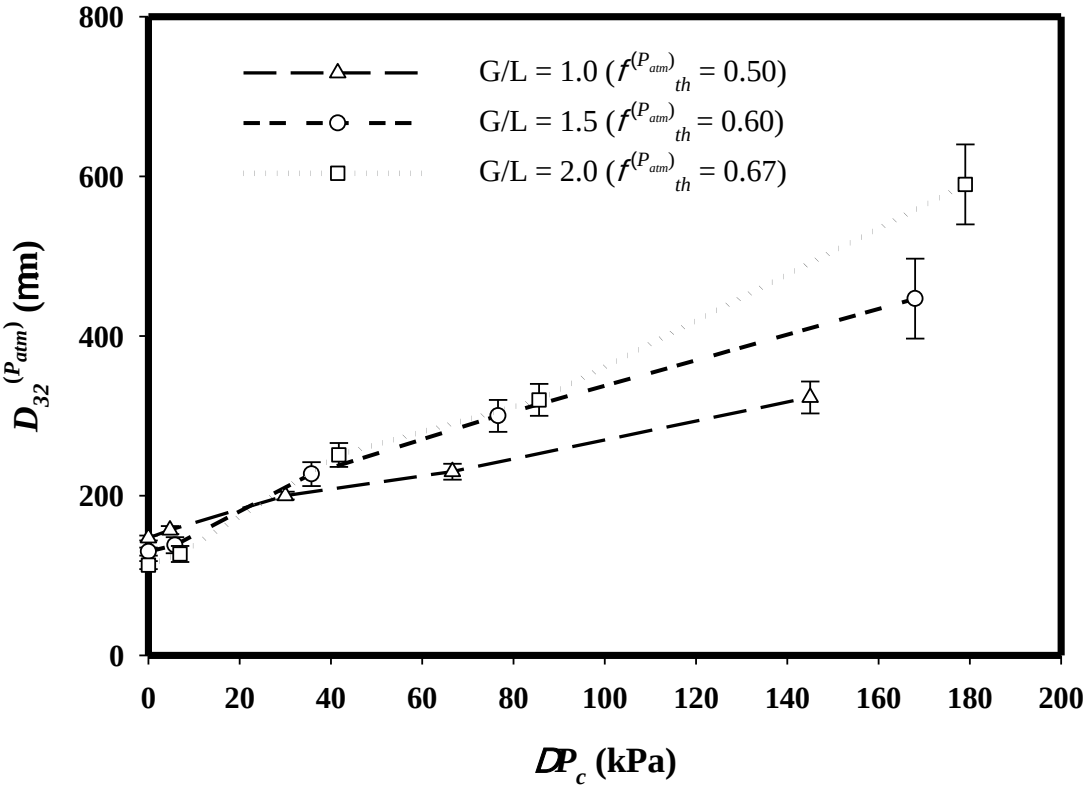

Fig. 5.7: Effects of pressure drop across constriction on mean bubble size of foams generated from fluid MF2 at N = 1000 rpm; Q_L = 5.0 L hr^{-1}; $Q_G^{(P_{atm})} = 5.0$ ($\phi_{th}^{(P_{atm})} = 0.50$), 7.5 ($\phi_{th}^{(P_{atm})} = 0.60$) and 10.0 L hr^{-1}($\phi_{th}^{(P_{atm})} = 0.67$).

Over the range of conditions investigated, the mean bubble size measured at the exit of the constriction increased approximately linearly as a function of ΔP_c, as shown in Fig. 5.7. In a short straight pipe (data points corresponding to approximately zero pressure drop), the G/L ratio has a relatively small effect on D_{32}. Upstream of the constriction, the mean bubble size is independent, within experimental error, of the orifice size used, as revealed by the data presented in Table 5.4. A reduction in orifice size corresponds to an increase in pressure inside the mixing-head chamber, the effect of which seems to be cancelled by a longer residence time leading to a constant mean bubble size. An identical maximum bubble size is expected,

provided the air volume fraction and the residence time are kept constant inside the mixing-head chamber, independent of the applied static pressure, since the critical Weber number is independent of pressure (Muller-Fischer and Windhab, 2007).

A higher G/L ratio, i.e. a higher gas holdup, causes a significantly larger increase in D_{32}, reflected in a greater slope of the linear trend. Qualitatively similar findings were reported by Muller and Fischer (2005) and Müller-Fischer, Suppiger *et al.* (2007) for different foam formulations and flow conditions. The results appear to suggest that at low pressure drops, the foam is able to squeeze through the constriction without incurring significant structural damage. As ΔP_c increases, the foam texture becomes coarser due to increased bubble coalescence. This effect seems to be even more significant for dryer foams probably because of the higher bubble density and thinner liquid films. To illustrate the severity of the foam degradation that can occur, flow experiments were conducted through an even narrower 0.4 mm orifice creating a much higher pressure drop of 2.5 bar, and the results are depicted in Fig. 5.8. The BSD becomes much wider and positively skewed. In this case, there was an almost 5-fold increase in the D_{32} from ~ 130 to ~ 600 μm.

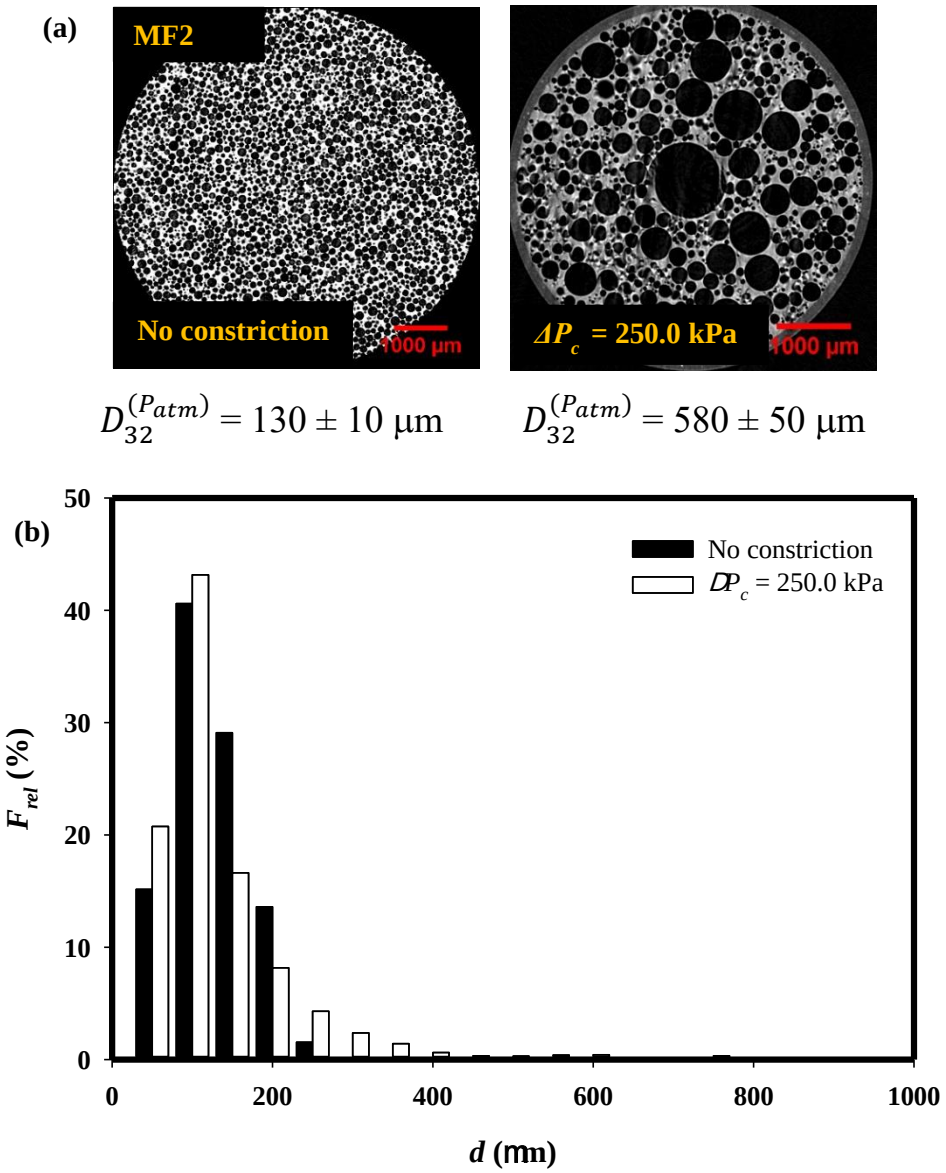

Fig. 5.8: Effects of pressure drop across constriction on bubble size of foams generated from MF2 at N = 1000 rpm; Q_L = 5.0 L hr^{-1}; $Q_G^{(P_{atm})}$ = 7.5 hr^{-1} (G/L = 1.5; $\phi_{th}^{(P_{atm})}$ = 0.60): (a) typical X-ray micro-CT foam images; and (b) bubble size distributions.

These results serve to demonstrate that even such statically highly stable foams, do incur significant structural transformations as a result of dynamic interactions with processing equipment. Hence, the transport and processing of these structured fluids should avoid high pressure drops and should be conducted as far as possible under conditions of pressure close to atmospheric.

5.3.4.2 Effects of PGE 55 concentration

Flow experiments were conducted through a short straight pipe without and with a constriction (0.8 mm orifice plate) at G/L = 1.5, using foams generated from fluids MF1, MF2 and MF3 containing respectively, 0.2, 0.5 and 1.0 wt% PGE 55 surfactant. It should be pointed out that the cac (critical aggregation concentration) of PGE 55 is very low (0.00001 wt%), such that the concentrations used here are orders of magnitude higher (Gupta *et al.*, 2016). In this case, maximum aeration efficiency was achieved under all conditions, as shown in Table 5.5. Whilst the pressure drop across the constriction is, within experimental error, the same for the three fluids, the relative increase in mean bubble size is greatest for fluid MF1 with the lowest PGE 55 content and reduces as the PGE 55 concentration increases for MF2 and MF3, as shown in Fig. 5.9.

Table 5.5: Effects of PGE 55 surfactant concentration on aeration efficiency and mean foam bubble size for fixed flow conditions at N = 1000 rpm; Q_L = 5.0 L hr^{-1}; $Q_G^{(P_{atm})} = 7.5$ (G/L = 1.5; $\phi_{th}^{(P_{atm})}$= 0.60). Values followed by different subscript letters in the same column are significantly different (p < 0.05).

Sample	ΔP_c (kPa)	τ (s)	$D_{32}^{(P)}$ (μm)	$D_{32}^{(P_{atm})}$ (μm)	$\phi_{th}^{(P)}$ (-)	$\phi_{th}^{(P_{atm})}$ (-)	ϕ_e (-)	$\eta = \phi_e/\phi_{th}$ (-)
MF1; G/L = 1.5	No constriction	25	–	143^{d} ± 3	**0.600**	**0.600**	**0.600**	**1.00**
D_o = 0.8 mm	32.7	29	143^{a} ± 10	430^{a} ± 10	0.452	0.600	0.600	1.00
MF2; G/L = 1.5	No constriction	25	–	130^{d} ± 10	**0.600**	**0.600**	**0.600**	**1.00**
D_o = 0.8 mm	35.7	29	130^{a} ± 10	227^{b} ± 10	0.442	0.600	0.600	1.00
MF3; G/L = 1.5	No constriction	25	–	110^{e} ± 3	**0.600**	**0.600**	**0.600**	**1.00**
D_o = 0.8 mm	36.2	29	110^{a} ± 10	174^{c} ± 10	0.441	0.600	0.600	1.00

Foams generated in the absence of a flow constriction have a relatively narrow BSD and have a peak at around 100 μm. Flow through the constriction, however, leads in all cases to a much broader positively skewed BSD. The effects are considerably more severe for fluid MF1 than MF2 and MF3. A possible reason for this may be due to the excess PGE 55 multilamellar vesicles available at higher concentrations to stabilise gas-liquid interfaces, clog Plateau borders and thin films and, thus, slow down liquid drainage and inhibit film rupture and bubble coalescence (Jabarkhyl *et al.*, 2019). In addition, the number of multi-bilayers under an interfacial monolayer is likely to be greater at a higher PGE concentration and hence the stability to foam expansion will also be greater.

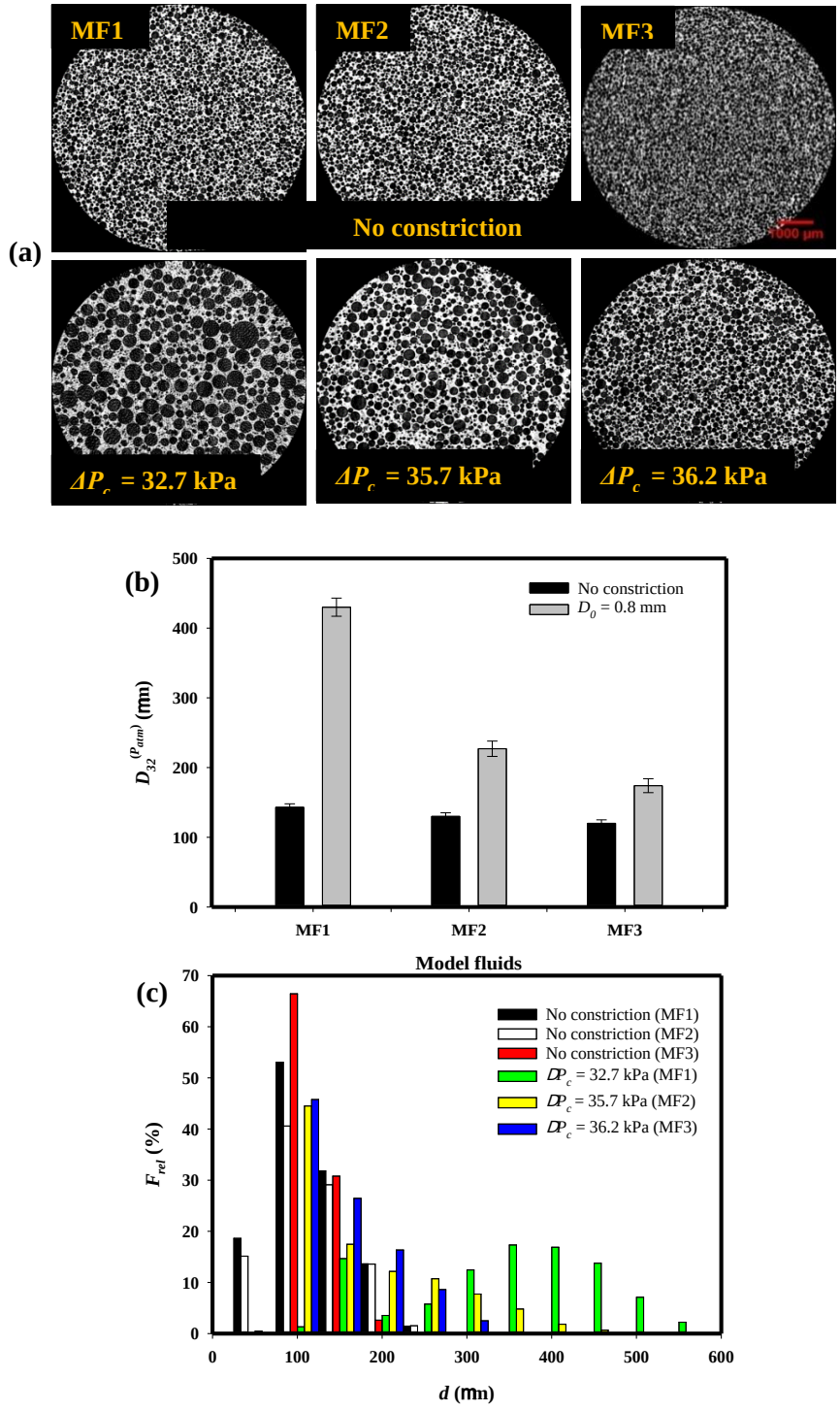

Fig. 5.9: Effects of PGE 55 concentration on bubble size of flowing foams generated from model fluids MF1 (0.2 wt%), MF2 (0.5 wt%) and MF3 (1.0 wt%) at N = 1000 rpm; Q_L = 5.0 L hr^{-1}; $Q_G^{(P_{atm})} = 7.5$ ($\phi_{th}^{(P_{atm})}$= 0.60): (a) X-ray micro-CT foam images; (b) mean bubble size variations; and (c) bubble size distributions.

Duerr-Auster *et al.* (2009) who studied the effects of pH on the foamability of PGE 55 solutions inside a kitchen mixer, found that the adsorption kinetics of PGE 55 improved leading to much enhanced foamability when the pH was reduced from 7 to 3. They attributed this improvement to the partial destruction of PGE 55 multilamellar vesicles, thereby exposing a higher fraction of the hydrophobic bilayer core to the air-water interface. They also found that acidity increased the rate of bubble coalescence under static conditions by dramatically reducing coalescence time. In this study, foams generated from fluid MF2 at pH 3 and pH 7 and G/L ratios of 1.0, 1.5 and 2.0 were allowed to flow through a short straight pipe with and without a 0.8 mm orifice plate fitted, but no significant effects were observed on either pressure drop or bubble size (as shown in Table 5.6). In this case, the improved adsorption kinetics of the PGE 55 surfactant was not sufficient to influence bubble coalescence during flow. Flow through the pipe with or without the constriction is relatively very fast and there is probably insufficient time for the diffusion of multilamellar vesicles of PGE 55 to have an effect.

Table 5.6: Effects of pH on dynamic stability of foams generated from MF2 at N = 1000 rpm Q_L = 5.0 L hr^{-1}; $Q_G^{(P_{atm})} = 5.0$, 7.5 and 10.0 L hr^{-1}. Values followed by different subscript letters in the same column are significantly different ($p < 0.05$).

pH	Sample	ΔP_c (kPa)	τ (s)	$D_{32}^{(P)}$ (μm)	$D_{32}^{(P_{atm})}$ (μm)	$\phi_{th}^{(P)}$ (-)	$\phi_{th}^{(P_{atm})}$ (-)	ϕ_e (-)	$\eta = \phi_e/\phi_{th}$ (-)
7	G/L = 1.0	No constriction	31	–	$147^{a} \pm 3$	**0.000**	**0.500**	**0.500**	**1.00**
	D_o = 0.8 mm	30.0	38	$147^{a} \pm 3$	$200^{b} \pm 5$	0.385	0.500	0.500	1.00
	G/L = 1.5	No constriction	25	–	$130^{c} \pm 3$	**0.600**	**0.600**	**0.600**	**1.00**
	D_o = 0.8 mm	35.7	34	$130^{b} \pm 5$	$227^{d} \pm 10$	0.442	0.600	0.600	1.00
	G/L = 2.0	No constriction	20	–	$113^{e} \pm 3$	**0.670**	**0.670**	**0.670**	**1.00**
	D_o = 0.8 mm	41.7	32	$113^{c} \pm 5$	$251^{f} \pm 5$	0.473	0.670	0.670	1.00
3	G/L = 1.0	No constriction	31	-	$152^{a} \pm 5$	**0.500**	**0.500**	**0.500**	**1.00**
	D_o = 0.8 mm	33.0	38	$152^{a} \pm 3$	$210^{b} \pm 5$	0.380	0.500	0.500	1.00
	G/L = 1.5	No constriction	25	-	$136^{b} \pm 5$	**0.600**	**0.600**	**0.600**	**1.00**
	D_o = 0.8 mm	36.1	34	$136^{b} \pm 5$	$234^{c} \pm 10$	0.440	0.600	0.600	1.00
	G/L = 2.0	No constriction	20	-	$117^{d} \pm 5$	**0.670**	**0.670**	**0.670**	**1.00**
	D_o = 0.8 mm	42.1	32	$117^{c} \pm 6$	$261^{e} \pm 5$	0.470	0.670	0.670	1.00

5.3.4.3 Effects of xanthan gum concentration

The above flow experiments were repeated at G/L = 1.5 to study the effects of varying the concentration of xanthan gum using foams generated from fluids MF4, MF5 and MF2 containing respectively, 0.25, 0.35 and 0.50 wt% XG, but the same PGE 55 concentration (0.5 wt%). In this case, maximum aeration efficiency was achieved under all conditions, as shown in Table 5.7. Foams generated in the absence of a flow constriction have a relatively narrow BSD and have a peak at around 100 µm. Flow through the constriction, however, leads in all cases to a right shift in the BSDs which become much broader and positively skewed. The effects are most severe for fluid MF4. The pressure drop across the constriction increases as a function of XG concentration, but the relative increase in mean bubble size is greatest for fluid MF4 with the lowest XG content and reduces as the XG concentration increases for MF5 and MF2, as shown in Fig. 5.10. The coarser foam texture at lower XG concentrations is probably due to the lower liquid viscosity causing weaker foam stability because of faster drainage, shorter thin liquid lifetime and higher rate of bubble coalescence.

Table 5.7: Effects of xanthan gum concentration on aeration efficiency and mean foam bubble size for fixed flow conditions at N = 1000 rpm; Q_L = 5.0 L hr^{-1}; $Q_G^{(P_{atm})} = 7.5$ L hr^{-1} ($\phi_{th}^{(P_{atm})}$= 0.60). Values followed by different subscript letters in the same column are significantly different ($P < 0.05$).

Sample	ΔP_c (kPa)	τ (s)	$D_{32}^{(P)}$ (μm)	$D_{32}^{(P_{atm})}$ (μm)	$\phi_{th}^{(P)}$ (-)	$\phi_{th}^{(P_{atm})}$ (-)	ϕ (-)	$\eta = \phi/\phi_{th}$ (-)
MF4; G/L = 1.5	No constriction	25	-	$150^{d} \pm 3$	**0.600**	**0.600**	**0.600**	**1.00**
D_o = 0.8 mm	25.6	28	$150^{a} \pm 10$	$338^{a} \pm 10$	0.478	0.600	0.600	1.00
MF5; G/L = 1.5	No constriction	25	-	$140^{d} \pm 3$	**0.600**	**0.600**	**0.600**	**1.00**
D_o = 0.8 mm	30.0	28	$140^{a} \pm 10$	$300^{b} \pm 10$	0.462	0.600	0.600	1.00
MF2; G/L = 1.5	No constriction	25	-	$130^{d} \pm 3$	**0.600**	**0.600**	**0.600**	**1.00**
D_o = 0.8 mm	35.7	29	$130^{a} \pm 10$	$227^{c} \pm 10$	0.442	0.600	0.600	1.00

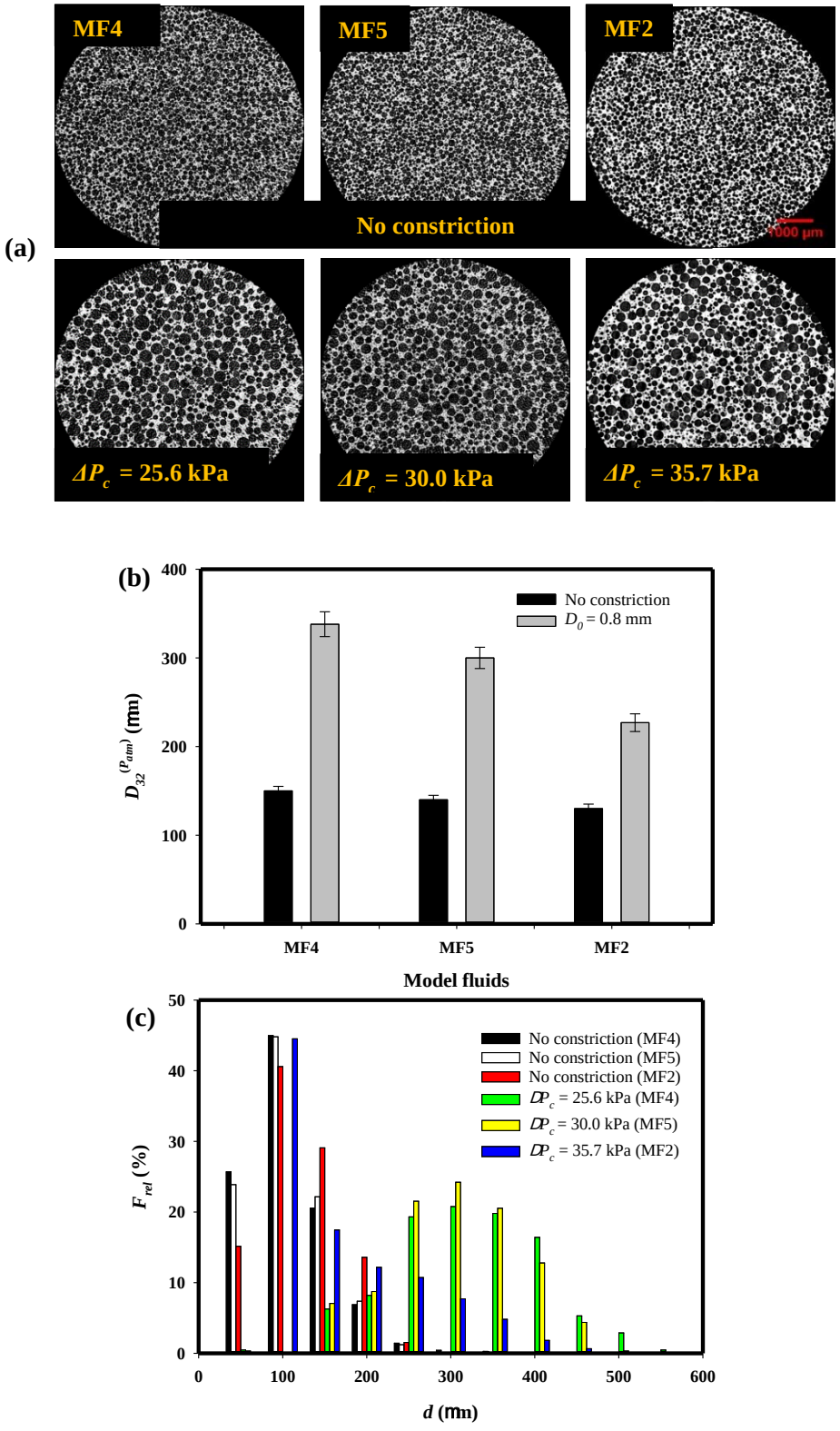

Fig. 5.10: Effects of xanthan gum concentration on bubble size of flowing foams generated from model fluids MF4 (0.25 wt%), MF5 (0.35 wt%) and MF2 (0.50 wt%) at N = 1000 rpm; Q_L = 5.0 L hr^{-1}; $Q_G^{(P_{atm})}$ = 7.5 L hr^{-1} (G/L = 1.5; $\phi_{th}^{(P_{atm})}$= 0.60): (a) X-ray micro-CT foam images; (b) mean bubble size variations; (c) bubble size distributions.

5.3.4.4 Effects of rotor speed

Similarly, flow experiments were again performed at G/L = 1.5 but varying the rotor speed, i.e., N = 500, 1000, 1500 and 2000 rpm, using foams generated from fluid MF2. Maximum aeration efficiency was achieved at all conditions investigated as shown in Table 5.8. Increasing N over this range led to a modest increase in pressure drop across the constriction which can be explained by the finer foams generated (i.e. more complex thin liquid film network) which dissipate more energy in flow (Jabarkhyl *et al.*, 2020). Flow through the constriction causes, in all cases, a considerable rise in the mean bubble size, as shown in Fig. 5.11. This is due to the combined influence of bubble coalescence and foam expansion. The relative increase in D_{32}, however, is lowest for N = 2000 rpm probably because of the much finer foam texture; in general, the finer the bubble size, the less the damage incurred through a constriction.

Table 5.8: Effects of rotor speed (N) on aeration efficiency and mean foam bubble size for fixed flow conditions at Q_L = 5.0 L hr^{-1}; $Q_G^{(P_{atm})} = 7.5$ L hr^{-1} (G/L = 1.5; $\phi_{th}^{(P_{atm})}$= 0.60).

Sample	ΔP_c (kPa)	τ (s)	$D_{32}^{(P)}$ (μm)	$D_{32}^{(P_{atm})}$ (μm)	$\phi_{th}^{(P)}$ (-)	$\phi_{th}^{(P_{atm})}$ (-)	ϕ (-)	$\eta = \phi/\phi_{th}$ (-)
N = 500 rpm	No constriction	25	–	230[b] ± 3	**0.600**	**0.600**	**0.600**	**1.00**
D_o = 0.8 mm	33.0	29	230[a] ± 10	340[a] ± 10	0.451	0.600	0.600	1.00
N = 1000 rpm	No constriction	25	–	130[d] ± 3	**0.600**	**0.600**	**0.600**	**1.00**
D_o = 0.8 mm	35.7	29	130[b] ± 10	227[b] ± 10	0.442	0.600	0.600	1.00
N = 1500 rpm	No constriction	25	–	94[f] ± 3	**0.600**	**0.600**	**0.600**	**1.00**
D_o = 0.8 mm	40.0	29	94[c] ± 10	195[c] ± 10	0.429	0.600	0.600	1.00
N = 2000 rpm	No constriction	25	–	77[g] ± 3	**0.600**	**0.600**	**0.600**	**1.00**
D_o = 0.8 mm	43.2	29	77[c] ± 10	122[e] ± 10	0.420	0.600	0.600	1.00

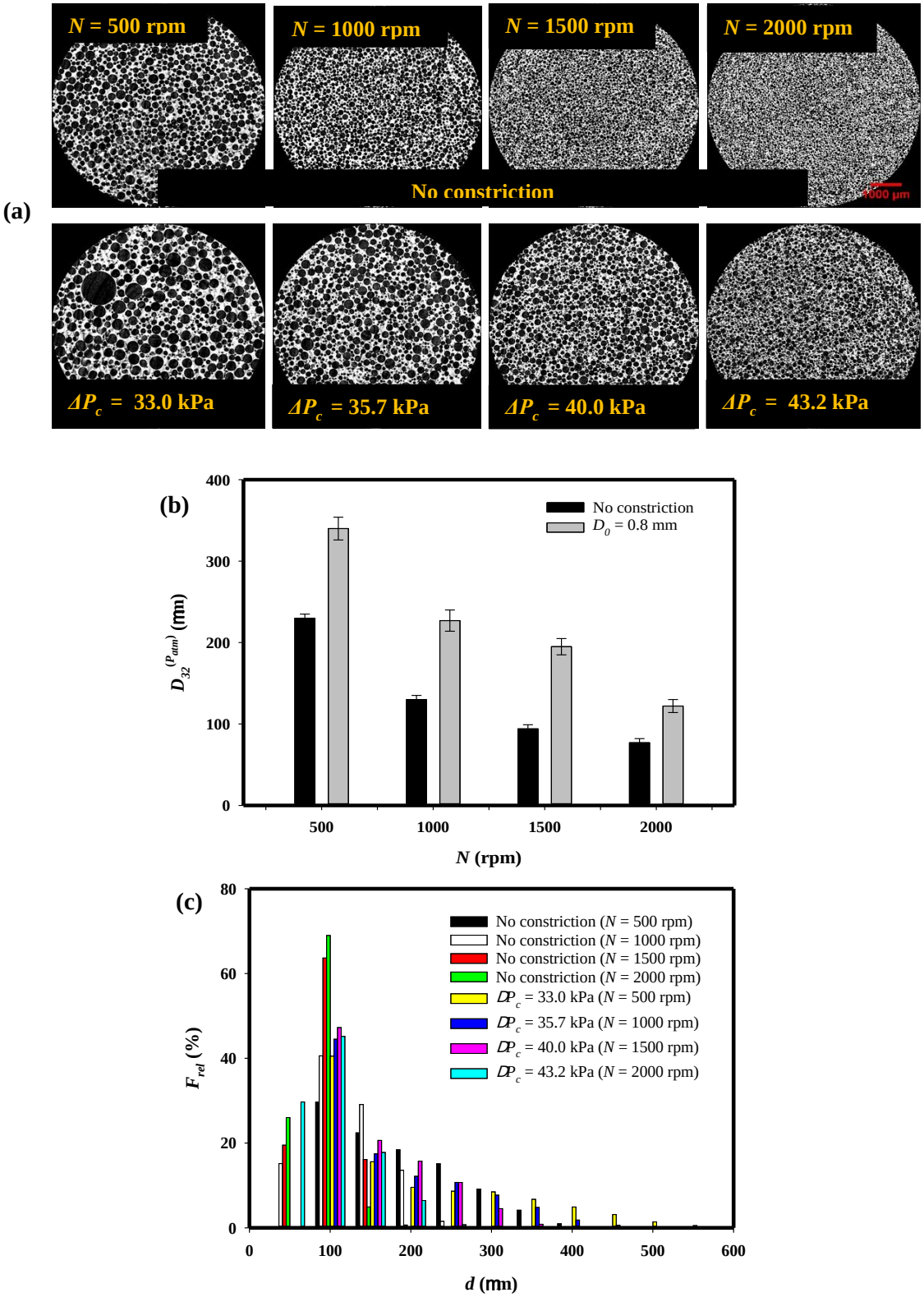

Fig. 5.11: Effects of rotor speed on bubble size of flowing foams generated from model fluids MF2 at N = 500, 1000, 1500 and 1750 rpm; Q_L = 5.0 L hr^{-1}; $Q_G^{(P_{atm})}$ = 7.5 L hr^{-1} (G/L = 1.5; $\phi_{th}^{(P_{atm})}$ = 0.60): (a) X-ray micro-CT foam images; (b) mean bubble size variations; (c) bubble size distributions.

In addition, as outlined in the literature review Chapter 2, the rate of deformation of larger air bubbles is much greater mainly due to the smaller Laplace pressure which might not be sufficient to resist the external stresses. As a result, the rate of film-thinning and hence coalescence is also higher.

5.3.5 Foam elasticity and static stability

5.3.5.1 Foam elasticity

Oscillatory tests were performed in the linear viscoelastic region to probe the unperturbed foam structure. The storage modulus (G') is a function of air volume fraction and bubble size distribution (Jabarkhyl *et al.*, 2020). For very wet foams (ϕ < ~ 0.50) bubble size distribution has negligible effects on (G'). Typical G' measurements for foams generated from fluid MF2 at G/L = 1.5 and N = 1000 rpm are shown in Fig. 5.12. G' is the highest for foam generated under ambient condition since this foam has a very fine texture. In contrast, G' decreases as the pressure drop incurred across the orifice constriction increases, owing to the coarser texture of the emerging foam and the loss of air at the highest pressure drop shown (Table 5.4).

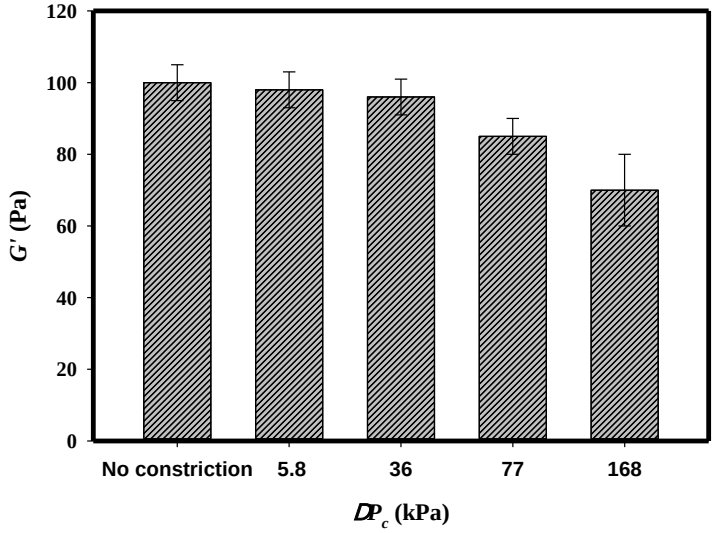

Fig. 5.12: Effects of pressure drop across constriction on elastic modulus of foam generated from fluid MF2 at N = 1000 rpm; Q_L = 5.0 L hr^{-1}; $Q_G^{(P_{atm})} = 7.5$ L hr^{-1} (G/L = 1.5; $\phi_{th}^{(P_{atm})}$= 0.60).

5.3.5.2 Foam drainage

The raw foams generated in the rotor-stator device are statically extremely stable at room temperature on a timescale of months. To assess the effects of the interaction with the constriction on the foam static stability, 50 ml foam samples were collected at the outlet of the flow pipe with and without a constriction. The sealed samples were then stored at a controlled temperature of 50℃ to enhance drainage and, consequently, shorten the foam lifetime and reduce experimental monitoring time. Typical foam drainage transients and foam half-life estimates for foams generated from fluid MF2 at G/L = 1.5 and N = 1000 rpm are shown in Fig. 5.13. Foams flowing in a short straight pipe without incurring a significant pressure drop have a finer texture which provides more resistance to liquid flow and, hence, they exhibit the slowest drainage time and the longest half-life. In contrast, the half-life is significantly reduced for foams having passed through the orifice constriction which have a coarser texture and may also contain less air as a result (Table 5.4). Results show that the higher the pressure drop incurred, the less the foam static stability.

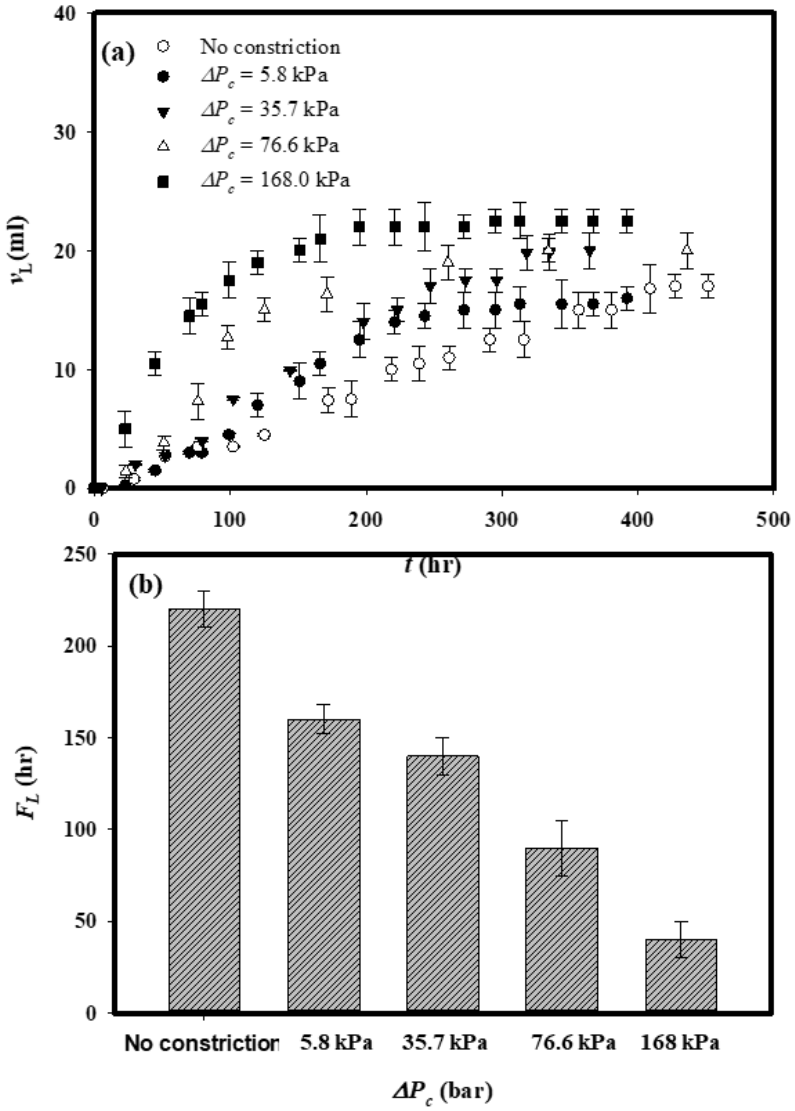

Fig. 5.13: Effects of pressure drop across constriction on drainage of foams generated from fluid MF2 at N = 1000 rpm; Q_L = 5.0 L hr^{-1}; $Q_G^{(P_{atm})}$ = 7.5 L hr^{-1} (G/L = 1.5; $\phi_{th}^{(P_{atm})}$= 0.60): (a) foam drainage transient; (b) foam half-life.

5.4 Conclusion

Foams generated from viscous shear-thinning fluids in a continuous multi rotor-stator device exhibit long term static stability on the order of months due to their fine texture consisting of a uniform bubble size distribution and the high viscosity of their base liquid. When operating under atmospheric condition, the effects of residence on bubble size distribution is maximum at lower rotor speed (N < 1250 rpm) and G/L ratio (< 1.5). Similarly, at a constant residence time, the data for Sauter mean diameter fall into two distinct regions: (i) a region of constant D_{32} corresponding to low and medium ϕ values; and (ii) a region of sharp decline in D_{32} at higher gas volume fractions.

Theoretical aeration efficiency was achieved when operating the multi-stage rotor-stator device under atmospheric condition without any blow-by occurring. This was also true when the wet foams were allowed to pass through a straight pipe. Flow through a short straight pipe incurs a low pressure drop and produces no tangible effects on foam structure, thus, preserving the original bubble size and static stability of the foam. At low pressure drops (< 50 kPa), foams are able to squeeze through a narrow orifice constriction without incurring significant structural transformations. At higher pressure drops (> 100 kPa), flow through the constriction causes significant bubble coalescence and, in some cases, loss of air volume leading to much coarser and much less stable foam. Increased surfactant content, liquid viscosity and rotor speed reduce bubble coalescence and help preserve foam structure during dynamic interaction with a flow constriction.

A higher G/L ratio, i.e. a higher gas holdup, causes a significantly larger increase in D_{32} and this effect seems to be even more significant for dryer foams probably because of the higher bubble density and thinner liquid films.

A higher surfactant PGE 55 content in the bulk implied a higher density of PGE 55 multilamellar vesicles which is possibly able to clog the Plateau borders and hence prevent bubble from coalescing during foam expansion. In addition, the number of multi-bilayers under an interfacial monolayer is likely to be greater at a higher PGE concentration and hence the stability to foam expansion. Similarly, a higher xanthan gum concentration meant thicker draining films which provides extra resistance to gravity drainage and hence bubble coalescence. The effects of rotor speed, however, became only significant at a rotor speed of N = 2000 rpm. Such a wet foam, with a more uniform bubble size distribution, was able to pass through a narrow orifice constriction with a relatively less bubble coalescence rate. As expected, the higher coalescence rate associated with larger air bubbles was mainly due to its smaller Laplace pressure which might not be able to resist the external stresses.

Notation

d	bubble diameter (m)
D_0	orifice plate diameter (m)
D_{32}	Sauter mean diameter (m)
$D_{32}^{(P_{atm})}$	Sauter mean diameter at atmospheric pressure (m)
$D_{32}^{(P)}$	Sauter mean diameter at pressure P (m)
F	frequency (Hz)
F_{rel}	relative frequency (%)
G'	storage modulus (Pa)
G'_0	storage modulus of liquid (Pa)
G''	loss modulus (Pa)
N	rotational speed (s^{-1})
P	level of statistical significance (-)
ΔP_c	Pressure loss across constriction (Pa)
ΔX	incremental horizontal pipe length (m)

Abbreviations

BSD	bubble size distribution
G/L	ratio of air and liquid volumetric flowrate
MF1	model fluid 1
MF2	model fluid 2
MF3	model fluid 3
MF4	model fluid 4
MF5	model fluid 5
PGE 55	polyglycerol ester of fatty acid
XG	Xanthan gum
X-ray micro-CT	X-ray micro-Computed Tomography

Greek symbols

τ	average residence time (s)
η	apparent viscosity (Pa.s)
ρ	density (kg m^{-3})
σ	surface tension (N m^{-1})
ϕ	experimental air volume fraction (-)
ϕ_{th}^{P}	theoretical air volume fraction at pressure *P* (-)
ϕ_{th}^{Patm}	theoretical air volume fraction at atmospheric pressure (-)
$\dot{\gamma}$	shear rate (s^{-1})
λ	fluid time constant (s)

Chapter 6: Rheological properties of wet foams generated from viscous pseudoplastic fluids

Foams generated from viscous non-Newtonian fluids have received insufficient attention in the literature despite their wide-ranging industrial applications. This study examines the steady shear flow and viscoelastic properties of wet foams generated in a continuous multi rotor-stator pilot-scale device. The foams are generated from viscous pseudoplastic liquids consisting of aqueous solutions of xanthan gum and caster sugar and stabilised with a non-ionic food grade surfactant (PGE 55). Rheological measurements were conducted inside a parallel plate geometry on a controlled stress/strain rheometer. The effects of foam microstructural properties as defined by the process parameters (rotor speed, foam air fraction) and liquid composition (xanthan gum concentration) are elucidated. Simultaneous in-situ visualisation of the foam during shearing revealed for the first time the existence of inward migration of liquid at high shear rates which is responsible for the time-dependence behaviour of the foams. The foam flow curves were successfully fitted to a generalised dimensionless form of the Carreau-Yasuda model with data for all conditions investigated collapsing approximately on one single curve, which allows prediction of foam apparent viscosity as a function of air volume fraction.

Keywords: Continuous foaming; non-Newtonian liquid; wet foam; Rheology; Bubble size distribution; Generalised Carreau-Yasuda model. **Chapter published:** Jabarkhyl, S., Barigou, M., Badve, M., Zhu, S., (2020). Rheological properties of wet foams generated from viscous pseudoplastic fluids. Innovative Food Science and Emerging Technologies, Vol. 59.

6.1 Introduction

Gas-liquid foams find numerous applications in various fields such as food processing, mineral transport, construction, oil and gas, cosmetics and firefighting. There are two well-described limiting gas-liquid foam structures: (*i*) 'wet' foams have high liquid content and mostly spherical bubbles, e.g. ice cream, with up to ~ 50% continuous phase; (*ii*) 'dry' foams have polyhedral cells and low liquid content, shaving foam, ~ 5% continuous phase. Bubble size generally ranges from about 10 μm to several mm. A packing transition region is reached and bubble size changes from spherical to polyhedral when the gas volume fraction reaches 0.64 for a monodispersed foam, or 0.74 – 0.78 for a polydispersed foam depending on the bubble size distribution (Sjoblom, 2001, Lexis and Willenbacher, 2014). As a two-phase system, both bubbly liquids and wet foams are prone to the process of destabilisation which consists of gravity drainage, coalescence and disproportionation (Kroezen and Wassink, 1987).

Gas-liquid foams are complex: they are compressible, non-linear viscoelastic materials; their viscosity is much larger than for the liquid constituent, and they often show an apparent yield stress (plasticity). Understanding of foam properties is therefore limited – design and control for applications is more art than science – and many issues remain unaddressed/unresolved, e.g. flow dynamics, structural behaviour, stability/metastability, and dependence of rheological properties on structure and physicochemical constitution. In particular, foams generated from viscous non-Newtonian fluids have received insufficient attention in the literature.

Inclusion of air bubbles into a liquid alters its rheological properties depending on several factors including the rheology of the foaming liquid, air volume fraction and bubble size distribution. Most of the existing studies have addressed the effects of aeration on Newtonian

liquids, with few studies investigating the rheological properties of wet foams made from non-Newtonian fluids. Torres, Hallmark and Wilson (2013) utilised aqueous guar gum solutions to generate bubbly liquids using a kitchen type planetary mixer and the behaviour was compared to a near Newtonian fluid - honey. Inclusion of air bubbles in both Newtonian (honey) and non-Newtonian fluids (guar gum solutions) caused significant time-dependence and normal forces. The former was attributed to microstructural changes that took place during the process of steady shear. For guar gum solutions lying in the semi-dilute and entanglement regime, they found that the bubble size distribution had a negligible effect on the steady shear rheology in comparison to the air volume fraction (Torres,Hallmark and Wilson, 2015a). Similar findings were also reported for shear-thinning k/l-hybrid carrageenan gum solutions (Torres,Hallmark and Wilson, 2015a).

Xanthan gum (XG) is an anionic polysaccharide widely employed in the food, personal care, oil recovery, agriculture and related sectors to impart non-Newtonian viscous properties to dispersions (Katzbauer, 1998). It is an anionic heter-polysaccride widely used in the food industry to impart stability to foams and emulsions. This particular food hydrocolloid has many useful properties such as high zero-shear viscosity at low shear rate and shear thinning properties at high shear rates (Xie and Hettiarachchy, 1998, Xu *et al.*, 2013, Zhong *et al.*, 2013, Laporte *et al.*, 2014, Laporte *et al.*, 2015, Laporte *et al.*, 2016).

In addition, the pseudoplastic dispersion properties are resistant to changes in pH and temperature. Recently, several studies have been reported in which XG is used as a foam stabiliser either on its own or in the presence of other food hydrocolloids such as guar gum (GG), Arabic gum and Persian gum. For example, Kabzinski *et al*., (2019) studied the impact

of addition of XG and GG on the rheological properties of foam generated using a continuous mechanical agitated column. A significant amount of thixotropic behaviour was observed for foams generated using XG and this was attributed to the shear disruption of the complex entangled network formed by the rod-like molecules (Kabziński *et al.*, 2019). Similarly, Dabestani and Yeganehzad (2019) looked at the effects of addition of Persian gum and XG on the foaming properties of pasteurised egg white. The addition of XG led to significant improvements in foam drainage and foam elasticity (Dabestani and Yeganehzad, 2019).

In the measurement of the rheological properties of two-phase dispersions, some complexities tend to arise such as shear banding, wall slip and microstructural transformations. For example, to describe the behaviour of dilute (< ≈ 10% v/v) emulsions under shear, use is often made of the capillary number representing the ratio of the shear force deforming the droplet to its internal capillary pressure force defined, thus:

$$Ca = \frac{\mu r \dot{\gamma}}{\sigma} \qquad \text{(Eq. 6.1)}$$

where *r* is the radius of the droplet, σ is the interfacial tension, $\dot{\gamma}$ is the imposed shear rate and μ is the viscosity of the continuous phase. However, for more concentrated dispersions including foams and emulsions exposed to shear, Golemanov *et al.* (2008) advocated the use of a dimensionless critical shear stress (τ^*) above which bubble/droplet breakage should be expected to occur, which is defined as:

$$\tau^* = \frac{\eta \dot{\gamma} r}{\sigma} \qquad \text{(Eq. 6.2)}$$

where η is the apparent viscosity of the two-phase dispersion. They utilised a parallel plate geometry to study the steady shear flow of a quasi-dry foam (92 – 98% air) and concentrated hexadecane-in-water emulsions (83 – 95% oil), and a light microscope to visualise the foam before and after shearing. A value of $\tau^* \approx 0.40$ was found for foams and a value $\tau^* \approx 0.15$ for emulsions. The observed time-dependence for both systems was attributed to bubble/droplet breakage (Golemanov *et al.*, 2008). Similarly, Torres, Gadala-Maria and Wilson (2013) reported that large bubbles in bubbly liquids tended to break under the application of shear and reported a slightly different value of $\tau^* \approx 0.30$ for bubbly liquids made of honey and $\tau^* \approx 0.03$ for bubbly liquids made of guar gum (Torres,Gadala-Maria and Wilson, 2013).

Existing rheological studies have focused on either bubbly liquids with a low gas content less than ≈ 50% or dry foams with gas fraction above ≈ 90% (see, for example, Torres, Gadala-Maria and Wilson, 2013; Golemanov *et al.*, 2008). There does not seem to be any studies that have addressed the rheology of wet foams made of non-Newtonian liquids with a gas fraction in the middle range closer to the packing transition regime. Therefore, in this chapter, an extensive study of the rheology of such wet foams with air fractions within the range 0.28 – 0.72 and varying bubble size distribution is conducted. A range of experimental conditions are investigated including rotor speed, gas-liquid ratio and apparent viscosity of the base fluid. Simultaneous in-situ visualisation of the foams under shear confirmed the absence of bubble breakage and, for the first time, unravelled the existence of inward radial shear-induced migration of liquid which is responsible for the time-dependence of the foams.

6.2 Materials and methods

6.2.1 Materials

6.2.1.1 Gillette shaving foam

A commercially available shaving foam (Gillette Foam Regular) was used as a model foam system to carry out steady state shear rheometry. The foam is generated from an aerosol can and it consisted of an approximately 9% liquid fraction with polyhedral bubble size of 18 μm (Habibi *et al.*, 2016). The foam generated was highly stable, consistent and reproducible.

6.2.1.2 Formulation and preparation of model fluids

Three model fluids (MF1, MF2, MF3) were employed in the experiments, which consisted of a mixture of polyglycerol fatty acid ester (PGE 55, DuPont, Denmark), xanthan gum (XG, supplied by Unilever), caster sugar (British sugar PLC, obtained from local supermarket) and sodium azide (ReagentPlus, ≥ 99.5%, Sigma Aldrich), all used without prior purification. The composition of these fluids is shown in Table 6.1. The density of the fluids was 1080 kg m^{-3} and the equilibrium surface tension measured by a Wilhelmy plate method was 38.0 ± 2 mN m^{-1}. The formulation of these model fluids provides a good mimic of the rheology of several food materials such as ice cream and whipped cream.

Table 6.1: Formulation of model fluids.

Model fluid	PGE 55 (wt%)	XG (wt%)	Sugar (wt%)
MF1	0.5	0.25	25
MF2	0.5	0.35	25
MF3	0.5	0.50	25

A Silverson high-shear mixer (Model L4RT, Silverson, UK) was used to mix the ingredients in distilled water held at 80 °C using a water bath, to ensure that the Krafft temperature (58 °C) of PGE 55 was exceeded (Duerr-Auster *et al.*, 2008, Curschellas *et al.*, 2012a). First, polyglycerol fatty acid ester (PGE 55) was added under agitation (6000-7000 rpm) and mixed thoroughly for at least 5 minutes prior to adding sugar and XG. Stirring was continued for another 5 min until all XG was completely dissolved. Sodium azide (0.025 wt%) was added to prevent microbial growth. The model fluids were then stored at 5 °C to degass and mature (hydration of XG) for at least 24 hours, to enable their rheology to fully stabilise. Inevitably, because of their high viscosity a small quantity of air still remained trapped in the form of tiny bubbles which were hard to remove without centrifugation. Centrifugation of the fluids, however, showed that the trapped air did not significantly alter their viscosity. Furthermore, in order to check that the high-shear processing used in their preparation did not affect the rheology of the fluids, we also prepared smaller volumes of such liquids using gentle mixing provided by a magnetic stirrer. There was no significant difference between the liquids obtained.

6.2.1.3 Foam generation and characterisation

The method of foam generation is the same as outlined in the previous chapters (see Chapter 4 for more details). A pilot-scale continuous rotor-stator (Megatron FM 12 – 50/2 HR) was used to aerate the model fluids and continuously generate foam. Experiments were conducted to generate foams of varying microstructure by using combinations of liquid flowrate within the range 0.5 – 5 L $h^{-1}$and air flowrate within the range 0.1 – 12.5 L hr^{-1}. These experiments showed a high degree of reproducibility in terms of gas volume fraction and mean bubble size of foam,

i.e. within ± 5% at the lowest rotor speed and within ± 1% at the highest speed. The air volume fraction in the foam is theoretically defined as:

$$\phi_{th} = \frac{Q_G}{Q_G + Q_L} \quad \text{(Eq. 6.3)}$$

where Q_G and Q_L are, respectively, the air and liquid volumetric flowrate. The experimental air fraction of the foam (ϕ_e) was measured by collecting foam samples at the exit of the rotor-stator device and determining the average mass of base liquid and foam that fill the same volume. An efficient foaming process will aim to maximise ϕ_e, but, in principle, this cannot exceed ϕ_{th}.

6.2.2 Methods

A parallel plate geometry was chosen to conduct the majority of rheological tests instead of other available geometries such as a cone and plate. The advantages of a parallel plate geometry are: (i) the adjustable gap height (h) and (ii) the ease at which the wall-slip can be minimised/eliminated using a serrated geometry or by simply attaching appropriate sandpaper. For dispersed systems (i.e. foams, particles and emulsions) containing large dispersed entities requires large h (at least 10 times greater than the maximum bubble size) to ensure that the experimental data is evaluated in terms of continuum mechanics (Lexis and Willenbacher 2014). The main drawback, however, of a parallel plate geometry is the non-uniform shear across the gap which, to mention, can be corrected using appropriate methods. In contrast, a cone and plate geometry provide a uniform shear across the small gap and hence no data correction is required. For dispersed systems, however, containing larger bubbles (such as foams in this study) the assumption of continuum mechanics is no longer valid and hence

implementation of a cone and plate geometry may lead to larger discrepancy as previously identified by Lexis and Willenbacher (2014).

6.2.3 Steady shear rheometry

The rheological measurements were conducted using a controlled stress/strain rheometer (Discovery HR-2, Hybrid Rheometer, TA, USA) equipped with a 40 mm parallel-plate geometry. No slip was detected for any of the model fluids, so a gap of 0.5 mm was adopted for their rheometry. However, minor slip was observed when such fluids were aerated, which was eliminated by using roughened plates (58 and 120 μm equivalent grit size). Tests conducted at different parallel-plate gaps (1.5 – 2.5 mm) showed negligible variation between the data sets and, hence, a 2 mm gap was adopted which is approximately an order of magnitude larger than the largest bubble size in any of the foams studied. Samples were carefully loaded to avoid structural damage and held at rest for a minimum of 5 minutes (for temperature equilibration and stress relaxation) before commencing each test. A solvent trap was used to avoid sample evaporation. In all cases, a measurement time of 5 s was used to obtain stead-state shear data. Every measurement was repeated at least three times and the reproducibility was within ±10%.

Fluid inertia and elasticity can cause deviations from viscometric flow at high velocities by superimposing a secondary flow on the primary shear flow. For both types of secondary flow, the primary indication of flow instability is an upturn in the shear-thinning trend of the material, i.e. increased viscosity at high shear rates, what is sometimes wrongly perceived as shear-thickening. The observation of such an apparent shear-thickening which is merely a manifestation of an increase in flow resistance, limits the high shear-rate experimental range for measuring simple shear rheological properties. The rheological data presented here did not

exhibit such effects and, hence, we can safely assume that the rheological testing was conducted under truly shear flow (Barnes *et al.*, 1989, Ewoldt,Johnston and Caretta, 2015). In addition, the Reynolds number indicating the transition from laminar to turbulent flow in parallel plate geometry was estimated to be in the range of 0.4 – 4.0 $\left(Re = \rho_f \Omega L^2/\eta_{app}\right)$. In the majority of cases, the values obtained are much lower than the critical Reynold's number quoted in the literature ($Re_c \geq 4.0$). Therefore, as mentioned above, for all the measurements conducted in this study, the measurement was conducted under laminar flow condition (Spagnolie, 2015).

The vast majority of the foams were very stable, incurring little drainage or coarsening over a period of a few hours. Foams obtained from formulations with low XG concentrations and G/L ratio (Table 6.1), albeit less stable, did not exhibit any significant structural changes over time periods equivalent to those required for rheological measurements. Complete flow curves were obtained at controlled strain rate by varying the shear rate in the range of 0.001 – 1000 s^{-1} and were well fitted by the Carreau rheological model ($R^2 \sim 0.991$). The Carreau incorporates both the upper and limiting viscosities, η_o and η_∞, corresponding, respectively, to the upper and lower Newtonian regions, and is given by (Yasuda,Armstrong and Cohen, 1981):

$$\eta = \eta_\infty + \frac{\eta_0 - \eta_\infty}{[1 + (\lambda\dot{\gamma})^2]^{n/2}} \qquad \text{(Eq. 6.4)}$$

where η is the apparent viscosity, $\dot{\gamma}$ is the shear rate, and λ and n are the Carreau time constant and rate constant, respectively. It should be noted that the model fluids and foams generated from them fall in the category of very shear-thinning fluids, i.e. fluids which display a high zero-shear viscosity in terms of an upper Newtonian region. If such a region is not covered in

the rheological measurements, the viscosity would appear to go to infinity at a certain minimum stress, which can be mistaken for a yield stress (Barnes *et al.*, 1989).

6.2.4 Normal stress measurements

Unlike shear stress, only elastic fluids exhibit normal stresses. A simple steady shear test was performed to measure the normal force, F_n, generated by the flow between parallel plates and obtain the normal stress difference ($N_1 - N_2$), thus (Steffe, 1996):

$$N_1 - N_2 = \frac{2F_n}{\pi R_{PP}^2}\left(1 + \frac{1}{2}\frac{d\ ln\ F_n}{d\ ln\ \dot{\gamma}_R}\right) \qquad \text{(Eq. 6.5)}$$

where, R_{pp} is the plate radius and $\dot{\gamma}_R$ is the shear rate at the rim. Normal stress measurement tends to be difficult. The procedure used here was similar to that adopted by Habibi *et al.*, (2016) to investigate commercial Gillette Shaving Foam. To erase prior shear history in the sample, pre-shearing for 30 seconds at a constant rate of 100 s^{-1} was conducted, after which the foams were allowed to rest for a minimum of 5 min before commencing a controlled-strain sweep test in the range $0.001 < \dot{\gamma} < 1000$ s^{-1}. This procedure enabled good reproducibility of results. There was, however, as previously reported by Habibi *et al.* (2016), poor reproducibility caused by large variations in normal stress measurements at lower shear rates ($\dot{\gamma} < \approx 10$ s^{-1}).

6.2.5 Oscillatory shear measurements

Dynamic oscillatory tests were conducted to measure the viscoelastic properties of the model fluids and foams. The linear viscoelastic region (LVR) was determined using an amplitude sweep test at 1 Hz frequency with % strain varying from 0.01 to 1000%. Subsequently, a frequency sweep test was conducted at 1% strain within the LVR, with frequency varying from 0.01 to 15 Hz to obtain the viscoelastic moduli (G', G'').

6.2.6 In-situ foam visualisation

Hysteresis loop tests conducted using shear stress sweeps showed significant irreversible time dependence of the foams. Samples taken at the end of these tests and imaged using X-ray micro-CT, as described above, showed no significant changes in the bubble size distribution. However, the foams were considerably drier having lost a significant amount of liquid which accumulated at the centre of the bottom plate. To probe this phenomenon further, a visualisation cell was used including a transparent glass bottom plate to enable simultaneous visualisation and rheological measurements as depicted in Fig. 6.1. The set-up consists of a protected silver mirror inclined at a 45° angle (Thorlabs LTD, UK) and a high-speed camera (FASTCAM MINI, Photron) attached to a light microscope (SZX12, Olympus, Germany). Several experiments were then conducted by applying a constant shear rate in the range of 5 – 600 s^{-1} for a duration of 300 s, while simultaneously capturing digital images at 30 s intervals at low shear rates and at 5 s intervals at high shear rates.

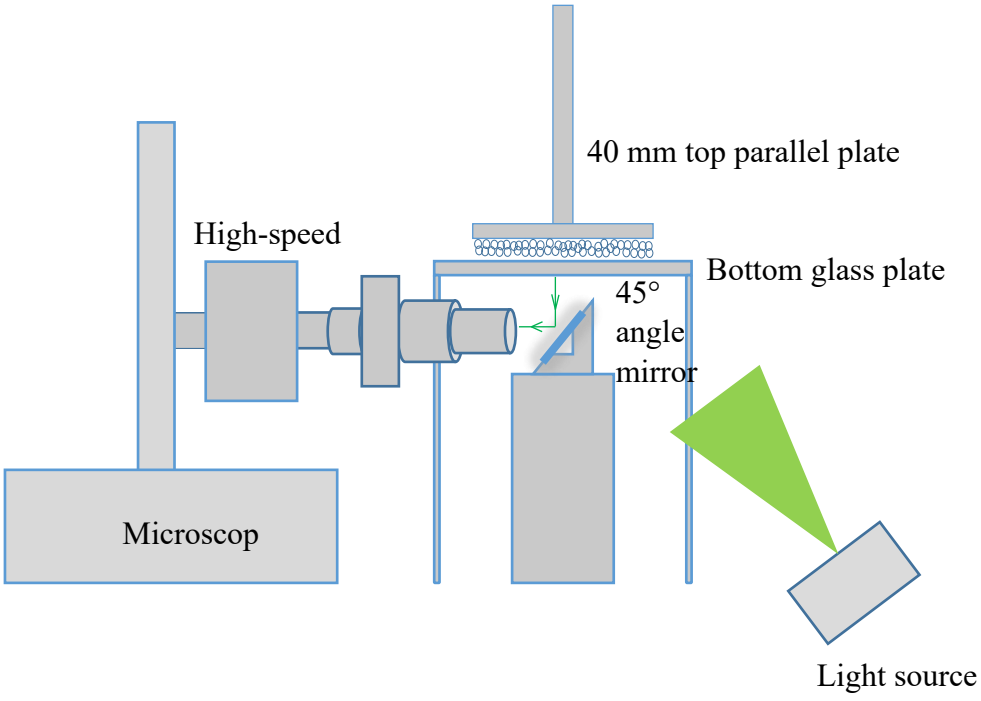

Fig. 6.1: Simultaneous rheometry and visualisation set-up.

6.3 Results and discussion

6.3.1 Preliminary studies

Rheometry of foams using rotational rheometers can be a cumbersome task since there are several experimental protocols that must be implemented in order to obtain reliable and reproducible results. One of these protocols involves the investigation of wall-slip phenomenon. Analogous to other multiphase systems (such as emulsions and solid suspensions) foams also exhibit wall-slip - the migration of the disperse gas phase away from the solid boundary. Therefore, to minimise or eliminate wall-slip, many experimental and theoretical procedures have been developed and proposed. The most common experimental procedure, however, is by simply attaching an appropriate sandpaper to the geometry or by using a sandblasted geometry (Lexis and Willenbacher, 2014, Habibi *et al.*, 2016, Laporte *et al.*, 2015). Another important factor that needs to be taken into consideration is the ratio between the gap of a rotational rheometer (i.e. Couette, parallel Plate, Cone and Plate, etc.) and the bubble diameter. This ratio needs to be at least of the order of 10 in order to obtain an accurate representation and measurement of the bulk rheology of foams. This is because the solid surface of the device can create a disturbance and therefore can affect both the volume fraction of the dispersed phase and its structure (Khan,Schnepper and Armstrong, 1988). In addition, as pointed out by Lexis (2015), the assumption of continuum mechanics is only valid when the gap of geometry is at least 10 times the maximum bubble size (Lexis, 2015).

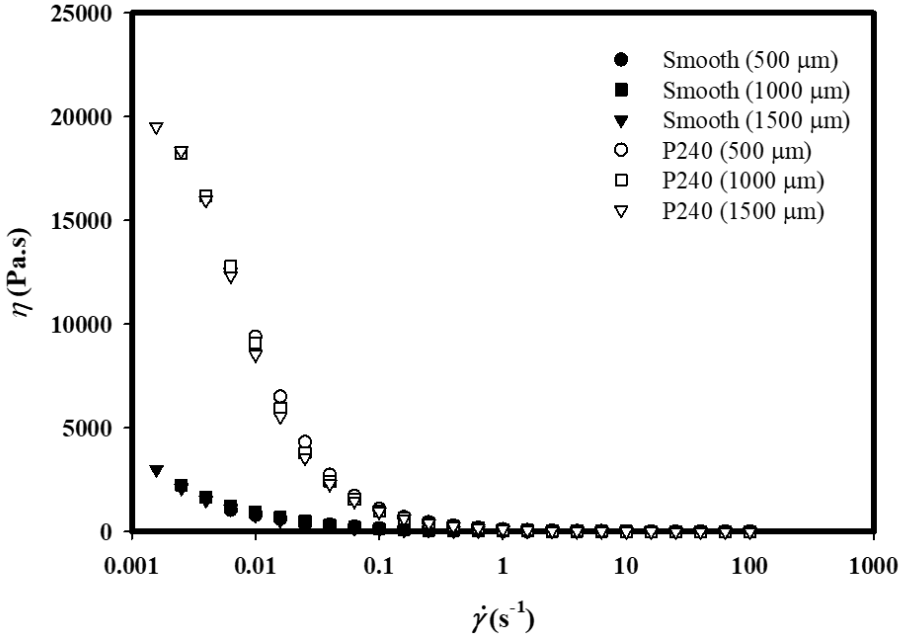

Fig. 6.2: Wall-slip investigation using Gillette shaving foam ($\phi \approx 0.09$) using smooth and serrated 40 mm parallel plate geometry.

As shown in Fig. 6.2, Gillette shaving foam had considerable amount of wall-slip when the rheometry was conducted on a smooth 40 mm parallel plate geometry at a plate gap width (h) of 0.5, 1.0 and 1.5 mm respectively. By attaching a P240 type sandpaper (equivalent to grit size of 58 μm), however, the wall-slip was diminished since the flow curves at different h are shown to collapse on a single curve. Similarly, the above procedure was also utilised on wet foams generated from shear-thinning model fluids using a continuous rotor-stator device. Typical results for wet foams generated from fluid MF2 at G/L = 1.0 ($\phi_e = 0.52$) and N = 1000 rpm is shown in Fig. 6.3. In contrast to Gillette shaving foam, there was minor slip associated with these wet foams which is possibly due to the sticky nature of the base liquid. Therefore, a 2.0 mm gap was sufficient to carry out a detailed rheological study on these wet foams. It is also important to state that, at low shear rates, below ~ 0.01 s^{-1}, for both Gillette shaving foam and wet foams generated in this study, there was ± 10% variation when trials were repeated at least

3 times. This variation is possibly due to several variables including variation in sample composition, prior residual stresses and other external factors.

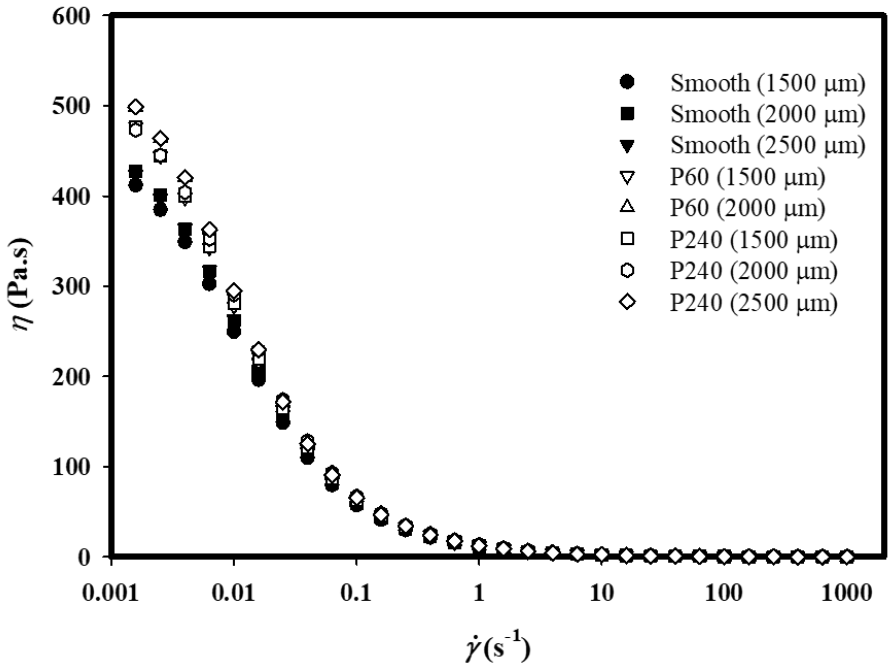

Fig. 6.3: Wall-slip investigation using fluid MF2, G/L = 1.0 (ϕ_e = 0.52); N = 1000 rpm using smooth and serrated 40 mm parallel plate geometry.

6.3.2 Aeration efficiency and bubble size distribution

Aeration efficiency is a pertinent feature of the foam generation process as it indicates the ability to incorporate all of the available air into the foaming liquid to make a homogeneous foam. Therefore, maximum aeration efficiency is achieved when the theoretical and experimental air volume fractions are equal (Eq. 6.3). We recently studied the effects of the processing parameters (rotor speed, air and liquid volumetric flow rates) and the physical properties of the base liquid (dynamic surface tension, liquid viscosity) on the incorporated air volume fraction (Jabarkhyl *et al.*, 2019). The aeration efficiency was a function of both the hydrodynamic conditions inside the mixing-head chamber and the concentration of PGE 55

used but was independent of the XG concentration. It should be noted that a 'blow-by' phenomenon can take place when operating at high G/L ratios, especially when the foaming fluid contains an insufficient amount of PGE 55, necessary to stabilise the bubble interfaces (Jabarkhyl *et al.*, 2019). This then results in some of the air bypassing the rotor-stator assembly in the form of large air slugs. However, 'blow-by' was not observed in this study.

The rotor speed and the G/L ratio were the dominant factors in determining the aeration efficiency and bubble size distribution. Increasing the rotor speed, exposes the bubbles to higher stresses inside the mixing-head chamber which ensures that large bubbles at the inlet are gradually broken down into smaller bubbles along the mixing-head chamber. Similarly, increasing the G/L ratio leads to a significant increase in the apparent viscosity of the air-liquid dispersion, causing additional shear stresses which break down larger air bubbles into smaller bubbles. Typical X-ray micro-CT images obtained for samples generated from model fluids MF1-MF3 at N = 1000 rpm and G/L = 1.5 (ϕ_e = 0.62) are shown in Fig. 6.4 and the corresponding bubble size distributions are plotted in Fig. 6.5a. Increasing the XG concentration (MF1 to MF2 to MF3 in Fig. 6.4a) leads to a reduction in bubble size, but beyond a certain value (~ 0.35 wt%) the effect becomes negligible. For a given XG concentration, increasing the rotor speed leads to a smaller more uniform bubble size distribution; typical results are shown in Fig. 6.4b and Fig. 6.5b for model fluid MF3 at G/L = 1.5 (ϕ_e = 0.62) at rotor speeds of 500 – 1750 rpm. In addition, at a given rotor speed, varying the G/L ratio in the range 0.5 – 1.0, corresponding to $0.33 \leq \phi \leq 0.50$, has no effect on the bubble size distribution (Fig. 6.4c, Fig. 6.5c). Beyond G/L = 1.0 the bubble size becomes smaller and more uniform.

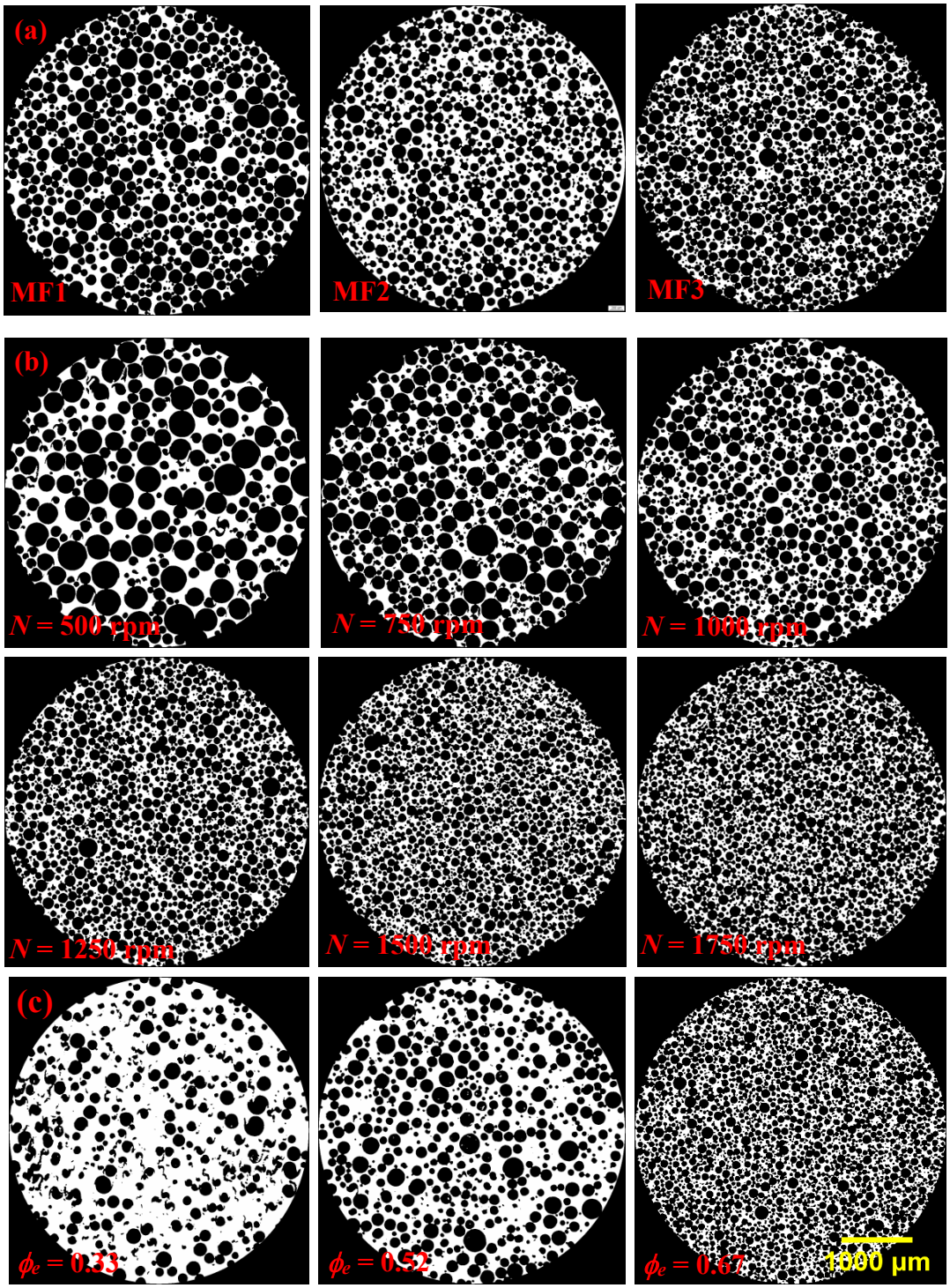

Fig. 6.4: Typical images of foams obtained using X-ray micro-CT: (a) model fluids MF1, MF2, MF3 at G/L = 1.5 (ϕ_e = 0.62), N = 1000 rpm; (b) model fluid MF3 at G/L = 1.5 (ϕ_e = 0.62), N = 500 – 1750 rpm; (c) model fluid MF3 at N = 1000 rpm, G/L = 0.5 (ϕ_e = 0.33), 1.0 (ϕ_e = 0.52), 2.0 (ϕ_e = 0.67).

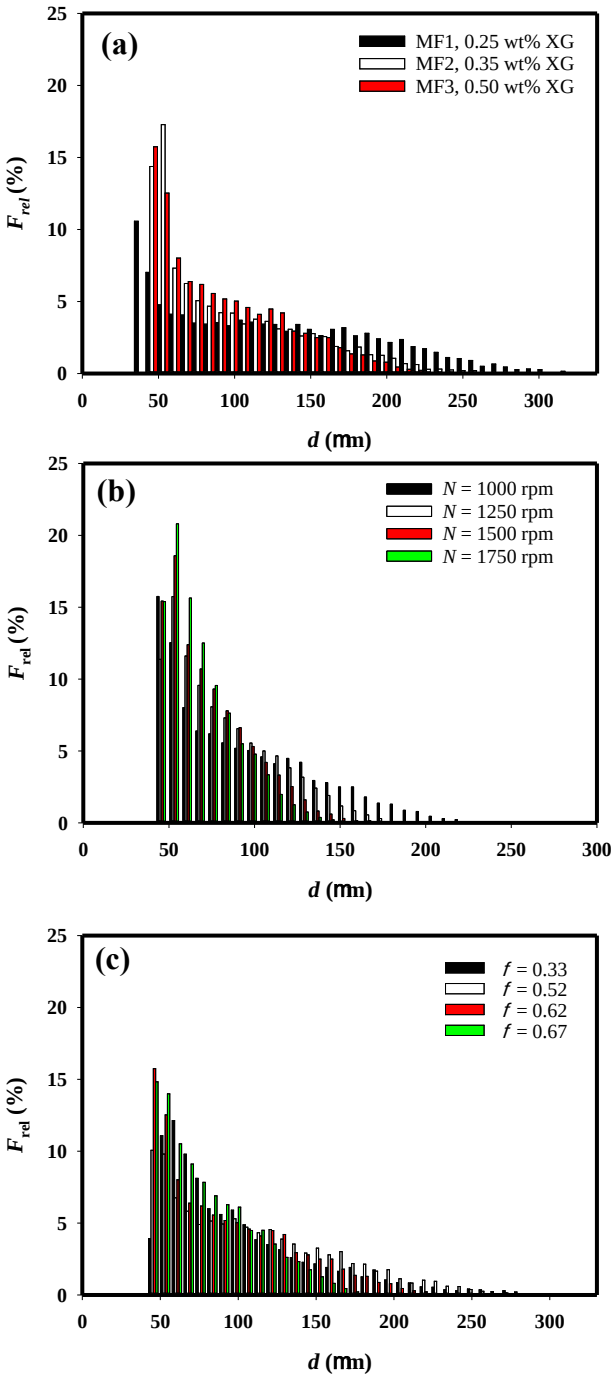

Fig. 6.5: Bubble size distribution of foams obtained from X-ray micro-CT: (a) model fluids MF1, MF2, MF3 at G/L = 1.5 (ϕ_e = 0.62), N = 1000 rpm; (b) model fluid MF3 at G/L = 1.5 (ϕ_e = 0.62), N = 500 – 1750 rpm; (c) model fluid MF3 at N = 1000 rpm, G/L = 0.5 (ϕ_e = 0.33), 1.0 (ϕ_e = 0.52), 2.0 (ϕ_e = 0.67).

6.3.3 Steady shear rheology

6.3.3.1 Effects of xanthan gum concentration

Xanthan gum (XG) is an anionic polysaccharide widely employed in the food, personal care, oil recovery, agriculture and related sectors to impart non-Newtonian viscous properties to foams and emulsions and enhance their stability (Katzbauer, 1998). Even at low concentrations, XG can impart strong shear-thinning characteristics caused by the presence of hydrogen bonds which can form cross-links to give a strong network. Upon shear, the cross-links can untangle and align with the shear-field leading to shear-thinning (Song,Kim and Chang, 2006). Wyatt *et al.*, (2009) identified four different concentration regimes that can exist in aqueous XG solutions. For concentrations > 2000 ppm, the solutions are in the entangled regime with a zero-shear viscosity scaling with concentration according to a power law with exponent 3.75. All of the experiments described here were conducted in this regime. Recently, Dakhil, Auhl and Wierschem (2019) reported that aqueous XG solutions exhibit appreciable normal stress differences only at very high shear rates ($\approx > 10^3\ s^{-1}$) which are attributed to the disentanglement of the polymer macromolecules rather than to viscoelastic deformation or collisions between macromolecules as is commonly the case for other polymeric systems such as guar gum and Boger fluids (Dakhil,Auhl and Wierschem, 2019).

The flow curves of the model fluids MF1, MF2, MF3 having, respectively, a xanthan gum (XG) concentration in the entanglement regime of 0.25, 0.35 and 0.50 wt% are presented in Fig. 6.6 together with the flow curves of corresponding wet foams (ϕ_e = 0.52; 0.62) generated at a rotor speed of 1000 rpm. All of these fluids exhibit typical shear-thinning or pseudoplastic behaviour consisting of an upper Newtonian region and a shear-thinning region tending to a lower Newtonian region which is less obvious in most cases at the shear rates investigated. Aeration

of the fluids even at such relatively low air fractions has a dramatic effect as it leads to the formation of wet foams exhibiting a shear-thinning behaviour similar to that of the base liquids but having viscosities one or two orders of magnitude greater. The higher the XG concentration, the higher the zero-shear viscosity of both the liquid and the wet foam, but the narrower the upper Newtonian region, i.e. transition from Newtonian to shear-thinning flow occurs at smaller critical shear rates (Table 6.2); this behaviour has been previously reported for pure XG solutions by Song et al. (2006) and for aerated Guar gum solutions by Torres et al. (2014). The trends observed here in Fig. 6.6 were reproduced by foams generated from all model fluids at all rotor speeds studied in the range 1000 – 1750 rpm (data not shown). The flow curves of all model fluids as well as of the wet foams shown in Fig. 6.6, were well fitted (R^2 ~ 0.991) by the Carreau model (Eq. 6.4) and the Carreau parameters are summarised in Table 6.2.

Table 6.2: Summary of Carreau model parameters for model fluids and their foams generated at N = 1000 rpm; G/L = 1.0 (ϕ_e = 0.52); G/L = 1.5 (ϕ_e = 0.62).

Sample	η_o (Pa.s)	η_∞ (Pa.s)	λ (s)	N (-)	R^2 (-)	$\dot{\gamma}_c$ (s^{-1})
MF1 (ϕ_e = 0.00)	9	0.007	15	0.30	0.998	0.0667
MF1 (ϕ_e = 0.52)	45	0.040	25	0.33	0.996	0.0400
MF1 (ϕ_e = 0.62)	100	0.050	40	0.33	0.999	0.0250
MF2 (ϕ_e = 0.00)	35	0.007	30	0.25	0.998	0.0333
MF2 (ϕ_e = 0.52)	170	0.040	85	0.30	0.996	0.0118
MF2 (ϕ_e = 0.62)	555	0.060	210	0.30	0.997	0.0056
MF3 (ϕ_e = 0.00)	100	0.007	35	0.20	0.999	0.0280
MF3 (ϕ_e = 0.52)	476	0.060	140	0.25	0.996	0.0079
MF3 (ϕ_e = 0.62)	840	0.070	200	0.25	0.999	0.0056

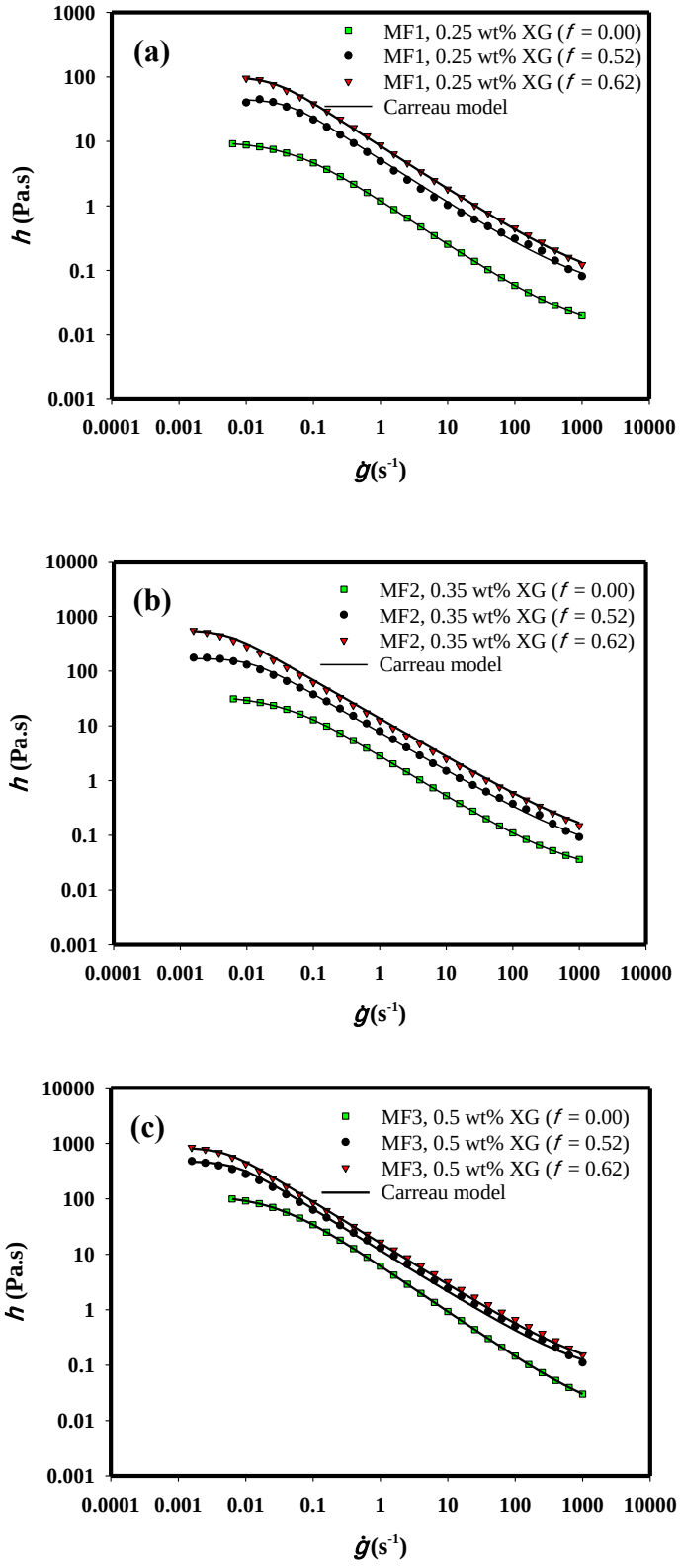

Fig. 6.6: Steady state flow curves of model fluids and foams generated at N = 1000 rpm; G/L = 1.0, 1.5: (a) MF1; (b) MF2; and (c) MF3.

The flow curves of the wet foams generated from the three model fluids are compared in Fig. 6.7. There is a significant difference between foam viscosities at lower shear rates, but the flow curves begin to collapse onto a single curve at higher shear rates ($\dot{\gamma} \approx > 100$ s^{-1}). Similar observations were reported by Torres et al. (2015) at $\dot{\gamma} \geq 350$ s^{-1} for bubbly liquids generated from guar gum solutions and they attributed this behaviour to molecular entanglement effects. Here, as the foams consist of a high liquid fraction, the substantially different viscosities of the liquids which depend strongly on their XG concentrations play a major role in the significant discrepancy between the flow curves observed at low shear rates. At higher shear rates ($\dot{\gamma} \approx$ >100 s^{-1}), however, visualisation of the flow between the parallel plates via the optical cell described above, Fig. 6.1, showed the onset of shear-induced migration of liquid taking place from the periphery of the parallel-plate geometry to the centre, as depicted in Fig. 6.8. Thus, the wet foams being stripped of their liquid, start to become gradually drier and display similar resistance to shear causing the flow curves to gradually merge.

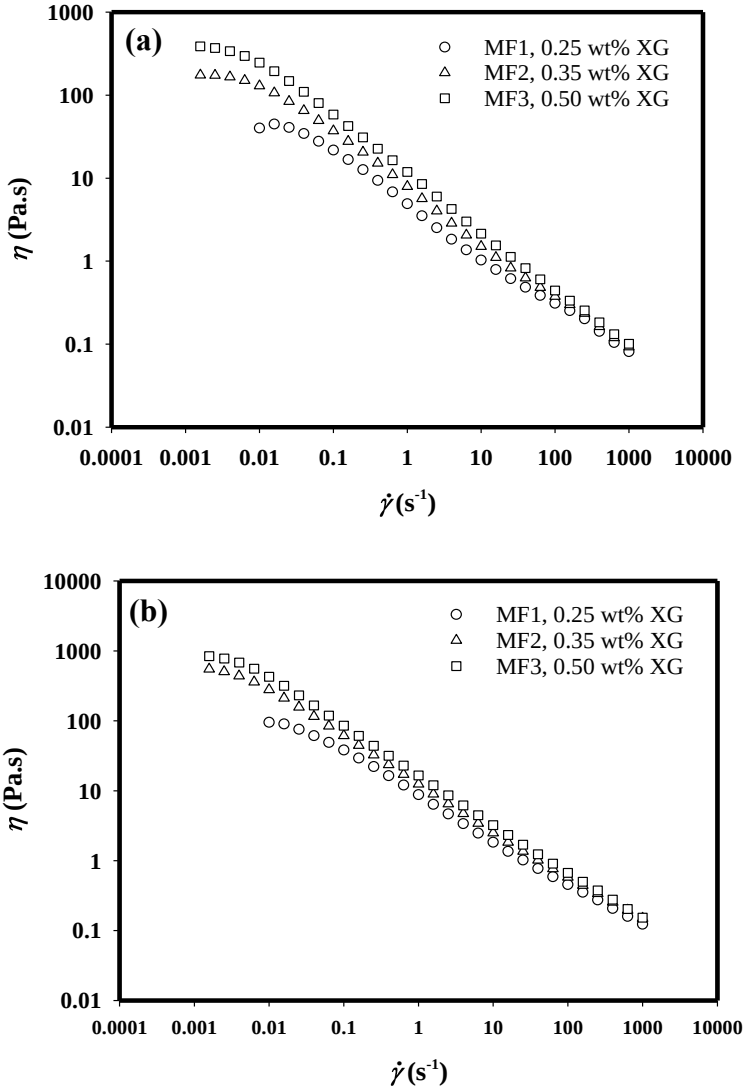

Fig. 6.7: Comparison of steady state flow curves of foams generated at N = 1000 rpm: (a) G/L = 1.0 (ϕ_e = 0.52); and (b) G/L = 1.5 (ϕ_e = 0.62).

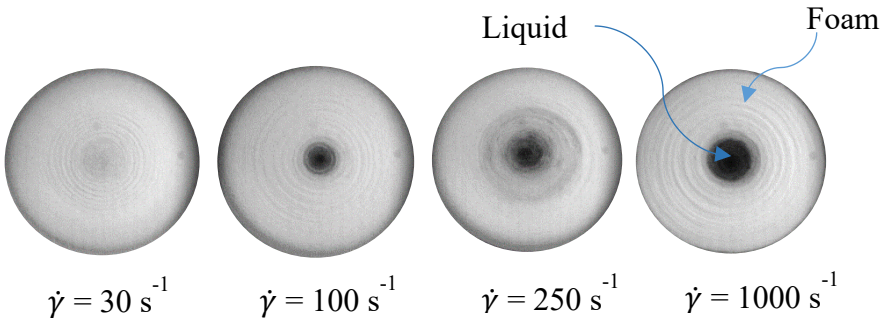

Fig. 6.8: Visualisation of shear-induced migration of liquid to the centre: fluid MF3, N = 1000 rpm, G/L = 1.0 (ϕ_e = 0.52).

6.3.3.2 Effects of initial bubble size distribution

The effects of the initial bubble size distribution were investigated by generating bubbly liquids and wet foams at rotor speeds ranging from 1000 – 1750 rpm. For $\phi_e < \approx 0.60$ and for all model fluids investigated, the flow curves of the foams are independent of N in spite of the bubble size distributions being markedly different, as shown in Fig. 6.9a. A similar behaviour was observed by Torres *et al.*, (2015) for bubbly liquids generated from guar gum solutions for $\phi_e < \approx 0.50$. However, for $\phi_e \approx > 0.60$, a smaller more uniform bubble size (as N increases) results in an increase in apparent viscosity of the aerated fluid as the flow curve shifts upwards (Fig. 6.9b). At high air volume fractions, the bubbles are much closer to each other, even though packing transition is not reached and, hence, the bubble matrix is more likely to undergo significant deformation under shearing. A finer foam texture should offer more resistance to deformation than a coarser foam because of the more complex thin liquid film network and the higher internal Laplace bubble pressure.

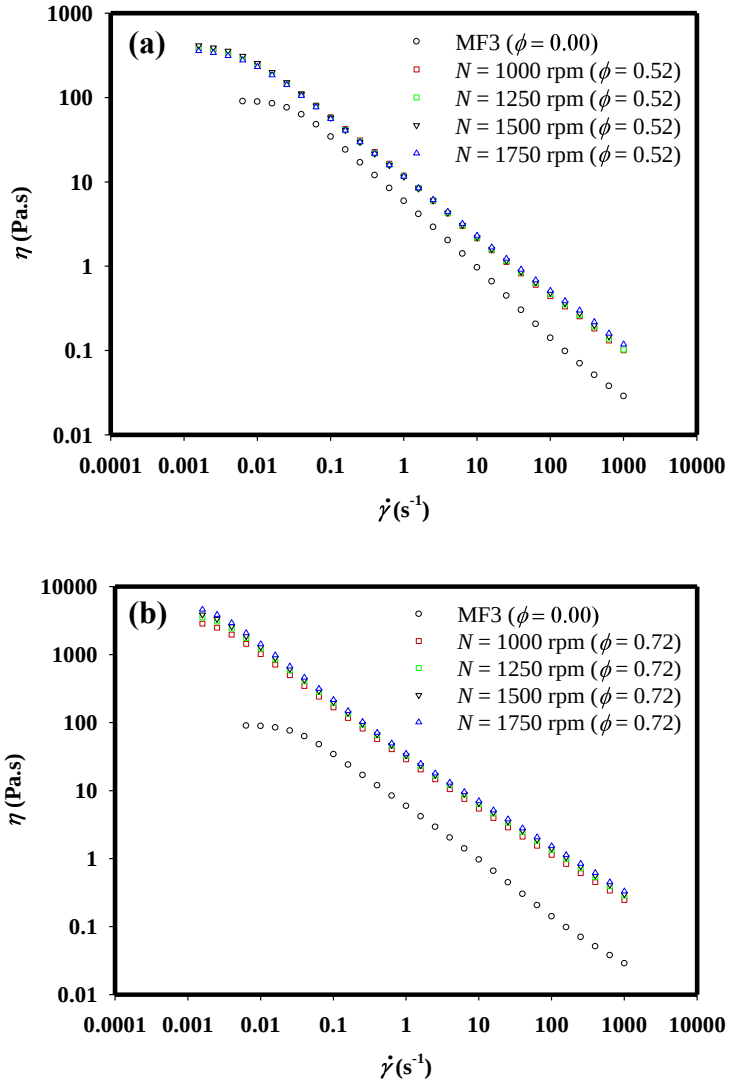

Fig. 6.9: Effects of initial bubble size distribution on the flow curve of the aerated MF3 fluid.

6.3.3.3 Effects of air volume fraction

The effects of air volume fraction were investigated over the range $0 \leq \phi \leq 0.72$, and are illustrated in Fig. 6.10a for foams generated from MF3 at N = 1000 rpm. The same shear-thinning behaviour was observed at all air fractions. The flow curves were well fitted by a Carreau model (Eq. 6.4) over a shear rate range of 0.001-1000 s^{-1}; the corresponding Carreau model parameters are summarised in Table 6.3. The zero-shear viscosity increases exponentially with ϕ. Similarly, the fluid time constant (λ) which can be considered a measure

of the rate of reversible microstructure breakdown which causes the initial transition from Newtonian to shear-thinning behaviour, also increases exponentially as a function of ϕ. Drier foams, therefore, are much more viscous, exhibit their shear-thinning behaviour at lower shear rates as indicated by their sharply declining critical shear rate ($\dot{\gamma}_c = 1/\lambda$) with ϕ (see Table 6.2).

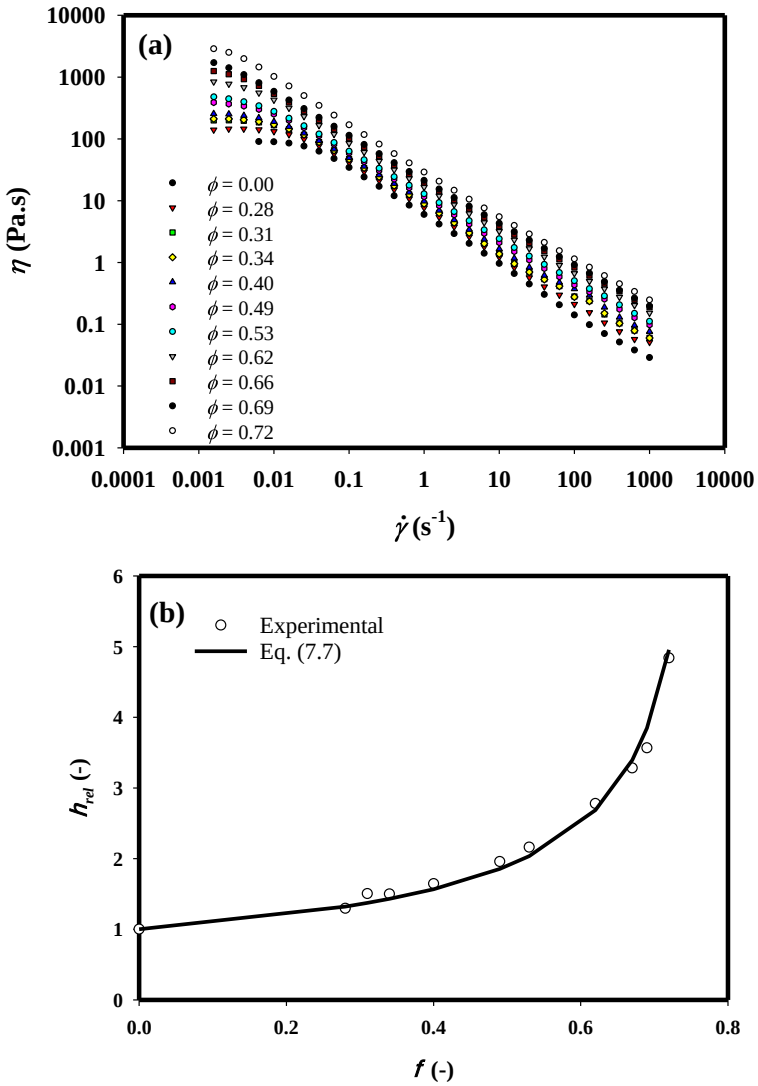

Fig. 6.10: Rheological behaviour of foams with varying air volume fraction generated from fluid MF3 at N = 1000 rpm: (a) flow curves; and (b) relative viscosity at $\dot{\gamma}$ = 0.1 s^{-1}.

Table 6.3: Summary of Carreau model parameters for model fluid MF3 and foams with varying air volume fraction generated at N = 1000 rpm; G/L = 0.4 – 2.5 ($0.28 \leq \phi \leq 0.72$).

ϕ_e (-)	η_o (Pa.s)	η_∞ (Pa.s)	λ (s)	n (-)	R^2 (-)	$\dot{\gamma}_c$ (s^{-1})
0.00	100	0.007	35	0.20	0.999	0.0286
0.28	140	0.008	50	0.25	0.999	0.0184
0.31	200	0.009	60	0.25	0.998	0.0170
0.34	210	0.010	70	0.25	0.999	0.0154
0.40	255	0.030	90	0.25	0.999	0.0126
0.49	380	0.040	110	0.25	0.996	0.0091
0.53	476	0.060	140	0.25	0.996	0.0079
0.62	840	0.070	200	0.25	0.999	0.0056
0.67	1250	0.100	250	0.25	0.996	0.0047
0.69	1708	0.100	300	0.25	0.987	0.0043
0.72	2860	0.100	400	0.25	0.999	0.0025

Torres *et al.*, (2015) found that the relative viscosity of bubbly liquids, i.e. the ratio of the apparent viscosity of the aerated fluid to that of the base liquid ($\eta_{rel} = \eta_f/\eta_l$), generated from guar gum in concentrations up to 10 g L^{-1} was satisfactorily fitted by the correlation developed by Stein and Spera (1992), thus:

$$\eta_{rel} = 1 + a'\phi \qquad \text{(Eq. 6.6)}$$

In their study, $a' = 1.25$ in contrast to a value of 13.1 found by Stein and Spera (1992) for dilute emulsions (ϕ < 0.3) (Stein and Spera, 1992). Our data could not be fitted by the above correlation but instead was very well fitted (R^2 = 0.994) by the Krieger Dougherty (1959) relationship for concentrated dispersions, as shown in (Eq. 6.7)\, thus:

$$\eta_{rel} = \frac{\eta_f}{\eta_l} = \left(1 - \frac{\phi}{\phi_m}\right)^{-[\eta]\phi_m} \qquad \text{(Eq. 6.7)}$$

where ϕ_m is the maximum packing fraction and $[\eta]$ is the intrinsic viscosity for a suspension of spheres. The intrinsic viscosity accounts for the particle/bubble shape characteristics while the maximum packing fraction accounts for particle shape characteristics, degree of flocculation, and particle size distribution. Here, ϕ_m = 0.78 for our polydisperse foams which is consistent with values reported in the literature for polydisperse dispersions (0.74 – 0.78), as discussed above (Sjoblom, 2001, Lexis and Willenbacher, 2014) and $[\eta]$ = 0.80 which is less than the value of 2.5 for monodispersed spheres (Krieger Dougherty, 1959) spheres, possibly due to deformation of bubble interfaces at high air volume fractions.

The viscosity curves in Fig. 6.10a could be fitted using a generalised dimensionless form of the Carreau-Yasuda model defined as (Boyd,Buick and Green, 2007):

$$\eta^+ = \frac{\eta}{\eta_0} = \left\{1 + \left(\frac{\lambda}{\lambda_0}.\frac{\dot{\gamma}}{\dot{\gamma}_c}\right)^a\right\}^{n-1/a} \qquad \text{(Eq. 6.8)}$$

where η^+ is the normalised zero-shear viscosity and a is a constant. The time constant is normalised by introducing λ_0 = 1 s. An excellent fit was obtained (R^2 = 0.993) as shown in Fig. 6.11 with all data collapsing approximately on one single curve, where n = 0.3, a = 2.0 and λ = 1.5 s.

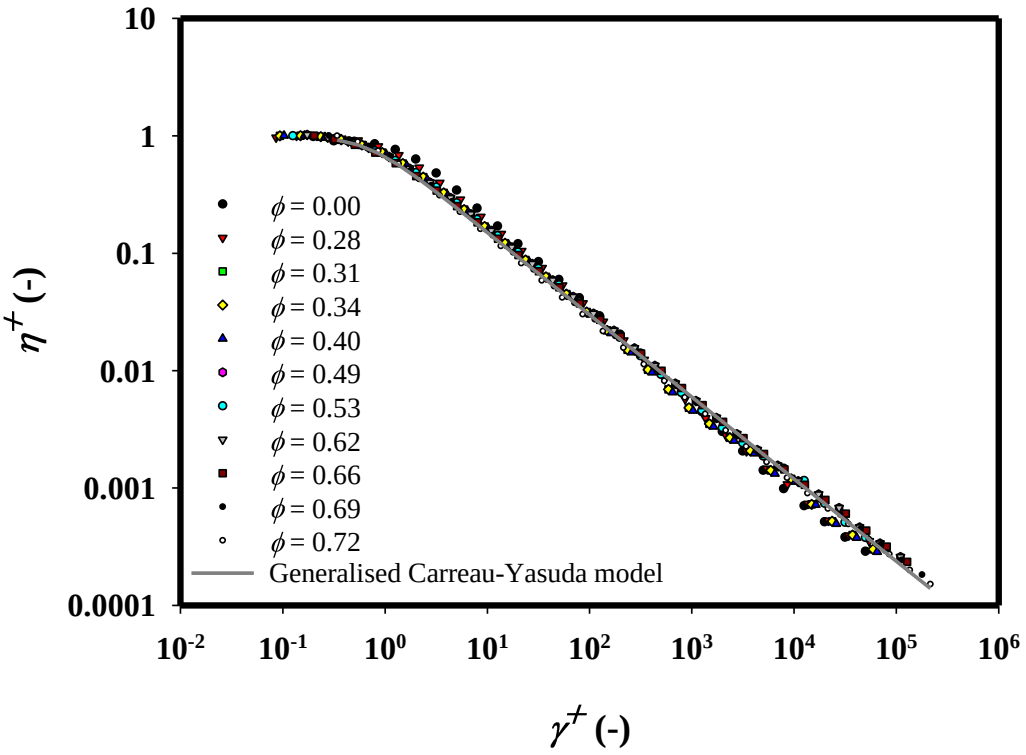

Fig. 6.11: Generalised Carreau-Yasuda model fitted to steady flow curves of fluid MF3 and foams shown in Fig 6.10a.

The zero-shear viscosity and critical shear rate functions in (Eq. 6.8) were determined experimentally and plotted in Fig. 6.12a. The zero-shear viscosity can be well predicted by the following correlation:

$$\eta_0 = Aexp^{(B\phi)} + Cexp^{(D\phi)} \qquad \text{(Eq. 6.9)}$$

where, A = 1.48 × 10^{-6}, B = 29.04, C = 48.35, and D = 4.32 (R^2 = 0.999). The critical shear rate (Fig. 6.12b) can be best modelled by introducing the following relationship which is of the same form as the dimensional Carreau-Yasuda model (Eq. 6.8), thus:

$$\frac{\dot{\gamma}_c - \dot{\gamma}_{c,\infty}}{\dot{\gamma}_{c,0} - \dot{\gamma}_{c,\infty}} = \left\{1 + (\propto \phi)^{\beta}\right\}^{\delta-1/\beta} \qquad \text{(Eq. 6.10)}$$

where in the range $0 < \phi < 0.72$, $\dot{\gamma}_{c,0} = 0.028$ s^{-1}, $\dot{\gamma}_{c,\infty} = 0.0009$ s^{-1}, $\propto = 1.30$, $\beta = 4.04$ and $\delta = -2.5$ ($R^2 = 0.992$). The model predicts an upper plateau corresponding to $\dot{\gamma}_{c,0}$ at low ϕ values, and a lower plateau corresponding to $\dot{\gamma}_{c,\infty}$ at high ϕ values. The above relationships should enable the prediction of the apparent viscosity of the types of aerated fluids studied here and should probably hold for other different formulations based on similar shear-thinning polymers. Such relationships would, for example, be useful additions to numerical codes to assist the modelling of such complex fluids.

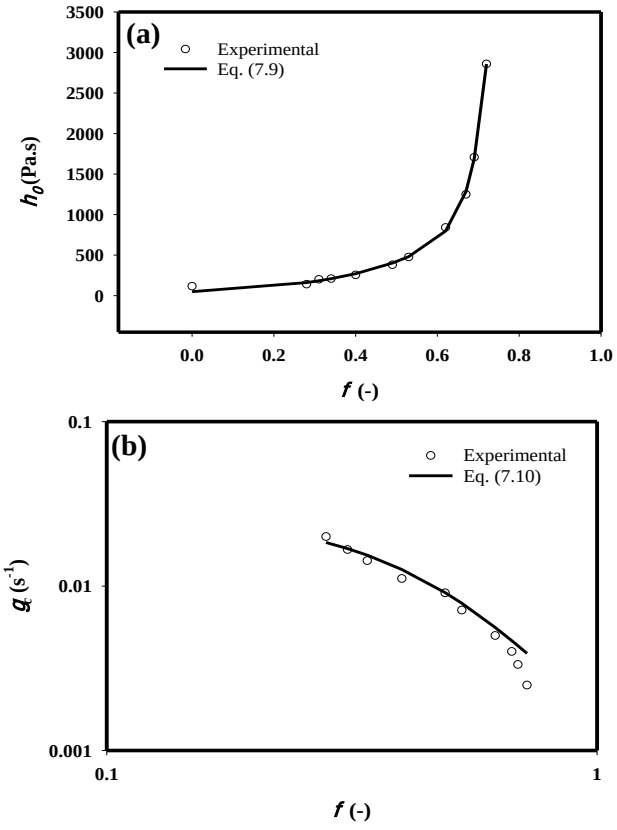

Fig. 6.12: Effects of air volume fraction of foams generated from fluid MF3 at N = 1000 rpm on: (a) zero-shear viscosity; and (b) critical shear rate.

6.3.3.4 Normal stresses

The single-phase fluids exhibited no significant normal stresses within the range of shear rates investigated ($0.001 > \dot{\gamma} < 1000\ s^{-1}$). A recent study conducted by Dakhil, Auhl and Wierschem (2018) on much more viscous aqueous XG solutions showed that normal stresses appeared only during the application of very high shear rates ($\dot{\gamma} > 1000\ s^{-1}$). Such normal stresses were attributed to the disentanglement of polyelectrolytes rather than viscoelastic deformation (Dakhil,Auhl and Wierschem, 2019). However, when foams with $\phi_e \approx \geq 0.67$ were sheared, significant normal forces were exhibited, as shown in Fig. 6.13. The normal stresses are smaller than but comparable to the shear stresses in the foam. Therefore, such foams would be expected to manifest significant elastic behaviour at high air fractions and high shear rates.

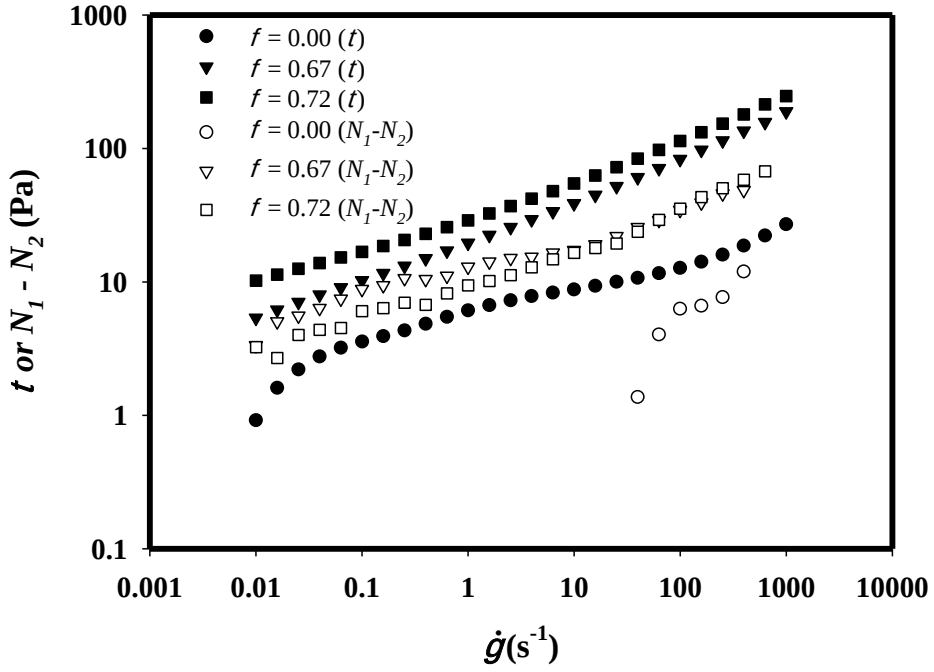

Fig. 6.13: Normal stress difference in foams generated from fluid MF3 at N = 1000 rpm.

There are several reasons why, for the wet foams generated at a higher air volume fraction, the magnitude of the normal stress approaches that of a shear stress. First, the bubble matrix becomes much more packed which exerts a significant amount of normal force on the upper plate. Secondly, the bubbles become much more uniform and smaller possessing a higher Laplace pressure which exerts a significant degree of normal force on the upper plate. This is evident during the measurement especially when operating at a higher shear rates investigated since the samples were ejected from the geometry.

6.3.4 Oscillatory shear measurements

6.3.4.1 Identification of linear viscoelastic region

Prior to frequency sweep tests, it was necessary to identify the linear viscoelastic region (LVR) using amplitude sweep test at 1 Hz frequency with percentage amplitude strain (% strain) varied in the range of 0.01 – 1000 %. Fig. 6.14 shows typical results for foam samples generated from fluid MF3 at N = 1000 rpm and G/L = 0.5, 1.0, 1.5 and 2.0. Both storage (G') and loss (G'') moduli were constant within 0.01 – 10 % amplitude strain values. The $G'$was always greater than G'' meaning these model fluids showed more elastic than viscous behaviour – as expected. At approximately 10 % strain amplitude, there was a rapid drop in both moduli and a cross-over was observed. Beyond this point, the microstructure is destroyed and hence the viscous moduli take precedent. Likewise, the mechanical spectra for foam samples generated from all model fluids showed a similar trend.

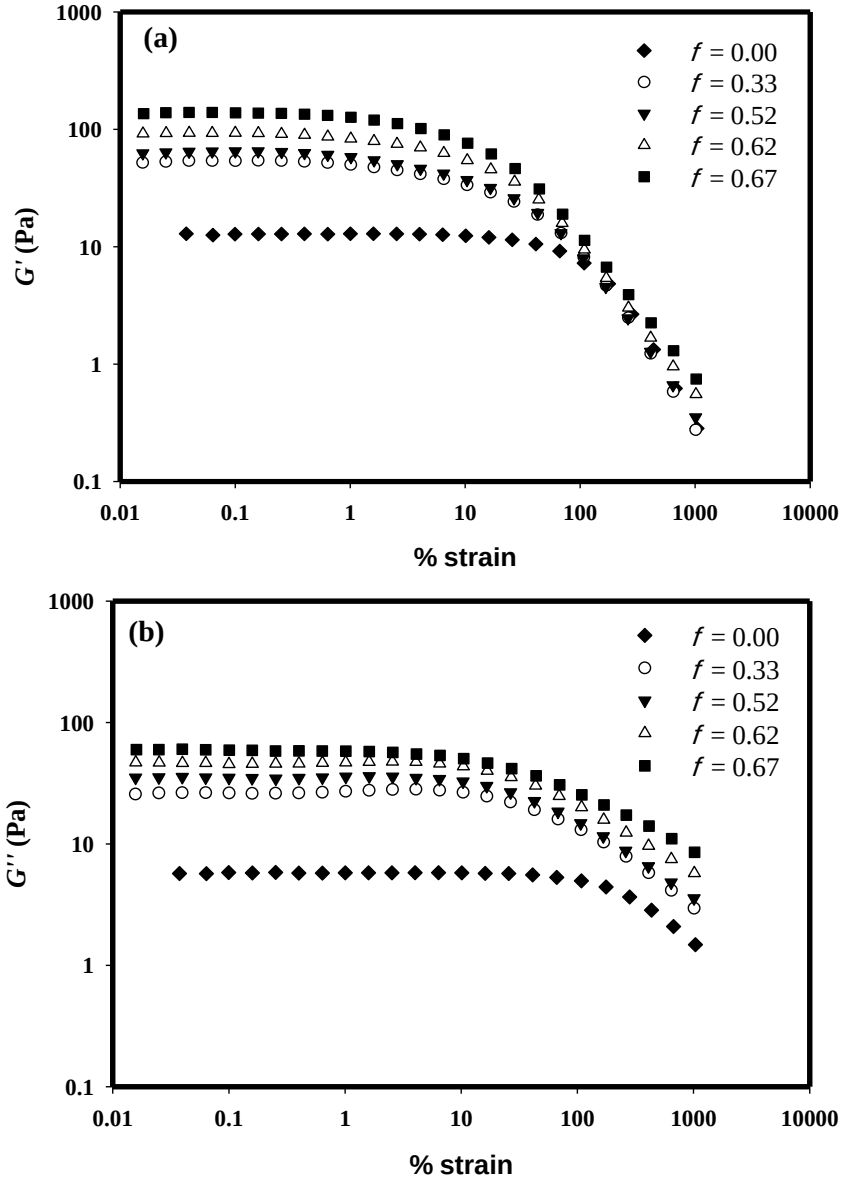

Fig. 6.14: Typical LVR's of fluid MF3 and wet foams obtained through oscillatory shear measurements at constant frequency of 1 Hz with % strain amplitude varying in the range of 0.01-1000%: (a) storage modulus (G'); and (b) loss modulus (G'').

6.3.4.2 Effects of xanthan gum concentration

Non-destructive oscillatory tests were conducted to probe the viscoelastic properties of the model fluids and foams generated at various air volume fractions. Typical mechanical spectra are presented in Fig. 6.15. For all fluids, both moduli are strongly dependent on frequency, increasing by at least three orders of magnitudes over the range studied. Aeration leads to enhancement of both moduli at all frequencies. The crossover frequency (where $G' = G''$) was found to be a function of both XG concentration and air volume fraction, as previously reported by Torres *et al.*, (2013; 2015) for aqueous guar gum solutions. For MF1 (0.25 wt% XG) and MF2 (0.35 wt% XG), the crossover frequency decreases as the air volume fraction increases, similar to data reported for other polysaccharide solutions in the entangled regime (Torres,Hallmark and Wilson, 2015b, Torres,Gadala-Maria and Wilson, 2013). In contrast, for MF2 which has a higher XG concentration (0.5 wt%), G' lies above G'' at all frequencies investigated and there is no cross over.

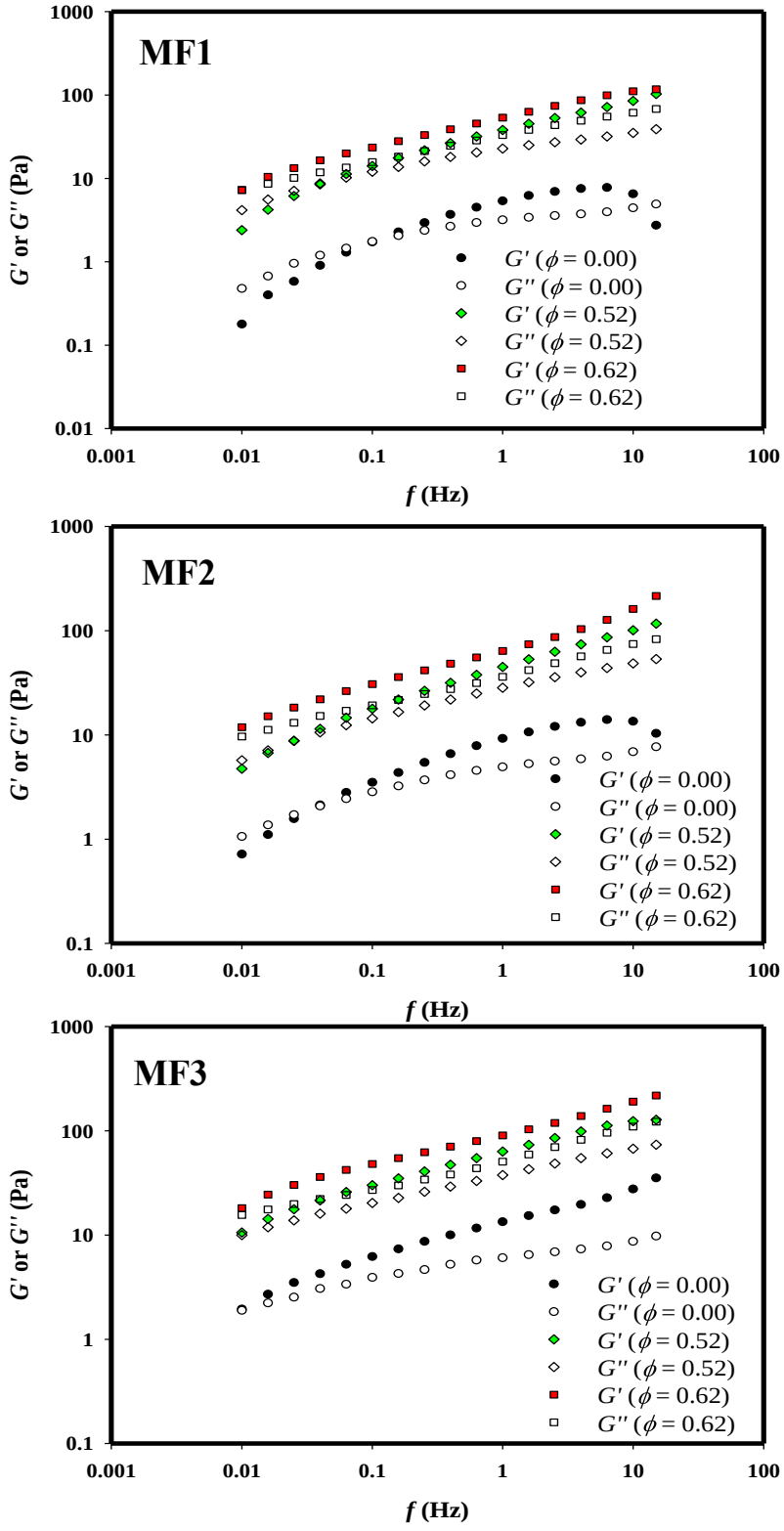

Fig. 6.15: Typical mechanical spectra of model fluids and foams generated at N = 1000 rpm.

6.3.4.3 Effects of air volume fraction and bubble size distribution

Increasing the rotor speed, as discussed above, reduces and homogenises the bubble size. For ϕ < ≈ 0.60, these refinements in bubble size had negligible effect on the storage modulus (G') of the aerated fluid relative to that of the base liquid (G_0'). Typical results for MF3 are depicted in Fig. 6.16. This result is in agreement with observations reported by Torres et al., (2015) for aqueous guar gum solutions. At higher gas fractions (ϕ ≈ > 0.60), however, the introduction of air causes G' to increase linearly with *N*, hence, generating substantial elasticity above that of the base liquid. X-ray micro-CT images showed the bubbles to be spherical in the air volume fractions range of $0.28 \leq \phi \leq 0.72$ and, hence, packing transition is not reached within the range of air fractions studied. As discussed above, the extra elasticity stems from the more complex film network and the higher internal Laplace bubble pressure.

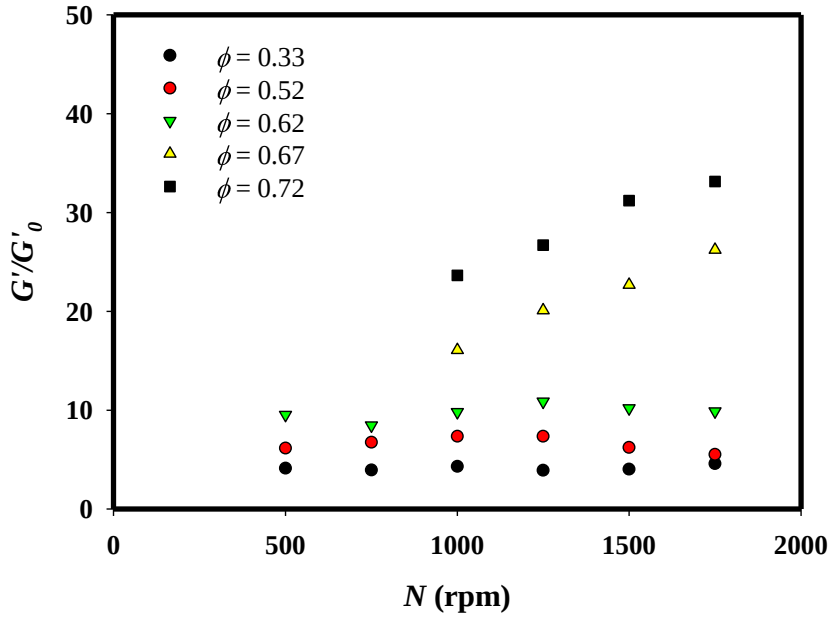

Fig. 6.16: Effects of rotor speed and air volume fractions on G'/G'_0 at 0.1 Hz for fluid MF3.

6.3.5 Visualisation of foams under steady shear

As discussed above, at high shear rates ($\dot{\gamma} \approx > 100\ s^{-1}$) the foam displays significant irreversible time dependence. Previously, this behaviour was attributed to significant microstructural changes caused by shearing, i.e. breakage of larger bubbles into smaller bubbles in both quasi-dry foams and bubbly liquids, which were measured by examining samples off-line at the end of shearing experiments (Torres,Gadala-Maria and Wilson, 2013, Golemanov *et al.*, 2008, Chesterton *et al.*, 2013). In our case, however, foam samples taken at the end of a shear rate sweep and imaged offline using X-ray micro-CT, showed little change in foam structure and bubble size distribution. Some authors defined a critical dimensionless shear stress criterion τ^* (Eq. 6.2) above which bubble breakage should occur. Slightly different values (0.03; 0.30; 0.40) have been reported for τ^* for different bubbly liquids and quasi-dry foams (Golemanov *et al.*, 2008, Torres,Hallmark and Wilson, 2014, Chesterton *et al.*, 2013).

Here, considering all the experimental conditions of fluid formulation, shear rate, rotor speed and air volume fraction, the value of the critical shear stress was within the range $0.0004 < \tau^* < 0.25$. These values are well below 0.40 which suggests that no bubble breakage should be expected in the rheometry experiments. Indeed, in-situ visualisation of the foams under shearing using the optical cell described above (Fig. 6.1), did confirm the absence of bubble breakage. The lack of foam breakage can be explained by considering the shear rates used to generate the foams in the multi rotor-stator device. The average shear rate in the mixing head chamber was well above the maximum shear rate used in the rheological characterisation of the foams. Hence, the foams are not expected to experience any further breakage since their texture has already been refined down to an equilibrium state in the processing unit.

Typical shear stress transients obtained at controlled shear rate are depicted in Fig. 6.17a, together with corresponding digital sample images in Fig. 6.17b taken at the end of the shearing experiment (300 s). The time dependence observed for $\dot{\gamma} \approx > 100$ s^{-1} in Fig. 6.17a is attributed to the onset of shear-induced migration of liquid taking place from the periphery of the parallel-plate geometry to the centre. The images in Fig. 6.17b depict the situation at the end of the experiment (300 s) where for $\dot{\gamma} \approx > 100$ s^{-1} a considerable amount of liquid has accumulated at the centre of the plates.

The extent of liquid accumulation at the centre of the plates varied as a function of a number of parameters including the foam liquid holdup, magnitude of shear rate, time of shearing, fluid composition, parallel plate gap and bubble size. Oscillations appear in the shear stress transients for $\dot{\gamma} \approx > 400$ s^{-1} (Fig. 6.17c). Visualisation of the aerated fluid at constant shear rate shows that such oscillations are caused by radial migration of liquid towards the centre of the parallel plates, followed by radial liquid redistribution from the centre backwards. These phenomena highlight the complexities involved in studying the rheology of aerated fluids, especially at high shear rates.

The transient observed during the application of a constant shear rate can be explained as follows. As stated previously, in the parallel plate geometry, the shear rate acting across the gap is non-uniform and hence there is a shear rate gradient across the gap forcing the liquid contained within the wet foam to flow from the periphery to the centre, i.e. shear-thinning effect. Simultaneously, the presence of an appreciable amount of normal force acting in the opposite direction causes the liquid to flow in the opposite direction. As a result, there is fluctuation observed in the shear stress response. Such a transient behaviour is undesirable for the processing of foams since it can significantly alter the microstructure of the final foam

product and hence its final quality attributes, i.e. texture, stability, flow and related mechanical properties. Therefore, it is advisable to avoid the processing of such foams under high steady shear conditions.

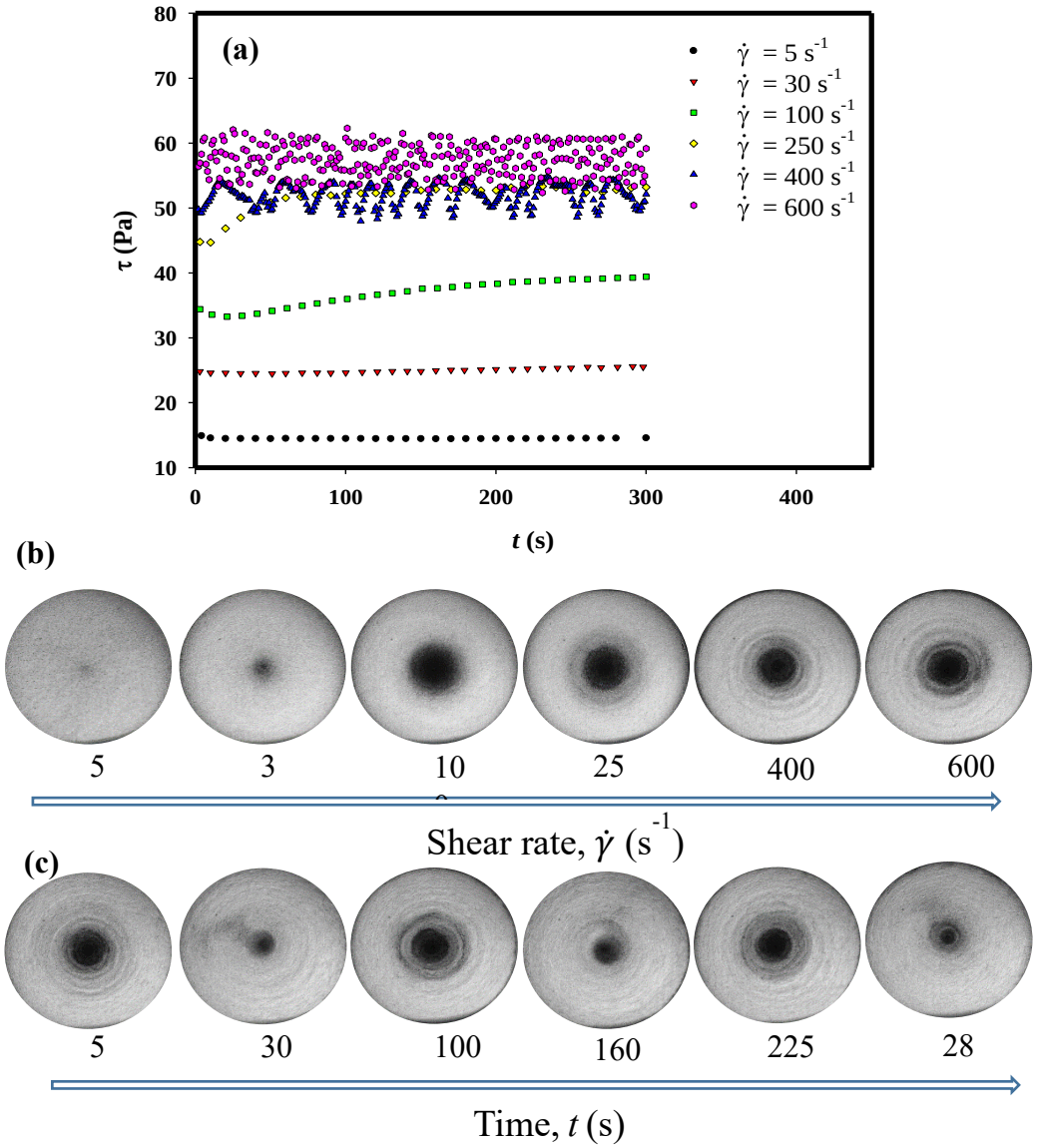

Fig. 6.17: Visualisation under steady shear of foams generated from fluid MF3 at G/L = 1.0; ϕ_e = 0.52; N = 1000 rpm: (a) typical shear stress transients; (b) digital images taken at t = 300 s; (c) digital images taken at $\dot{\gamma}$ = 600 s^{-1}.

6.4 Conclusion

The rheological properties of wet foams produced in a continuous pilot-scale multi rotor-stator device have been studied. The foams were generated from viscous shear-thinning liquids consisting of aqueous solutions of xanthan gum in the entanglement regime and caster sugar and stabilised with a non-ionic food grade surfactant (PGE 55). At air volume fractions of $\phi <$ ≈ 0.60, the bubble size distribution had a negligible effect on the steady shear flow curves and viscoelastic properties of the foam. However, at air volume fractions of $\phi \approx > 0.60$, the apparent viscosity and storage moduli increase significantly as bubble size becomes smaller and more uniform with increasing rotor speed. This in turn leads to a The foam flow curves were well fitted by a generalised dimensionless form of the Carreau-Yasuda with all data collapsing on approximately a single curve over the range of air volume fractions investigated ($0 \leq \phi \leq 0.72$). The foams exhibited significant normal stresses but only for the highest air fractions studied (ϕ $\approx > 0.67$).

At high air volume fractions, the magnitude of the normal stress approaches that of a shear stress possibly due to several reasons. First, the bubble matrix becomes much more packed which exerts a significant amount of normal force on the upper plate. Secondly, the bubbles become much more uniform and smaller possessing a higher Laplace pressure which exerts a significant degree of normal force. This is evident during the measurement especially at high shear rates investigated at which point the sample is ejected from the geometry.

The low value of the critical dimensionless shear stress ($\tau^* < 0.25$) suggested that under steady shear conditions, no bubble breakage should be observed, which was confirmed by simultaneous in-situ visualisation of the foam. The time dependence of the foams exhibited at

high shear rates ($\dot{\gamma} \approx > 100$ s^{-1}) is attributed to the onset of shear-induced migration of liquid taking place from the periphery of the parallel-plate geometry to the centre, as confirmed by in-situ flow visualisation during shearing. At much higher shear rates ($\dot{\gamma} \approx > 400$ s^{-1}), oscillations appear in the shear stress transients which are caused by radial migration of liquid towards the centre of the parallel plates, followed by radial liquid redistribution from the centre backwards.

A possible mechanism for the radial migration of liquid is proposed to be due to the combined influence of shear-thinning effects and normal force. The former causes the liquid contained within the matrix of the wet foams to radially migrate from the periphery to the centre of the parallel plate geometry. Whereas, the former force causes the liquid to flow in the opposite direction and hence the observation of fluctuation in the shear stress. To elucidate the magnitude of these forces will require further experimental work. In summary, these phenomena highlight the complexities involved in studying the rheology of aerated fluids, especially at high shear rates.

Notation

a	Carreau-Yasuda rate constant (-)
d	bubble diameter (m)
D_{32}	Sauter mean diameter (m)
f	frequency (Hz)
F_{rel}	relative number bubble frequency (%)
G/L	ratio of volumetric flowrate of air to liquid (-)
G'	storage modulus (Pa)
G'_0	storage modulus of liquid (Pa)
G''	loss modulus (Pa)
MF1	model fluid 1
MF2	model fluid 2
MF3	model fluid 3
n	flow behaviour index (-)
N	rotational speed (s^{-1})
N_1-N_2	normal stress difference (Pa)
PGE 55	polyglycerol ester of fatty acid (-)
t	time (s)
XG	Xanthan gum (-)
X-ray micro-CT	X-ray micro-Computed Tomography (-)

Greek symbols

η	apparent viscosity (Pa.s)
η_0	upper Newtonian region viscosity (Pa.s)
η_∞	lower Newtonian region viscosity (Pa.s)
η_{rel}	relative viscosity (Pa.s)
η^+	normalised zero-shear viscosity (-)
ϕ	air volume fraction (-)
ϕ_e	experimental air volume fraction (-)
$\dot{\gamma}$	shear rate (s^{-1})

γ^+	normalised shear rate (-)
$\dot{\gamma}_c$	critical shear rate (s^{-1})
τ	shear stress (Pa)
τ^*	dimensionless critical shear stress (-)
λ	Carreau-Yasuda time constant (s)

Abbreviations

BSD	bubble size distribution
G/L	ratio of air and liquid volumetric flowrate
MF1	model fluid 1
MF2	model fluid 2
MF3	model fluid 3
PGE 55	polyglycerol ester of fatty acid
XG	Xanthan gum
X-ray micro-CT	X-ray micro-Computed Tomography

Chapter 7: Conclusions and Future Work

The main objectives of the work presented in this thesis were to establish optimum processing conditions and liquid formulation parameters for the formation of fine-textured and statically stable wet foams from shear-thinning fluids using a continuous multi-stage rotor-stator device and to study its flow behaviour and dynamic interaction with processing equipment. The use of a non-ionic surfactant, PGE 55, xanthan gum and castor sugar enabled the generation of highly statically and quasi-dynamically stable foams. Therefore, in the proceeding sections, a summary of each results chapter along with the key findings will be provided. In addition, recommendations for potential future work on some of the experimental concepts developed within this thesis are elucidated.

7.1 Conclusions

7.1.1 Foam Imaging – comparison between 2D light microscopy and 3D X-ray micro-Computed Tomography techniques

Two-dimensional light microscopy imaging technique is well-established for the determination of bubble size distribution and hence Sauter mean bubble diameter. The method, however, requires significant sample tempering; it is semi-automatic; tedious; and hence suffers from several shortcomings. Significant discrepancies can arise when unstable, non-homogenous foams possessing larger air bubbles are investigated. Any out-of-focus bubbles, when analysed, can either under- or over-predict the actual bubble size distribution and hence the final mean bubble diameter. The degree of error arising is strongly dependent on several factors including the number of bubbles analysed, the depth of the visualisation chamber and image processing procedure implemented. For wet foams investigated in this study, a minimum of 500 bubbles are necessary to obtain a statistically representative and reliable Sauter mean diameter.

For the majority of cases, X-ray micro-CT was successful in imaging the microstructure of a range of wet foams generated from shear-thinning fluids using a continuous rotor-stator device. An imaging protocol developed enabled the 2D and 3D processing of these images using a CTan software. Low to negligible discrepancy was obtained between 2D and 3D analysis mainly due to small bubble size and a uniform bubble size distribution. The air volume fraction predicted by the Saltykove's analysis was close to the experimental value but slightly lower than predicted by the CTan software. The approximately 8% discrepancy is possibly due to the noise introduced during image thresholding using CTan. In addition, a comparison of D_{32} values

obtained shows a similar trend but with CTan predicting a smaller value of 296 μm in comparison to 360 μm from 2D analysis and 346 μm using Saltykove's analysis. The under-prediction by the CTan was not surprising since during image processing some of the larger bubbles were split into many smaller bubbles as described in section 3.3.2.1. Indeed, X-ray micro-CT is a very powerful non-invasive technique for obtaining three-dimensional microstructure as well as detailed quantitative information on the inner cellular structure. Such information included voidage, bubble size distribution, degree of anisotropy and cell-wall thickness.

X-ray micro-CT technique also has its limitations. For the very wet foams generated at $N < 750$ rpm and G/L ratio < 1.0, gravity drainage is the predominant mechanism and hence likely to take place during X-ray imaging leading to poor quality images in which the bubbles are distorted at the edges. Automatic 3-D analysis using CTan was not possible since these distorted bubbles were split into many smaller bubbles giving rise to error. In contrast, foam coarsening is the predominant mechanism for wet foams generated at high G/L ratio (i.e. > 2.0) and rotor speeds (N > 1750 rpm). These foams possessed smaller bubbles and a more packed bubble matrix. The former leads to higher Laplace pressure which in turn increases the rate of disproportionation due to increased air solubility. The latter meant neighbouring bubbles were more likely to contact each other and hence coalesce. Therefore, any foam sample which has a destabilisation time constant of less than X-ray scanning duration (approx. 20 minutes in this study) is likely to affect image acquisition and hence 3D image processing using CTan software.

In summary, this study has shown that X-ray micro-CT is useful in obtaining detailed 3D microstructural details which is important for a wide range of industries including food

processing. Such information, for example, can be used to relate the microstructure to flow and rheological properties.

7.1.2 Foams generated from viscous non-Newtonian shear-thinning liquids in a continuous multi rotor-stator device

Aeration is ubiquitous in the food industry and innovative ways to generate stable foams with fine texture from viscous non-Newtonian media are needed to satisfy the increasing demand for better quality, healthier and cheaper products. The use of continuous multi rotor-stator devices operating in turbulent flow and under atmospheric pressure achieves optimum aeration efficiency and prevents foam expansion. The use of an effective surfactant such as PGE 55 and a thickener such as xanthan gum help provide the desired fine texture and stability for longer shelf-life.

A multi rotor-stator device is effective for producing foams in highly viscous media. This study focused on the production of wet foams from pseudoplastic model fluids using a continuous rotor-stator device. For a fixed 12 rotor-stator units and hence geometry, the combined influence of processing parameters (rotor speed, gas-liquid volumetric flowrate (G/L ratio)) and liquid bulk properties (surfactant PGE 55 content, xanthan gum concentration) were extensively investigated. Hydrodynamic conditions and liquid formulation are critical to aeration efficiency. Independent of residence time, aeration efficiency was achieved for the majority of rotor speeds and G/L ratios investigated and hence 'blow-by' phenomenon only took place at very high G/L ratios and at N < 750 rpm. Blow-by (formation of undispersed gas slugs) was independent of xanthan gum concentration and the effects of PGE 55 concentration only became apparent at low rotor speed and higher G/L ratios. Operating at very high G/L ratios ≈

> 2.5, blow-by phenomenon was unavoidable and hence theoretical aeration efficiency was not achieved for any of the rotor speed investigated. In these cases, the air left the mixing-head chamber in the form of undispersed gas-slugs i.e. blow-by took place.

Rotor speed, dispersion viscosity and high residence times are critical to foam microstructure. In general, with an increase in rotor speed, an exponential decrease in Sauter mean bubble diameter was found and the effects of rotor speed and hence energy input became less significant at the highest rotor speed investigated. At a much higher rotor speeds (N > 1750 rpm), an equilibrium is reached between bubble breakage and coalescence. This is attributed to the chain melting of the monolayer which causes the bubble surface to become fluid-like and hence can be easily displaced/rearranged. Thus, operating at rotor speed beyond 1750 rpm is not economical in terms of energy efficiency and in terms of obtaining the desired microstructure. Similarly, increasing the G/L ratio led to a smaller bubble size and a more uniform bubble size distribution. This was counter-intuitive to expectation since operating at a higher G/L ratio led to a reduction in residence time and hence the shear history of the dispersion inside the mixing-head chamber. The inconsistency, however, was attributed to an increase in foam apparent viscosity achieved at a higher G/L ratio which in turn imparts additional forces which breaks down larger air bubbles into many smaller bubbles.

The shear rate inside the mixing-head chamber was estimated by using an equation proposed by Muller-Fischer, Bleuler, and Winfhab, (2007) and hence for the majority of experimental conditions investigated, turbulent flow regime was identified. In turbulent flow, the Power number is constant and hence independent of Reynolds number. In contrast, another method proposed by Metzner and Otto (1957) predicted, for the vast majority of experimental conditions, a laminar flow. The energy input during the production of foam using a continuous

rotor-stator is an important parameter for process design and optimisation. As expected, both G/L ratio and *N* were responsible for the energy input. Operating beyond 1750 rpm is not desirable in terms of energy efficiency and foam microstructure. Similarly, a Weber number definition, proposed by Thakur and Djelveh (2003), was utilised to combine the effects of processing parameters and liquid properties so that a generalised curve could be obtained. Such a graph revealed the existence of two turbulent flow regime namely inertial and viscous.

Foam static stability, govern by the combined effects of gravity drainage, collapse and coarsening, was assessed by storing under a controlled temperature environment. In 3D foams all these processes occur simultaneously and at varying rates. Depending on the storage temperature, foams generated under most processing conditions were statically stable for a long period of time – up to many months. In addition, other factors responsible for imparting high static stability to wet foams were the air volume fraction, rotor speed, xanthan gum and PGE 55 concentration.

Wet foams drainage, collapse and coarsening was drastically reduced when stored at a lower temperature (i.e. 5 °C) and this was attributed to the lower mobility of multilamellar vesicles of PGE 55. As a result, they are more likely to clog the Plateau borders and hence significantly diminishing foam drainage and collapse. Similarly, an increase in XG concentration led to an increase in zero-shear Newtonian viscosity of the bulk liquid which was able to resist the gravitational forces and hence foam drainage and collapse. In addition, increasing the PGE 55 content meant a higher density of multilamellar vesicles of PGE 55 in the bulk and at the interface and thus providing more resistance to foam drainage and collapse.

Foam coarsening was assessed by acquiring three-dimensional images using X-ray micro-CT technique for a set period of time. A higher G/L ratio and rotor speed were the main parameters responsible for the increased rate of coarsening – disproportionation and bubble coalescence. A higher G/L ratio and rotor speed led to the formation of thinner film network and hence the resulting foams were more prone to the process of coarsening.

7.1.3 Dynamic interactions of foamed viscous shear-thinning fluids with an orifice flow constriction

A foam flow rig was built to investigate the effects of rapid pressure drop on wet foams' microstructure. The effects of orifice aperture, surfactant PGE 55 content, xanthan gum concentration and rotor speed were elucidated. Wet foams were generated in the absence and presence of a narrow orifice flow constriction to achieve rapid pressure drop. Unsurprisingly, in the absence of a flow constriction, flow through a short straight pipe incurred insignificant pressure drop which was not sufficient to cause structural transformation. Surprisingly, these wet foams also showed high static stability and resistant to structural transformation even when passed through a narrow orifice constriction of 1.8 mm aperture; provided no significant pressure drop took place. Significant structural transformation, however, took place when such wet foams were exposed to high pressure drop (> 100 kPa) and the effects became more apparent at a higher gas-liquid volumetric flowrate (G/L) ratio. A combination of higher bubble density and thinner film network were some of the parameters responsible for the increased coalescence rate. A loss of foam air volume as a result of foam expansion and bubble coalescence led to a much coarser and highly statically unstable foams.

Increasing the surfactant PGE 55 content, xanthan gum concentration and rotor speed led to improved resistant to structural transformation. A higher PGE 55 content in the bulk implied a higher density of PGE 55 multilamellar vesicles which is possibly able to clog the Plateau borders and hence prevent bubble from coalescing during foam expansion. Similarly, a higher xanthan gum concentration meant thicker draining film which provides extra resistance to gravity drainage and hence bubble coalescence. The effects of rotor speed, however, became only significant at a rotor speed of N = 2000 rpm. Such a wet foam, with a more uniform bubble size distribution, was able to pass through a narrow orifice constriction with a relatively less bubble coalescence rate. It is therefore apparent that the rate of bubble coalescence is ultimately dependent on the rate of film thinning. In summary, any parameter/process that can improve the stability of the thin film essentially leads to improved resistant of foam to bubble coalescence. For example, air bubbles with a smaller diameter possess larger Laplace pressure which is able to resist external deformational forces such as mechanical, shear and elongational. Similarly, increasing the bulk liquid viscosity (i.e. by varying the micelles concentration) leads to a reduction in film thinning and hence coalescence.

In the food processing industry, it is a common practice to conduct foaming operation under pressurised conditions (i.e. 2 – 3 bar) using a continuous rotor-stator device so as to reduce the air volume fraction inside the mixing-head chamber and hence the rate of bubble coalescence. In this study, for a fixed 12 rotor-stator pairs and formulation, however, to avoid the process of bubble coalescence, it is crucial and recommended to generate foams under ambient conditions.

7.1.4 Rheological properties of wet foams generated from viscous pseudoplastic fluids

The use of a multi rotor-stator device is efficient at producing foams with a variety of textures and gas holdup from viscous fluids of complex non-Newtonian behaviour relevant to many industries, in particular food processing. Detailed knowledge of the rheological behaviour of such complex structured fluids and its generalisation to a wide range of formulation and characteristics, as developed in this work, is key to product rheological tailoring, process design and optimisation, scaleup and validation of numerical models and simulations. Understanding of the effects of the texture of foams on their rheology is important for the handling of foams, their interaction with processing equipment and the preservation of their microstructure.

An extensive study of wet foams rheometry consisting of steady shear flow and dynamical oscillatory tests were conducted using a 40 mm parallel plate geometry. Model shear-thinning fluids were foamed in a continuous rotor-stator device and foam texture modified by changing the composition and processing parameters. All model fluids showed strongly shear-thinning characteristics and the flow curves were well-fitted to the Carreau model. A typical flow curve is divided into three distinct regions consisting of zero-shear Newtonian, shear-thinning and a high-shear Newtonian, respectively. As expected, for an aqueous polysaccharide solution in the entanglement regime, the Carreau parameters were found to be a function of xanthan gum concentration. The critical shear rate, indication of transitioning from zero-shear Newtonian to shear-thinning region, was found to be a function of xanthan gum concentration and it decreased as the concentration was increased.

Foam viscosity is well described by a generalised Carreau-Yasuda dimensionless model. Inclusion of air, in the form of micro-bubbles, into all model fluids through means of mechanical whipping led to a considerable enhancement of shear-thinning characteristics. For the very wet foams, $\phi < \approx 0.60$, the foam texture had insignificant effect on the resulting flow curve. The effects of foam texture on the flow curve, however, became apparent for the wet foams generated at a higher air volume fraction. At $\phi \approx > 0.67$, a combination of increased bubble density, complex film network and the higher internal Laplace pressure associated with smaller air bubbles led to a significant increase in apparent viscosity especially at lower shear rates. All flow curves were successfully fitted and hence collapsed onto a single generalised Carreau-Yasuda model.

Unlike shear stresses, only certain fluids possess normal stresses and in this study a procedure developed for Gillette shaving foam was used to assess normal forces associated with model fluids and wet foams. At low shear rates, as previously observed in the literature, a significant amount of scatter was observed and this is attributed to many factors including variability in foam sample, surface tension effects, external noise and prior shear history of the sample. For the model fluids and for the very wet foams, zero to negligible normal forces were recorded especially when operating at a low shear rate range. For the wet foams generated at $\phi \approx > 0.67$ the magnitude of normal force reached that of a shear force. Such foams had a considerable normal stress difference and hence were ejected from the geometry upon approaching shear rate of 1000 s^{-1} and beyond.

Dynamic oscillatory tests were also conducted in the linear viscoelastic region (LVR) to probe the unperturbed structure of the model fluids and wet foams generated at various air volume

fractions. For all model fluids, both storage and loss moduli (*G'* and *G''*) were found to be a function of frequency with both increasing significantly with xanthan gum concentration and air volume fraction. In addition, both moduli increased as bubbles became smaller and the bubble size distribution more uniform. The smaller bubbles provided more resistance to the flow deformation as a result of an increased Laplace pressure. Similarly, a smaller and a more uniform bubble size distribution meant a much more complex interfacial network (consisting of films and Plateau borders) providing extra resistance to deformation.

Flow complexities can arise when investigating the rheological properties of complex fluids such as wet foams generated in this study especially when operating under high shear rates. Wall-slip phenomenon is one possibility which, however, was minimised using serrated geometry and by adopting a wider gap geometry. Another possibility includes bubble breakage that can occur which can significantly alter the experimental results and hence final conclusions. Wet foams generated in this study were highly statically and quasi-dynamically stable, even when passed through a short straight pipe and through a narrow orifice constriction without significant pressure drop occurring. Instead, using simultaneous in-situ foam visualisation showed, for the first time, the phenomenon of shear-induced migration of liquid. This is a process in which the liquid contained in the complex network of bubble films and Plateau borders of wet foams is migrated away from the periphery to the centre of a parallel plate geometry. Several factors are responsible for the phenomenon of shear-induced migration of liquid including the plate gap, model fluid composition, shear rate, roughness of plates and polydispersity.

7.2 Future Work

7.2.1 Foam Imaging – comparison between 2D light microscopy and 3D X-ray micro-Computed Tomography techniques

Currently, there is a huge demand for tools and techniques that can non-invasively probe the real 3D microstructure of complex fluids such as wet foams studied in this thesis. X-ray micro-CT is one such technique capable of achieving three-dimensional microstructural details. First and foremost, the technique can be extended to reveal the 3D microstructure of unstable wet foams generated in this thesis since there is a possibility that a large discrepancy exists between the 2D and 3D structural analysis. One way of achieving this is by implementing a better and more robust X-ray micro-CT device capable of operating at a much higher scanning speed. In addition, stereological technique (see for example Lim and Barigou, 2004) can be implemented to reveal the actual 3D microstructural information. The above is necessary for industries relying on interfacial area and for using the experimental data in computational fluid dynamics (CFD) simulation. Finally, the image acquisition and processing techniques developed in this thesis can be extended to study other more complex fluids including wet foams derived from other foaming formulation and foam generation techniques.

7.2.2 Foams generated from viscous non-Newtonian shear-thinning liquids in a continuous multi rotor-stator device

Foaming viscous non-Newtonian liquids using a multi-stage continuous rotor-stator device is vital for a wide range of industries especially for food processing since most real-life formulation (for instance whipped cream and ice cream) consists of complex fluids. For the study conducted, first and foremost, it is necessary to experimentally obtain the power

characteristics of the rotor-stator geometry so that a comparison can be made with results obtained from empirical correlation proposed by Krozen and Groot Wassink (1988). The actual power consumption is important if one is to optimise and scale-up the process. In addition, both results can be compared to studies performed by using computational fluid dynamics (CFD). It will also be interesting to perform a dimensionless analysis procedure (using Buckingham Pi theorem) so that results can be plotted in terms of dimensionless groups and hence compared to other foaming formulation and processing geometries.

Apart from the above studies, there are many other possibilities for experimental and theoretical work. The model fluids adopted in this thesis can be rendered more complex by adding additional ingredients such as oil, fat and other emulsifying agents such as whey protein, class II Hydrophobins and food-grade particles. Apart from imparting complexities so that it mimics the real-life formulation, the addition of such ingredients can also bring additional complexities such as synergistic capabilities which needs to be considered and investigated accordingly.

7.2.3 Dynamic interactions of foamed viscous shear-thinning fluids with an orifice flow constriction

Presently, there are very few empirical studies dedicated to the flow of wet foams through processing geometries. In this thesis, a systematic empirical study was conducted to shed some light on the possible mechanisms and interaction of wet foams with a narrow orifice aperture as a flow constriction. The wet foams studied were opaque and hence were more difficult to image in-situ just before and after the flow constriction. Therefore, primarily, any future work should focus on how to improve the in-situ foam imaging acquisition technique so that a more accurate and more representative foam microstructure is obtained just before and after the flow constriction. One experimental possibility is by diverting the flow into an X-ray micro-CT

device and analysing the foam microstructure in 3D just before and after the flow constriction. In addition, theoretical simulation can be performed using, for example, computational fluid dynamics (CFD) so that the actual mechanism and forces responsible for the bubble deformation and coalescence are obtained.

Apart from the orifice flow constriction, any potential future studies should also focus on implementing additional flow geometries such as a 2D Hele-Shaw cell, perforated plates, converging-diverging nozzles, etc. In the former geometry, a much detailed microstructural and flow information can be obtained such as the velocity profile, pressure drop, foam morphology, texture sensor, individual bubble deformation and breakage. Similarly, the model fluid recipe can be rendered more complex by adding, for example, fat and oil so that it can better mimic the formulation of ice cream and whipped cream. Such foams are likely to be more dynamically stable and hence more interesting to study. In addition, alternative surfactants such as class II Hydrophobins, which have shown incredible static stability, can be added to increase both foam static and dynamic stability.

7.2.4 Rheological properties of wet foams generated from viscous pseudoplastic fluids

Simultaneous in-situ visualisation foam visualisation and rheometry studies of complex fluids (such as foams, emulsions and suspensions) is vital for a wide range of industries. Currently, there are very limited studies dedicated to such complex systems and hence the possibility of extending the in-situ foam visualisation developed in this work is numerous. For instance, one can look at the behaviour of polydispersed foams with larger air bubbles under parallel plate and cone-plate geometries. In such foams, when operating at a higher shear rates, the bubbles

are more likely to deform and break. Therefore, a detailed study can be conducted so that the actual mechanisms responsible for the shear-induced migration of liquid and bubble breakage are deciphered. One can also look at ways of improving the image acquisition technique so that an automatic image analysis is made possible so that a detailed microstructural transformation during flow is obtained.

In the food processing and related industries, apart from the commonly measured shear stresses, normal, elongational and extensional forces also play a major role. Therefore, it will be interesting to study these forces in detail so that a complete picture of the rheological properties is obtained. Extensional rheology can be performed using, for instance, the Cambridge Trimaster filament thinning and breakup device commonly known as CaBER.

8. Appendix

8.1 Matlab code for detection of spherical bubbles

```
%% Turn off warning messages
warning('off','images:imfindcircles:warnForSmallRadius');
warning('off','images:initSize:adjustingMag');
warning('off','images:imfindcircles:warnForLargeRadiusRange');

%% Numbers of files in input folder
files = [];
Input folder = 'Images';    % Input folder name

j=1;
%% Read files and analyse circles
for i=1:length(files)
   clear image centres
   filename=num2str(files(i));
   image=imread([Inputfolder '/' filename],'BMP');
   [centres,radii_a] = imfindcircles(image, [5 20], 'ObjectPolarity','dark');

   if i==1
      radii(:,i)=radii_a;
   end
   if i~=1
      j=length(radii_a);
      k=length(radii(:,i-1));
      radii(end+1:j,i-1)=nan;
      %for a=j:k
         %radii(a,i-1)=[];
      %end
      %radii([j:k],i-1)=zeros(k-j,1);
      radii(:,i)=radii_a;
   end
   circles(i) = length(radii(:,i));    %number of circles
   figure(i)
   imshow(image);
   ax(i)=gca;
   viscircles(ax(i),centres,radii(:,i));
   pause(1);
   disp(['Image ',num2str(i),' has ',num2str(circles(i)),' circles']);
end
```

8.2 Mean and standard deviation against number of bubbles counted

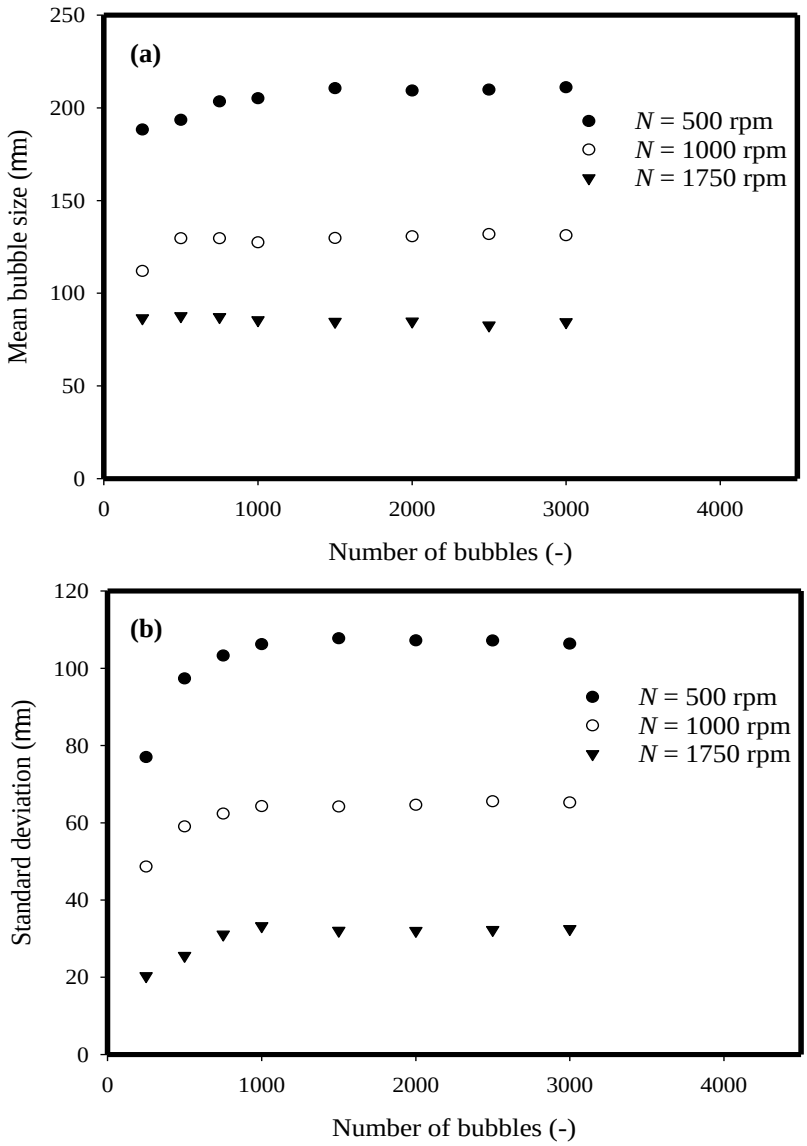

Figure 8.1: Effect of number of bubbles analysed on mean and standard deviation for foam generated from fluid MF2 ar G/L = 1.0.

8.3 Detailed calculation for determining the amount of PGE 55 needed to fully stabilise a given amount of air-water interface

For effective foaming operation, it is essential to determine the optimum amount of surfactant needed to fully stabilise a given air-water interface. Non-ionic surfactants such as PGE 55 has a very low critical aggregation concentration (cac), i.e. the concentration above which vesicles are formed. In the case of PGE 55, this is indeed the case since the cac has been found to be very low (0.00001 wt%). Therefore, it is essential to estimate the amount of PGE 55 needed to stabilise a given amount of dispersion. In the literature, the effective area occupied by the headgroup of PGE 55 is found to be 3 nm^2 (Duerr-Auster *et al.*, 2007). By knowing this, the amount of PGE needed to stabilise a total volume of 200 mL dispersion of 60% air volume fraction can be estimated as follows:

$$Total\ surface\ area = number\ of\ bubbles \times surface\ of\ the\ bubble \quad (Eq.8.1)$$

$$number\ of\ bubbles = \frac{volume\ of\ air\ (\phi) \times total\ volume}{volume\ of\ bubble} \quad (Eq.8.2)$$

$$volume\ of\ bubble = \frac{4}{3}\pi\left(\frac{D_{32}}{2}\right)^3 \quad (Eq.8.3)$$

$$area\ of\ bubble = 4\pi\left(\frac{D_{32}}{2}\right)^2 \quad (Eq.8.4)$$

$$Total\ surface\ area\ (T_s) = \frac{6 \times \phi \times total\ volume}{D_{32}} \quad (Eq.8.5)$$

$$m_{PGE\ 55} = \frac{T_s \times molecular\ weight\ of\ PGE\ 55}{a_0 \times Avogadro's\ number} \quad (Eq.8.6)$$

Where the Avogadro's number equal to 6.022×10^{23} mol^{-1} and the molecular weight of PGE 55 is found to be 770 mol g^{-1} (Tchuenbou-Magaia, 2012). By substituting the relevant numbers in the above Eq. 8.1-8.6, the amount of PGE 55 needed to fully stabilise the dispersion is 0.012 g which is smaller than the amount added to each model fluids (0.066 g for MF1, 0.164 g for MF2 and 0.328 g for MF3). Even though, the calculation above predicts that there is enough PGE 55 available to fully stabilise the air-water interface, however, it is important to remember that this particular commercially available surfactant contains impurities including traces amount of charged species which can have an influence on the surface coverage.

8.4 Determination of Reynold's number through narrow orifice plates:

The Reynold's number through the narrow orifice plates was computed using Eq. 8.7 and 8.8 below derived for non-Newtonian incompressible fluids (Rituraj and Vacca, 2017).

$$\dot{\gamma} = \frac{3n+1}{4n} \times \frac{132 Q_f}{\pi d_0^3} \qquad (Eq. 8.7)$$

$$Re = \frac{\rho_f v_f d_0}{\mu_{fapp}} = \frac{4 \rho_f Q_f}{\pi d_0 \mu_{fapp}} \qquad (Eq. 8.8)$$

$$\beta = \frac{d_0}{D} \qquad (Eq. 8.9)$$

Where n is the power law index, d_0 is the orifice diameter, D is the pipe diameter, v_f is the foam velocity, Q_f is the foam volumetric flowrate and μ_{fapp} is the foam apparent viscosity measured offline by taking sample at the outlet of rotor-stator device (Rituraj and Vacca, 2017). Note, the above procedure does not take into account foam compressibility and expansion.

References

ALARGOVA, R. G., WARHADPANDE, D. S., PAUNOV, V. N. & VELEV, O. D. 2004. Foam Superstabilization by Polymer Microrods. *Langmuir,* 20**,** 10371-10374.

ARJMANDI-TASH, O., TRYBAŁA, A., MAHDI, F., KOVALCHUK, N. & STAROV, V. 2016. Foams Built Up by Non-Newtonian Polymeric Solutions: Free Drainage. *Colloids and Surfaces A: Physicochemical and Engineering Aspects*.

ARONSON, A. S., BERGERON, V., FAGAN, M. E. & RADKE, C. J. 1994. The influence of disjoining pressure on foam stability and flow in porous media. *Colloids and Surfaces A: Physicochemical and Engineering Aspects,* 83**,** 109-120.

ASGHARI, A. K., NORTON, I., MILLS, T., SADD, P. & SPYROPOULOS, F. 2016. Interfacial and foaming characterisation of mixed protein-starch particle systems for food-foam applications. *Food Hydrocolloids,* 53**,** 311-319.

BADVE, M. & BARIGOU, M. 2020. Local description of foam flow, deformation and pressure drop in narrow constricted channels. *International Journal of Multiphase Flow,* 128**,** 103279.

BALERIN, C., AYMARD, P., DUCEPT, F., VASLIN, S. & CUVELIER, G. 2007. Effect of formulation and processing factors on the properties of liquid food foams. *Journal of Food Engineering,* 78**,** 802-809.

BARIGOU, M., DESHPANDE, N. S. & WIGGERS, F. N. 2001. An enhanced electrical resistance technique for foam drainage measurement. *Colloids and Surfaces A: Physicochemical and Engineering Aspects,* 189**,** 237-246.

BARIGOU, M. & DOUAIRE, M. 2013. 9 - X-ray micro-computed tomography for resolving food microstructures. *In:* MORRIS, V. J. & GROVES, K. (eds.) *Food Microstructures.* Woodhead Publishing.

BARNES, H. A., JOHN FLETCHER HUTTON, K. W. H. A. B., HUTTON, J. F. & WALTERS, K. 1989. *An Introduction to Rheology,* Elsevier Science.

BIKERMAN, J. J. 1973. *Foams,* New York, Springer-Verlag.

BINKS, B. P. 2002. Particles as surfactants—similarities and differences. *Current Opinion in Colloid & Interface Science,* 7**,** 21-41.

BISPERINK, C. G. J., RONTELTAP, A. D. & PRINS, A. 1992. Bubble-size distributions in foams. *Advances in Colloid and Interface Science,* 38**,** 13-32.

BLIJDENSTEIN, T. B. J., GANZEVLES, R. A., DE GROOT, P. W. N. & STOYANOV, S. D. 2013. On the link between surface rheology and foam disproportionation in mixed hydrophobin HFBII and whey protein systems. *Colloids and Surfaces A: Physicochemical and Engineering Aspects,* 438**,** 13-20.

BOGDANOVIC, M., GAJBHIYE, R. N. & KAM, S. I. 2009. Experimental study of foam flow in horizontal pipes: Two flow regimes and its implications. *Colloids and Surfaces A: Physicochemical and Engineering Aspects,* 344**,** 56-71.

BOYD, J., BUICK, J. M. & GREEN, S. 2007. Analysis of the Casson and Carreau-Yasuda non-Newtonian blood models in steady and oscillatory flows using the lattice Boltzmann method. 19**,** 093103.

BRICEÑO, M. I. & JOSEPH, D. D. 2003. Self-lubricated transport of aqueous foams in horizontal conduits. *International Journal of Multiphase Flow,* 29**,** 1817-1831.

BURKE, J., COX, A., PETKOV, J. & MURRAY, B. S. 2014. Interfacial rheology and stability of air bubbles stabilized by mixtures of hydrophobin and β-casein. *Food Hydrocolloids,* 34**,** 119-127.

CALABRESE, R. V., CHANG, T. P. K. & DANG, P. T. 1986. Drop breakup in turbulent stirred-tank contactors. Part I: Effect of dispersed-phase viscosity. *AIChE Journal,* 32**,** 657-666.

CALVERT, J. R. 1988. The flow of foam through constrictions. *International Journal of Heat and Fluid Flow,* 9**,** 69-73.

CALVERT, J. R. 1990. Pressure drop for foam flow through pipes. *International Journal of Heat and Fluid Flow,* 11**,** 236-241.

CAMPBELL, G. M. & MOUGEOT, E. 1999. Creation and characterisation of aerated food products. *Trends in Food Science & Technology,* 10**,** 283-296.

CHEN, M., SALA, G., MEINDERS, M. B. J., VAN VALENBERG, H. J. F., VAN DER LINDEN, E. & SAGIS, L. M. C. 2017. Interfacial properties, thin film stability and foam stability of casein micelle dispersions. *Colloids and Surfaces B: Biointerfaces,* 149**,** 56-63.

CHESTERTON, A. K. S., DE ABREU, D. A. P., MOGGRIDGE, G. D., SADD, P. A. & WILSON, D. I. 2013. Evolution of cake batter bubble structure and rheology during planetary mixing. *Food and Bioproducts Processing,* 91**,** 192-206.

COSTEUX, S., BARGER, M., LUKER, K., BADAMI, A. & WALTON, K. 2011. *Facile TPO dispersion using extensional mixing*.

COX, A. R., ALDRED, D. L. & RUSSELL, A. B. 2009. Exceptional stability of food foams using class II hydrophobin HFBII. *Food Hydrocolloids,* 23**,** 366-376.

COX, A. R., CAGNOL, F., RUSSELL, A. B. & IZZARD, M. J. 2007. Surface Properties of Class II Hydrophobins from Trichoderma reesei and Influence on Bubble Stability. *Langmuir,* 23**,** 7995-8002.

COX, P. W. & HOOLEY, P. 2009. Hydrophobins: New prospects for biotechnology. *Fungal Biology Reviews,* 23**,** 40-47.

CULLEN, P. J. 2009. *Food Mixing: Principles and Applications*, Wiley.

CURSCHELLAS, C., GUNES, D. Z., DEYBER, H., WATZKE, B., WINDHAB, E. & LIMBACH, H. J. 2012a. Interfacial aspects of the stability of polyglycerol ester covered bubbles against coalescence. *Soft Matter,* 8**,** 11620-11631.

CURSCHELLAS, C., KELLER, R., BERGER, R., RIETZLER, U., FELL, D., BUTT, H.-J. & LIMBACH, H. J. 2012b-a. Scanning force microscopy as a tool to investigate the properties of polyglycerol ester foams. *Journal of Colloid and Interface Science,* 374**,** 164-175.

CURSCHELLAS, C., KELLER, R., BERGER, R., RIETZLER, U., FELL, D., BUTT, H. J. & LIMBACH, H. J. 2012b-b. Scanning force microscopy as a tool to investigate the properties of polyglycerol ester foams. *J Colloid Interface Sci,* 374**,** 164-75.

CURSCHELLAS, C., KOHLBRECHER, J., GEUE, T., FISCHER, P., SCHMITT, B., ROUVET, M., WINDHAB, E. J. & LIMBACH, H. J. 2013. Foams Stabilized by Multilamellar Polyglycerol Ester Self-Assemblies. *Langmuir,* 29**,** 38-49.

CURSCHELLAS, C., NAGY, K., WINDHAB, E. & LIMBACH, H. J. 2013b. Characteristics of polyglycerol ester and its different fractions. *Journal of Colloid and Interface Science,* 393**,** 182-191.

DABESTANI, M. & YEGANEHZAD, S. 2019. Effect of Persian gum and Xanthan gum on foaming properties and stability of pasteurized fresh egg white foam. *Food Hydrocolloids*, 87**,** 550-560.

DAKHIL, H., AUHL, D. & WIERSCHEM, A. 2019. Infinite-shear viscosity plateau of salt-free aqueous xanthan solutions. *Journal of Rheology,* 63**,** 63-69.

DALEN, G. & KOSTER, M. 2012. *2D & 3D particle size analysis of micro-CT images*.

DAMODARAN, S. 2005. Protein Stabilization of Emulsions and Foams. *Journal of Food Science,* 70**,** R54-R66.

DAUGELAITE, D. 2011. *TIME DEPENDENT STUDIES OF FOAM STABILITY USING IMAGE ANALYSIS, ELECTRICAL RESISTIVITY AND ULTRASOUND* Doctor of Philosophy, Univeristy of Manitoba.

DAUGELAITE, D., GUILLERMIC, R. M., SCANLON, M. G. & PAGE, J. H. 2016. Quantifying liquid drainage in egg-white sucrose foams by resistivity measurements. *Colloids and Surfaces A: Physicochemical and Engineering Aspects,* 489**,** 241-248.

DESHPANDE, N. S. & BARIGOU, M. 2000. The flow of gas–liquid foams in vertical pipes. *Chemical Engineering Science,* 55**,** 4297-4309.

DESHPANDE, N. S. & BARIGOU, M. 2001. The flow of gas–liquid foams through pipe fittings. *International Journal of Heat and Fluid Flow,* 22**,** 94-101.

DESHPANDE, N. S. & BARIGOU, M. 2001a. Foam flow phenomena in sudden expansions and contractions. *International Journal of Multiphase Flow,* 27**,** 1463-1477.

DESHPANDE, N. S. & BARIGOU, M. 2001b. The flow of gas–liquid foams through pipe fittings. *International Journal of Heat and Fluid Flow,* 22**,** 94-101.

DICKINSON, E. 2010. Food emulsions and foams: Stabilization by particles. *Current Opinion in Colloid & Interface Science,* 15**,** 40-49.

DICKINSON, E., ETTELAIE, R., MURRAY, B. S. & DU, Z. 2002. Kinetics of disproportionation of air bubbles beneath a planar air-water interface stabilized by food proteins. *J Colloid Interface Sci,* 252**,** 202-13.

DICKINSON, E. & MCCLEMENTS, D. J. 1995. *Advances In Food Colloids,* Springer US.

DIMITROVA, L. M., BONEVA, M. P., DANOV, K. D., KRALCHEVSKY, P. A., BASHEVA, E. S., MARINOVA, K. G., PETKOV, J. T. & STOYANOV, S. D. 2016. Limited coalescence and Ostwald ripening in emulsions stabilized by hydrophobin HFBII and milk proteins. *Colloids and Surfaces A: Physicochemical and Engineering Aspects,* 509**,** 521-538.

DIMITROVA, L. M., PETKOV, P. V., KRALCHEVSKY, P. A., STOYANOV, S. D. & PELAN, E. G. 2017. Production and characterization of stable foams with fine bubbles from solutions of hydrophobin HFBII and its mixtures with other proteins. *Colloids and Surfaces A: Physicochemical and Engineering Aspects,* 521**,** 92-104.

DJELVEH, G. & GROS, J. B. 1995. Estimation of physical properties of foamed foods using energy dissipation in scraped-surface heat exchangers. *Journal of Food Engineering,* 26**,** 45-56.

DJELVEH, G., GROS, J. B. & CORNET, J. F. 1998. Foaming process analysis for a stirred column with a narrow annular region. *Chemical Engineering Science,* 53**,** 3157-3160.

DRENCKHAN, W. & SAINT-JALMES, A. 2015. The science of foaming. *Adv Colloid Interface Sci,* 222**,** 228-59.

DU, D., ZHANG, J., SUN, S., ZHANG, N., WANG, D. & LI, Y. 2015. Mechanistic study on foam lamellae flow characteristics in tubes. *Materials Research Innovations,* 19**,** S5-526-S5-529.

DU, L., DING, Y., PROKOP, A. & TANNER, R. D. 2001. Measurement of bubble size distribution in protein foam fractionation column using capillary probe with photoelectric sensors. *Applied Biochemistry and Biotechnology,* 91**,** 387-404.

DUERR-AUSTER, N., EISELE, T., WEPF, R., GUNDE, R. & WINDHAB, E. J. 2008. Influence of pH on colloidal properties and surface activity of polyglycerol fatty acid ester vesicles. *Journal of Colloid and Interface Science,* 327**,** 446-450.

DUERR-AUSTER, N., GUNDE, R., MÄDER, R. & WINDHAB, E. J. 2009. Binary coalescence of gas bubbles in the presence of a non-ionic surfactant. *Journal of Colloid and Interface Science,* 333**,** 579-584.

DUERR-AUSTER, N., GUNDE, R. & WINDHAB, E. J. 2008. Structure and mechanical properties of a polyglycerol ester at the air-water surface. *Langmuir,* 24**,** 12282-9.

DUERR-AUSTER, N., KOHLBRECHER, J., ZUERCHER, T., GUNDE, R., FISCHER, P. & WINDHAB, E. 2007. Microstructure and Stability of a Lamellar Liquid Crystalline and Gel Phase Formed by a Polyglycerol Ester Mixture in Dilute Aqueous Solution. *Langmuir,* 23**,** 12827-12834.

DURR-AUSTER, N. 2008. *Formation and Stability of a Liquid Foam Prepared from a Lamellar Surfactant Dispersio.* Doctor of Sciences, Swiss Federal Institute of Technology Zurich.

DÜRR-AUSTER, N. 2008. *Formation and Stability of a Liquid Foam Prepared from a Lamellar Surfactant Dispersion.* Doctor of Sciences, Swiss Federal Institute of Technology Zurich.

DUTTA, A., CHENGARA, A., NIKOLOV, A. D., WASAN, D. T., CHEN, K. & CAMPBELL, B. 2004. Destabilization of aerated food products: effects of Ostwald ripening and gas diffusion. *Journal of Food Engineering,* 62**,** 177-184.

EASTOE, J. & TABOR, R. F. 2014. Chapter 6 - Surfactants and Nanoscience. *In:* BERTI, D. & PALAZZO, G. (eds.) *Colloidal Foundations of Nanoscience.* Amsterdam: Elsevier.

EISNER, M. D., JEELANI, S. A. K., BERNHARD, L. & WINDHAB, E. J. 2007. Stability of foams containing proteins, fat particles and nonionic surfactants. *Chemical Engineering Science,* 62**,** 1974-1987.

ELLIS, A. L. & LAZIDIS, A. 2018. Foams for Food Applications. *In:* GUTIÉRREZ, T. J. (ed.) *Polymers for Food Applications.* Cham: Springer International Publishing.

ELLIS, A. L., NORTON, A. B., MILLS, T. B. & NORTON, I. T. 2017. Stabilisation of foams by agar gel particles. *Food Hydrocolloids,* 73**,** 222-228.

EWERT, J., CLAAßEN, W., GLÜCK, C., ZEEB, B., WEISS, J., HINRICHS, J., STRESSLER, T. & FISCHER, L. 2016. A non-invasive method for the characterisation of milk protein foams by image analysis. *International Dairy Journal,* 62**,** 1-9.

EWOLDT, R. H., JOHNSTON, M. T. & CARETTA, L. M. 2015. Experimental Challenges of Shear Rheology: How to Avoid Bad Data. *In:* SPAGNOLIE, S. E. (ed.) *Complex Fluids in Biological Systems: Experiment, Theory, and Computation.* New York, NY: Springer New York.

FAMEAU, A.-L. & SALONEN, A. 2014. Effect of particles and aggregated structures on the foam stability and aging. *Comptes Rendus Physique,* 15**,** 748-760.

FARHADI, H., RIAHI, S., AYATOLLAHI, S. & AHMADI, H. 2016. Experimental study of nanoparticle-surfactant-stabilized CO2 foam: Stability and mobility control. *Chemical Engineering Research and Design,* 111**,** 449-460.

FAUSER, H., VON KLITZING, R. & CAMPBELL, R. A. 2015. Surface Adsorption of Oppositely Charged C14TAB-PAMPS Mixtures at the Air/Water Interface and the Impact on Foam Film Stability. *The Journal of Physical Chemistry B,* 119**,** 348-358.

FISCHER, P. & WINDHAB, E. J. 2011. Rheology of food materials. *Current Opinion in Colloid & Interface Science,* 16**,** 36-40.

FOEGEDING, E. A., LUCK, P. J. & DAVIS, J. P. 2006. Factors determining the physical properties of protein foams. *Food Hydrocolloids,* 20**,** 284-292.

GAILLARD, T., HONOREZ, C., JUMEAU, M., ELIAS, F. & DRENCKHAN, W. 2015. A simple technique for the automation of bubble size measurements. *Colloids and Surfaces A: Physicochemical and Engineering Aspects,* 473**,** 68-74.

GAILLARD, T., ROCHÉ, M., HONOREZ, C., JUMEAU, M., BALAN, A., JEDRZEJCZYK, C. & DRENCKHAN, W. 2017. Controlled foam generation using cyclic diphasic flows through a constriction. *International Journal of Multiphase Flow,* 96**,** 173-187.

GAJBHIYE, R. N. & KAM, S. I. 2012. The effect of inclination angles on foam rheology in pipes. *Journal of Petroleum Science and Engineering,* 86–87**,** 246-256.

GERMAIN, J. C. & AGUILERA, J. M. 2014. Multi-scale properties of protein-stabilized foams. *Food Structure,* 1**,** 55-70.

GHARSALLAOUI, A., CASES, E., CHAMBIN, O. & SAUREL, R. 2009. Interfacial and Emulsifying Characteristics of Acid-treated Pea Protein. *Food Biophysics,* 4**,** 273-280.

GOLEMANOV, K., TCHOLAKOVA, S., DENKOV, N. D., ANANTHAPADMANABHAN, K. P. & LIPS, A. 2008. Breakup of bubbles and drops in steadily sheared foams and concentrated emulsions. *Physical Review E,* 78**,** 051405.

GRACE†, H. P. 1982. DISPERSION PHENOMENA IN HIGH VISCOSITY IMMISCIBLE FLUID SYSTEMS AND APPLICATION OF STATIC MIXERS AS DISPERSION DEVICES IN SUCH SYSTEMS. *Chemical Engineering Communications,* 14**,** 225-277.

GREEN, A. J., LITTLEJOHN, K. A., HOOLEY, P. & COX, P. W. 2013. Formation and stability of food foams and aerated emulsions: Hydrophobins as novel functional ingredients. *Current Opinion in Colloid & Interface Science,* 18**,** 292-301.

GRIFFIN, W. C. 1949. Classification of surface-active agents by "HLB". *J. Soc. Cosmet. Chem.,* 1**,** 311-326.

GUO, E., ZENG, G., KAZANTSEV, D., ROCKETT, P., BENT, J., KIRKLAND, M., VAN DALEN, G., EASTWOOD, D. S., STJOHN, D. & LEE, P. D. 2017. Synchrotron X-ray tomographic quantification of microstructural evolution in ice cream – a multi-phase soft solid. *RSC Advances,* 7**,** 15561-15573.

GUPTA, M., HOOGHTEN, R. V., FISCHER, P., GUNES, D. Z. & VERMANT, J. 2016. Limiting coalescence by interfacial rheology: over-compressed polyglycerol ester layers. *Rheologica Acta,* 55**,** 537-546.

HABIBI, M., DINKGREVE, M., PAREDES, J., DENN, M. M. & BONN, D. 2016. Normal stress measurement in foams and emulsions in the presence of slip. *Journal of Non-Newtonian Fluid Mechanics,* 238**,** 33-43.

HAEDELT, J., PYLE, D. L., BECKETT, S. T. & NIRANJAN, K. 2005. Vacuum-induced Bubble Formation in Liquid-tempered Chocolate. *Journal of Food Science,* 70**,** E159-E164.

HALL, S., COOKE, M., EL-HAMOUZ, A. & KOWALSKI, A. J. 2011. Droplet break-up by in-line Silverson rotor–stator mixer. *Chemical Engineering Science,* 66**,** 2068-2079.

HANSELMANN, W. & WINDHAB, E. 1998. Flow characteristics and modelling of foam generation in a continuous rotor/stator mixer. *Journal of Food Engineering,* 38**,** 393-405.

HEKTOR, H. J. & SCHOLTMEIJER, K. 2005. Hydrophobins: proteins with potential. *Current Opinion in Biotechnology,* 16**,** 434-439.

HELLER, J. P. & KUNTAMUKKULA, M. S. 1987. Critical review of the foam rheology literature. *Industrial & Engineering Chemistry Research,* 26**,** 318-325.

HERZHAFT, B., KAKADJIAN, S. & MOAN, M. 2005. Measurement and modeling of the flow behavior of aqueous foams using a recirculating pipe rheometer. *Colloids and Surfaces A: Physicochemical and Engineering Aspects,* 263**,** 153-164.

HEUER, A., COX, A. R., SINGLETON, S., BARIGOU, M. & GINKEL, M.-V. 2007. Visualisation of foam microstructure when subject to pressure change. *Colloids and Surfaces A: Physicochemical and Engineering Aspects,* 311**,** 112-123.

HINZE, J. O. 1955. Fundamentals of the hydrodynamic mechanism of splitting in dispersion processes. *AIChE Journal,* 1**,** 289-295.

HOFFER, M. S. & RUBIN, E. 1969. Flow Regimes of Stable Foams. *Industrial & Engineering Chemistry Fundamentals,* 8**,** 483-490.

HOROZOV, T. S. 2008. Foams and foam films stabilised by solid particles. *Current Opinion in Colloid & Interface Science,* 13**,** 134-140.

IJMER, J., REZA, C. & ARIFFIN, B. S. 2014. *Measurement of the Thickness of Thin Foam Films by Laser Interferometry*.

INDRAWATI, L. & NARSIMHAN, G. 2008. Characterization of protein stabilized foam formed in a continuous shear mixing apparatus. *Journal of Food Engineering,* 88**,** 456-465.

IVANOV, I. B., DANOV, K. D. & KRALCHEVSKY, P. A. 1999. Flocculation and coalescence of micron-size emulsion droplets. *Colloids and Surfaces A: Physicochemical and Engineering Aspects,* 152**,** 161-182.

JABARKHYL, S., BARIGOU, M., BADVE, M. & ZHU, S. 2020. Rheological properties of wet foams generated from viscous pseudoplastic fluids. *Innovative Food Science & Emerging Technologies***,** 102304.

JABARKHYL, S., BARIGOU, M., ZHU, S., RAYMENT, P., LLOYD, D. M. & ROSSETTI, D. 2019. Foams generated from viscous non-Newtonian shear-thinning liquids in a continuous multi rotor-stator device. *Innovative Food Science & Emerging Technologies***,** 102231.

JAKUBCZYK, E. & NIRANJAN, K. 2006a. Transient development of whipped cream properties. *Journal of Food Engineering,* 77**,** 79-83.

JAKUBCZYK, E. & NIRANJAN, K. 2006b. Transient development of whipped cream properties. *Journal of Food Engineering - J FOOD ENG,* 77**,** 79-83.

JANG, W., NIKOLOV, A., WASAN, D. T., CHEN, K. & CAMPBELL, B. 2005. Prediction of the Bubble Size Distribution during Aeration of Food Products. *Industrial & Engineering Chemistry Research,* 44**,** 1296-1308.

K. S. CHESTERTON, A., E. MEZA, B., MOGGRIDGE, G., A. SADD, P. & WILSON, I. 2011. *Rheological characterisation of cake batters generated by planetary mixing: Elastic versus viscous effects*.

KABZIŃSKI, M., NEUPAUER, K., NOWAK, M., KRUK, J. & KACZMARCZYK, K. 2019. The impact of addition of xanthan gum and guar gum on rheological properties of foams produced by continuous method. *Polimery,* 64**,** 538-541.

KARAKASHEV, S. I. & GROZDANOVA, M. V. 2012. Foams and antifoams. *Advances in Colloid and Interface Science,* 176-177**,** 1-17.

KATZBAUER, B. 1998. Properties and applications of xanthan gum. *Polymer Degradation and Stability,* 59**,** 81-84.

KHAN, S. A., SCHNEPPER, C. A. & ARMSTRONG, R. C. 1988. Foam Rheology: III. Measurement of Shear Flow Properties. *Journal of Rheology,* 32**,** 69-92.

KHRISTOV, K., EXEROWA, D. & MINKOV, G. 2002. Critical capillary pressure for destruction of single foam films and foam: effect of foam film size. *Colloids and Surfaces A: Physicochemical and Engineering Aspects,* 210**,** 159-166.

KIM, I., WORTHEN, A. J., JOHNSTON, K. P., DICARLO, D. A. & HUH, C. 2016. Size-dependent properties of silica nanoparticles for Pickering stabilization of emulsions and foams. *Journal of Nanoparticle Research,* 18**,** 82.

KOSTOGLOU, M., GEORGIOU, E. & KARAPANTSIOS, T. D. 2011. A new device for assessing film stability in foams: Experiment and theory. *Colloids and Surfaces A: Physicochemical and Engineering Aspects,* 382**,** 64-73.

KRÄGEL, J., DERKATCH, S. R. & MILLER, R. 2008. Interfacial shear rheology of protein–surfactant layers. *Advances in Colloid and Interface Science,* 144**,** 38-53.

KRALOVA, I. & SJÖBLOM, J. 2009. Surfactants Used in Food Industry: A Review. *Journal of Dispersion Science and Technology,* 30**,** 1363-1383.

KREITH, F., MANGLIK, R. M. & BOHN, M. S. 2012. *Principles of Heat Transfer, SI Edition,* Cengage Learning.

KROEZEN, A. B. J., GROOT WASSINK, J. & BERTLEIN, E. 1988a. Foam generation in a rotor—stator mixer. *Chemical Engineering and Processing: Process Intensification,* 24**,** 145-156.

KROEZEN, A. B. J., GROOT WASSINK, J. & BERTLEIN, E. 1988b. Foam generation in a rotor—stator mixer: schaumerzeugung in einem rotor—stator mischer. *Chemical Engineering and Processing: Process Intensification,* 24**,** 145-156.

KROEZEN, A. B. J. & WASSINK, J. G. 1987. Bubble size distribution and energy dissipation in foam mixers. *Journal of the Society of Dyers and Colourists,* 103**,** 386-394.

KRUGLYAKOV, P. M., KARAKASHEV, S. I., NGUYEN, A. V. & VILKOVA, N. G. 2008. Foam drainage. *Current Opinion in Colloid & Interface Science,* 13**,** 163-170.

KRUSTEV, R. & MÜLLER, H. J. 1999. Effect of Film Free Energy on the Gas Permeability of Foam Films. *Langmuir,* 15**,** 2134-2141.

KULMYRZAEV, A., BRYANT, C. & MCCLEMENTS, D. 2000. Influence of Sucrose on the Thermal Denaturation, Gelation, and Emulsion Stabilization of Whey Proteins. *Journal of agricultural and food chemistry,* 48**,** 1593-7.

KULMYRZAEV, A., CANCELLIERE, C. & MCCLEMENTS, D. J. 2000. Characterization of aerated foods using ultrasonic reflectance spectroscopy. *Journal of Food Engineering,* 46**,** 235-241.

LAM, S., VELIKOV, K. P. & VELEV, O. D. 2014. Pickering stabilization of foams and emulsions with particles of biological origin. *Current Opinion in Colloid & Interface Science,* 19**,** 490-500.

LAPORTE, M., DELLA VALLE, D., LOISEL, C., MARZE, S., RIAUBLANC, A. & MONTILLET, A. 2015. Rheological properties of food foams produced by SMX static mixers. *Food Hydrocolloids,* 43**,** 51-57.

LAPORTE, M., LOISEL, C., DELLA VALLE, D., RIAUBLANC, A. & MONTILLET, A. 2014. Flow process conditions to control the void fraction of food foams in static mixers. *Journal of Food Engineering,* 128**,** 119-126.

LAPORTE, M., MONTILLET, A., DELLA VALLE, D., LOISEL, C. & RIAUBLANC, A. 2016. Characteristics of foams produced with viscous shear thinning fluids using microchannels at high throughput. *Journal of Food Engineering,* 173**,** 25-33.

LATIEF, F., MOHAMMAD, I. & RARASATI, A. 2019. Pore structure characterization of concrete mixtures with different aggregates using digital image processing and analysis. *Journal of Physics: Conference Series,* 1280**,** 022078.

LAZIDIS, A., HANCOCKS, R. D., SPYROPOULOS, F., KREUß, M., BERROCAL, R. & NORTON, I. T. 2016. Whey protein fluid gels for the stabilisation of foams. *Food Hydrocolloids,* 53**,** 209-217.

LECH, F. J., WIERENGA, P. A., GRUPPEN, H. & MEINDERS, M. B. J. 2015. Stability Properties of Surfactant-Free Thin Films at Different Ionic Strengths: Measurements and Modeling. *Langmuir,* 31**,** 2777-2782.

LENG, D. & CALABRESE, R. 2004. Immiscible Liquid–Liquid Systems.

LESZCZYŃSKI, B., GANCARCZYK, A., WRÓBEL, A., PIĄTEK, M., ŁOJEWSKA, J., KOŁODZIEJ, A. & PĘDRYS, R. 2016. Global and Local Thresholding Methods Applied to X-ray Microtomographic Analysis of Metallic Foams. *Journal of Nondestructive Evaluation,* 35**,** 35.

LEXIS, M. 2015. *Rheology of Protein Foams.* Doctor of Philosphy, Karlsruhe Institute of Technology.

LEXIS, M. & WILLENBACHER, N. 2014. Yield stress and elasticity of aqueous foams from protein and surfactant solutions – The role of continuous phase viscosity and interfacial properties. *Colloids and Surfaces A: Physicochemical and Engineering Aspects,* 459**,** 177-185.

LIM, K. S. & BARIGOU, M. 2004. X-ray micro-computed tomography of cellular food products. *Food Research International,* 37**,** 1001-1012.

LINDER, M. B. 2009. Hydrophobins: Proteins that self assemble at interfaces. *Current Opinion in Colloid & Interface Science,* 14**,** 356-363.

LISZKA-SKOCZYLAS, M., PTASZEK, A. & ŻMUDZIŃSKI, D. 2014. The effect of hydrocolloids on producing stable foams based on the whey protein concentrate (WPC). *Journal of Food Engineering,* 129**,** 1-11.

LV, Q., LI, Z., LI, B., LI, S. & SUN, Q. 2015. Study of Nanoparticle–Surfactant-Stabilized Foam as a Fracturing Fluid. *Industrial & Engineering Chemistry Research,* 54**,** 9468-9477.

MAESTRO, A., GUZMÁN, E., ORTEGA, F. & RUBIO, R. G. 2014. Contact angle of micro- and nanoparticles at fluid interfaces. *Current Opinion in Colloid & Interface Science,* 19**,** 355-367.

MAESTRO, A., SANTINI, E., ZABIEGAJ, D., LLAMAS, S., RAVERA, F., LIGGIERI, L., ORTEGA, F., RUBIO, R., #XF3, G., N. & GUZMAN, E. 2015. Particle and Particle-Surfactant Mixtures at Fluid Interfaces: Assembly, Morphology, and Rheological Description. *Advances in Condensed Matter Physics,* 2015**,** 17.

MAGARKAR, A., MELE, N., ABDEL-RAHMAN, N., BUTCHER, S., TORKKELI, M., SERIMAA, R., PAANANEN, A., LINDER, M. & BUNKER, A. 2014. Hydrophobin Film Structure for HFBI and HFBII and Mechanism for Accelerated Film Formation. *PLoS Comput Biol,* 10.

MALDONADO-VALDERRAMA, J. & LANGEVIN, D. 2008. On the difference between foams stabilized by surfactants and whole casein or beta-casein. comparison of foams, foam films, and liquid surfaces studies. *J Phys Chem B,* 112**,** 3989-96.

MARIGO, M., DESHPANDE, N. & WIGGERS, F. 2001. An enhanced electrical resistance technique for foam drainage measurement. *Colloids and Surfaces A-physicochemical and Engineering Aspects - COLLOID SURFACE A,* 189**,** 237-246.

MARY, G., MEZDOUR, S., DELAPLACE, G., LAUHON, R., CUVELIER, G. & DUCEPT, F. 2013. Modelling of the continuous foaming operation by dimensional analysis. *Chemical Engineering Research and Design,* 91**,** 2579-2586.

MASSEY, A. H. & NIRANJAN, K. 2001. Air Inclusion Into a Model Cake Batter Using a Pressure Whisk: Development of Gas Hold-up and Bubble Size Distribution. *Journal of Food Science,* 66**,** 1152-1157.

MCCLEMENTS, D. J. 2004. Protein-stabilized emulsions. *Current Opinion in Colloid & Interface Science,* 9**,** 305-313.

MENDEZ, N. F. G., DJELVEH, G. & GROS, J. B. 1993. Performance of Scraped Surface Heat Exchangers in Foaming Food Processes. *LWT - Food Science and Technology,* 26**,** 538-543.

METZNER, A. B. & REED, J. C. 1955. Flow of non-newtonian fluids—correlation of the laminar, transition, and turbulent-flow regions. *AIChE Journal,* 1**,** 434-440.

MEZDOUR, S., SÉGUINEAU DE PRÉVAL, E., GRANDA, P., CUVELIER, G. & DUCEPT, F. 2017. *Impact of Interfacial Characteristics on Foam Structure: Study on Model Fluids and at Pilot Scale*.

MÜLLER-FISCHER, N., BLEULER, H. & WINDHAB, E. J. 2007a. Dynamically enhanced membrane foaming. *Chemical Engineering Science,* 62**,** 4409-4419.

MÜLLER-FISCHER, N., SUPPIGER, D. & WINDHAB, E. J. 2007b. Impact of static pressure and volumetric energy input on the microstructure of food foam whipped in a rotor–stator device. *Journal of Food Engineering,* 80**,** 306-316.

MÜLLER-FISCHER, N. & WINDHAB, E. J. 2005. Influence of process parameters on microstructure of food foam whipped in a rotor–stator device within a wide static pressure range. *Colloids and Surfaces A: Physicochemical and Engineering Aspects,* 263**,** 353-362.

MURRAY, B. S. 2007. Stabilization of bubbles and foams. *Current Opinion in Colloid & Interface Science,* 12**,** 232-241.

MURRAY, B. S., DICKINSON, E., GRANSARD, C. & SÖDERBERG, I. 2006. Effect of thickeners on the coalescence of protein-stabilized air bubbles undergoing a pressure drop. *Food Hydrocolloids,* 20**,** 114-123.

MURRAY, B. S., DICKINSON, E., LAU, C. K., NELSON, P. V. & SCHMIDT, E. 2005. Coalescence of Protein-Stabilized Bubbles Undergoing Expansion at a Simultaneously Expanding Planar Air−Water Interface. *Langmuir,* 21**,** 4622-4630.

NAGATA, S. 1975. *Mixing: principles and applications*, Kodansha.

NARCHI, I., VIAL, C. & DJELVEH, G. 2009. Effect of protein–polysaccharide mixtures on the continuous manufacturing of foamed food products. *Food Hydrocolloids,* 23**,** 188-201.

NARCHI, I., VIAL, C., LABBAFI, M. & DJELVEH, G. 2011. Comparative study of the design of continuous aeration equipment for the production of food foams. *Journal of Food Engineering,* 102**,** 105-114.

NGUYEN, A. A. S., H. 2003. *Colloidal Science of Flotation*, CRC Press.

NGUYEN, C. V., YUSA, S.-I. & PHAN, C. M. 2016. Stability of Aqueous Film with a Photo-Responsive Surfactant. *JOURNAL OF CHEMICAL ENGINEERING OF JAPAN,* 49**,** 714-719.

NICOLAI, T. & DURAND, D. 2013. Controlled food protein aggregation for new functionality. *Current Opinion in Colloid & Interface Science,* 18**,** 249-256.

NICORESCU, I., VIAL, C., LOISEL, C., RIAUBLANC, A., DJELVEH, G., CUVELIER, G. & LEGRAND, J. 2010. *Influence of protein heat treatment on the continuous production of food foams*.

OBOROCEANU, D., WANG, L., MAGNER, E. & AUTY, M. A. E. 2014. Fibrillization of whey proteins improves foaming capacity and foam stability at low protein concentrations. *Journal of Food Engineering,* 121**,** 102-111.

ÖZCAN-TAŞKıN, G., KUBICKI, D. & PADRON, G. 2011. Power and flow characteristics of three rotor-stator heads. *The Canadian Journal of Chemical Engineering,* 89**,** 1005-1017.

PARK, C. & HERMANOWICZ, S. W. 2014. A multi-point electrical resistance measurement system for characterization of foam drainage regime and stability. *AIChE Journal,* 60**,** 3143-3150.

POLITOVA, N., TCHOLAKOVA, S., VALKOVA, Z., GOLEMANOV, K. & DENKOV, N. D. 2018. Self-regulation of foam volume and bubble size during foaming via shear mixing. *Colloids and Surfaces A: Physicochemical and Engineering Aspects,* 539**,** 18-28.

PRIMO-MARTÍN, C., WANG, M., LICHTENDONK, W. J., PLIJTER, J. J. & HAMER, R. J. 2005. An explanation for the combined effect of xylanase–glucose oxidase in dough systems. *Journal of the Science of Food and Agriculture,* 85**,** 1186-1196.

PUGH, R. J. 2016a. *Bubble and Foam Chemistry,* Cambridge UK, Cambridge University Press.

PUGH, R. J. 2016b. Generation of bubbles and foams. *In:* PUGH, R. J. (ed.) *Bubble and Foam Chemistry.* Cambridge: Cambridge University Press.

RAIKOS, V. 2010. Effect of heat treatment on milk protein functionality at emulsion interfaces. A review. *Food Hydrocolloids,* 24**,** 259-265.

RIO, E., DRENCKHAN-ANDREATTA, W., SALONEN, A. & LANGEVIN, D. 2013. Unusually stable Liquid Foams. *Advances in Colloid and Interface Science,* 205.

RITURAJ, F. & VACCA, A. 2017. Modeling the Flow of Non-Newtonian Fluids Through Sharp Orifices. *Journal of Fluids Engineering,* 140.

RODRÍGUEZ PATINO, J. M., DOLORES NARANJO DELGADO, M. & LINARES FERNÁNDEZ, J. 1995. Stability and mechanical strength of aqueous foams containing food proteins. *Colloids and Surfaces A: Physicochemical and Engineering Aspects,* 99**,** 65-78.

SAADATFAR, M., GARCIA-MORENO, F., HUTZLER, S., SHEPPARD, A. P., KNACKSTEDT, M. A., BANHART, J. & WEAIRE, D. 2009. Imaging of metallic foams using X-ray micro-CT. *Colloids and Surfaces A: Physicochemical and Engineering Aspects,* 344**,** 107-112.

SAGIS, L. M. C., DE GROOT-MOSTERT, A. E. A., PRINS, A. & VAN DER LINDEN, E. 2001. Effect of copper ions on the drainage stability of foams prepared from egg white. *Colloids and Surfaces A: Physicochemical and Engineering Aspects,* 180**,** 163-172.

SAHU, J. K. & NIRANJAN, K. 2009. Gas–Liquid Mixing. *Food Mixing.*

SAINT-JALMES, A. 2006. Physical chemistry in foam drainage and coarsening. *Soft Matter,* 2**,** 836-849.

SCHOR, M., REID, J. L., MACPHEE, C. E. & STANLEY-WALL, N. R. 2016. The Diverse Structures and Functions of Surfactant Proteins. *Trends in Biochemical Sciences,* 41**,** 610-620.

SEGUINEAU DE PREVAL, E., FABRICE, D., GÉRARD, C. & SAMIR, M. 2014a. Effect of bulk viscosity and surface tension kinetics on structure of foam generated at the pilot scale. *Food Hydrocolloids,* 34**,** 104-111.

SEGUINEAU DE PREVAL, E., FABRICE, D., GILLES, M., GÉRARD, C. & SAMIR, M. 2014b. Influence of surface properties and bulk viscosity on bubble size prediction during foaming operation. *Colloids and Surfaces A: Physicochemical and Engineering Aspects,* 442**,** 88-97.

SHALABY, H. 2007. ON THE POTENTIAL OF LARGE EDDY SIMULATION TO SIMULATE CYCLONE SEPARATORS.

SHERIF, T., AHMED, R., SHAH, S. & AMANI, M. 2016. Rheological correlations for oil-based drilling foams. *Journal of Natural Gas Science and Engineering,* 35, Part A**,** 1249-1260.

SILVA, S., ESPIGA, A., NIRANJAN, K., LIVINGS, S., GUMY, J.-C. & SHER, A. 2008. Chapter 16 - Formation and Stability of Milk Foams. *In:* CAMPBELL, G. M., SCANLON, M. G. & PYLE, D. L. (eds.) *Bubbles in Food 2.* AACC International Press.

SINGH, H. 2011. Aspects of milk-protein-stabilised emulsions. *Food Hydrocolloids,* 25**,** 1938-1944.

SJOBLOM, J. 2001. *Encyclopedic Handbook of Emulsion Technology*, CRC Press.

SÖDERBERG, I., DICKINSON, E. & MURRAY, B. S. 2003. Coalescence stability of gas bubbles subjected to rapid pressure change at a planar air/water interface. *Colloids and Surfaces B: Biointerfaces,* 30**,** 237-248.

SONG, K.-W., KIM, Y.-S. & CHANG, G.-S. 2006. Rheology of concentrated xanthan gum solutions: Steady shear flow behavior. *Fibers and Polymers,* 7**,** 129-138.

SPAGNOLIE, S. 2015. *Complex Fluids in Biological Systems,* New York, Springer-Verlag

STEIN, D. J. & SPERA, F. J. 1992. Rheology and microstructure of magmatic emulsions: theory and experiments. *Journal of Volcanology and Geothermal Research,* 49**,** 157-174.

STEVENSON, P. 2012. *Foam engineering : fundamentals and applications / edited by Paul Stevenson*, Chichester, West Sussex : Wiley, 2012.

STOCCO, A., RIO, E., BINKS, B. P. & LANGEVIN, D. 2011. Aqueous foams stabilized solely by particles. *Soft Matter,* 7**,** 1260-1267.

TCHOLAKOVA, S., LESOV, I., GOLEMANOV, K., DENKOV, N. D., JUDAT, S., ENGEL, R. & DANNER, T. 2011. Efficient Emulsification of Viscous Oils at High Drop Volume Fraction. *Langmuir,* 27**,** 14783-14796.

TCHUENBOU-MAGAIA, F. L. 2012. *HYDROPHOBINS AND AIR FILLED EMULSIONS.* Doctor of Philosophy, University of Birmingham.

TCHUENBOU-MAGAIA, F. L., NORTON, I. T. & COX, P. W. 2009. Hydrophobins stabilised air-filled emulsions for the food industry. *Food Hydrocolloids,* 23**,** 1877-1885.

THAKUR, R. K., VIAL, C. & DJELVEH, G. 2003. Influence of operating conditions and impeller design on the continuous manufacturing of food foams. *Journal of Food Engineering,* 60**,** 9-20.

THAKUR, R. K., VIAL, C. & DJELVEH, G. 2005. Combined effects of process parameters and composition on foaming of dairy emulsions at low temperature in an agitated column. *Journal of Food Engineering,* 68**,** 335-347.

THAKUR, R. K., VIAL, C., NIGAM, K. D. P., NAUMAN, E. B. & DJELVEH, G. 2003. Static Mixers in the Process Industries—A Review. *Chemical Engineering Research and Design,* 81**,** 787-826.

TORRES, M. D., GADALA-MARIA, F. & WILSON, D. I. 2013. Comparison of the rheology of bubbly liquids prepared by whisking air into a viscous liquid (honey) and a shear-thinning liquid (guar gum solutions). *Journal of Food Engineering,* 118**,** 213-228.

TORRES, M. D., HALLMARK, B. & WILSON, D. I. 2014. Effect of concentration on shear and extensional rheology of guar gum solutions. *Food Hydrocolloids,* 40**,** 85-95.

TORRES, M. D., HALLMARK, B. & WILSON, D. I. 2015a. Effect of bubble volume fraction on the shear and extensional rheology of bubbly liquids based on guar gum (a Giesekus fluid) as continuous phase. *Journal of Food Engineering,* 146**,** 129-142.

TORRES, M. D., HALLMARK, B. & WILSON, D. I. J. R. A. 2015b. Determination of the shear and extensional rheology of bubbly liquids with a shear-thinning continuous phase. 54**,** 461-478.

VANKOVA, N., TCHOLAKOVA, S., DENKOV, N. D., IVANOV, I. B., VULCHEV, V. D. & DANNER, T. 2007. Emulsification in turbulent flow 1. Mean and maximum drop diameters in inertial and viscous regimes. *J Colloid Interface Sci,* 312**,** 363-80.

WALSTRA, P. Principles of Foam Formation and Stability. 1989 London. Springer London, 1-15.

WANG, J., NGUYEN, A. V. & FARROKHPAY, S. 2016. A critical review of the growth, drainage and collapse of foams. *Advances in Colloid and Interface Science,* 228**,** 55-70.

WU, H., SHU, S., YANG, N., LIAN, G., ZHU, S. & LIU, M. 2014. Modeling of power characteristics for multistage rotor–stator mixers of shear-thinning fluids. *Chemical Engineering Science,* 117**,** 173-182.

XIE, Y. R. & HETTIARACHCHY, N. S. 1998. Effect of xanthan gum on enhancing the foaming properties of soy protein isolate. *Journal of the American Oil Chemists' Society,* 75**,** 729.

XU, L., XU, G., LIU, T., CHEN, Y. & GONG, H. 2013. The comparison of rheological properties of aqueous welan gum and xanthan gum solutions. *Carbohydrate Polymers,* 92**,** 516-522.

YASUDA, K., ARMSTRONG, R. C. & COHEN, R. E. 1981. Shear flow properties of concentrated solutions of linear and star branched polystyrenes. *Rheologica Acta,* 20**,** 163-178.

ZAYAS, J. F. 1997. Foaming Properties of Proteins. *In:* ZAYAS, J. F. (ed.) *Functionality of Proteins in Food.* Berlin, Heidelberg: Springer Berlin Heidelberg.

ZHANG, Y., CHANG, Z., LUO, W., GU, S., LI, W. & AN, J. 2015. Effect of starch particles on foam stability and dilational viscoelasticity of aqueous-foam. *Chinese Journal of Chemical Engineering,* 23**,** 276-280.

ZHONG, L., OOSTROM, M., TRUEX, M. J., VERMEUL, V. R. & SZECSODY, J. E. 2013. Rheological behavior of xanthan gum solution related to shear thinning fluid delivery for subsurface remediation. *Journal of Hazardous Materials,* 244–245**,** 160-170.

ŻMUDZIŃSKI, D., PTASZEK, P., KRUK, J., KACZMARCZYK, K., ROŻNOWSKI, W., BERSKI, W., PTASZEK, A. & GRZESIK, M. 2014. The role of hydrocolloids in mechanical properties of fresh foams based on egg white proteins. *Journal of Food Engineering,* 121**,** 128-134.

ZOHEIDI, L., CHIN, H., RAUH, C. & DELGADO, A. 2016. Flow Characterization of Milk Protein Foam Transport in Horizontal Channels. *Journal of Food Process Engineering***,** n/a-n/a.